Tesi di Dottorato, Version 1
May 19, 2005

Measurement of the CKM angle γ with a D^0 Dalitz analysis of the $B^{\pm} \to D^{(*)}K^{\pm}$ decays in BaBar

Nicola Neri

Università di Pisa & INFN Pisa, Italy

Contents

Introduction

The primary goal of the *BABAR* experiment, is the detection of the *CP* violation in the B system via the precise measurement of the elements of the CKM matrix in order to verify the consistency of the Standard Model Theory (SM). The SM contains three generation of quarks and leptons and their interaction are mediated by gauge bosons according to the $SU(3)_C \times SU(2)_L \times U(1)_Y$ gauge field theory. Over the past thirty years the SM has been confirmed by many precise experimental measurements. The SM accomplishes CP violation introducing complex coupling costants in the flavor mixing mechanism. Nevertheless, there are several reasons why the SM is not completely satisfactory as *the* theory of elementary particles.

As an example, from a cosmological viewpoint, there is a serious problem with the matter-antimatter asymmetry in the universe. This cannot be explained solely by the CP violation that occurs in the SM, which originates from quark-flavor mixing.

In the program of quark flavor physics, one way to explore physics beyond the SM is to improve substantially the precision of the CKM matrix element measurements. This can be done in many different ways and eventually any inconsistency with the SM predictions would imply new physics.

The *BABAR* experiment proved its ability to measure a number of decay modes of the B meson and to extract Cabibbo-Kobayashi-Maskawa (CKM) matrix elements and other interesting observables. For instance, the precision of the measurement of the angle β of the unitarity triangle through the $B^0 \to J/\psi K^0_S$ time-dependent asymmetry reached the $\lesssim 10\%$ level [2, 3]. Through the $B^0 \to \rho\rho$ decay it was possible to measure the value of the angle α [4, 5], and direct *CP* asymmetry has been observed in the $B^0 \to K^+\pi^-$ decay [6, 7]. The measurement of the angle γ of the CKM unitarity triangle [8] is the next crucial test of the *CP* violation picture inside the SM.

In Chapter 1, we introduce the theoretical framework, discussing the origin of *CP* violation, how to reveal it in particle physics decays and the rule of the CKM matrix. Moreover we present several methods for measuring γ along with the discussion of their advantages and drawbacks. In Section 1.5 it is discussed the method for the γ measurement, by a D^0 Dalitz analysis, argument of this theses. In Chapter 2 we present the *BABAR* detector, operating at SLAC laboratory, the Stanford Linear Accelerator Center. All the subdetectors are briefly described focusing on their importance concerning the analysis. The data sample, and the event selection within the background reduction and parametrization is presented in chapter 3. In Chapter 4 we describe the determination of the D^0 decay amplitude through a Dalitz analysis of the D^0 tagged sample via the $D^{*+} \to D^0\pi^+$ decays, while in chapter 5 it is discussed the likelihood fit for the *CP* violating parameters, which exploits the interference of the $\mathcal{A}(b \to u\bar{c}s)$ and $\mathcal{A}(b \to c\bar{u}s)$ decay amplitudes in the B decay. In Chapter 6 it is described the statistical method we have used in order to extract the value of the angle γ from the fitted *CP* parameters. Finally we discuss the results of the analysys and the perspectives for the future in chapter 7.

1 Theoretical Framework

Fundamental discrete symmetries have provided a guidance in our evolving understanding of elementary particle interactions. The discrete simmetry C (charge inversion) conjugating all internal quantum numbers, *e.g.*, $Q \to -Q$ for electromagnetic charge, P (parity, or space reflection), $\vec{x} \to -\vec{x}$, are preserved by strong and electromagnetic processes, but violated by weak decays. The CP transformation combines charge inversion and parity, and it is an exact symmetry in strong and electromagnetic processes and it is still preserved in most of weak interaction processes. The CP symmetry is, however, violated in certain rare processes, as discovered in neutral K decays in 1964 [1] through the observation of $K_L^0 \to \pi^+\pi^-$, and recently observed in neutral B decays [2, 3]. A K_L meson decays more often to $\pi^- e^+ \overline{\nu}_e$ than to $\pi^+ e^- \nu_e$, thus allowing electrons and positrons to be unambiguously distinguished, but the decay-rate asymmetry is only at the 0.003 level. The CP-violating effects observed in B decays are larger: the CP asymmetry in $B^0\overline{B}^0$ meson decays to CP eigenstates like $J/\psi K_S$ is about 0.73. CP violation has not yet been observed in the decays of any charged mesons, or in neutral D or B_s mesons, or in the lepton-neutrino sector.

In addition to parity and to continuous Lorentz transformations, there is one other space-time operation that could be a symmetry of the interactions: time reversal T, $t \to -t$. Violations of T symmetry have been observed in neutral K decays [9], and are expected as a corollary of CP violation if the combined CPT transformation is a fundamental symmetry of Nature. All observations indicate that CPT is indeed a symmetry of Nature. Furthermore, one cannot build a Lorentz-invariant quantum field theory with a Hermitian Hamiltonian that violates CPT.

1.1 CP Violation in Field Theories

In order to understand how a field theory can accomplish CP violation, one need to know the transformation properties of the fields under the various discrete symmetries. For a Dirac spinor we have:

$$P\psi(t,\mathbf{x})P^{-1} = \gamma^0\psi(t,-\mathbf{x}), \tag{1}$$

$$T\psi(t,\mathbf{x})T^{-1} = -\gamma^1\gamma^3\psi(-t,\mathbf{x}), \tag{2}$$

$$C\psi(t,\mathbf{x})C^{-1} = -i(\bar{\psi}(t,\mathbf{x})\gamma^0\gamma^2)^T. \tag{3}$$

The Lagrangian, being a Lorentz scalar, can only depend on terms bilinear in fermion fields (and not on single fermion fields). The transformation properties of various fermion bilinears under CP are summarized in the table below. Here the shorthand $(-1)^\mu \equiv 1$ for $\mu = 0$ and $(-1)^\mu \equiv -1$ for $\mu = 1, 2, 3$ (namely, $(-1)^\mu a^\mu = a_\mu$) is used.

$$\begin{array}{lcccc} \text{term} & \bar{\psi}_i\psi_j & i\bar{\psi}_i\gamma^5\psi_j & \bar{\psi}_i\gamma^\mu\psi_j & \bar{\psi}_i\gamma^\mu\gamma^5\psi_j \\ CP\text{−transformed term} & \bar{\psi}_j\psi_i & -i\bar{\psi}_j\gamma^5\psi_i & -(-1)^\mu\bar{\psi}_j\gamma^\mu\psi_i & -(-1)^\mu\bar{\psi}_j\gamma^\mu\gamma^5\psi_i \end{array} \tag{4}$$

Similarly, the *CP* transformation properties of scalar (H), pseudoscalar (A) and vector boson (W) fields, and also of the derivative operator are given by

$$\begin{array}{cccccc} \text{term} & H & A & W^{\pm\mu} & \partial_\mu \\ CP\text{−transformed term} & H & -A & -(-1)^\mu W^{\mp\mu} & (-1)^\mu \partial_\mu \end{array} . \tag{5}$$

Taking into account the Lorentz invariance and hermiticity of the Lagrangian, the above *CP* transformation rules imply that each of the combinations of fields and derivatives that appear in the Lagrangian transforms under *CP* to its hermitian conjugate. However, there are coefficients in front of these expressions which represent either coupling constants or particle masses and which do not transform under *CP*. If any of these quantities are complex, then the coefficients in front of *CP*-related terms are complex conjugates of each other. In such a case, *CP* is not necessarily a good symmetry of the Lagrangian. When the rates of physical processes that depend on these Lagrangian parameters are calculated, there can be *CP*-violating effects, namely rate differences between pairs of *CP* conjugate processes. Examples are given below.

Note, however, that not all Lagrangian phases are physically meaningful quantities. Consider the Lagrangian that contains the most general set of complex coupling constants consistent with all other symmetries in the theory. That is to say *CP* symmetry is not imposed, and hence any coupling is allowed to be complex (unless the Hermitian structure of the Lagrangian automatically requires it to be real). Now any complex field in the Lagrangian can be redefined by an arbitrary phase rotation; such rotations will not change the physics, but will change the phases of some set of terms in the Lagrangian. Consider for example a typical Yukawa-type term,

$$y_{ij} H \bar{\psi}_i \psi_j + \text{hermitian conjugate}. \tag{6}$$

The phase of y_{ij} can be changed by redefining the phase of any one of the three fields $H,\ \psi_i,\ \psi_j$ that enter this term. In general such redefinitions will also change the phase of any other terms in the Lagrangian that involve these same fields, unless the complex conjugate field appears with the same power in the same term. Some set of couplings can be made real by making such field redefinitions. However if any non-zero phases for couplings remain after all possible field redefinitions have been used to eliminate as many of them as possible, then there is *CP* violation. It is a matter of simple counting for any Lagrangian to see whether this occurs. If all phases can be removed in this way then that theory is automatically *CP*-conserving. In such a theory it is impossible to introduce any *CP* violations without adding fields or removing symmetries so that additional couplings appear. (This is the case for the Standard Model with only two generations and a single Higgs multiplet.)

If some phases survive the redefinitions, there is, in general, convention-dependence as to where the complex phases appear. One can choose to make certain terms real and leave others complex, but a different choice, related to the first by field redefinitions, has the same physical consequences. Only those differences between pairs of phases that are unchanged by such redefinitions are physically meaningful.

1.1.1 Flavor Mixing and CKM Matrix

Within the Standard Model, *CP* symmetry is broken by complex phases in the Yukawa couplings (that is, the couplings of the Higgs scalar to quarks). When all manipulations to remove unphysical phases in this model are exhausted, one finds that there is a single *CP*-violating parameter [8]. In the basis of mass eigenstates, this single phase appears in the 3×3 unitary matrix that gives the W-boson couplings to an up-type antiquark and a down-type quark. (If the Standard Model is supplemented with Majorana mass terms for the neutrinos, the analogous mixing matrix for leptons has three *CP*-violating phases.) The beautifully consistent and economical Standard-Model description of *CP* violation in terms of Yukawa couplings, known as the Cabibbo-Kobayashi-Maskawa (CKM) mechanism [8], agrees with all measurements to date.

Of all the Standard Model quark parameters, only the Cabibbo-Kobayashi-Maskawa (CKM) phase is *CP* violating. Having a single source of *CP* violation, the Standard Model is very predictive for *CP* asymmetries: some vanish, and those that do not are correlated.

To be precise, *CP* could be violated also by strong interactions. The experimental upper bound on the electric dipole moment of the neutron implies, however, that $\theta_{\rm QCD}$, the non-perturbative parameter that determines the strength of this type of *CP* violation, is tiny, if not zero. (The smallness of $\theta_{\rm QCD}$ constitutes a theoretical puzzle, known as 'the strong *CP* problem.') In particular, it is irrelevant to our discussion of meson decays.

The charged current interactions (that is, the $W^{\pm}$ interactions) for quarks are given by

$$-\mathcal{L}_{W^{\pm}} = \frac{g}{\sqrt{2}}\, \overline{u_{Li}}\, \gamma^{\mu}\, (V_{\rm CKM})_{ij}\, d_{Lj}\, W^{+}_{\mu} + \text{h.c.}$$

Here $i, j = 1, 2, 3$ are generation numbers. The Cabibbo-Kobayashi-Maskawa (CKM) mixing matrix for quarks is a 3×3 unitary matrix [8]. Ordering the quarks by their masses, *i.e.* $(u_1, u_2, u_3) \to (u, c, t)$ and $(d_1, d_2, d_3) \to (d, s, b)$, the elements of $V_{\rm CKM}$ are written as follows:

$$V_{\rm CKM} = \begin{pmatrix} V_{ud} & V_{us} & V_{ub} \\ V_{cd} & V_{cs} & V_{cb} \\ V_{td} & V_{ts} & V_{tb} \end{pmatrix} .$$

While a general 3×3 unitary matrix depends on three real angles and six phases, the freedom to redefine the phases of the quark mass eigenstates can be used to remove five of the phases, leaving a single physical phase, the Kobayashi-Maskawa phase, that is responsible for all *CP* violation in meson decays in the Standard Model.

The fact that one can parametrize $V_{\rm CKM}$ by three real and only one imaginary physical parameters can be made manifest by choosing an explicit parametrization. The Wolfenstein parametrization[10] is particularly useful:

$$V_{\rm CKM} = \begin{pmatrix} 1 - \frac{1}{2}\lambda^2 - \frac{1}{8}\lambda^4 & \lambda & A\lambda^3(\rho - i\eta) \\ -\lambda + \frac{1}{2}A^2\lambda^5[1 - 2(\rho + i\eta)] & 1 - \frac{1}{2}\lambda^2 - \frac{1}{8}\lambda^4(1 + 4A^2) & A\lambda^2 \\ A\lambda^3[1 - (1 - \frac{1}{2}\lambda^2)(\rho + i\eta)] & -A\lambda^2 + \frac{1}{2}A\lambda^4[1 - 2(\rho + i\eta)] & 1 - \frac{1}{2}A^2\lambda^4 \end{pmatrix} .$$

Here $\lambda = |V_{us}| = 0.22$ plays the role of an expansion parameter, and η represents the *CP* violating phase. Terms of $\mathcal{O}(\lambda^6)$ were neglected.

The unitarity of the CKM matrix leads to various relations among the matrix elements; *e.g.*,

$$V_{ud}V_{ub}^* + V_{cd}V_{cb}^* + V_{td}V_{tb}^* = 0 \ .$$

This relation requires the sum of three complex quantities to vanish and so can be geometrically represented in the complex plane as a triangle (see Fig.1). The angles of this triangle,

$$\begin{aligned}
\alpha \equiv \varphi_2 &\equiv \arg\left(-\frac{V_{td}V_{tb}^*}{V_{ud}V_{ub}^*}\right) , \\
\beta \equiv \varphi_1 &\equiv \arg\left(-\frac{V_{cd}V_{cb}^*}{V_{td}V_{tb}^*}\right) , \\
\gamma \equiv \varphi_3 &\equiv \arg\left(-\frac{V_{ud}V_{ub}^*}{V_{cd}V_{cb}^*}\right) ,
\end{aligned} \tag{7}$$

are physical quantities and can, in principle, be independently measured by CP asymmetries in B decays. The notations (α, β, γ) and $(\varphi_1, \varphi_2, \varphi_3)$ are both in common usage.

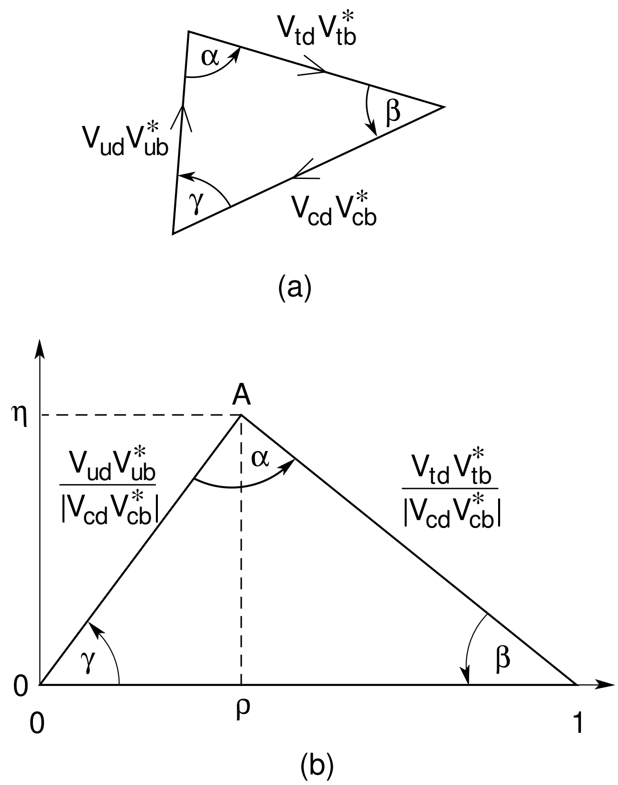

Figure 1: *Graphical representation of the unitarity constraint* $V_{ud}V_{ub}^* + V_{cd}V_{cb}^* + V_{td}V_{tb}^* = 0$ *as a triangle in the complex plane.*

1.2 *CP* Violation in *B* Decays

The possible manifestations of *CP* violation can be classified in a model independent way:

1. *CP* violation in decay, which occurs in both charged and neutral decays, when the amplitude for a decay and its *CP* conjugate process have different magnitudes,

2. *CP* violation in mixing, which occurs when the two neutral mass eigenstate cannot be chosen to be *CP* eigenstates,

3. *CP* violation in the interference between decays with and without mixing, which occurs in decays into final states that are common to B^0 and $\bar{B}^0$. (It often occurs in combination with the other two types but, important for *BABAR*, there are cases when, to an excellent approximation, it is the only effect.)

In each case it is useful to identify a particular *CP*-violating quantity that is independent of phase conventions and discuss the types of processes that depend on this quantity.

1.2.1 *CP* Violation in Decay

Let's define the decay amplitudes,

$$A_f = \langle f|H|B^0\rangle, \tag{8}$$
$$\bar{A}_f = \langle f|H|\bar{B}^0\rangle, \tag{9}$$

where A_f is the $B^0 \to f$ amplitude and $\bar{A}_{\bar{f}}$ is the *CP* conjugate amplitude to the final state f. For any final state f, the quantity $|\frac{\bar{A}_{\bar{f}}}{A_f}|$ is independent of phase conventions and physically meaningful. There are two types of phases that may appear in A_f and $\bar{A}_{\bar{f}}$.

Complex parameters in any Lagrangian term that contributes to the amplitude will appear in complex conjugate form in the *CP* conjugate amplitude. Thus their phases appear in A_f and $\bar{A}_{\bar{f}}$ with opposite signs. In the Standard Model these phases occur only in the CKM matrix which is part of the electroweak sector of the theory, hence these are often called "weak phases". The weak phase of any single term is convention dependent. However the difference between the weak phases in two different terms in A_f is convention independent; the initial and final states are the same for every term and thus any phase rotation of the fields that appear in these states will affect all terms in the same way.

A second type of phase can appear in scattering or decay amplitudes even when the Lagrangian is real. Such phases do not violate *CP*, since they appear in A_f and $\bar{A}_{\bar{f}}$ with the same sign. Their origin is the possible contribution from intermediate on-shell states in the decay process, that is an absorptive part of an amplitude that has contributions from coupled channels. Usually the dominant rescattering is due to strong interactions, hence the designation "strong phases" for the phase shifts so induced. Again only the relative strong phases of different terms in a scattering amplitude have physical content, an overall phase rotation of the entire amplitude has no physical consequences.

Thus it is useful to write each contribution to A in three parts: its magnitude A_i; its weak phase term $e^{i\phi_i}$; and its strong phase term $e^{i\delta_i}$. Then, if several amplitudes contribute to $B^0 \to f$, the amplitude A_f and the *CP* conjugate amplitude $\bar{A}_{\bar{f}}$ to the final state f, are given by:

$$A_f = \sum_i A_i e^{i(\delta_i+\phi_i)}, \quad \bar{A}_{\bar{f}} = e^{2i(\xi_f-\xi_B)} \sum_i A_i e^{i(\delta_i-\phi_i)}, \tag{10}$$

where ξ_f and ξ_B are arbitrary and unphysical phases introduced by the *CP* transformation, which depend on the particular flavor content of the state, according to:

$$CP|B^0\rangle = \quad e^{+i\xi_{B^0}}\,|\overline{B}^0\rangle \quad , \quad CP|f\rangle = e^{+i\xi_f}\,|\bar{f}\rangle \ ,$$

with

$$CP|\overline{B}^0\rangle = \quad e^{+i\xi_{B^0}}\,|B^0\rangle \quad , \quad CP|\bar{f}\rangle = e^{+i\xi_f}\,|f\rangle \ ,$$

so that $(CP)^2 = 1$. The phases and ξ_{B^0} and ξ_f are arbitrary and unphysical because of the flavor symmetry of the strong interaction.(If f is a CP eigenstate then $e^{2i\xi_f} = \pm 1$ is its CP eigenvalue.)

The convention-independent quantity is then

$$\left|\frac{\bar{A}_{\bar{f}}}{A_f}\right| = \left|\frac{\sum_i A_i e^{i(\delta_i-\phi_i)}}{\sum_i A_i e^{i(\delta_i+\phi_i)}}\right|. \tag{11}$$

When *CP* is conserved, the weak phases ϕ_i are all equal. Therefore, from Eq. (11) one sees that

$$|\bar{A}_{\bar{f}}/A_f| \neq 1 \quad \Longrightarrow \quad CP \text{ violation.} \tag{12}$$

This type of *CP* violation is here called *CP violation in decay.* It is often also called *direct CP violation.* It results from the *CP*-violating interference among various terms in the decay amplitude. From Eq. (11) it can be seen that a *CP* violation of this type will not occur unless at least two terms that have different weak phases acquire different strong phases, since:

$$|A|^2 - |\bar{A}|^2 = -2\sum_{i,j} A_i A_j \sin(\phi_i - \phi_j)\sin(\delta_i - \delta_j). \tag{13}$$

Any *CP* asymmetries in charged B decays,

$$a_f = \frac{\Gamma(B^+ \to f) - \Gamma(B^- \to \bar{f})}{\Gamma(B^+ \to f) + \Gamma(B^- \to \bar{f})}, \tag{14}$$

are from *CP* violation in decay. In terms of the decay amplitudes

$$a_f = \frac{1 - |\bar{A}/A|^2}{1 + |\bar{A}/A|^2}. \tag{15}$$

CP violation in decays can also occur for neutral meson decays, where it competes with the other two types of *CP* violation effects described below. There is experimental evidence for *CP* violation in decay in the neutral K system [11] [12] [13] and in the neutral B system [6] [7].

1.2.2 *CP* Violation in Mixing

The *CP* violation in mixing interests the neutral B system. An arbitrary linear combination of the neutral B-meson flavor eigenstates ,

$$a|B^0\rangle + b|\bar{B}^0\rangle, \tag{16}$$

is governed by a time-dependent Schrödinger equation

$$i\frac{d}{dt}\begin{pmatrix} a \\ b \end{pmatrix} = H\begin{pmatrix} a \\ b \end{pmatrix} \equiv (M - \frac{i}{2}\Gamma)\begin{pmatrix} a \\ b \end{pmatrix} \tag{17}$$

for which M and Γ are 2×2 Hermitian matrices. CPT invariance guarantees $H_{11} = H_{22}$. The off-diagonal terms in these matrices, M_{12} and Γ_{12}, are particularly important in the discussion of *CP* violation. They are the dispersive and absorbtive parts respectively of the transition amplitude from B^0 to $\bar{B}^0$. (Note that both of these can be complex quantities because of complex coupling constants.) In the Standard model these contributions arise from the box diagrams with two W exchanges.

The light B_L and heavy B_H mass eigenstates are given by

$$|B_L\rangle = p|B^0\rangle + q|\bar{B}^0\rangle, \tag{18}$$

$$|B_H\rangle = p|B^0\rangle - q|\bar{B}^0\rangle. \tag{19}$$

The complex coefficients p and q obey the normalization condition

$$|q|^2 + |p|^2 = 1. \tag{20}$$

A second quantity that is independent of phase conventions and physically meaningful is

$$\left|\frac{q}{p}\right|^2 = \left|\frac{M_{12}^* - \frac{i}{2}\Gamma_{12}^*}{M_{12} - \frac{i}{2}\Gamma_{12}}\right|. \tag{21}$$

When *CP* is conserved, the mass eigenstates must be *CP* eigenstates. In that case the relative phase between M_{12} and Γ_{12} vanishes. Therefore, Eq. (21) implies

$$|q/p| \neq 1 \quad \Longrightarrow \quad CP \text{ violation.} \tag{22}$$

This type of *CP* violation is here called *CP violation in mixing*; it is often referred to as *indirect CP violation*. It results from the mass eigenstates being different from the *CP* eigenstates. *CP* violation in mixing has been observed unambiguously in the neutral kaon system.

For the neutral B system, this effect could be observed through the asymmetries in semileptonic decays:

$$a_{\rm sl} = \frac{\Gamma(\bar{B}^0_{\rm phys}(t) \to \ell^+\nu X) - \Gamma(B^0_{\rm phys}(t) \to \ell^-\nu X)}{\Gamma(\bar{B}^0_{\rm phys}(t) \to \ell^+\nu X) + \Gamma(B^0_{\rm phys}(t) \to \ell^-\nu X)}. \tag{23}$$

In terms of $|q/p|$,

$$a_{\rm sl} = \frac{1 - |q/p|^4}{1 + |q/p|^4}, \tag{24}$$

which follows from

$$\langle \ell^-\nu X|H|B^0_{\rm phys}(t)\rangle = (q/p)g_-(t)A^*, \quad \langle \ell^+\nu X|H|\bar{B}^0_{\rm phys}(t)\rangle = (p/q)g_-(t)A. \tag{25}$$

1.2.3 *CP* Violation in the Interference Between Decays With and Without Mixing.

Finally, consider neutral B decays into final CP eigenstates, f_{CP} [14, 15, 16]. Such states are accessible in both B^0 and $\bar{B}^0$ decays. The quantity of interest here that is independent of phase conventions and physically meaningful is

$$\lambda \equiv \frac{q}{p}\frac{\bar{A}_{f_{CP}}}{A_{f_{CP}}} \equiv \eta_{f_{CP}}\frac{q}{p}\frac{\bar{A}_{\bar{f}_{CP}}}{A_{f_{CP}}}. \tag{26}$$

When CP is conserved, $|q/p| = 1$, $|\bar{A}_{\bar{f}_{CP}}/A_{f_{CP}}| = 1$, and furthermore, the relative phase between (q/p) and $(\bar{A}_{\bar{f}_{CP}}/A_{f_{CP}})$ vanishes. Therefore, Eq. (26) implies

$$\lambda \neq \pm 1 \quad \Longrightarrow \quad CP \text{ violation.} \tag{27}$$

Note that both *CP* violation in decay (12) and *CP* violation in mixing (22) lead to (27) through $|\lambda| \neq 1$. However, it is possible that, to a good approximation, $|q/p| = 1$ and $|\bar{A}/A| = 1$, yet there is *CP* violation:

$$|\lambda| = 1, \qquad \mathrm{Im}\,\lambda \neq 0. \tag{28}$$

This type of *CP* violation is called *CP violation in the interference between decays with and without mixing* here; sometimes this is abbreviated as "interference between mixing and decay". This type of *CP* violation has also been observed in the neutral kaon system [1].

For the neutral B system, *CP* violation in the interference between decays with and without mixing can be observed by comparing decays into final *CP* eigenstates of a time-evolving neutral B state that begins at time zero as B^0 to those of the state that begins as a $\bar{B}^0$:

$$a_{f_{CP}} = \frac{\Gamma(B^0_{\mathrm{phys}}(t) \to f_{CP}) - \Gamma(\bar{B}^0_{\mathrm{phys}}(t) \to f_{CP})}{\Gamma(B^0_{\mathrm{phys}}(t) \to f_{CP}) + \Gamma(\bar{B}^0_{\mathrm{phys}}(t) \to f_{CP})}. \tag{29}$$

It is shown ([17]) that this time-dependent asymmetry is given by:

$$a_{f_{CP}} = \frac{(1 - |\lambda_{f_{CP}}|^2)\cos(\Delta m_B t) - 2\,\mathrm{Im}\,\lambda_{f_{CP}}\sin(\Delta m_B t)}{1 + |\lambda_{f_{CP}}|^2}. \tag{30}$$

This asymmetry will be non-vanishing if any of the three types of *CP* violation are present. However, for decays such that $|\lambda| = 1$ (the 'clean' modes *e.g.* $B^0 \to J/\psi K^0_S$,$B^0 \to J/\psi K^0_L$), Eq. 30 simplifies considerably:

$$a_{f_{CP}} = -\,\mathrm{Im}\,\lambda_{f_{CP}}\sin(\Delta m_B\ t)\ . \tag{31}$$

1.3 Motivation for Measuring γ

The measurement of the matrix elements of the CKM matrix is one of the most stringent test of the Standard Model and for this reason it represents also a window for New Physics. Intense experimental efforts are now underway in B-physics and for this program is crucial to determine the angles of the Unitary Triangle from the experiments. The angle γ defined as,

$$\gamma = \arg(-V_{ud}V_{ub}^*/V_{cd}V_{cb}^*), \tag{32}$$

is the argument of the complex number $\bar{\rho} + i\bar{\eta}$. It defines the coordinates of the apex of the Unitarity Triangle in the complex plane, for this reason an independent measurement of this angle is a major issue for such a program. The angle γ is by far the most difficult to measure. The $\sin 2\beta$ measurement has reached a good level of precision. The world average uses measurements from the decays $B^0 \to J/\psi K_S^0$, $J/\psi K_L^0$, $\psi(2S)K_S^0$, $\chi_{c1}K_S^0$, $\eta_c K_S^0$ and $J/\psi K^{*0}$ ($K^{*0} \to K_S^0\pi^0$) and gives

$$\sin 2\beta_{[c\bar{c}]} = 0.739 \pm 0.048 \text{ [18]}.$$

It is dominated by the measurements from *BABAR* [2] and Belle [3]. The angle α has been contrained by *BABAR* measurements [6, 7], which yield:

$$\alpha = (94 \pm 12 \pm 13)^\circ,$$

where the first error is experimental and the second error is due to penguin uncertainty.

The measurement of the γ angle can test the consistency of the CKM picture through the relation:

$$\alpha + \beta + \gamma = 180^\circ.$$

The measurement of the angle γ of the CKM unitarity triangle is the next crucial test of the Standard Model in the fermion sector and of the *CP* violation picture. However other effect can change the various quantities which, in the Standard Model, measure the angle γ. Hence γ should be measured in a variety of ways, to check whether one consistently finds the same results. There are indeed several methods to accomplish this task and they are expected to be affected differently by new physics. A precise measurement of the Unitarity Triangle Angles is also, for such reasons, a probe for searching New Physics effects beyond the Standard Model.

1.4 An Overview of Methods for the γ Measurement

There are several decay channels that can be used to extract information on γ, and each has distinct merits and drawbacks. Regarding the final state $B^\pm \to D^{(*)}K^\pm$, as it can be reached through two different quark processes, $b \to c\bar{u}s$ and $b \to u\bar{c}s$ transtions, and respectively $B^- \to D^0K^-$ and $B^- \to \overline{D}^0K^-$, we will refer in the following to the combination of D^0 and $\overline{D}^0$ with the symbol D unless explicitely stated. Here, we will discuss the following channels: $B^\pm \to D^{(*)}K^\pm$ with D^0_{CP} modes (GLW method), $B^\pm \to D^{(*)}K^\pm$ with D^0 doubly Cabibbo suppressed (ADS method), $B^0 \to D^{(*)-}\pi^+$ modes for the $\sin(2\beta + \gamma)$ measurement.

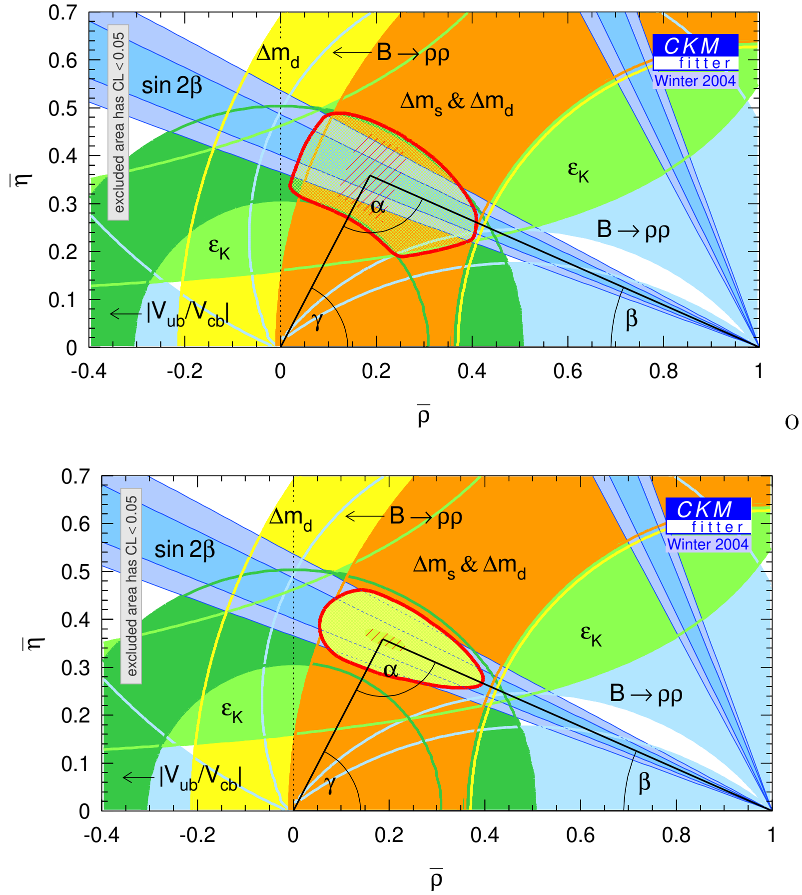

Figure 2: *Confidence levels in the $\bar{\rho}\bar{\eta}$ plane for the global CKM fit (not included experimental contraints on γ). The shaded areas indicate the regions of $\geq$ 5% CLs. For* $\sin 2\beta$ *the* $\geq 32\%$ *and* $\geq 5\%$ *CL constraints are shown. The upper (lower) plot excludes (includes) the constraints from* $\sin 2\beta$ *and* $\sin 2\alpha$ *in the combined fit. The hatched area in the center of the combined fit result indicates the region where theoretical errors dominate. The lower plot corresponds to the standard CKM fit.*

1.4.1 A Method Using $B^{\pm} \to D^{(*)}K^{\pm}$ Decays (GLW method)

This method considers the decays $B^{\pm} \to D^{(*)}K^{\pm}$, where D is D^0_{CP}. This method is the first originally proposed by Gronau, London and Wyler. It takes advantage of the interference into the final common D^0_{CP} eigenstates. The main result of this method is that γ can be extracted in a theoretically-clean manner if one reconstructs D^0_{CP}-even and D^0_{CP}-odd decays. On the contrary, an 8-fold ambiguity on the value of γ is not solved and the statistics needed for a precise measurement is much greater than the one available at the B-factories.
Applying an appropriate CP phase convention to simplify the following discussion, the CP eigenstates $|\mathsf{D^0}_{\pm}\rangle$ of the neutral D meson system with CP eigenvalues ± 1 are given by

$$\left|\mathsf{D^0}_{\pm}\right\rangle = \frac{1}{\sqrt{2}}\left(\left|\mathsf{D^0}\right\rangle \pm \left|\bar{\mathsf{D}}^0\right\rangle\right), \tag{33}$$

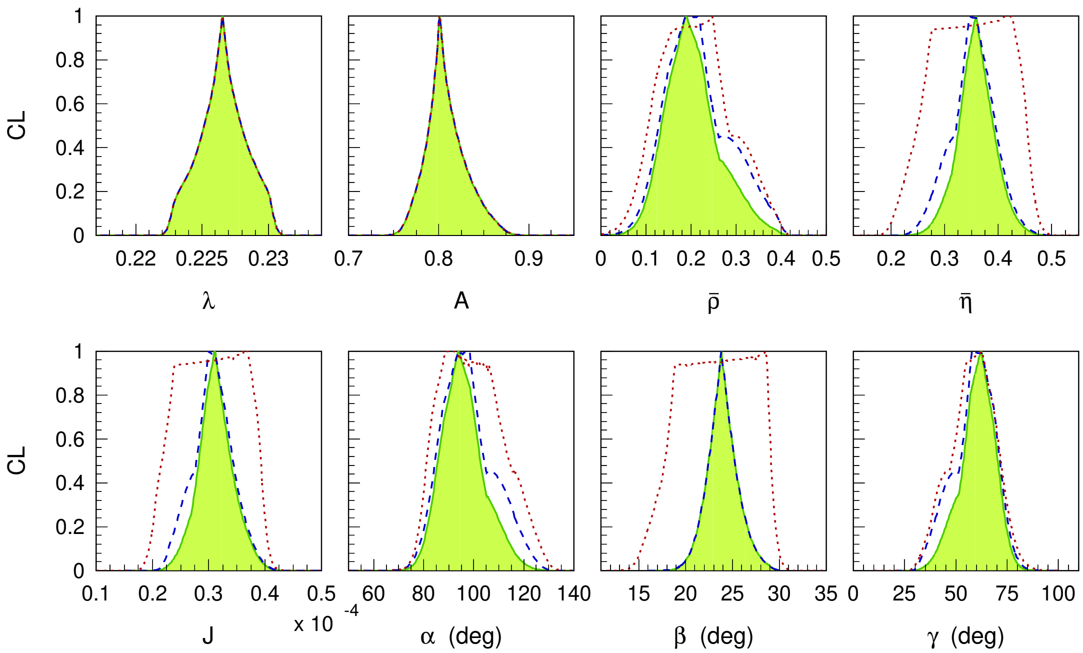

Figure 3: *Confidence levels for the Wolfenstein parameters (λ,A,$\bar{\rho}$,$\bar{\eta}$) and UT surface (J), and angles (α,β,γ) obtained from the standard CKM fit (shaded areas). The dotted curves give the results without using* $\sin 2\beta$ *and* $\sin 2\alpha_{[\rho\rho]}$ *in the fit, while the dashed line excludes only* $\sin 2\alpha_{[\rho\rho]}$.

so that the $B^\pm \to D^0_+ K^\pm$ transition amplitudes can be expressed as [19]

$$\begin{aligned} \sqrt{2}A(B^+ \to D^0_+ K^+) &= A(B^+ \to D^0 K^+) + A(B^+ \to \overline{D}^0 K^+) && (34) \\ \sqrt{2}A(B^- \to D^0_+ K^-) &= A(B^- \to \overline{D}^0 K^-) + A(B^- \to D^0 K^-). && (35) \end{aligned}$$

These relations, which are exact, can be represented as two triangles in the complex plane. Taking into account that the $B^+ \to DK^+$ decays originate from $\overline{b} \to \overline{u}\, c\, \overline{s}$ and $\overline{b} \to \overline{c}\, u\, \overline{s}$ quark-level transitions (see Fig. 4) yields

$$\begin{aligned} A(B^+ \to D^0 K^+) &= e^{i\gamma}\lambda\, |V_{cb}| R_B\, |a|\, e^{i\Delta_a} \;=\; e^{2i\gamma}\, A(B^- \to \overline{D}^0 K^-) && (36) \\ A(B^+ \to \overline{D}^0 K^+) &= \lambda\, |V_{cb}||A|\, e^{i\Delta_A} \;=\; A(B^- \to D^0 K^-)\ , && (37) \end{aligned}$$

where $R_B = \frac{1-\lambda^2/2}{\lambda}\left|\frac{V_{ub}}{V_{cb}}\right|$ measures one side of the unitarity triangle. The quantities $|a|$, $|A|$ are magnitudes of hadronic matrix elements of current–current operators, and Δ_a, Δ_A denote the corresponding CP-conserving strong phases. Consequently, the modes $B^+ \to D^0 K^+$ and $B^+ \to \overline{D}^0 K^+$ exhibit no CP-violating effects. However, if $\gamma \neq 0$, one finds

$$|A(B^+ \to D^0_+ K^+)| \neq |A(B^- \to D^0_+ K^-)|\ . \qquad (38)$$

Observation of such a CP-violating effect would rule out superweak scenarios in an unambiguous way.

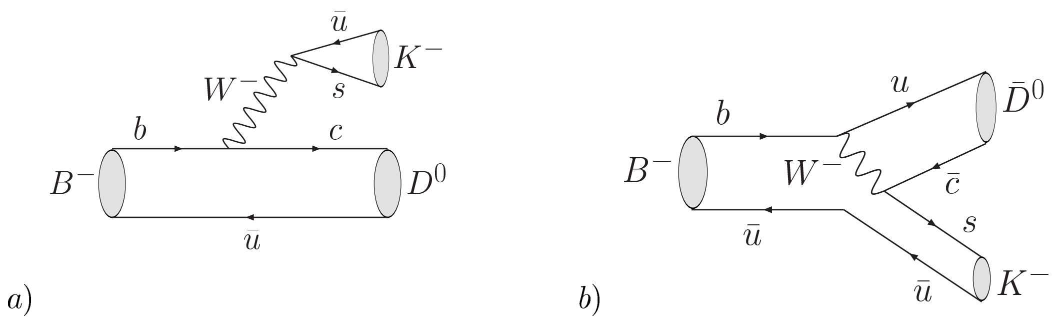

Figure 4: *Diagrams contributing to $B^\pm \to DK^\pm$ and related modes.*

Combining all these considerations, the triangle relations (34) and (35), which are depicted in Fig. 5, can be used to extract γ by measuring only the rates of the six processes. This approach was proposed by Gronau, London and Wyler (GLW method) [19], [20]. It is theoretically clean and suffers from no hadronic uncertainties. As can be seen easily from Fig. 5, this method works also for vanishing *CP*-conserving strong phases in the $B^\pm \to DK^\pm$ modes. Although there would be no *CP* violation in $B^\pm \to D^0_+ K^\pm$ in this case, the extraction of γ is still possible. Unfortunately the amplitude triangles are expected to be very squashed ones since $B^- \to \overline{D}^0 K^-$ is both color- and CKM-suppressed with respect to $B^- \to D^0 K^-$:

$$r_B = \frac{|A(B^- \to \overline{D}^0 K^-)|}{|A(B^- \to D^0 K^-)|} = R_B \, \frac{|a|}{|A|} \approx 0.36 \, \frac{a_2}{a_1} \approx 0.1. \tag{39}$$

Here a_1 and a_2 are the usual phenomenological color-factors [21]. The observables are:

$$\begin{aligned} \mathcal{R}_{CP\pm} &\equiv \frac{\mathcal{B}\left(B^- \to D^0_{CP\pm} K^-\right) + \mathcal{B}\left(B^+ \to D^0_{CP\pm} K^+\right)}{\mathcal{B}\left(B^- \to D^0 K^-\right) + \mathcal{B}\left(B^+ \to \overline{D}^0 K^+\right)} \\ &\equiv 1 + {r_B}^2 \pm 2 r_B \cos\delta \sin\gamma \end{aligned} \tag{40}$$

$$\begin{aligned} \mathcal{A}_{CP\pm} &\equiv \frac{\mathcal{B}\left(B^- \to D^0_{CP\pm} K^-\right) - \mathcal{B}\left(B^+ \to D^0_{CP\pm} K^+\right)}{\mathcal{B}\left(B^- \to D^0_{CP\pm} K^-\right) + \mathcal{B}\left(B^+ \to D^0_{CP\pm} K^+\right)} \\ &\equiv \frac{\pm 2 \, r_B \sin\delta \sin\gamma}{\mathcal{R}_{CP\pm}} \end{aligned} \tag{41}$$

BABAR and Belle have measured recently the branching fractions of the D^0 decay modes $D^0_+ \to \pi^+\pi^-, K^+K^-$ and of the $D^0_- \to K^0_S\pi^0, K^0_S\phi, K^0_S\omega$ [22]. The small value of r_B does not permit a precise measurement of the angle γ with the current statistics.

Therefore the original GLW method [19, 20] is unfortunately very difficult in practice.

1.4.2 Enhanced *CP* Violation in $B^\pm \to D^{(*)} K^\pm$ Decays (ADS method)

The primary problem with respect to the GLW method is the fact that CP violating asymmetries tend to be small since $B^- \to \bar{D}^0 K^-$ is color suppressed whereas $B^- \to D^0 K^-$ is

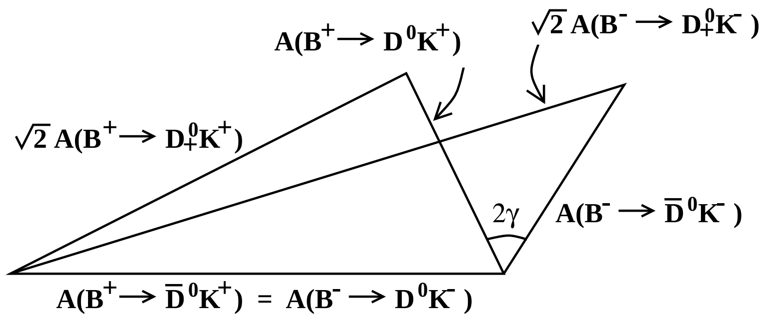

Figure 5: *Triangle relations among $B^{\pm} \to DK^{\pm}$ decay amplitudes.*

color allowed. Moreover, when the appropriate CKM factors are taken into account, the former amplitude is typically an order of magnitude smaller than the latter. In the GLW method the interference effects are therefore limited to $\mathcal{O}(10\%)$, which indicates the maximum possible size for CP violation via this method. To overcome this we choose instead D^0-modes, f, that are not CP-eigenstates. Especially appealing are modes f such that $D^0 \to f$ is doubly Cabibbo suppressed while $\bar{D}^0 \to f$ is Cabibbo allowed. In the following we assume $f = K^+\pi^-$ for semplicity even if the method applies in principle to a generic D^0 doubly Cabibbo suppressed final state ($e.g. f = K^+\pi^-,\ K^+\pi^-\pi^0,$ etc.). As a result, the two interfering amplitudes become comparable.

In a paper [23], Atwood, Dunietz, and Soni (ADS) proposed a variation of the Gronau-London-Wyler (GLW) method [19] for determining the Unitarity Triangle angle γ which takes advantage of a flaw in the GLW method – doubly-CKM-suppressed D^0 decays. The idea is fairly simple. One must measure the B^+ and B^- decay rates (separately of course) to a final state that can be reached from primarily two amplitudes, each of the same order of magnitude, where the amplitudes have a relative weak phase of γ. One amplitude is from a doubly-suppressed B decay (e.g. a $b \to u\bar{c}s$ transition) combined with a favored D decay. The other amplitude is from a favored B decay (e.g. a $b \to c\bar{u}s$ transition) combined with a doubly-suppressed D decay (e.g. $D^0 \to K^+\pi^-$). The Feynman diagrams for the two B decays are shown in Figure 4. The non-zero relative weak phase between the two amplitudes opens the possibility of direct CP violation *if* there is also a non-zero strong phase difference between the two amplitudes. Explicitly, the direct CP asymmetry is given by

$$A_{CP} = \frac{2\, r_B r_D \sin\gamma \sin\delta}{{r_B}^2 + {r_D}^2 + 2 r_B r_D \cos\gamma \cos\delta}, \tag{42}$$

where δ is the overall strong phase difference, γ is the weak phase difference, r_B is defined in Eq. 39, and r_D is the magnitude of the ratio of amplitudes of the D^0 Cabibbo suppressed respect to the D^0 Cabibbo allowed decay,

$$r_D \equiv \frac{|A(D^0 \to K^+\pi^-)|}{|A(D^0 \to K^-\pi^+)|}. \tag{43}$$

Experimentally, in order to avoid having to measure absolute branching fractions and to have a more theoretically clean measurement, it is advantageous to normalize the ADS decay rate with a related mode. In this particular case, the perfect mode is D^0K^- with $D^0 \to K^-\pi^+$, which is the combination of the favored B decay with the favored D decay. Using the current notation it gives the ratio,

$$\mathcal{R}_{ADS}(f=[K\pi]) \equiv \frac{\mathcal{B}(B^- \to [K^+\pi^-]_D K^-) + \mathcal{B}(B^+ \to [K^-\pi^+]_D K^+)}{\mathcal{B}(B^- \to [K^-\pi^+]_D K^-) + \mathcal{B}(B^+ \to [K^+\pi^-]_D K^+)} \quad (44)$$

$$\mathcal{R}_{ADS}(f) = {r_D}^2 + {r_B}^2 + 2(r_B\, r_D)\cos\gamma\cos(\delta_B+\delta_D) \quad (45)$$

where δ_D is the strong phase in the D^0 decay.

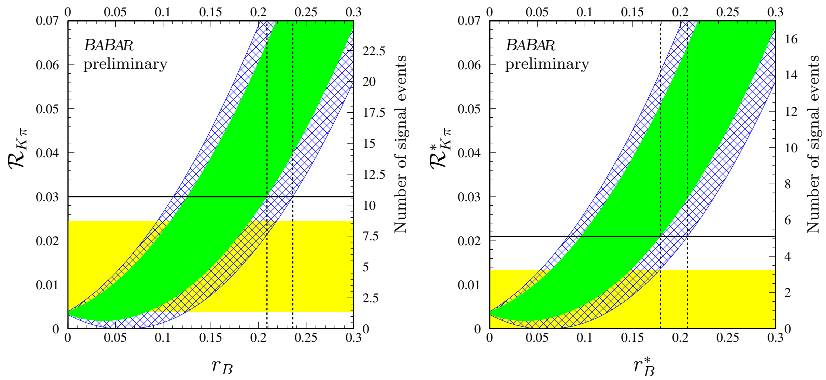

Figure 6: Expectations for $\mathcal{R}^{(*)}_{K\pi} \equiv \mathcal{R}_{ADS}(f=[K\pi])$ and the number of signal events *vs.* $r^{(*)}_B$. Dark filled-in areas: allowed regions for any value of $\delta^{(*)}$, with a $\pm1\sigma$ variation on r_D, and $48^\circ < \gamma < 73^\circ$. Hatched area: additional allowed regions with no constraint on γ. Note that the uncertainty on r_D has a very small effect on the size of the allowed regions. The horizontal lines represents the 90% C.L. limit $\mathcal{R}_{K\pi} < 0.030$ and $\mathcal{R}^*_{K\pi} < 0.021$ The vertical dashed lines are drawn at $r_B = 0.209$, $r_B = 0.235$, $r^*_B = 0.179$, and $r^*_B = 0.208$. They represent the 90% C.L. upper limits on r_B and r^*_B with and without the constraint on γ. The light filled in areas represent the 68% C.L. regions corresponding to $\mathcal{R}_{K\pi} = 0.013\pm^{0.011}_{0.009}$ and $\mathcal{R}^*_{K\pi} = 0.003\pm^{0.010}_{0.007}$.

The current measurements of $R_{ADS}(K\pi)$ [24] consent to pose an upper limit on the value of r_B and r^*_B [1]

$$r_B \leq 0.23 \quad (90\%\ C.L.) \quad (46)$$
$${r^*_B}^2 \leq (0.16)^2 \quad (90\%\ C.L.)$$

but do not permit a direct measurement of γ. In any case the analysis can bring useful informations once the results are combined with other γ related measurements.

1.4.3 Extraction of $\sin(2\beta+\gamma)$ with $B^0 \to D^{(*)-}\pi^+$ modes

In the B^0 system it is possible to measure $2\beta+\gamma$ as a CP violation effect in the interference between decays with and without mixing, as explained in Par. 1.2.3. It is affected by a

[1] $r^*_B = \frac{|A(B^-\to\bar{D}^{*0}K^-)|}{|A(B^-\to D^{*0}K^-)|}$, amplitude ratio for $B^- \to D^{*0}K^-$ decay mode

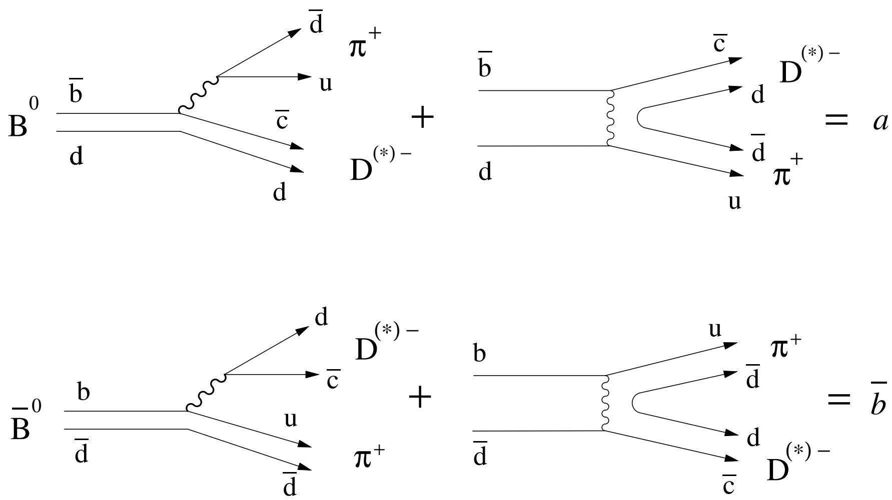

Figure 7: *Diagrams for* $B^0, \bar{B}^0 \to D^{(*)-}\pi^+$.

strong phase, there is, however, no penguin contribution. One could fully reconstruct the $D^-\pi^+$ and $D^{*-}\pi^+$ final states, or one could use a partial-reconstruction technique where $\bar{D}^0$ of the decay $D^{*-} \to \bar{D}^0\pi^-$ is not explicitly detected. The latter has more statistics but with more background. In both cases, the value of r, the ratio of Cabibbo-favored amplitude to the Cabibbo-suppressed amplitude, needs to be input externally. This requires a theoretical uncertainty to be taken into account.

For the final state $D^{(*)-}\pi^+$, the amplitudes of diagrams shown in Figure 7 interfere. Here f denotes a final state with valence-quark content $c\overline{d}\,d\overline{u}$, for example $D^{*+}\pi^-$. The transition amplitudes can be expressed as hadronic matrix elements of low energy effective Hamiltonians ($\mathcal{H}_{\rm eff}$),

$$A(\overline{B}^0 \to f) \;\equiv\; \left\langle f \left| \mathcal{H}_{\rm eff}(\overline{B}^0 \to f) \right| \overline{B}^0 \right\rangle = \frac{G_{\rm F}}{\sqrt{2}}\,\overline{v}\;\overline{M}_f \tag{47}$$

$$A(B^0 \to f) \;\equiv\; \left\langle f \left| \mathcal{H}_{\rm eff}(B^0 \to f) \right| B^0 \right\rangle \;=\; e^{i\phi_{\rm CP}(B_d)}\frac{G_{\rm F}}{\sqrt{2}}\,v^* M_{\overline{f}} \tag{48}$$

where the relevant CKM factors take the form,

$$\overline{v} \equiv V_{ud}^* V_{cb} = \left(1 - \frac{1}{2}\lambda^2\right) A\lambda^2, \quad v \equiv V_{cd}^* V_{ub} = -A\lambda^4 R_b\, e^{-i\gamma}, \tag{49}$$

and $M_{\overline{f}}$ and $\overline{M}_f$ are the strong hadronic matrix elements. Consequently, the observable $\lambda(B_d \to f)$, which has been defined in Eq. 26 contains essentially all the information needed to evaluate the mixing-induced and direct *CP*-violating asymmetries,

$$\lambda(B_d \to f) = \frac{q}{p}\,\frac{A(\overline{B}^0 \to f)}{A(B^0 \to f)} = -\,e^{-i\phi_{\rm M}^{(d)}}\,\frac{\overline{v}}{v^*}\,\frac{\overline{M}_f}{M_{\overline{f}}} = -\,e^{-i(2\beta+\gamma)}\,\frac{1}{\lambda^2 R_b}\,\frac{\overline{M}_f}{M_{\overline{f}}}\,, \tag{50}$$

where the phase convention $\phi_{\rm M}^{(d)} = 2\beta$ is used. The additional convention-dependent phase $\phi_{\rm CP}(B_d)$ is canceled by the one introduced through the B^0–$\overline{B}^0$ mixing phase [25]. An analogous calculation yields

$$\lambda(B_d \to \bar{f}) = -\,e^{-i\phi_{\rm M}^{(d)}}\,\frac{v}{\overline{v}^*}\,\frac{M_{\overline{f}}}{\overline{M}_f} = -\,e^{-i(2\beta+\gamma)}\lambda^2 R_b\,\frac{M_{\overline{f}}}{\overline{M}_f}. \tag{51}$$

If one measures the corresponding *CP* asymmetries, both $\lambda(B_d \to f)$ and $\lambda(B_d \to \bar{f})$ can be determined up to discrete ambiguities and allow a *theoretically clean* determination of $2\beta+\gamma$ from

$$\lambda(B_d \to f)\ \lambda(B_d \to \bar{f}) = e^{-2i(2\beta+\gamma)}. \tag{52}$$

Since 2β, *i.e.* the B^0–$\overline{B}^0$ mixing phase, can be determined from *CP* violation in decays such as $B^0 \to J/\psi K_S^0$, one can extract γ from (52). It is interesting to note that this approach is still possible if B^0–$\overline{B}^0$ mixing receives sizeable *CP*-violating new-physics contributions, since it is unlikely that the $B_d \to D^{(*)\pm}\pi^\mp$ decay amplitudes are affected strongly by physics beyond the Standard Model. The current measurements from *BABAR* and Belle pose weak constraints on the angle γ. In Fig. 8 is shown the CL for γ from $B^0 \to D^{(*)-}\pi^+$ measurements, compared to the prediction from the standard CKM fit.

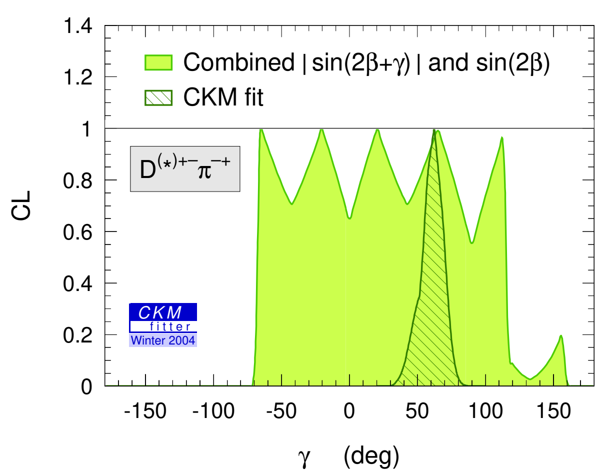

Figure 8: *Confidence level obtained for the UT angle γ when using BABAR and Belle's results on $|\sin 2(\beta+\gamma)|$ and $|\cos 2(\beta+\gamma)|$ combined with the world average of $\sin 2(\beta)_{[c\bar{c}]}$. Also shown is the prediction from the standard CKM fit.*

1.5 Measurement of γ with a Dalitz Analysis of Three-Body D^0 Decays

The main advantage of the GLW method is that, in principle, the hadronic parameters can be cleanly extracted from data, by measuring the $B^{\pm} \to D^0 K^{\pm}$ and $B^{\pm} \to \overline{D}^0 K^{\pm}$ decay rates. In practice, the measurement of γ is complicated by the 8-fold ambiguity and by the small value of the ratio of the interfering amplitudes r_B(see Eq. 55) and it is a not easy task. Moreover if the strong phase in the B decay vanishes, measuring γ makes use of terms $\mathcal{O}({r_B}^2)$, instead of terms $\mathcal{O}(r_B)$. In general large interfering amplitudes with large relative strong phases improve the sensitivity to the γ measurement.

A new method for measuring γ has been proposed recently [26], which uses $B^{\pm} \to D^{(*)} K^{\pm}$ followed by a multibody D decay (*e.g.* $D^0 \to K_S^0 \pi^+ \pi^-$,$D^0 \to K_S^0 K^+ K^-$). The advantage of this method is that one expects large strong phases due to the presence of resonances. No branching ratio measurements are needed and only charged particles are involved in the final states, which results in a higher reconstruction efficiency and low background. The price to pay is the that one needs a detailed study of the resonances and their interference through a *Dalitz plot* technique [27].

Two different approaches can be followed to measure the γ angle. The first is model independent and it is discussed in section 1.5.1, the second, model dependent is discussed in section 1.5.2.

1.5.1 Model independent determination of γ

Let us focus on the following cascade decay [2]

$$B^- \to DK^- \to (K_S \pi^- \pi^+)_D K^-, \tag{53}$$

and define the amplitudes

$$\begin{aligned} A(B^- \to D^0 K^-) &\equiv A_B, &(54)\\ A(B^- \to \overline{D}^0 K^-) &\equiv A_B r_B e^{i(\delta_B - \gamma)}. &(55)\end{aligned}$$

The same definitions apply to the amplitudes for the CP conjugate cascade $B^+ \to DK^+ \to (K_S\, \pi^+ \pi^-)_D K^+$, with the change of weak phase sign $\gamma \to -\gamma$ in (55). We have set the strong phase of A_B to zero by convention, so that δ_B is the difference of strong phases between the two amplitudes. For the CKM elements, the usual convention of the weak phases has been used. The value of $|A_B|$ is known from the measurement of the $B^- \to D^0 K^-$ decay width using flavor specific decays of D^0. The amplitude $A(B^- \to \overline{D}^0 K^-)$ is color suppressed and cannot be determined from experiment in this way [23]. The color suppression together with the experimental values of the ratio of the relevant CKM elements leads to the theoretical expectation $r_B \sim 0.1$.

For the three-body D meson decay we define

$$\begin{aligned} A_D(s_{12}, s_{13}) \equiv A_{12,13}\, e^{i\delta_{12,13}} &\equiv A(D^0 \to K_S(p_1)\pi^-(p_2)\pi^+(p_3)) &(56)\\ &= A(\overline{D}^0 \to K_S(p_1)\pi^+(p_2)\pi^-(p_3)), &(57)\end{aligned}$$

[2] In the following discussion we neglect $D^0 - \bar{D}^0$ mixing, which is a good approximation in the context of the Standard Model [26].

where $s_{ij} = (p_i + p_j)^2$, and p_1, p_2, p_3 are the momenta of the K_S, π^-, π^+ respectively. We also set the magnitude $A_{12,13} \geq 0$, such that $\delta_{12,13}$ can vary between 0 and 2π. In the last equation the CP symmetry of the strong interaction together with the fact that the final state is a spin zero state has been used. With the above definitions, the amplitude for the cascade decay is

$$A(B^- \to (K_S\pi^-\pi^+)_D K^-) = A_B \mathcal{P}_D (A_D(s_{12}, s_{13}) + r_B e^{i(\delta_B - \gamma)} A_D(s_{13}, s_{12})) \tag{58}$$

where $\mathcal{P}_D$ is the D meson propagator. Next, we write down the expression for the reduced partial decay width

$$\begin{aligned} d\hat{\Gamma}(B^- \to (K_S\pi^-\pi^+)_D K^-) &= \Big(A_{12,13}^2 + r_B^2\, A_{13,12}^2 \\ &+ 2r_B\ \mathrm{Re}\left[A_D(s_{12}, s_{13})\, A_D^*(s_{13}, s_{12})\, e^{-i(\delta_B - \gamma)}\right]\Big) dp, \end{aligned} \tag{59}$$

where dp denotes the phase space variables, and we used the extremely accurate narrow width approximation for the D meson propagator.

The moduli of the D decay amplitude $A_{12,13}$ can be measured from the Dalitz plot of the $D^0 \to K_S\pi^-\pi^+$ decay. To perform this measurement the flavor of the decaying neutral D meson has to be tagged. This can be best achieved by using the charge of the soft pion in the decay $D^{*+} \to D^0\pi^+$.

However, the phase $\delta_{12,13}$ of the D meson decay amplitude is not measurable in B-factories without further model dependent assumptions. If the three-body decay $D^0 \to K_S\pi^-\pi^+$ is assumed to be resonance dominated, the D^0 decay amplitude can be parametrized as a sum of Breit-Wigner functions, determining also the relative phases of the resonant amplitudes. This is further discussed in section 1.5.2. The other option is to use data from charm factory, where weighted averages of the sine and the cosine of the relevant phase difference may be measured [26]. Here we assume that no charm factory data is available and develop the formalism without any model dependent assumptions.

Obviously, to compare with the data, an integration over at least some part of the Dalitz plot has to be performed. We therefore partition the Dalitz plot into n bins and define

$$c_i \equiv \int_i dp\ A_{12,13}\, A_{13,12}\, \cos(\delta_{12,13} - \delta_{13,12}), \tag{60}$$

$$s_i \equiv \int_i dp\ A_{12,13}\, A_{13,12}\, \sin(\delta_{12,13} - \delta_{13,12}), \tag{61}$$

$$T_i \equiv \int_i dp\ A_{12,13}^2, \tag{62}$$

where the integrals are done over the phase space of the i-th bin. The variables c_i and s_i contain differences of strong phases and are therefore unknowns in the analysis. The variables T_i, on the other hand, can be measured from the flavor tagged D decays as discussed above, and are assumed to be known inputs of the analysis.

Due to the symmetry of the interference term, it is convenient to use pairs of bins that are placed symmetrically about the $12 \leftrightarrow 13$ line, as shown in Fig. 9. Consider an even, $n = 2k$, number of bins. The k bins lying below the symmetry axis are denoted by index i,

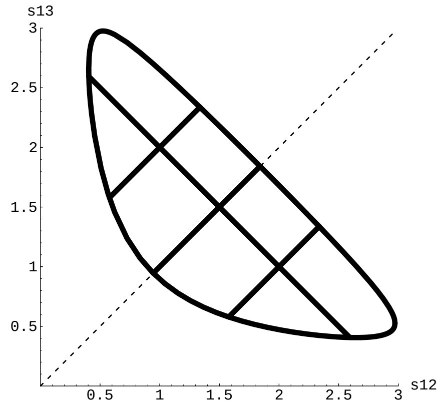

Figure 9: The partitions of Dalitz plot as discussed in text. The symmetry axis is the dashed line. On the axes we have $s_{12} = m^2_{K_s\pi^-}$ and $s_{13} = m^2_{K_s\pi^+}$ in GeV^2.

while the remaining bins are indexed with $\bar{i}$. The $\bar{i}$-th bin is obtained by mirroring the i-th bin over the axis of symmetry. The variables c_i, s_i of the i-th bin are related to the variables of the $\bar{i}$-th bin by

$$c_{\bar{i}} = c_i, \qquad s_{\bar{i}} = -s_i, \tag{63}$$

while there is no relation between T_i and $T_{\bar{i}}$. Note that had one used $12 \leftrightarrow 13$ symmetric bins centered on the symmetry axis, one would have had $s_i = 0$.

Together with the information available from the B^+ decay, we arrive at a set of $4k$ equations:

$$\begin{aligned}
\hat{\Gamma}^-_i \equiv \int_i d\hat{\Gamma}(B^- \to (K_S\pi^-\pi^+)_D K^-) = & \\
& T_i + r_B^2 T_{\bar{i}} \ + 2r_B[\cos(\delta_B - \gamma)c_i + \sin(\delta_B - \gamma)s_i], \\
\hat{\Gamma}^-_{\bar{i}} \equiv \int_{\bar{i}} d\hat{\Gamma}(B^- \to (K_S\pi^-\pi^+)_D K^-) = & \\
& T_{\bar{i}} + r_B^2 T_i \ + 2r_B[\cos(\delta_B - \gamma)c_i - \sin(\delta_B - \gamma)s_i], \\
\hat{\Gamma}^+_i \equiv \int_i d\hat{\Gamma}(B^+ \to (K_S\pi^-\pi^+)_D K^+) = & \\
& T_{\bar{i}} + r_B^2 T_i \ + 2r_B[\cos(\delta_B + \gamma)c_i - \sin(\delta_B + \gamma)s_i], \\
\hat{\Gamma}^+_{\bar{i}} \equiv \int_{\bar{i}} d\hat{\Gamma}(B^+ \to (K_S\pi^-\pi^+)_D K^+) = & \\
& T_i + r_B^2 T_{\bar{i}} \ + 2r_B[\cos(\delta_B + \gamma)c_i + \sin(\delta_B + \gamma)s_i],
\end{aligned} \tag{64}$$

where $\hat{\Gamma}^{\pm}_{\bar{i}}$ are the partial widths in each bin i, which are proportional to the number of events in each bin. These equations are related to each other through $12 \leftrightarrow 13$ and/or $\gamma \leftrightarrow -\gamma$ exchanges. All in all, there are $2k + 3$ unknowns in (64),

$$c_i, \ s_i, \ r_B, \ \delta_B, \ \gamma, \tag{65}$$

so that the $4k$ relations (64) are solvable for $k \geq 2$. In other words, a partition of the D meson Dalitz plot to four or more bins allows for the determination of γ without hadronic uncertainties. When $c_i = 0$ or $s_i = 0$ for all i, some equations become degenerate and γ

cannot be extracted. However, due to resonances, we do not expect this to be the case. Degeneracy also occurs if $\delta_B = 0$. In this case, γ can still be extracted if some of the c_i and/or s_i are independently measured.

This approach does not depend on any model, as it relies on event counting in each bin of the Dalitz plane. From pseudo-experiment studies however we demonstrated that it requires more statistics that the one available at present, to reach a comparable sensitivity to the model dependent approach (see next subsection).

1.5.2 Model dependent approach: assuming Breit-Wigner dependence

A model dependency to parametrize the Dalitz structure can be introduced to reduce the number of the unknown parameters to extract from the data. If the functional dependence of both the moduli and the phases of the D^0 meson decay amplitudes $A_D(s_{12}, s_{13})$ were known, then the analysis would be simplified. There would be only three variables, r_B, δ_B, and γ, that need to be fitted to the reduced partial decay widths in Eq. 59. A plausible assumption is that a significant part of the three-body $D^0 \to K_S\pi^-\pi^+$ decay proceeds via resonances. These include decay transitions of the form $D^0 \to K_S\rho^0 \to K_S\pi^-\pi^+$ or $D^0 \to K^{*-}(892)\pi^+ \to K_S\pi^-\pi^+$, as well as decays through higher resonances, e.g., $f_0(980)$, $f_2(1270)$, $f_0(1370)$ or $K_0^*(1430)$. An important feature is that there exists an overlap region of Cabibbo allowed $D^0 \to K^{*-}(892)\pi^+$, $D^0 \to K_S\rho^0$ decays, where the variation of strong phase will be large, allowing for the extraction of γ.

The decay amplitude can then be fit to a sum of Breit-Wigner functions and a constant term. Following the notations of Ref. [29] we write

$$\begin{aligned} A_D(s_{12}, s_{13}) &= A(D^0 \to K_S(p_1)\pi^-(p_2)\pi^+(p_3)) = \\ &= a_0 e^{i\delta_0} + \sum_r a_r e^{i\delta_r} \mathcal{A}_r(s_{12}, s_{13}), \end{aligned} \tag{66}$$

where the first term corresponds to the non-resonant term and the second to the resonant contributions with r denoting a specific resonance. The functions $\mathcal{A}_r$ are products of Breit-Wigner functions and appropriate Legendre polynomials that account for the fact that D meson is a spin 0 particle. Explicit expressions can be found in Appendix 4.1.1.

One of the strong phases δ_i in the ansatz (66) can be put to zero, while others are fit to the experimental data together with the amplitudes a_i. The obtained functional form of $A_D(s_{12}, s_{13})$ can then be fed to Eq. 59, which is then fit to the Dalitz plot of the $B^\pm \to (K_S\pi^-\pi^+)_D K^\pm$ decay with r_B, δ_B and γ left as free parameters.

The amplitudes for the B^- and B^+ can be respectively written as :

$$\begin{aligned} M_- &= f(s_{12}, s_{13}) + r_b e^{i(\delta_B - \gamma)}\, f(s_{13}, s_{12}) \\ M_+ &= f(s_{12}, s_{13}) + r_b e^{i(\delta_B + \gamma)}\, f(s_{13}, s_{12}) \end{aligned} \tag{67}$$

where $f(s_{12}, s_{13})$ is the amplitude of the $D^0 \to K_s\pi^-\pi^+$ decay. Once the function f is fixed using a model for the $D^0 \to K_s\pi^-\pi^+$ decay, the Dalitz distributions can be fitted simultaneously using the expressions for the two amplitudes and r_B, δ_B and γ can be measured.
It is worth noting that the function $f(s_{12}, s_{13})$ can be obtained from data using the flavour tagged D sample from the continuum : $D^{*+} \to D^0\pi_s^+$ as described in Section 4.

The same analysis is possible for the $B^- \to D^{*0}K^-$ decay. The fit technique is identical to the $B^- \to D^0 K^-$ decays but the values for r_B and δ_B are different and will be indicated in the following as r_B^* and δ_B^*.

1.5.3 Some peculiarities of the Dalitz plot analysis

The observables $\hat{\Gamma}_i^{\pm}$ defined in (64) can be used to experimentally look for direct CP violation. Explicitly,

$$a_{\rm CP}^{i,\bar{i}} \equiv \hat{\Gamma}_{i,\bar{i}}^- - \hat{\Gamma}_{\bar{i},i}^+ = 4 r_B \sin\gamma \left[c_i \sin\delta_B \mp s_i \cos\delta_B \right], \tag{68}$$

Nonzero $a_{\rm CP}$ requires non-vanishing strong and weak phases. Due to the resonances, we expect the strong phase to be large. Therefore, it may be that direct CP violation can be established in this mode even before the full analysis to measure γ is conducted. With more data, γ can be extracted assuming Breit-Wigner resonances (cf. section 1.5.2). Eventually, a model independent extraction of γ can be done (cf. section 1.5.1).

The above proposed method for the model independent measurement of γ involves a four-fold ambiguity in the extracted value. The set of equations (64) is invariant under each of the two discrete transformations

$$P_\pi \equiv \{\delta_B \to \delta_B + \pi, \gamma \to \gamma + \pi\}, \tag{69}$$
$$P_- \equiv \{\delta_B \to -\delta_B, \gamma \to -\gamma, s_i \to -s_i\}. \tag{70}$$

The discrete transformation P_π is a symmetry of the amplitude 58 and is thus an irreducible uncertainty of the method. It can be lifted if the sign of either $\cos\delta_B$ or $\sin\delta_B$ is known. The ambiguity due to P_- can be resolved if the sign of $\sin\delta_B$ is known or if the sign of s_i can be determined in at least some part of the Dalitz plot for instance by fitting a part of the Dalitz plot to Breit-Wigner functions.

2 The *BABAR* experiment at PEP-II

The primary goal of the *BABAR* experiment is the systematic study of CP-violation asymmetries in neutral and charged B decays. In particular, time-dependent asymmetries in the decay of neutral B mesons to CP eigenstates have determined the optimization of the detector. Secondary goals are precision measurements of bottom and charmed meson decays, along with τ decays, which become accessible with the high luminosity of the PEP-II B Factory [30]. The detailed physics program is documented in the *BABAR* Physics Book [31].

The PEP-II B Factory is an asymmetric e^+e^- collider designed to operate at the energy of 10.580 GeV corresponding to the $\Upsilon(4S)$ mass peak value. The resonance decays exlcusively into $B\overline{B}$ couples, precisly 50% B^+B^- and 50% $B^0\overline{B}^0$. The design average luminosity was $3 \times 10^{33}\,\mathrm{cm}^{-2}\,\mathrm{s}^{-1}$, which on has been satisfied and improved reaching a peak luminosity of $9.2 \times 10^{33}\,\mathrm{cm}^{-2}\,\mathrm{s}^{-1}$. The electron beam has an energy of 9.0 GeV while the positron beam has an energy of 3.1 GeV resulting in a boost of the $\Upsilon(4S)$ resonance in the laboratory frame of about $\beta\gamma = 0.56$. The Lorentz boost is fundamental for the study of the time-dependent CP asymmetries in the neutral B meson system. The average separation of the B mesons due to the boost is approximately $\beta\gamma c\tau \simeq 250\,\mu$m, where τ is the B^0 lifetime, an accessible measurement for the SVT vertex detector which has a precision on the single decay vertex of 80 μm.

Fig. 10 shows a longitudinal section through the detector center. The detector is installed at the PEP-II interaction region. To maximize the geometric acceptance for the boosted $\Upsilon(4S)$ decays, the whole detector is offset relative to the beam-beam interaction point (IP) by 0.37 m in the direction of the lower energy beam.

The inner detector consists of a silicon vertex tracker, a drift chamber, a ring-imaging Čerenkov detector, and a CsI calorimeter. These detector systems are surrounded by a superconducting solenoid that generates a field of 1.5 T. The steel flux return is instrumented for muon and neutral hadron detection. The polar angle coverage extends to 350 mrad in the forward direction and 400 mrad in the backward direction, defined relative to the high energy beam. The right handed coordinate system is anchored on the main tracking system, the drift chamber, with the z-axis coinciding with its principal axis. The positive y-axis points upward and the positive x-axis points away from the center of the PEP-II storage rings.

A trigger system is used to enhance interesting collision events with respect to background coming, for instance, from interactions of beams with residual gas. A first level trigger (L1) is implemented in hardware and is designed to provide a maximal output rate of 2 kHz. A third level one (L3) is realized in software and its output rate is limited to 120 Hz by the downstream storage and processing capacity.

Simulation of *BABAR* detector response is realized with a GEANT3-based [32] application of the Monte Carlo simulation technique. Particle production and decays are simulated in an event generator program interfaced to LUND/JETSET [33]. The description of radiation by charged particles is realized using PHOTOS [34].

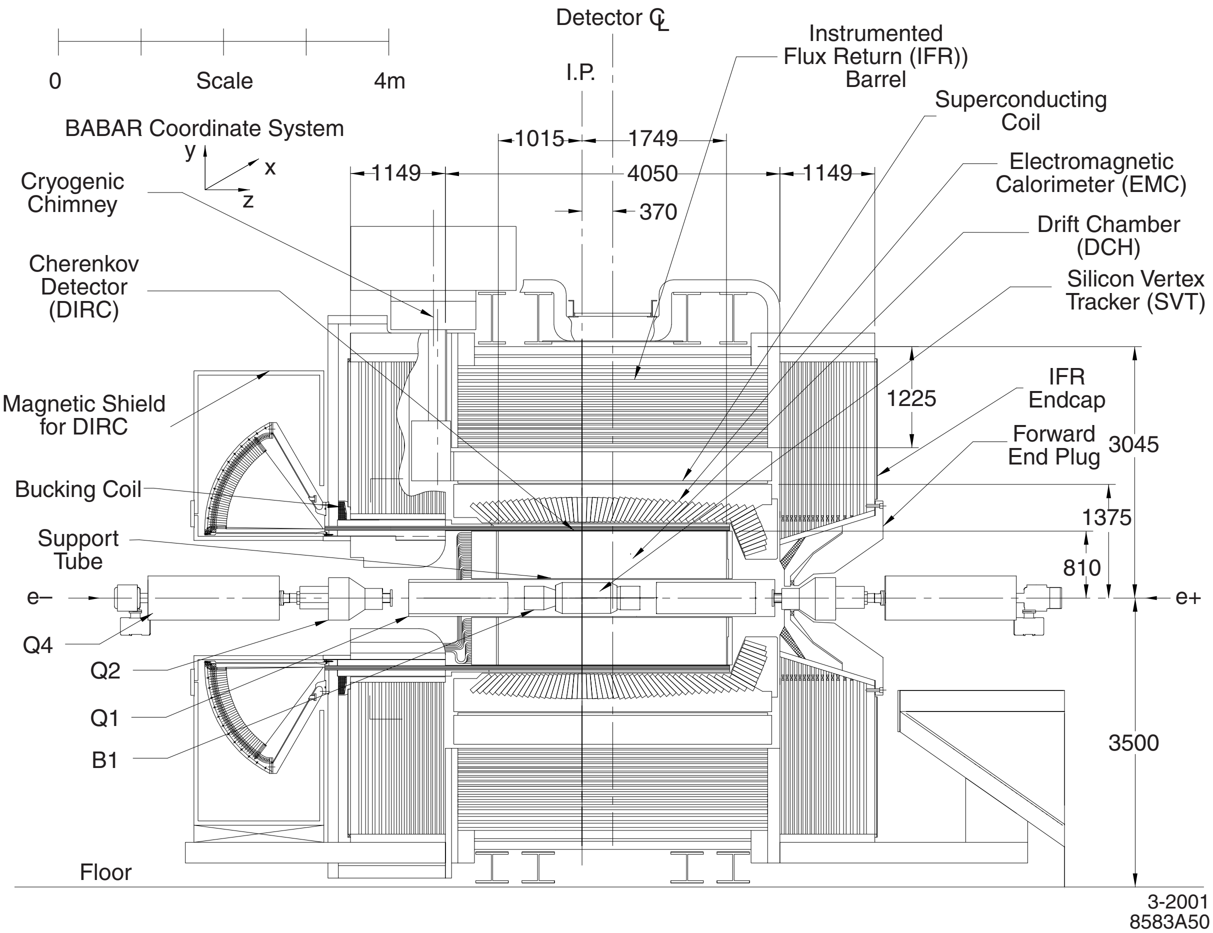

Figure 10: Longitudinal section of *BABAR* detector.

2.1 The B-factory PEP-II

PEP-II is an e^+e^- storage ring system designed to operate at a center of mass (CMS) energy of 10.58 GeV, corresponding to the mass of the $\Upsilon(4S)$ resonance. The parameters of these energy asymmetric storage rings are presented in Tab. 2.1. Values are given both for the design and for typical colliding beam operation in the first year. HER and LER refer to the high energy e^- and low energy e^+ ring, respectively. σ_{Lx}, σ_{Ly}, and σ_{Lz} refer to the horizontal, vertical, and longitudinal r.m.s. size of the luminous region. PEP-II has surpassed its design goals, both in terms of the instantaneous and the integrated daily luminosity, with significantly fewer bunches than anticipated.

Parameters	Design	Typical
Energy HER/LER (GeV)	9.0/3.1	9.0/3.1
Current HER/LER (A)	0.75/2.15	1.48/2.50
# of bunches	1658	553-829
Bunch spacing (ns)	4.2	6.3-10.5
σ_{Lx} (μm)	110	120
σ_{Ly} (μm)	3.3	5.6
σ_{Lz} (μm)	9000	9000
Luminosity ($10^{33}\,\mathrm{cm}^{-2}\mathrm{s}^{-1}$)	3	9.0
Daily int. luminosity (pb^{-1}/d)	135	700

Table 1: PEP-II beam parameters. Values are given both for the design and for typical colliding beam operation.

Most of the data are recorded at the peak of the $\Upsilon(4S)$ resonance: they are referred to as *on-resonance data*. In Tab.2.1 the main processes active at the $\Upsilon(4S)$ resonance are summarized with their cross sections: the production of light quark pairs (u, d, s) and *charm* quark pairs is usually referred to as *continuum* production. In order to allow for studies of this non-resonant continuum about 12% of data are taken at a CMS energy 40 MeV below the $\Upsilon(4S)$. They are commonly referred to as *off-resonance data*.

The bunches collide head-on and are separated magnetically in the horizontal plane by a pair of dipole magnets (*B1* in Fig.10), followed by a series of offset quadrupoles: they are permanent magnets made of samarium-cobalt placed inside the field of the *BABAR* solenoid. The collision axis is off-set from the z-axis of the *BABAR* detector by about 20 mrad in the horizontal plane to minimize the perturbation of the beams by the solenoid field.

The beam parameters that are most critical for the *BABAR* performance are the luminosity, the energies of the two beams, and the position, angles, and size of the luminous region (*beamspot*). While PEP-II measures radiative Bhabha scattering to provide a fast monitor of the relative luminosity for operations, *BABAR* derives the absolute luminosity offline from other QED processes, primarily e^+e^- and $\mu^+\mu^-$ production. During operation, the mean energies of the two beams are calculated from the total magnetic bending strength and the average deviations of the accelerating frequencies from their central values. While the systematic uncertainty in the PEP-II calculation of the absolute beam energies is estimated to be 5–10 MeV, the relative energy setting for each beam is accurate and stable to about

$e^+e^- \to$	Cross-section (nb)
$b\bar{b}$	1.05
$c\bar{c}$	1.30
$s\bar{s}$	0.35
$u\bar{u}$	1.39
$d\bar{d}$	0.35
$\tau^+\tau^-$	0.94
$\mu^+\mu^-$	1.16
e^+e^-	~ 40

Table 2: Production cross-sections at $\sqrt{s} = M_{\Upsilon(4S)}$. The *Bhabha* cross-section into e^+e^- is the effective cross-section, expected within the experimental acceptance.

1 MeV. The r.m.s. energy spreads of the LER and HER beams are 2.3 MeV and 5.5 MeV, respectively.

The direction of the beams relative to *BABAR* is measured iteratively run-by-run using $e^+e^- \to e^+e^-$ (*Bhabha*) and $e^+e^- \to \mu^+\mu^-$ (*dimuon*) events.

The size and position of the luminous region are critical parameters for the time dependent analyses and their values are monitored continuously online and offline. The design values for the size of the luminous region are presented in Tab. 2.1. The vertical size is too small to be measured directly. It is inferred from the measured luminosity, the horizontal size, and the beam currents; it varies typically by 1–2 μm.

The transverse position, size, and angles of the luminous region relative to the *BABAR* coordinate system are determined by analyzing the distribution of the distance of closest approach to the z-axis of the tracks in well measured two-track events as a function of the azimuth ϕ. The longitudinal parameters are derived from the longitudinal vertex distribution of the two tracks. The uncertainties in the average beam position are of the order of a few μm in the transverse plane and 100 μm along the collision axis. Run-by-run variations in the beam position are comparable to these measurement uncertainties, indicating that the beams are stable over the period of a typical run. These measurements are also checked offline by measuring the primary vertices in multi-hadron events[3]. The measured horizontal and longitudinal beam sizes, corrected for tracking resolution, are consistent with those measured by PEP-II.

In Fig.11 the integrated luminosity delivered by PEP-II and recorded by *BABAR* is shown up to the end of July 2004. The dataset is divided in four different time periods:

- **Run1**, corresponding to data collected in 2000
- **Run2**, corresponding to the period January 2001- July 2002
- **Run3**, corresponding to the period November 2002 - July 2003

[3]By vertexing all the reconstructed tracks in the event it is possible to have an estimate of the position of the *primary vertex*, that is of the $\Upsilon(4S)$ decay point. Because of the boost along z inducing a relative displacement of the two B mesons the resolution of this method is rather poor and it is worsened by the presence of long-lived particles in the transverse plane.

- **Run4**, corresponding to the period September 2003 - July 2004

In this analysis **Run1** to **Run4** data are used.

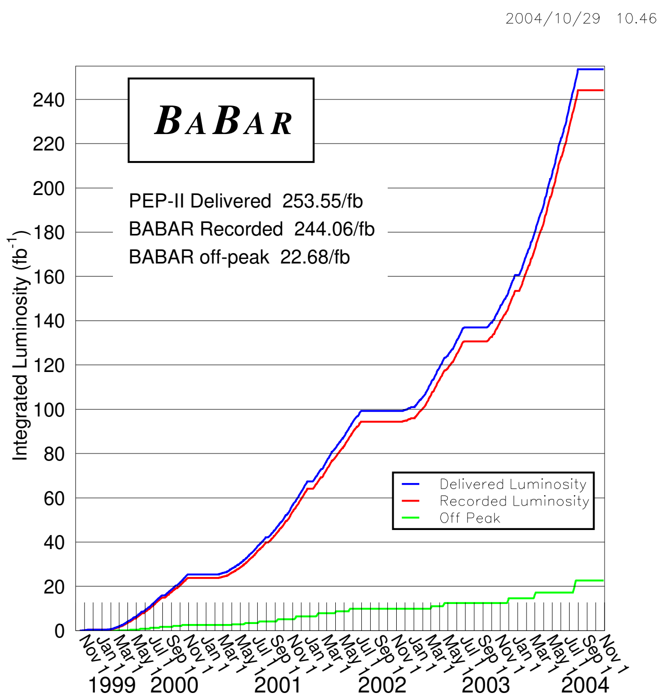

Figure 11: PEP-II delivered and recorded luminosity from the beginning of data taking.

2.2 Detector overview

The *BABAR* detector was designed and built by a large international team of scientists and engineers. Details of its original design are documented in the Technical Design Report [35], issued in 1995. The detector is described in detail in [36], here we present an overview of the subdetectors and we describe their importance in the present analysis.

Figure 10 shows a longitudinal section through the detector center. The detector surrounds the PEP-II interaction region. To maximize the geometric acceptance for the boosted

$\Upsilon(4S)$ decays, the whole detector is offset relative to the beam-beam interaction point (IP) by 0.37 m in the direction of the lower energy beam.

The inner detector consists of a silicon vertex tracker, a drift chamber, a ring-imaging Čerenkov detector, and a CsI calorimeter. These detector systems are surrounded by a superconducting solenoid that is designed for a field of 1.5 T. The steel flux return is instrumented for muon and neutral hadron detection. The polar angle coverage extends to 350 mrad in the forward direction and 400 mrad in the backward direction, defined relative to the high energy beam. As indicated in the two drawings, the right handed coordinate system is anchored on the main tracking system, the drift chamber, with the z-axis coinciding with its principal axis. This axis is offset relative to the beam axis by about 20 mrad in the horizontal plane. The positive y-axis points upward and the positive x-axis points away from the center of the PEP-II storage rings.

The detector is of compact design, its transverse dimension being constrained by the 3.5 m elevation of the beam above the floor. The solenoid radius was chosen by balancing the physics requirements and performance of the drift chamber and calorimeter against the total detector cost. As in many similar systems, the calorimeter was the most expensive single system and thus considerable effort was made to minimize its total volume without undue impact on the performance of either the tracking system or the calorimeter itself. The forward and backward acceptance of the tracking system are constrained by components of PEP-II, a pair of dipole magnets (B1) followed by a pair of quadrupole magnets (Q1). The vertex detector and these magnets are placed inside a support tube (4.5 m long and 0.217 m inner diameter) that is cantilevered from beamline supports. The central section of this tube is fabricated from a carbon-fiber composite.

Since the average momentum of charged particles produced in B-meson decay is less than 1 GeV/c, the precision of the measured track parameters is heavily influenced by multiple Coulomb scattering. Similarly, the detection efficiency and energy resolution of low energy photons are severely impacted by material in front of the calorimeter. Thus, special care has been taken to keep material in the active volume of the detector to a minimum.

An overview of the coverage, the segmentation, and performance of the *BABAR* detector systems is presented in Table 3.

The charged particle tracking system is made of two components, the silicon vertex tracker (SVT) and the drift chamber (DCH).

The SVT has been designed to measure angles and positions of charged particles just outside the beam pipe. The SVT is composed of five layers of double-sided silicon strip detectors that are assembled from modules with readout at each end, thus reducing the inactive material in the acceptance volume. The inner three layers primarily provide position and angle information for the measurement of the vertex position. They are mounted as close to the water-cooled beryllium beam pipe as practical, thus minimizing the impact of multiple scattering in the beam pipe on the extrapolation to the vertex. The outer two layers are at much larger radii, providing the coordinate and angle measurements needed for linking SVT and DCH tracks.

The principal purpose of the DCH is the momentum measurement for charged particles. It also supplies information for the charged particle trigger and a measurement of dE/dx for particle identification. The DCH is of compact design, with 40 layers of small, approximately hexagonal cells. Longitudinal information is derived from wires placed at small angles to the principal axis. By choosing low-mass wires, and a helium-based gas mixture the multiple scattering inside the DCH is minimized. The readout electronics are mounted on the backward endplate of the chamber, minimizing the amount of material in front of the calorimeter endcap.

The DIRC, the detector of internally reflected Čerenkov light, is a novel device providing separation of pions and kaons from about 500 MeV/c to the kinematic limit of 4.5 GeV/c. Čerenkov light is produced in 4.9 m long bars of synthetic fused silica of rectangular cross section, 1.7 cm $\times$ 3.5 cm, and transported by total internal reflection, preserving the angle of emission, to an array of photomultiplier tubes. This array forms the backward wall of a toroidal water tank that is located beyond the backward end of the magnet. Images of the Čerenkov rings are reconstructed from the position and time of arrival of the signals in the photomultiplier tubes.

The electromagnetic calorimeter (EMC) is designed to detect electromagnetic showers with excellent energy and angular resolution over the energy range from 20 MeV to 4 GeV. This coverage allows the detection of low energy π^0s and η^0s from B decays and higher energy photons and electrons from electromagnetic, weak, and radiative processes. The EMC is a finely segmented array of projective geometry made of thallium doped cesium iodide (CsI(Tl)) crystals. The crystals are arranged in modules that are supported individually from an external support structure. This structure is built in two sections, a barrel and a forward endcap. To obtain the desired resolution, the amount of material in front of and in-between the crystals is held to a minimum. The individual crystals are read out by pairs of silicon PIN diodes. Low noise analog circuits and frequent, precise calibration of the electronics and energy response over the full dynamic range are crucial for maintaining the desired performance.

The instrumented flux return (IFR) is designed to identify muons and to detect neutral hadrons. For this purpose, the magnet flux return steel in the barrel and the two end doors is segmented into layers, increasing in thickness from 2 cm on the inside to 10 cm at the outside. Between these steel absorbers, single gap resistive plate chambers (RPCs) are inserted which detect streamers from ionizing particles via external capacitive readout strips. There are 19 layers of RPCs in the barrel sectors and 18 layers in the end doors. Two additional cylindrical layers of RPCs with four readout planes are placed at a radius just inside the magnet cryostat to detect particles exiting the EMC.

2.3 *BaBar* tracking system

The charged particle tracking system is made of two components, the silicon vertex tracker (SVT) and the drift chamber (DCH). The rule of the tracking system is fundamental in this analysis as the information of the decay vertex helps discriminating the signal events from the combinatoric events, which have a poor vertex probability. The precise reconstruction of the track parameters and momentum improves the resolution on the invariant masses, used as discriminating variables in this analysis.

Table 3: Overview of the coverage, segmentation, and performance of the *BABAR* detector systems. The notation (C), (F), and (B) refers to the central barrel, forward and backward components of the system, respectively. The detector coverage in the laboratory frame is specified in terms of the polar angles θ_1 (forward) and θ_2 (backward). The number of readout channels is listed. The dynamic range (resolution) of the FEE circuits is specified for pulse height (time) measurements by an ADC (TDC) in terms of the number of bits (nsec). Performance numbers are quoted for 1 GeV/c particles, except where noted.

System	θ_1 (θ_2)	No. Channels	ADC (bits)	TDC (ns)	No. Layers	Segmentation	Performance
SVT	20.1° (-29.8°)	150K	4	-	5	50-100 μm $r-\phi$ 100-200 μm z	$\sigma_{d_0} = 55\,\mu$m $\sigma_{z_0} = 65\,\mu$m
DCH	17.2° (-27.4°)	7,104	8	2	40	6-8 mm drift distance	$\sigma_\phi = 1$ mrad $\sigma_{tan\lambda} = 0.001$ $\sigma_{\mathbf{p}^t}/\mathbf{p}^t = 0.47\%$ $\sigma(dE/dx) = 7.5\%$
DIRC	25.5° (-38.6°)	10,752	-	0.5	1	35 × 17 mm ^{2} ($r\Delta\phi \times \Delta r$) 144 bars	$\sigma_{\theta_C} = 2.5$ mrad per track
EMC(C)	27.1° (-39.2°)	2 × 5760	17–18	—	1	47 × 47 mm ^{2} 5760 cystals	$\sigma_E/E = 3.0\%$ $\sigma_\phi = 3.9$ mrad
EMC(F)	15.8° (27.1°)	2 × 820			1	820 crystals	$\sigma_\theta = 3.9$ mrad
IFR(C)	47° (-57°)	22K+2K	1	0.5	19+2	20-38 mm	90% $\mu^\pm$ eff. 6-8% $\pi^\pm$ mis-id
IFR(F)	20° (47°)	14.5K			18	28-38 mm	(loose selection, 1.5–3.0 GeV/c)
IFR(B)	-57° (-26°)	14.5K			18	28-38 mm	

2.3.1 SVT: silicon vertex tracker

The SVT, the silicon vertex tracker has been designed to reconstruct the decay vertex position with a precision better than 80 μm and to provide standalone tracking reconstruction for tracks with transverse momentum in the range $50 - 120\,\mathrm{MeV}/c$. SVT provides the best measurement of the track angles, which is required to achieve design resolution for the Čerenkov angle for high momentum tracks. It is optimized in order to have the largest acceptancy in the CM frame; it extends down to 20° in the forward direction and up to 30° in the backword direction. The limit are posed by the B1 permanent magnet used to direct the colliding beams close to the interaction region. The SVT must withstand 2 MRad of ionizing radiation. A radiation monitoring system capable of aborting the beams is required. The expected radiation dose is 1 Rad/day in the horizontal plane immediately outside the beam pipe (where the highest radiation is concentrated), and 0.1 Rad/day on average otherwise. The SVT is cooled to remove the heat generated by the electronics. In addition, it operates in the 1.5 T magnetic field.

It consists of five layers of double-sided silicon strip detectors (Figures 12 and 13) that are assembled from modules with readout at each end, thus reducing the amount of inactive material in the acceptance volume. The inner three layers primarily provide position and angle information for the measurement of the vertex position. They are mounted as close to the water-cooled beryllium beam pipe as practical (at a radius $r = 3.2\,cm$), thus minimizing the impact of multiple scattering in the beam pipe on the extrapolation to the vertex. The outer two layers are located at a much larger radius ($r = 9.1\,cm$) in order to provide the coordinate and angle measurements needed for linking SVT and DCH tracks.

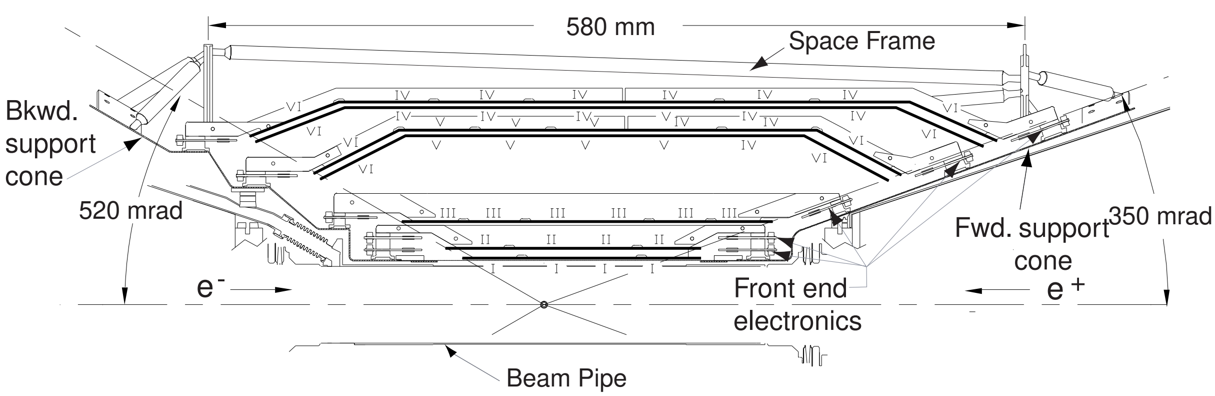

Figure 12: Schematic view of SVT: longitudinal section. The roman numerals label the six different types of sensors.

The five layers of double-sided silicon strip sensors, which form the SVT detector, are organized in 6, 6, 6, 16, and 18 modules, respectively. The strips on the opposite sides of

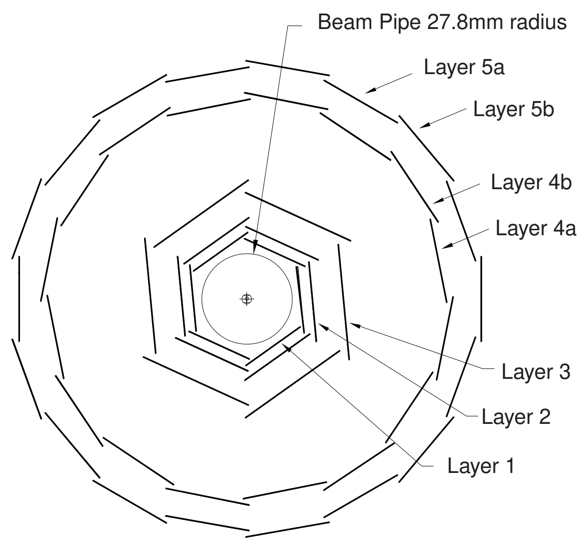

Figure 13: Schematic view of SVT: tranverse section.

each sensor are oriented orthogonally to each other: the ϕ measuring strips (ϕ *strips*) run parallel to the beam and the z measuring strips (z *strips*) are oriented transversely to the beam axis. The modules of the inner three layers are straight, while the modules of layers 4 and 5 are *arch*-shaped (Figure 12).

This arch design was chosen to minimize the amount of silicon required to cover the solid angle, while increasing the crossing angle for particles near the edges of acceptance. The modules are divided electrically into two half-modules, which are read out at the ends.

The total active silicon area is $0.96\,\mathrm{m}^{\,2}$ and the material traversed by particles is $\sim 4\%$ of a radiation length. The geometrical acceptance of SVT is 90% of the solid angle in the c.m. system, typically 86% are used in charged particle tracking.

The efficiency of the associated hits to the tracks transversing the active volume is 97% on average. Only 4 readout sections are defective out of 208 due to installations problems. The hit resolution is around $10\,\mu$m for perpendicular tracks to the silicon wafer in the innest layers. The SVT has been operating efficiently since the installation in the *BABAR* experiment in May 1999, the radion dose is within the planned budget and no failures have been observed due to radiation damage.

2.3.2 DCH: drift chamber

The principal purpose of the DCH is momentum measurement for charged particles. It also supplies information for the charged particle trigger and a measurement of dE/dx for particle identification. The DCH is of compact design, with 40 layers of small, approximately hexagonal cells. Longitudinal information is derived from wires placed at small angles (*stereo layers*) to the principal axis. Wires in the *axial layers* are parallel to the principal axis and both axial and stereo layers provide curvature measurement of tracks. By choosing low-mass wires, and a helium-based gas mixture the multiple scattering inside the DCH is kept to a minimum. At normal incidence the DCH is $1.08\,10^{-2}$ radiation length long. The readout

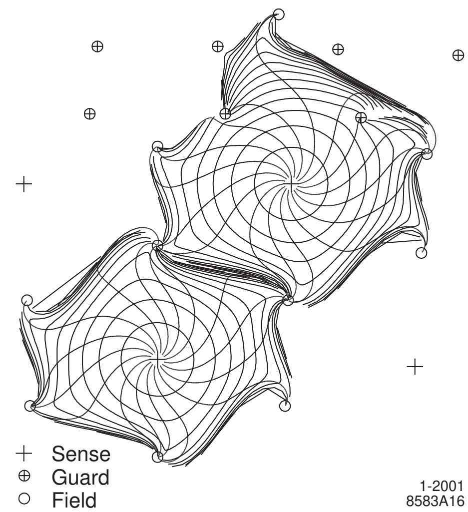

Figure 14: Drift cell isochrones (contours of equal drift times of ions) in cells of layers 3 and 4 of an axial superlayer. The isochrones are spaced by 100 ns. They are circular near the sense wires, but become irregular near the field wires, and extend into the gap between superlayers.

electronics is mounted on the backward endplate of the chamber, minimizing the amount of material in front of the calorimeter endcap. Each of the 7,104 small drift cell consists of one sense wire surrounded by six field wires, as shown in Fig. 14. While the field wires are at ground potential, a positive high voltage is applied to the sense wires. An avalanche gain of approximately 5×10^4 is obtained at a typical operating voltage of 1960 V and with a 80:20 helium:isobutane gas mixture. During part of year 2000 the operating voltage was lowered to 1900 V to preserve some damaged section of the DCH. The main effect was a reduced hit efficiency and, consequently, a reduced tracking efficiency and a worse momentum resolution with some impact on the final data analysis. During year 2001 data-taking the operating voltage was set to 1930 V .

The global coordinate system is defined by the DCH position: because of seismic activity the SVT moves with respect to the DCH so it must be periodically aligned as a whole in the DCH system. Moreover, the SVT is not a perfect rigid body and the relative position of its 340 modules must be determined too. The alignement procedure is performed using tracks from $e^+e^- \rightarrow \mu^+\mu^-$ events and cosmic rays. It consists of two steps. A global alignement procedure, updated on a run-by-run basis, able to detemine the six global alignment parameters, three translations and three rotations, by minimizing the difference between the track parameters obtained with the SVT-only and the DCH-only fits. A SVT local alignement procedure is more complex, and, since the local internal positions are relatively stable, is performed only when needed, typically after magnet quenches or detector access. The SVT local alignement can represent a source of systematic bias or distortion in the measurement of Δz and therefore it must be accounted for in the CP asymmetry analysis.

The reconstruction of charged particle tracks relies on information from both tracking systems, the SVT and the DCH. Charged tracks are defined by five parameters $(d_0, \phi_0, \omega, z_0, \tan\lambda)$ and their associated error matrix. These parameters are measured at the point of closest approach to the z-axis; d_0 and z_0 are the distances of this point from the origin of the coordinate system in the x–y plane and along the z-axis, respectively. The angle ϕ_0 is the azimuth of the track, λ is its dip angle relative to the transverse plane, and $\omega = 1/p_t$ is its curvature. d_0 and ω are signed variables, their sign depending on the charge of the track. The track finding and the fitting procedures make use of Kalman filter algorithm [37] that takes into account the detailed distribution of material in the detector and the full map of the magnetic field. Charged particle tracking has been studied with large samples of cosmic ray muons, e^+e^-, $\mu^+\mu^-$, and $\tau^+\tau^-$ events, as well as multi-hadrons.

2.3.3 Tracking efficiency

Track reconstruction uses information from the SVT, the DCH and the L3 trigger. The absolute event timing information (the event start time t_0) is determined iteratively by the track finding algorithms along with the five helix parameters.

The L3 trigger includes an algorithm that performs track pattern recongnition in the DCH and, subsequently, a rough track fitting with an estimate of t_0. This track pattern recongnition is based on the L1 *track segment* finder modules.[4] In the subsequent reconstruction steps, tracks are selected by performing helix fits to the hits used by the L3 track finding algorithm. A search for additional hits in the DCH that may belong on these tracks is performed, while t_0 is further improved by using only hits associated with tracks. Two more sophisticated tracking procedures are applied which are designed to find tracks that either do not pass through the entire DCH or do not originate from the IP. These algorithms primarily use track segments that have not already been assigned to other tracks, and thus benefit from a progressively cleaner tracking environment with a constantly improving t_0. At the end of this process, tracks are again fitted using a Kalman filter method. The resulting tracks are then extrapolated into the SVT and SVT track segments are added, provided they are consistent with the expected error in the extrapolation through the intervening material and inhomogeneous magnetic field. Among the possible SVT segments, those with the smallest residuals and the largest number of SVT layers are retained and a Kalman fit is performed to the full set of DCH and SVT hits. Any remaining SVT hits are then passed to two complementary standalone track finding algorithms. Finally, an attempt is made to combine tracks that are only found by one of the two tracking systems and thus recover tracks scattered in the material of the support tube.

The efficiency for reconstructing tracks in the DCH has been measured as a function of transverse momentum, polar and azimuthal angles in multi-track events. These measurements rely on specific final states and exploit the fact that the track reconstruction can be performed independently in the SVT and the DCH.

The absolute DCH tracking efficiency is determined as the ratio of the number of reconstructed DCH tracks to the number of tracks detected in the SVT, with the requirement that they fall within the acceptance of the DCH.

[4]These L1 modules identify in each DCH superlayers structures of four contiguous *hits*, called *track segments*.

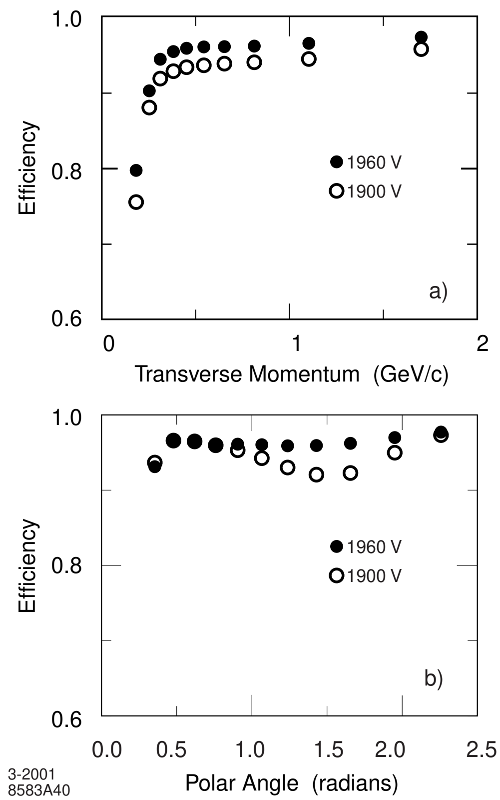

Figure 15: Track reconstruction efficiency in the DCH at operating voltages of 1900 V and 1960 V, as a function of a) transverse momentum, and b) polar angle. The efficiency is measured in multi-hadron events as the fraction of all tracks detected in the SVT for which the DCH portion is also reconstructed.

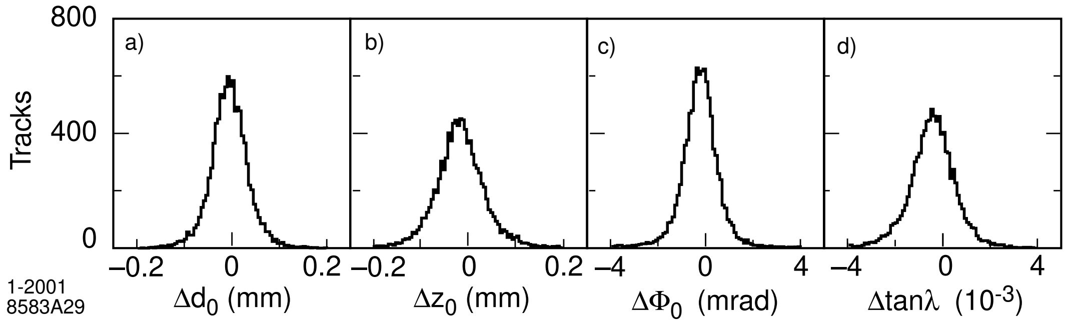

Figure 16: Measurements of the differences between the fitted track parameters of the two halves of cosmic ray muons, with transverse momenta above 3 GeV/c, a) Δd_0, b) Δz_0, c) $\Delta\phi_0$, and d) $\Delta\tan\lambda$.

Such studies have been performed using different samples of multi-hadron events. Fig. 15 shows the result of one of these studies for the two voltage settings in **Run1**. The presence of additional SVT hits originated from machine background produces "fake" tracks. The DCH tracking efficiency errors are dominated by the uncertainty in the correction for these fake tracks. At the design voltage of 1960 V, the per-track efficiency averages $(98 \pm 1)\%$ for $p_t > 200\,\mathrm{MeV}/c$ and polar angles $\theta > 500\,\mathrm{mrad}$. The data recorded at 1900 V show a reduction in efficiency by about 5% for tracks at close to normal incidence, indicating that the cells are not fully efficient at this voltage.

2.3.4 Track Parameter Resolutions

The resolution in the five track parameters is monitored using e^+e^- and $\mu^+\mu^-$ events. It is further investigated offline for tracks in multi-hadron events and cosmic ray muons.

Cosmic rays that are recorded during normal data-taking offer a simple way of studying the track parameter resolution. The upper and lower halves of the cosmic ray tracks traversing the DCH and the SVT are fitted as two separate tracks, and the resolution is derived from the difference of the measured parameters for the two track halves. To assure that the tracks pass close to the IP, cuts are applied on the d_0, z_0, and $\tan\lambda$. The results of this comparison for the coordinates of the point of closest approach and the angles are shown in Fig. 16 for tracks with momenta above p_t of 3 GeV/c. The distributions are symmetric; the non-Gaussian tails are small. The distributions for the differences in z_0 and $\tan\lambda$ show a clear offset, attributed to residual problems with the internal alignment of the SVT. Based on the full width at half maximum of these distributions the resolutions for single tracks can be stated as

$$\sigma_{d_0} = 23\mu m \qquad \sigma_{\phi_0} = 0.43\,\mathrm{mrad}$$
$$\sigma_{z_0} = 29\mu m \qquad \sigma_{\tan\lambda} = 0.53 \cdot 10^{-3}.$$

The dependence of the resolution in d_0 and z_0 on the transverse momentum p_t is presented in Fig. 17. The measurement is based on tracks in multi-hadron events. The resolution is determined from the width of the distribution of the difference between the measured

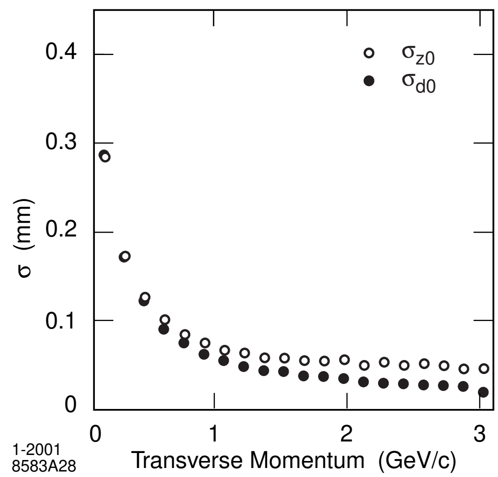

Figure 17: Resolution in the parameters d_0 and z_0 for tracks in multi-hadron events as a function of the transverse momentum. The data are corrected for the effects of particle decays and vertexing errors.

parameters, d_0 and z_0, and the coordinates of the vertex reconstructed from the remaining tracks in the event. These distributions peak at zero, but have a tail for positive values due to the effect of particle decays. Consequently, only the negative part of the distributions reflects the measurement error and is used to extract the resolution. Event shape cuts and a cut on the χ^2 of the vertex fit are applied to reduce the effect of weak decays on this measurement. The contribution from the vertex errors are subtracted in quadrature from the measured resolutions. The d_0 and z_0 resolutions so measured are about $25\,\mu$m and $40\,\mu$m respectively at $p_t = 3\,\mathrm{GeV}/c$. These values agree well with expectations, and are also in reasonable agreement with the results obtained from cosmic rays.

Fig. 18 shows the estimated error in the measurement of the difference along the z-axis between the vertices of the two neutral B mesons. One of the B's is fully reconstructed, the other serves as a flavor tag (see Chapter 4). The r.m.s. of $190\,\mu$m is dominated by the reconstruction of the tagging B, the r.m.s. resolution for the fully reconstructed B meson is $70\,\mu$m.

While the position and angle measurements near the IP are dominated by the SVT, the DCH contributes primarily to the p_t measurement. Fig. 19 shows the resolution in the transverse momentum derived from cosmic muons. The data are well represented by a linear function, given by $\sigma_{p_t}/p_t = (0.13 \pm 0.01)\% \cdot p_t + (0.45 \pm 0.03)\%$, where the transverse momentum p_t is measured in GeV/c. These values for the resolution parameters are very close to the initial estimates and can be well reproduced by Monte Carlo simulations.

2.4 Particle Identification

The study of *CP*-violation using hadronic final states of the $B\overline{B}$ meson system requires the ability to identify the b-quark charge of one of the B mesons via the cascade decay $b \to c \to s$, while fully reconstructing the final state of the other over a large region of

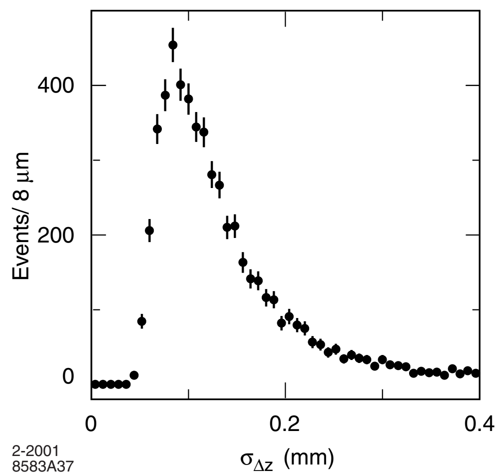

Figure 18: Estimated error in the difference Δz between the B meson vertices for a sample of events in which one B^0 is fully reconstructed.

solid angle and momentum. The momenta of the kaons used for flavor tagging extend up to about 2 GeV/c, with most of them below 1 GeV/c, since they come from the secondary decays of charmed mesons. *Particle Identification* (PID) below 700 MeV/c exploits primarily the dE/dx measurements in the DCH and SVT. In Fig.20 dE/dx in the DCH as a function of track momenta is shown for different control samples of particles. Tracks originating from the B, expecially in the case of charmless decays, have typical momentum larger than this range. In this case, the discriminating power between pions and kaons from the tracking system is to poor to allow a cleean separation of kaons and pions.

BABAR therefore includes a dedicated PID subdetector, made by a new kind of ring-imaging Čerenkov detector called the DIRC [38] (Detector of Internally Reflected *Čerenkov* light). It was designed to be able to provide π/K separation of $\sim 4\ \sigma$ or greater, for all tracks from B-meson decays from the pion Čerenkov threshold up to 4.2 GeV/c.

The DIRC is placed before the calorimeter and therefore it should be thin and uniform in terms of radiation lengths, to minimize degradation of the calorimeter energy resolution, and small in the radial dimension, to reduce the volume, hence, the cost of the calorimeter. Finally, for operating at high luminosity, it needs fast signal response, and a good tolerance to high backgrounds.

Fig. 21 shows a schematic of the DIRC geometry that illustrates the principles of light production, transport, and imaging. The radiator material of the DIRC is synthetic, fused silica in the form of long, thin bars with rectangular cross section. These bars serve both as radiators and as light pipes for the portion of the light trapped in the radiator by total internal reflection. Fused, synthetic silica is chosen because of its resistance to ionizing radiation, its long attenuation length, large index of refraction, low chromatic dispersion within the wavelength acceptance of the DIRC, and because it allows an excellent optical finish on the surfaces of the bars.

In the following, the variable θ_c is used to designate the Čerenkov angle, ϕ_c denotes the azimuthal angle of a Čerenkov photon around the track direction, and n represents the mean

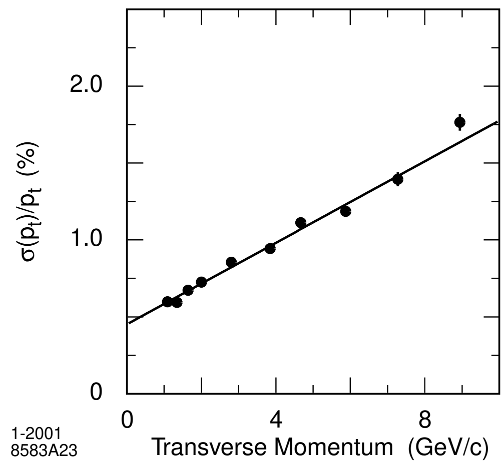

Figure 19: Resolution in the transverse momentum p_t determined from cosmic ray muons traversing both the DCH and the SVT.

index of refraction of fused silica ($n = 1.473$), with the familiar relation

$$\cos\theta_c = 1/n\beta \tag{71}$$

($\beta = v/c,\ v =$ velocity of the particle, $c =$ velocity of light).

For particles with $\beta \approx 1$, some photons will always lie within the total internal reflection limit, and will be transported to either one or both ends of the bar, depending on the particle incident angle. To avoid instrumenting both ends of the bar with photon detectors, a mirror is placed at the forward end, perpendicular to the bar axis, to reflect incident photons to the backward, instrumented end.

Once photons arrive at the instrumented end, most of them emerge into a water-filled expansion region, called the *standoff box*. A fused silica *wedge* at the exit of the bar reflects photons at large angles relative to the bar axis. It thereby reduces the size of the required detection surface and recovers those photons that would otherwise be lost due to internal reflection at the fused silica/water interface. The photons are detected by an array of densely packed photomultiplier tubes (PMTs), each surrounded by reflecting *light catcher* cones to capture light which would otherwise miss the active area of the PMT. The PMTs are placed at a distance of about 1.2 m from the bar end. The expected Čerenkov light pattern at this surface is essentially a conic section, where the cone opening-angle is the Čerenkov production angle modified by refraction at the exit from the fused silica window.

The DIRC is intrinsically a three-dimensional imaging device. Photons are focused onto the phototube detection surface via a *pinhole* defined by the exit aperture of the bar, so that the photon propagation angles can be measured. Imaging in the DIRC occurs in three dimensions, by recording the time of the PMT signal. As the track position and angles are known from the tracking system, the two angles (θ_c, ϕ_c) can be determined. This over-constraint on the angles is particularly useful in dealing with ambiguities and high background rates.

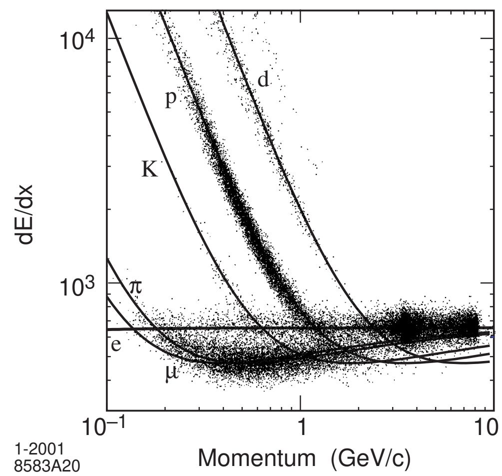

Figure 20: Measurement of dE/dx in the DCH as a function of track momenta. The data include large samples of beam background triggers, as evident from the high rate of protons. The curves show the Bethe-Bloch predictions derived from selected control samples of particles of different masses. is clear that dE/dx in the DCH is able to separate pion from kaon at relatively low momenta

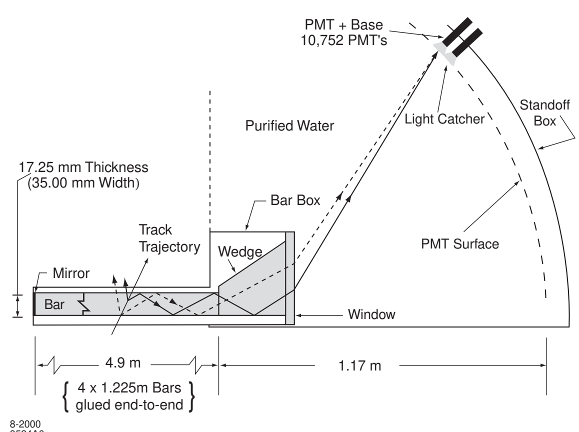

Figure 21: Schematics of the DIRC fused silica radiator bar and imaging region. Not shown is a 6 mradangle on the bottom surface of the wedge.

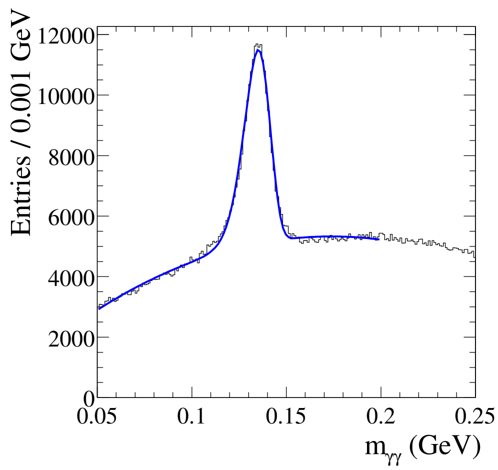

Figure 22: Invariant mass of two photons in $B\overline{B}$ events. The energies of the photons and the π^0 are required to exceed 30 MeV and 300 MeV, respectively. The solid line is a fit to the data.

2.5 Electromagnetic Calorimeter

The electromagnetic calorimeter (EMC) is designed to detect electromagnetic showers with excellent energy and angular resolution over the energy range from 20 MeV to 4 GeV. This coverage allows the detection of low energy π^0s and η^0s from B decays and higher energy photons and electrons from electromagnetic, weak, and radiative processes. The EMC is a finely segmented array of projective geometry made of thallium doped cesium iodide (CsI(Tl)) crystals. The crystals are arranged in modules that are supported individually from an external support structure. This structure is built in two sections, a barrel and a forward endcap. To obtain the desired resolution, the amount of material in front of and in-between the crystals is minimized. The individual crystals are read out by pairs of silicon PIN diodes. Low noise analog circuits and frequent, precise calibration of the electronics and energy response over the full dynamic range are crucial for maintaining the desired performance.

Neutral particles (photons, π^0, neutral hadrons) are detected in the EMC as clusters of close crystals where energy has been deposited They are required to be not matched to any charged track estrapolated from tracking volume to EMC inner surface. Quality requirements applied to those clusters allow to reject fakes or particles (especially low energy photons) not coming from the collision events.

Figure 22 shows the two-photon invariant mass in $B\overline{B}$ events. The reconstructed π^0 mass is measured to be 135.1 MeV/c^2 and is stable to better than 1% over the full photon energy range. The width of 6.9 MeV/c^2 agrees well with the prediction obtained from detailed Monte-Carlo simulations. In low-occupancy $\tau^+\tau^-$ events, the width is slightly smaller, 6.5 MeV/c^2, for π^0 energies below 1 GeV. A similar improvement is also observed in analyses using selected isolated photons in hadronic events.

The measurement of the angular resolution is based on the analysis of π^0 and η decays to two photons of approximately equal energy. The result is presented in Figure 23. The resolution varies between about 12 mrad at low energies and 3 mrad at high energies. A fit

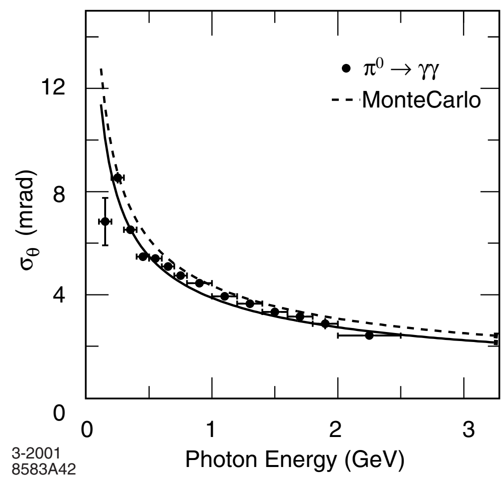

Figure 23: The angular resolution of the EMC for photons from π^0 decays. The solid curve is a fit to Equation 72.

to an empirical parameterization of the energy dependence results in

$$\begin{aligned}\sigma_\theta &= \sigma_\phi \\ &= (\frac{3.87 \pm 0.07}{\sqrt{E(\,\mathrm{GeV})}} \;+\; 0.00 \pm 0.04)\ \text{mrad.}\end{aligned} \tag{72}$$

These fitted values are slightly better than would be expected from detailed Monte Carlo simulations.

EMC is also crucial for electron identification. Different criteria are established to select electron with different level of purity. Electrons are separated from charged hadrons primarily on the basis of the ratio of the energy E deposited in the EMC to the track momentum p ($\frac{E}{p}$) and of LAT (defined in section 3.2). In addition, the dE/dx energy loss in the DCH and the DIRC Cherenkov angle are required to be consistent with an electron. The most important variable for the discrimination of hadrons is the ratio of the shower energy to the track momentum (E/p).

2.6 Instrumented Flux Return

The instrumented flux return (IFR) is designed to identify muons and to detect neutral hadrons. For this purpose, the magnet flux return steel in the barrel and the two end doors are segmented into layers, increasing in thickness from 2 cm on the inside to 10 cm at the outside. Between these steel absorbers, single gap resistive plate chambers (RPCs) are inserted which detect streamers from ionizing particles via external capacitive readout strips: the signals are read out on both sides of the gap by external electrodes made of aluminum strips. There are 19 layers of RPCs in the barrel sectors and 16 (18) layers in the forward (backard) endcap. The total thickness of steel at normal incidence is 65 cm in the barrel region, 80 (60) cm in the forward (backard) endcaps. Two additional cylindrical layers of

RPCs with four readout planes are placed just in front of the magnet cryostat to detect particles exiting the EMC.

Muons are identified by measuring the number of traversed interaction lenghts in the entire detector and comparing it with the number of expected interaction lenghts for a muon of a given momentum. Moreover, the projected intersections of a track with the RPC planes are computed and, for each readout plane, all strips clusters detected within a predefined distance from the predicted intersection are associated with the track: the average number and the r.m.s. of the distribution of RPC strips per layer gives additional μ/π discriminating power. We expect in fact the average number of strips per layer to be larger for pions producing an hadronic interaction than for muons. Other variables exploiting clusters distribution shapes are constructed. Selection criteria based on all these variables are applied to select muons. The performance of the muon selection has been tested on samples of kinematically identified muons from $\mu\mu ee$ and $\mu\mu\gamma$ final states and pions from three-prong τ decays and $K_S \to \pi^+\pi^-$ decays. As illustrated in Fig. 24, a muon detection efficiency of $\sim 90\%$ has been achieved in the momentum range of $1.5 < p < 3.0\,\mathrm{GeV}/c$ with a pion misidentification probability of about 6–8%. Decays in flight contribute about 2% to this probability. The fake rate can be reduced by a factor of about two by applying a tighter selection criteria which lower the muon detection efficiency to about 80%.

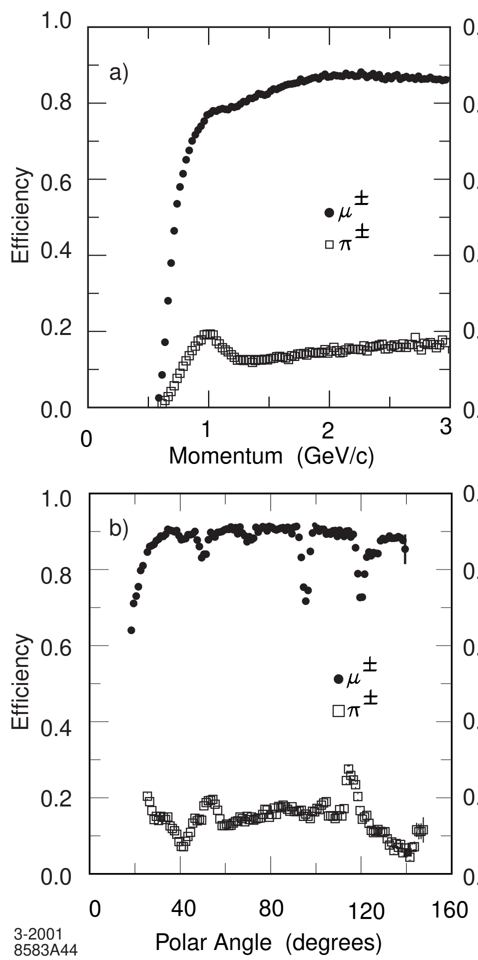

Figure 24: Muon efficiency (left scale) and pion misidentification probability (right scale) as a function of a) the laboratory track momentum, and b) the polar angle (for $1.5 < p < 3.0\,\mathrm{GeV}/c$ momentum), obtained with loose selection criteria.

3 Selection of the Events

We discuss the reconstruction of the decay modes $B^{\pm} \to D^{(*)}K^{\pm}$ with the $D^{*} \to D\pi^0, D\gamma$ and $D \to K^0_S\pi^+\pi^-$. The event selection will be discussed along with the background rejection criteria. Particularly important is the characterization of the background events, which in principle diluites the sensitivity to the CP parameters. We show DATA/Monte Carlo for the relevant variables of the analysis.

3.1 Kinematics variables for signal selection

Kinematical variables are used in the analysis to characterize the B signal events. They use the constraints of the conservation of the 4-momentum in the B decay process. These variables, which make optimum use of the measured quantities and are largely uncorrelated, are Lorentz-invariants which can be evaluated both in the laboratory and c.m. frames. The first variable, ΔE, can be expressed in Lorentz invariant form as

$$\Delta E = (2q_B q_0 - s)/2\sqrt{s}, \tag{73}$$

where $\sqrt{s} = 2E^{\star}_{beam}$ is the total energy of the e^+e^- system in the c.m. frame, and q_B and $q_0 = (E_0, \vec{p}_0)$ are the Lorentz vectors representing the momentum of the B candidate and of the e^+e^- system, $q_0 = q_{e+} + q_{e-}$. In the c.m. frame, ΔE takes the familiar form

$$\Delta E = E^{\star}_B - E^{\star}_{beam}, \tag{74}$$

here $E^{\star}_B$ is the reconstructed energy of the B meson. The ΔE distribution receives a sizable contribution from the beam energy spread, but it is generally dominated by the detector resolution and it depends on the particular B decay. In our specific case, $\sigma_{\Delta E} \simeq 15-17\,\mathrm{MeV}$, depending on the decay mode, as we will show in the following sections.
The second variable is the energy-substituted mass, m_{ES}, defined as $m^2_{\mathrm{ES}} = q^2_B$. In the laboratory frame, m_{ES} can be determined from the measured three-momentum $\vec{p}_B$ of the B candidate without explicit knowledge of the masses of the decay products:

$$m_{\mathrm{ES}} = \sqrt{(s/2 + \vec{p}_B \cdot \vec{p}_0)^2/E_0^2 - p_B^2}. \tag{75}$$

In the c.m. frame ($\vec{p}_0 = 0$), this variable reduces to:

$$m_{\mathrm{ES}} = \sqrt{E^{\star 2}_{beam} - p^{\star 2}_B}, \tag{76}$$

where $p^{\star}_B$ is the c.m. momentum of the B meson, derived from the momenta of its decay products, and the B-meson energy is substituted by $E^{\star}_{beam}$. The resolution in m_{ES} is dominated by the spread in $E^{\star}_{beam}$, $\sigma_{E^{\star}_{beam}} \simeq 2.6\,\mathrm{MeV}$.

3.2 Event shape variables and background rejection

The rejection of *continuum* events [5] is an important issue for this analysis. The cross-section for continuum events is ~ 3 times bigger than for the process $e^+e^- \to \Upsilon(4S)$, and they represent the most relevant source of background for this analysis. Event shape variables have been considered in order to suppress this source of background:

[5] with *continuum* events we refer to $e^+e^- \to q\overline{q}$ events, where $q = u, d, s, c$ quarks

- **Thrust** The thrust axis of an event, $\hat{T}$, is defined to be the direction which maximizes the sum of the longitudinal momenta of the particles. Thrust, T, is related to this direction [40] by

$$T = \frac{\sum_i |\hat{T} \cdot \mathbf{p}_i|}{\sum_i |\mathbf{p}_i|}. \tag{77}$$

  The allowed range of T is (0.5, 1), where $T \sim 1$ corresponds to a highly directional event, and $T = 0.5$ corresponds to an isotropic event. Thrust distributions for typical signal events are uniform in the allowed range while continuum background events are peaked around $\sim 0.9 - 1.0$.

  In a typical background event for a two-body decay, the decay products of the B candidate each lie in one of the two jets and are therefore approximately back-to-back. Thus the decay axis of the B candidate is roughly collinear with the thrust axis for the rest of the event. For a true signal event, the B decay axis is uncorrelated with the thrust axis of the rest of the event, which in that case comes from the decay of the other B meson. For background discrimination, one can consider the cosine of the angle θ_{thr} between the thrust axis of the rest of the event and the B direction.

- **Sphericity** As with thrust, sphericity provides good separation of $q\overline{q}$ continuum events and signal due to the jet structure of $q\overline{q}$ events. Sphericity is a measure of the sum of the squares of transverse momenta for each track with respect to the event axis. It is defined over the interval (0,1), with highly directional events having low sphericity, and isotropic events corresponding to sphericity = 1.

  Sphericity is defined [41] as,

$$S = \frac{3}{2}(\lambda_2 + \lambda_3)\,, \tag{78}$$

  where λ_2 and λ_3 are the two larger eigenvalues of the sphericity tensor

$$S^{\alpha\beta} = \frac{\sum_i p_i^\alpha p_i^\beta}{\sum_i \mathbf{p}_i^2}\,, \tag{79}$$

  where $\alpha, \beta = 1{,}2{,}3$ corresponds to the x, y, z components respectively. The Sphericity Axis of the system is determined by the direction of the eigenvector corresponding to the largest eigenvalue. The sphericity axis of the rest of the event is used in an analogous way to the thrust axis of the rest of the event.

- **Fox-Wolfram Moments** The Fox-Wolfram moments, H_l, are defined [42] as,

$$H_l = \sum_{i,j} \frac{|\mathbf{p}_i|.|\mathbf{p}_j|}{E_{\text{vis}}^2} P_l(\cos\theta_{ij}) \tag{80}$$

  where P_l are the Legendre polynomials, $\mathbf{p}_{i,j}$ are the particle momenta, θ_{ij} is the opening angle between particles i and j, and E_{vis} is the total visible energy of the event.

  Neglecting particle masses, energy-momentum conservation requires that $H_0 = 1$. For 2-jet events, $H_1 = 0$ and $H_l \sim 1$ for l even, and $H_l \sim 0$ for l odd. For this application the ratio of Fox-Wolfram 2nd to 0th moments is used as the discriminating variable.

Fisher discriminant $\mathcal{F}$: it is a linear combination of shape functions or other kinematical functions which has optimized coeffiencients for signal-background separation. [6]

It can be expressed as:

$$\mathcal{F} = \sum_i c_i f_i \tag{81}$$

where the c_i are the optimal coefficients, trained on signal and background data and f_i are the discriminating functions. We have chosen $f_i = \cos\theta_{thr}, \cos\theta^{\star}_B, P_0, P_2$ where θ_{thr} is the angle of the thrust axis of the B with respect to the rest of the event, $\theta^{\star}_B$ is the angle of the B with respect to the nominal z direction of the beams, in the $\Upsilon(4S)$ rest frame, and P_0, P_2, are the Legendre polynomial functions of order zero and two respectively. Adding more variables the separation of signal and background did not improve sensitively. The $\cos\theta^{\star}_B$ variable for $B\overline{B}$ events follows the distribution of a polarized vector decaying into two pseudoscalars: $\frac{dN}{d\cos\theta^{\star}_B} \propto (sin\theta^{\star}_B)^2$. Differently for the continuum events it is distributed according to the $e^+e^- \rightarrow q\overline{q}$ process: $\frac{dN}{d\cos\theta^{\star}_B} \propto (1+\cos\theta^{\star}_B)^2$. The control sample selection and Fisher parametrization are discussed in section 3.4.5 and 3.5.4. The actual Fisher discriminant formula is:

$$\mathcal{F} = 0.595 + 0.1372\ \cos\theta^{\star}_B - 0.2983\ \mathrm{P}_2 + 0.1172\ \mathrm{P}_0 - 1.6151\ |\cos\theta_{thr}| \tag{82}$$

Shape variables are also useful for neutral tracks discrimination. Hadrons sometimes interact with the calorimeter by ionization and excitation alone, and sometimes they interact hadronically, initiating a hadronic shower. In the latter case, they can deposit a large fraction of their energy in the calorimeter, which can make them difficult to distinguish from electromagnetic deposits. The longitudinal and lateral energy distributions of hadronic showers differ significantly from those of electromagnetic showers, being characterized by the longer length scale of the nuclear interaction length, compared with the radiation length.

- **LAT** In order to describe the lateral energy distributions of showers, the following variables are defined: N, the number of crystals associated with the shower, E_i, the energy deposited in the i-th crystal, numbering them such that $E_1 > E_2 > \ldots > E_N$, and r_i, φ_i, the polar coordinates in the plane perpendicular to the line pointing from the interaction point to the shower center (see Fig. 25). Using these variables, one can define [43] the variable

$$LAT = \frac{\sum\limits_{i=3}^{N} E_i r_i^2}{\sum_{i=3}^{N} E_i r_i^2 + E_1 r_0^2 + E_2 r_0^2}, \tag{83}$$

  where r_0 is the average distance between two crystals, which is approximately 5 cm for the *BABAR* calorimeter. This variable is constructed to discriminate between electromagnetic and hadronic showers based on their average properties. The summation in

[6] Let us assume that the Fisher discriminant $\mathcal{F} = \sum_i c_i f_i$, has a distribution with a standard deviation σ_{bkg} and mean value μ_{bkg} for the background events and σ_{Sig}, μ_{Sig} for signal events respectively. We call $D = \frac{(\mu_{\mathsf{bkg}} - \mu_{\mathsf{Sig}})^2}{\sigma^2_{\mathsf{bkg}} + \sigma^2_{\mathsf{Sig}}}$ the distance of the two distributions. We determine the optimal coefficients c_i of the Fisher by maximizing the distance D.

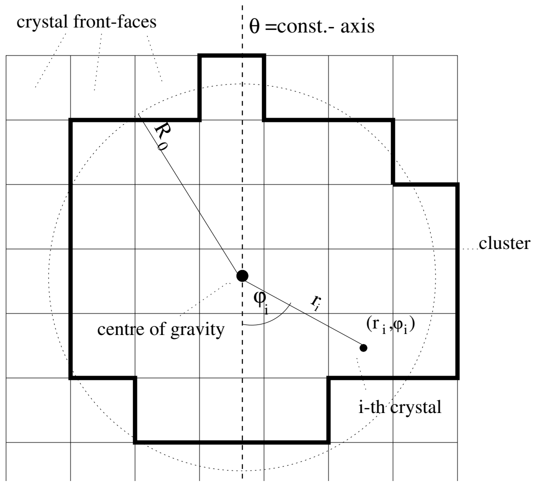

Figure 25: Definition of the variables r_i, φ_i and R_0

the numerator omits the two crystals containing the highest amounts of energy. Electrons deposit most of their energy in two or three crystals, so that the value of LAT is small for electromagnetic showers. Multiplying the energies by the squared distances enhances the effect for hadronic showers, compared with electronic.

3.3 Pion-Kaon separation

In order to reduce the background coming from misidentified charged pions, we apply particle identification (PID) requirements of the *BABAR* standard `SMS selector`, a particle identification algorithm which uses a likelihood function based on dE/dx information in the SVT and DCH and the measurement of the Čerenkov angle in the DIRC. Here, the kaon vs. pion version (`SMS kaon selector`) is used. The p.d.f. associated to SVT and DCH is a Gaussian, whose mean value comes from the dE/dx calibration. The σ of the distribution, which is momentum dependent, is obtained by the calibration of both the subdetectors. In the case of DIRC, we use a combination of a Poisson factor (describing fluctuations in the number of Čerenkov γ's produced in the DIRC) and a Gaussian distribution.

The Gaussian part of the DIRC likelihood l_i ($l \in$ electron, muon, pion, kaon or proton) is parameterized fitting the following parameters:

- the expected value of Čerenkov angle, given by the relation $\cos\theta_C = 1/\beta n$, where β is the Lorentz factor $\beta = p/E$ and n is the refraction index of the material crossed by the particle ($n = 1.473$ for DIRC silica bars in *BABAR*)
- measured Čerenkov angle
- the σ parameter of the Gaussian, as a function of incoming track momentum, obtained from a control sample of $D^{*+} \to D^0(K^+\pi^+)\pi^+$. The obtained K/π separation is shown in Fig. 26.

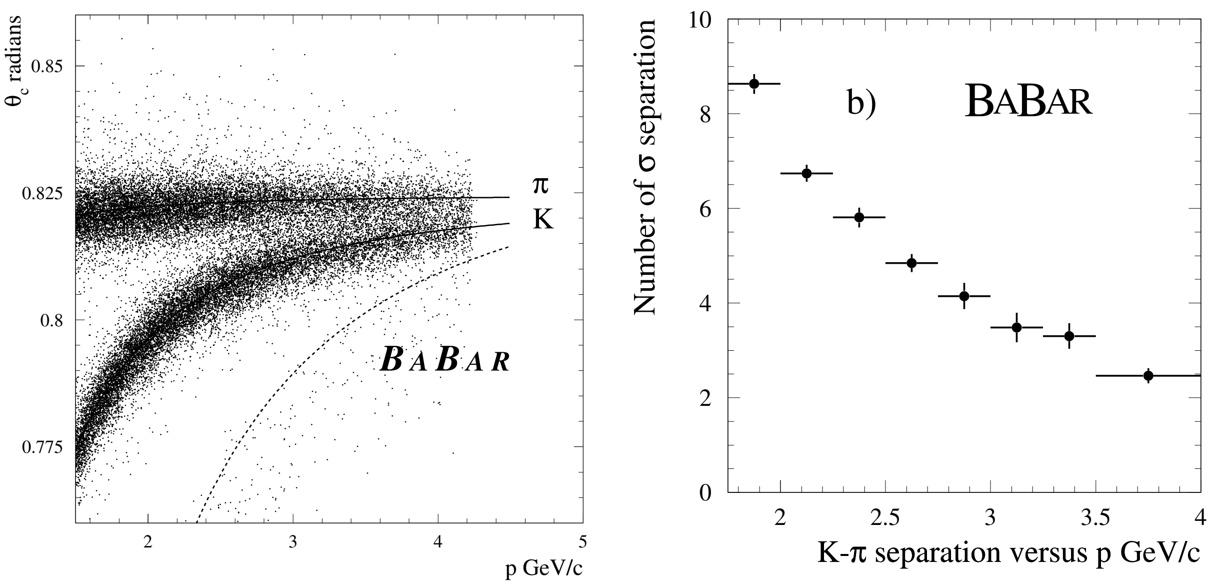

Figure 26: The Čerenkov angle (left) and K–π separation (right) as functions of momentum for tracks in the D^0 control sample.

Labeling as t the heaviest particle above the Čerenkov threshold, all the particles heavier than t are associated to a constant probability of 0.2 (being five the considered mass hypotheses). The Poisson factor is calculated using

- N_S, the fitted number of signal photons
- N_B, the fitted number of background photons (at least three)
- expected number of photons (N_{exp}).

N_{exp} is taken from default lookup tables, as a function of mass hypothesis, charge, momentum and polar angle of the track.

Depending on the momentum of the track, all the informations or some of them are combined in a global likelihood and the ratio of the two considered hypotheses h_1 and h_2 is compared to a given threshold ($l_{h_1}/l_{h_2} > r_{h_2}$) in order to decide if the tracks is in agreement with the h_1 hypothesis more than to the h_2 one.

In particular, we consider the application of this selector, called `SMS selector`, to the case of kaon vs. pion discrimination. The `SMS kaon selector` provides five different selection criteria, based on the different likelihood threshold after the rejection of a triangular region in the (θ_C,p) plane, as shown in Fig. 27. The goodness of the selection criteria is fixed by the fraction of tracks identified as kaons, out of a pure kaon sample, and the pion misidentification, i.e. the fraction of tracks identified as kaons, out of a pure pion sample. The different criteria are defined as:

- `NotAPion`, requiring

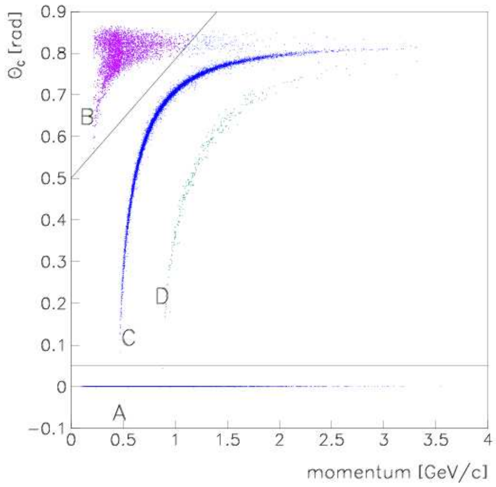

Figure 27: Distribution of a sample of pure kaons in the (θ_C,momentum) plane. Kaons appear also in signal regions of other particle hypotheses. The triangular region used for the definition of `SMS kaon selector` criteria is shown.

  - momentum $p < 0.5$ GeV/c (< 0.6 GeV/c) for SVT (DCH) and > 0.6 GeV/c for DIRC.
  - $r_\pi l_\pi > l_K$ and $r_\pi l_\pi > l_p$, being $r_\pi = 0.1$ (1.0) for $p \leq 0.5$ GeV/c and $r_p = 1$. ($p > 0.5$ GeV/c).

- `VeryLoose`, same than `NotAPion`, but using the product of the likelihoods over the whole momentum range
- `Loose`, requiring
  - momentum $p < 0.7$ GeV/c (> 0.6 GeV/c) for SVT and DCH (for DIRC).
  - $r_\pi l_\pi > l_K$ if no DIRC informations are available
  - $r_\pi l_\pi > l_K$ and $r_p l_p > l_K$, being $r_p = 1$
  - $r_\pi = 15$, $r_\pi = 1$, and $r_\pi = 80$ for 0.5 GeV/c$< p <$ 0.7 GeV/c, 0.7 GeV/c$< p <$ 2.7 GeV/c and $p > 2.7$ GeV/c respectively.
- `Tight`, requiring
  - momentum $p < 0.7$ GeV/c (> 0.6 GeV/c) for SVT and DCH (for DIRC).
  - $r_\pi l_\pi > l_K$ and $r_p l_p > l_K$, being $r_p = 1$
  - $r_\pi = 15$, $r_\pi = 1$, and $r_\pi = 80$ for 0.5 GeV/c$< p <$ 0.7 GeV/c, 0.7 GeV/c$< p <$ 2.7 GeV/c and $p > 2.7$ GeV/c respectively.
- `VeryTight`, requiring
  - momentum $p < 0.6$ GeV/c (> 0.6 GeV/c) for SVT and DCH (for DIRC).

– $r_\pi l_\pi > l_K$ if no DIRC informations are available
– $r_\pi l_\pi > l_K$ and $r_p l_p > l_K$, being $r_p = 1$
– $r_\pi = 20$, $r_\pi = 3$, and $r_\pi = 200$ for 0.4 GeV/c$< p <$ 0.7 GeV/c, 0.7 GeV/c$< p <$ 2.5 GeV/c and $p >$ 2.5 GeV/c respectively.

3.4 $B^- \to D^0 K^-$ decay mode

We have analyzed a skimmed collection of the events in order to reduce the large amount of data and minimize the CPU time for the processing. The rejection is mainly for background continuum events as we have required $|\cos\theta_{thr}| \leq 0.8$ along with $m_{\mathrm{ES}} \geq 5.2\,\mathrm{MeV}/c^2$ and $|\Delta E| \leq 200\,\mathrm{MeV}$. The size of data reduces to 1% of the total while the signal efficiency is still greater than 80%. Here we are going to discuss the selection criteria we have applied in this analysis for the selection of the signal events.

3.4.1 Selection criteria

B^- candidates are formed by combining a mass constrained D^0 candidate with a charged bachelor track [7] identified as a Kaon, according to the `SMS kaon selector` with `Tight` criteria applied. To guarantee the quality of the B decay vertex the χ^2 probability is required to be greater than 0. Same conditions is required for the D^0 decay vertex. The particle identification for the bachelor track, reduces the contamination from the higher statistics decay $B^\pm \to D^0\pi^\pm$ and it helps also reducing other sources of background coming from generic $B\overline{B}$ decays. The D^0 candidates are reconstructed in the $D^0 \to K^0_S\pi^+\pi^-$ final state and K^0_S candidates are selected from pairs of opposite charge tracks, with invariant mass within $9\,\mathrm{MeV}/c^2$ from the nominal K^0_S mass [44], $|m_{K^0_S} - m_{PDG}| \leq 9\,\mathrm{MeV}/c^2$. The tracks from the neutral kaon are requested to originate from the same point, moreover in order to suppress the $D^0 \to 4\pi$ background we request the cosine of the angle between the line direction of the K^0_S and its momentum to satisfy the condition $\cos\alpha_{K^0_S} \geq 0.99$. The overall efficiency on the signal events is equal to 18.0 ± 0.1 %.

The selection criteria have been choosen in order to maximize the significativity of the signal [8] favouring high selection efficiency, where the value of the significativity was constant within the error. The final refinements of the criteria, specially on the value of ΔE region, has been determined on pseudo Monte Carlo experiments according to the configuration with the best sensitivity on γ. The optimal set of cuts was found to be:

- $|\cos\theta_{thr}| <\ 0.8$
- `SMS kaon selector:  Tight` on bachelor track
- $|M(D^0) - M(PDG)| <\ 12\ \mathrm{MeV}/c^2$
- $|M(K^0_S) - M(PDG)| <\ 9\ \mathrm{MeV}/c^2$

[7]The bachelor track is the charged track from the primary B decay-vertex
[8]Significativity: $Signif = S/\sqrt{S+B}$ where S, B is the number of signal, background events respectively

- $P(\chi^2, D^0) > \ 0.0$ [9]
- $P(\chi^2, B) > \ 0.0$ [10]
- $\cos\alpha_{K^0_S} > \ 0.99$
- $|\Delta E| < \ 30$ MeV

The number of events with multiple B candidates is very small: about 1% for the final sample of events with $m_{\rm ES} \in [5.2, 5.3]$ MeV/c^2 and $\Delta E \in [-30, +30]$ MeV. A single candidate is retained per event : the one with the D^0 mass closest to the PDG value. Figure 28 shows the $\rm m_{ES}$ distribution after applying the final selection criteria. The agreement between the data and Monte Carlo is satisfactory. Figure 28 shows also the various background components. From Monte Carlo studies we see that the $B\overline{B}$ component is not dominated by a single decay mode. It is clear that the main background comes from the continuum events. This background can be reduced by the use of the standard Fisher variable technique (we will discuss in sections 3.4.5 and 3.5.4).

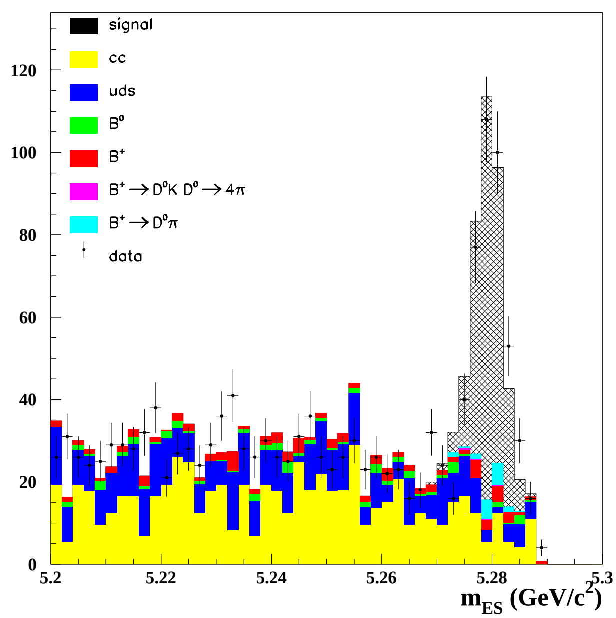

Figure 28: $m_{\rm ES}$*distribution obtained after applying the final selection criteria. The Monte Carlo samples are all shown together with the data represented by point with error bars.*

3.4.2 Data/Monte Carlo comparisons

Data/Monte Carlo comparison plots for the relevant variables for the analysis has been evaluated. For all the cases the colored histograms display the various Monte Carlo components and the points represent the data.

[9] The probability of the χ^2 is defined positive but very few bad vertexes have $P(\chi^2, D^0)$ equal to zero due to the numerical rounding approximation.

[10] Similar behaviour to $P(\chi^2, D^0)$.

Comparisons for some selection variables are shown in Figure 29 for $\cos\alpha_{K_S^0}$, K_S^0 invariant mass, and for the D^0 invariant mass. The mass distributions are plotted with respect to the PDG mass. The data distributions are slightly shifted compared to the Monte Carlo ones, the cuts are far enough so that the efficiency obtained on Monte Carlo will still be correct. These plots have been obtained after all the cuts but the one on the displayed variable.

The distributions for $|\cos\theta_{thr}|$ and for the Fisher variables are reported in Figure 30, after all the cuts and for all the events entering in the Likelihood (5.2 GeV/c^2 < $m_{\rm ES}$< 5.3 GeV/c^2).

Finally one can compare the distribution for ΔE in the $m_{\rm ES}$ signal region ($m_{\rm ES}$> 5.272 GeV/c^2). This is shown on Figure 31.
Similar data-Monte Carlo agreement is reproduced for the $B^- \to D^{*0}K^-$ events, which we are going to discuss in section 3.5.

3.4.3 Signal yields

It is worth saying that the yields and the parameters used in the fit for the *CP* violating parameters are extracted from a likelihood fit we are going to discuss in detail in section 5. In this section we describe the sample composition and the background characterization. The yields and the values of the parameters presented in this paragraph are obtained from simple one dimensional fit, and they will be revaluated with a more refined fit as explained in section 5.

To model the $\rm m_{ES}$ distribution, an empirical background function [11] [63] plus a Gaussian for the signal has been used. The fit yields to the following number of signal (Sig) events in data and Monte Carlo :

$$N_{\sf Sig,data}(D^0K) = 306.3 \pm 22.3 \quad S/\sqrt{S+B} = 14.0 \quad f_{\sf Sig,data}(D^0K) = 0.67 \pm 0.05 \quad (85)$$
$$N_{\sf Sig,mc}(D^0K) = 300.6 \pm 22.9 \quad S/\sqrt{S+B} = 13.9 \quad f_{\sf Sig,mc}(D^0K) = 0.64 \pm 0.05 \quad (86)$$

where $f_{\sf Sig} = \frac{N_{DK}+N_{D\pi}+N_{D0\to 4\pi}}{N_{\rm cand}}$ in the $m_{\rm ES}$ signal region (>5.272 GeV/c^2).

It is important to notice that the contribution from the "peaking background" is very small and is essentially due to the $D^0\pi^-$ events. By a simple counting of Monte Carlo events, the fraction of this background amount to $f_{{\sf Sig},mc}(D^0K) = 0.035 \pm 0.012$
This fraction could be also obtained from data by fitting the ΔE distribution. Figure 31 shows the ΔE distribution with the final selection criteria and considering the events in the range $m_{\rm ES} > 5.272\,{\rm GeV}/c^2$. The different components are also shown.
For this purpose we have considered the ΔE distribution in the range [-0.120,0.120] GeV [12]. The events from DK (Sig) and $D\pi$ (Dh) have been parametrized with a Gaussian distribution. For the DK events the Gaussian is centered on zero and its width is $\sigma_{\sf Sig,mc}(D^0K) = (14.6 \pm 0.2)$ MeV.

[11] The empirical function has been named ARGUS function:

$$Argus(m) = m\sqrt{1-(\frac{m}{m_0})^2} \quad e^{c[1-(\frac{m}{m_0})^2]} \tag{84}$$

where m is $m_{\rm ES}$, m_0 is the $m_{\rm ES}$ kinematic limit fixed to $5.290\,{\rm GeV}/c^2$ and c is the slope parameter.

[12] Only the region between [-0.100,0.120] has been considered in the fit to exclude the contribution from the D^*K events

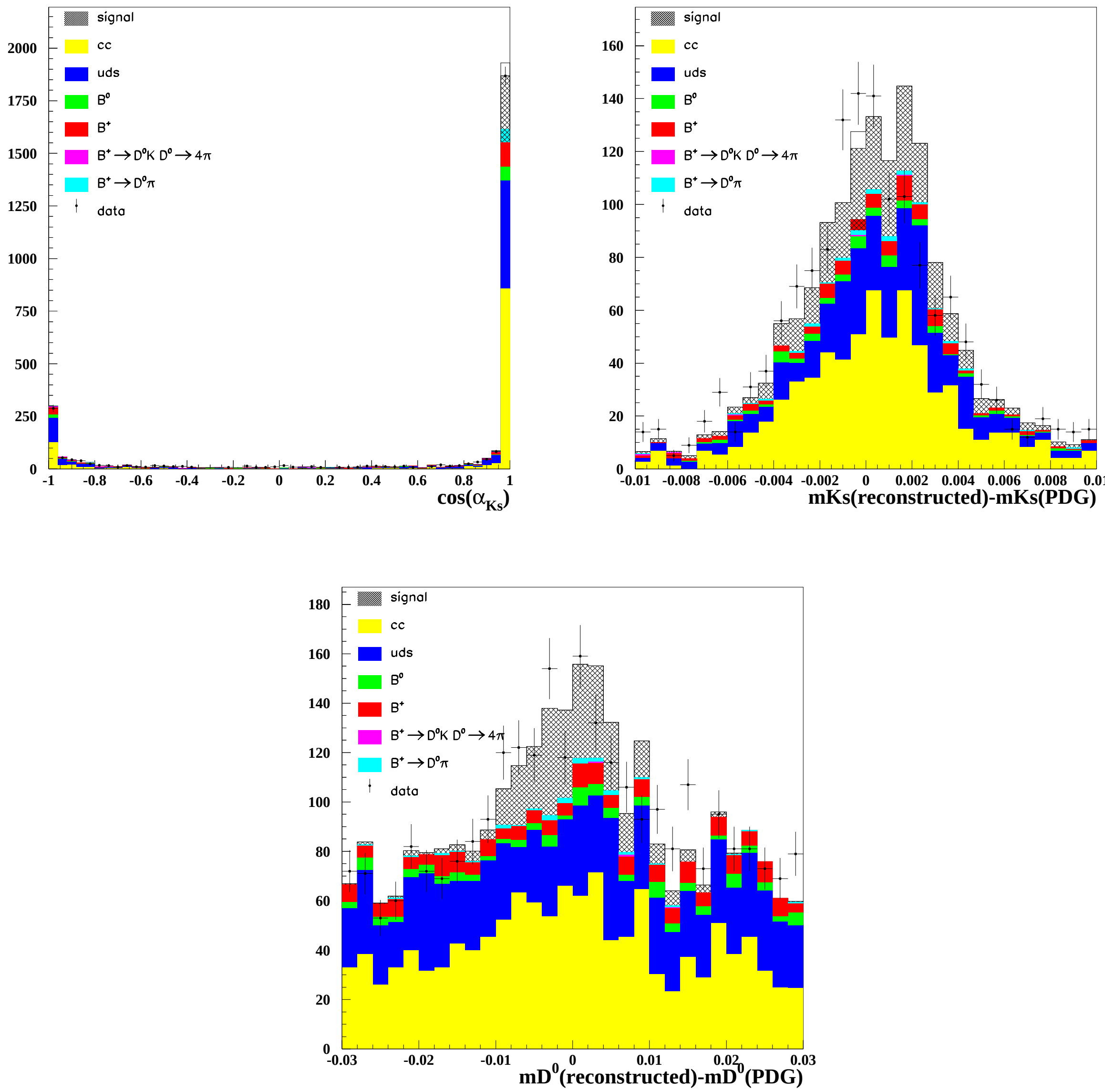

Figure 29: *Data/Monte Carlo comparisons for the* $\cos\alpha_{K^0_S}$, *the* K^0_S *invariant mass (relative to the PDG value) and for the* D^0 *invariant mass variables. The distributions are obtained after all the cuts but the one on the displayed variable.*

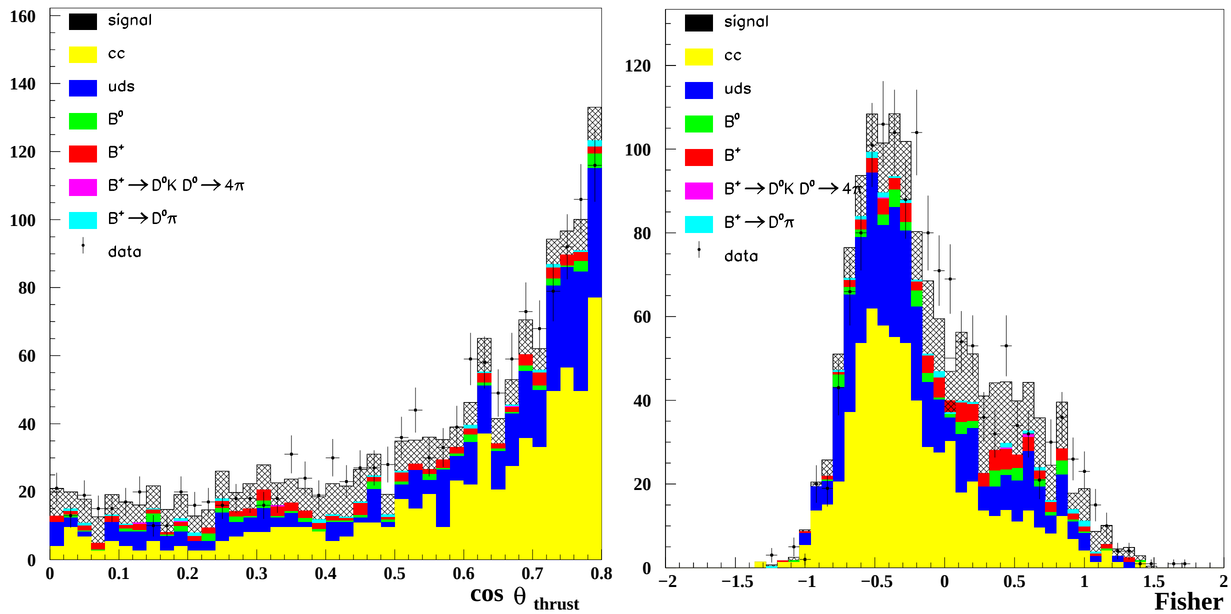

Figure 30: *Data/Monte Carlo comparisons for the* $|\cos\theta_{thr}|$ *and the Fisher variables. The distributions are obtained after all the cuts but the one on the displayed variable.*

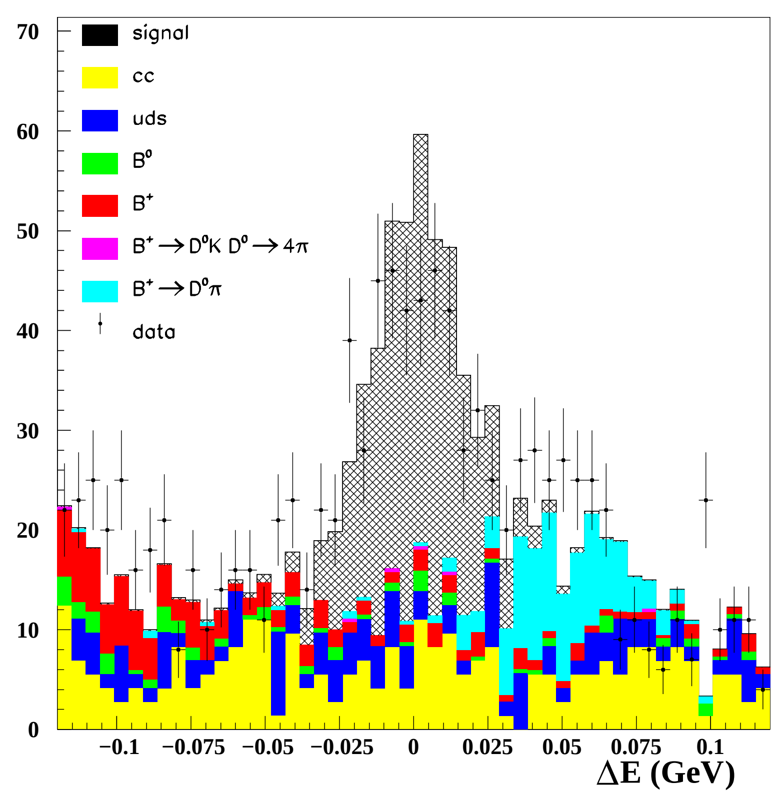

Figure 31: *Data Monte/Carlo comparison for the* ΔE *variable. The distributions are obtained after all the cuts but the one on the displayed variable.*

The Gaussian distribution for the $D\pi$ events is centered on $\mu_{\mathsf{Dh,mc}}(D^0K) = (50.2 \pm 1.2)$ MeV with width $\sigma_{\mathsf{Dh,mc}}(D^0K) = (18.7 \pm 1.0)$ MeV. The parameters from the two Gaussian distributions are related. In fact the Gaussian describing the ΔE distribution of the $D\pi$ events is shifted by about 50 MeV and its resolution is the result of the convolution of the bachelor track momentum resolution and the ΔE resolution of the DK events :

$$
\begin{aligned}
N &= N_{\mathsf{Sig}} e^{-\frac{(\Delta E-\mu)^2}{2\,\sigma^2_{\mathsf{Sig}}}} + N_{\mathsf{Dh}} e^{-\frac{(\Delta E-(\mu+0.05))^2}{2\,\sigma^2_{\mathsf{Dh}}}} + P1 \\
& \sigma^2_{\mathsf{Dh}} = \sigma^2_{\mathsf{Sig}} + K^2 \\
& K = \sqrt{\sigma^2_{\mathsf{Dh,mc}} - \sigma^2_{\mathsf{Sig,mc}}} = 0.010
\end{aligned}
\tag{87}
$$

The global fit on the data and Monte Carlo have been performed using eq. 87 where $P1$ is a linear polynomial function and the width of the Gaussian distribution σ_{Sig} has been obtained from the $D\pi$ control sample. The results of the fits are shown in Figure 32 and in the range $\Delta E \in$ [-0.030,0.030] GeV we obtain :

$$
\begin{aligned}
f_{\mathsf{Dh,data}}(D^0K) = 0.044 \pm 0.009 \quad N_{\mathsf{Sig,data}}(D^0K) = 323.0 \pm 23.0 \\
f_{\mathsf{Dh,mc}}(D^0K) = 0.059 \pm 0.012 \quad N_{\mathsf{Sig,mc}}(D^0K) = 288.2 \pm 21.0
\end{aligned}
$$

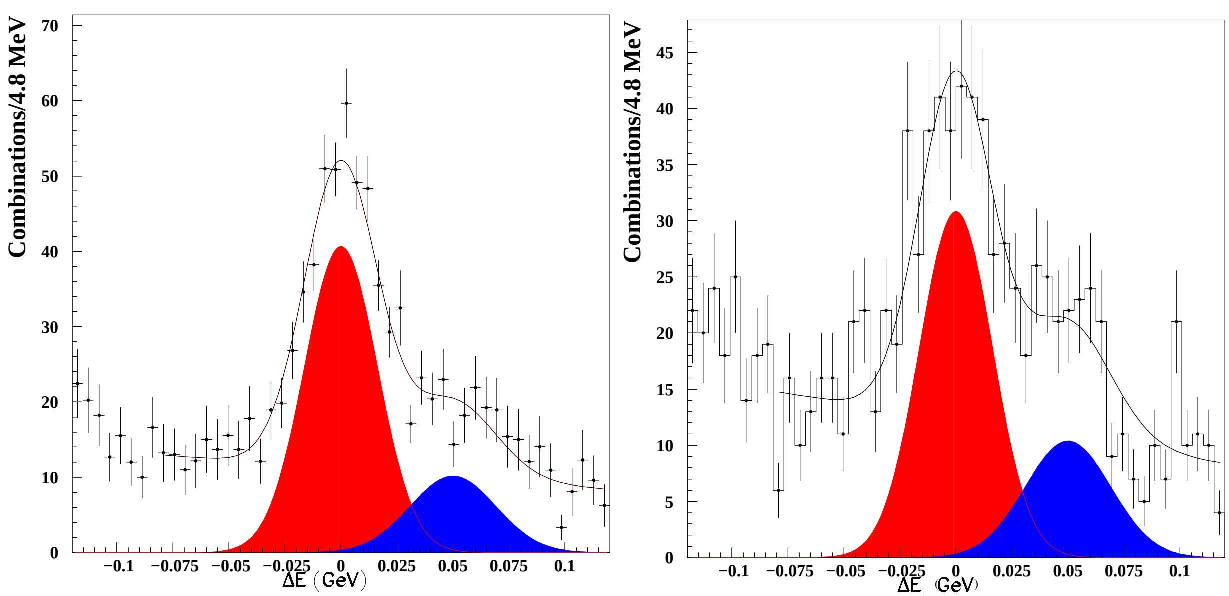

Figure 32: *The plots on left (right) show the ΔE distribution as obtained on the Monte Carlo (data) with the fit superimposed. The two Gaussian distributions for the DK and the $D\pi$ events are also shown.*

The contribution of another possible source of peaking background, $D^0 \to 4\pi$ was found to be <1% after the cut on $\cos\alpha_{K^0_S}$.

3.4.4 Background characterization

So far we have shown so far that the only significant background which give a peak on $\mathrm{m_{ES}}$ distribution is coming from the $\mathrm{D}\pi$ events. These events contains only genuine D^0. Their fraction is fitted on the data, (see above) $f_{\mathsf{Dh,data}}(D^0K) = (5.9 \pm 1.2)\%$.
In the following we consider the background events which are the combinatorics on the m_{ES} distribution and, as shown before, amounts to $1 - f_{\mathsf{Sig,data}}(D^0K) = 0.781 \pm 0.016$ over the full m_{ES} region.
For properly considering the Dalitz distributions of the background the two most important ingredients are : the presence or not of a genuine D^0 and the charge correlation with the bachelor kaon. In fact, events with a true D^0 combined with a randomly flavor-tagged kaon could be a potentially important background because for half of the cases the kaons is of opposite sign and these events can be taken as $B^+ \to \bar{D}^0K^+$.
For this reason we decide to consider separately the background from the continuum and the background from the $B\overline{B}$ events and to split each of this category, whenever the D^0 is true or not.
The relative fraction, normalized to the total not -peaking background, of the continuum events (Cont) is obtained by fitting the $\mathrm{m_{ES}}$ distribution from the Monte Carlo and it amounts to : $f_{\mathsf{Cont,mc}}(D^0K) = 0.854 \pm 0.040$.
We now consider the fraction of genuine D^0 in the background combinatorial sample. Due to the ΔE cut we do expect a little contamination from genuine D^0 events from D^* decays. In the simulation events we found that the fraction of this events is $< 2\%$ and its contribution has been neglected in the following. A sizeable contribution has been found in the continuum events, totally coming from the $c\bar{c}$ events ; by simply counting the events on the Monte Carlo we obtain :

$$R_{\mathsf{Cont,mc}}(D^0K) = 0.300 \pm 0.027 \tag{88}$$

The total fraction of the genuine D^0 in the combinatorial background can be obtained on the data and compared with the one from the Monte Carlo. For this purpose we have considered the event satisfying $m_{\mathrm{ES}} < 5.272\,\mathrm{GeV}/c^2$ and having removed the cut on the D^0 mass. Figure 33 shows the D^0 invariant mass for data and Monte Carlo events. For simulated events the plot has been obtained using the corrected relative integrated luminosities processed for the uds, $c\bar{c}$ and the $B\overline{B}$ events. The fit to the D^0 invariant mass has been performed by fixing the mean and the width of the D^0 to 1864 MeV/c^2 and 7 MeV/c^2 as found on the $c\bar{c}$ simulation. The fraction of the genuine D^0 is found to be :

$$\begin{aligned} R_{\mathsf{all,data}}(D^0K) &= 0.20 \pm 0.04 && (89)\\ R_{\mathsf{all,mc}}(D^0K) &= 0.25 \pm 0.05 && (90) \end{aligned}$$

According to the statistical error the agreement between data and Monte Carlo is reasonable.
Considering that the only genuine D^0 come from the $c\bar{c}$, the following values are obtained :

$$\begin{aligned} R_{\mathsf{Cont,data}}(D^0K) &= 0.221 \pm 0.042 && (91)\\ R_{\mathsf{Cont,mc}}(D^0K) &= 0.27 \pm 0.06 && (92) \end{aligned}$$

Another important ingredient is the fraction of events with a genuine D^0 associated with a negative charged track h^-:

$$R^{RS}_{\mathsf{Cont,mc}}(D^0K) \equiv \frac{N(D^0h^-)}{N(D^0h^+) + N(D^0h^-)} = 0.208 \pm 0.033 \quad (93)$$

This fraction is obtained from Monte Carlo simulatation because there are not enough off-peak data to determine such a value. In case of a genuine D^0 the Dalitz distribution can be taken from the one of the D^0 or a $\bar{D}^0$ depending of the charge correlation with the Kaon and according to this fraction.
The summary of the values and errors obtained for the different parameters is given in Table 4 for the channel $D^0 \to K^0_S\pi^+\pi^-$.

Parameter	Value from Data	Value from Monte Carlo
$f_{\mathsf{Sig}}(D^0K)$ ($m_{\mathrm{ES}} > 5.272\,\mathrm{GeV}/c^2$)	0.672 ± 0.049	0.643 ± 0.049
$f_{\mathsf{Sig}}(D^0K)$ ($m_{\mathrm{ES}} > 5.2\,\mathrm{GeV}/c^2$)	0.219 ± 0.016	0.221 ± 0.023
$f_{\mathsf{Dh}}(D^0K)$	0.059 ± 0.012	0.028 ± 0.012
$f_{\mathsf{Cont}}(D^0K)$ ($m_{\mathrm{ES}} > 5.272\,\mathrm{GeV}/c^2$)	-	0.854 ± 0.040
$f_{\mathsf{Cont}}(D^0K)$ ($m_{\mathrm{ES}} > 5.2\,\mathrm{GeV}/c^2$)	-	0.905 ± 0.012
$R_{\mathsf{Cont}}(D^0K)$	0.221 ± 0.042	0.27 ± 0.06
$R^{RS}_{\mathsf{Cont}}(D^0K)$	-	0.208 ± 0.033

Table 4: *Values for parameters used in the likelihood. Whenever possible the values obtained from Data are used.*

3.4.5 The $B^- \to D^0\pi^-$ control sample

A very similar analysis can be performed to select on the data the more copious $B^- \to D^0\pi^-$ final states. All the selection criteria are identical to those applied for the $B^- \to D^0K^-$ analysis except that the events are selected in ΔE region in the range [+20.0,+80.0] MeV/c^2 (see Figure 32). In order to have completely independent samples the bachelor pion is required not to be identified as a `SMS Tight` kaon.
The $\mathrm{m_{ES}}$ distribution for the different components and for the data are shown in Figures 34. The efficiency obtained on $B^- \to D^0\pi^-$ signal Monte Carlo is estimated to be $\epsilon = 12.5 \pm 0.1\%$. The fit yields to the following number of events in data and Monte Carlo :

$$N_{\mathsf{Dh,data}}(D^0K) = 3644 \pm 65 \quad S/\sqrt{S+B} = 57.1 \quad f_{\mathsf{Dh,data}}(D^0K) = 0.895 \pm 0.016 \quad (94)$$
$$N_{\mathsf{Dh,mc}}(D^0K) = 3658 \pm 61 \quad S/\sqrt{S+B} = 42.9 \quad f_{\mathsf{Dh,mc}}(D^0K) = 0.901 \pm 0.021 \quad (95)$$

The overall background fraction is smaller than in the $B^- \to D^0K^-$ sample. Nevertheless the $B\overline{B}$ background shows more important and complicated peaking structure coming from many different components (*e.g.* charmless events, $\ell^+\ell^-$ K^0_S π events) with respect to DK case. It has to be noted that in the signal region ($\mathrm{m_{ES}}$>5.272) the $B\overline{B}$ events amounts to about (95%) of the total number of the events. Thus, this sample can be used to obtained

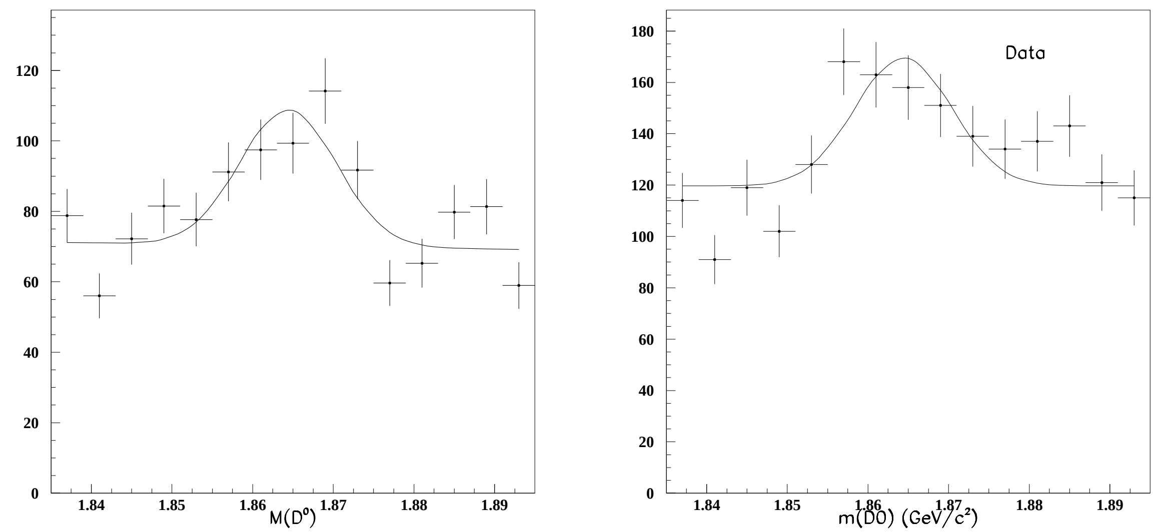

Figure 33: *The plots on left (right) show the D^0 invariant mass distribution as obtained on the Monte Carlo (data) for events satisfying $m_{\rm ES} < 5.272\,{\rm GeV}/c^2$ and removing the cut on the D^0 mass. The result of the fit is superimposed.*

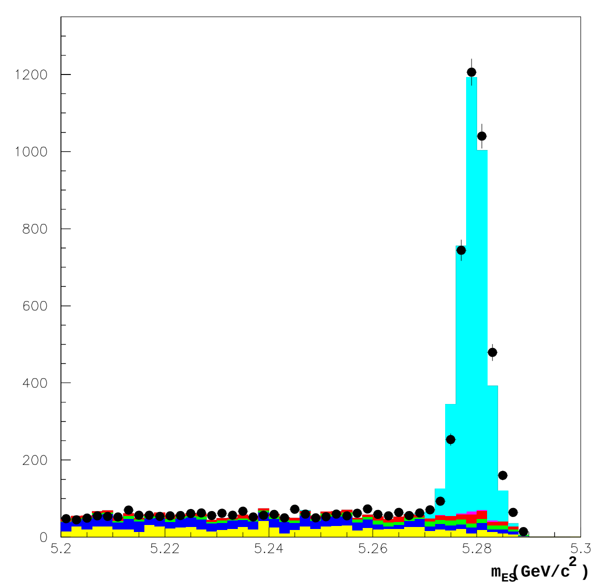

Figure 34: *$D\pi$ control sample. The $m_{\rm ES}$ distribution obtained applying the final selection criteria. The Monte Carlo samples are all shown together with the data represented by point with error bars.*

some important parameter for the analysis.
The Fisher discriminant variable has been obtained directly on data using the $D\pi$ events. The off-peak data and the events selected in the signal region for m_{ES} distribution have been used for getting the Fisher variable for the continuum and the $B\overline{B}$ events respectively. For

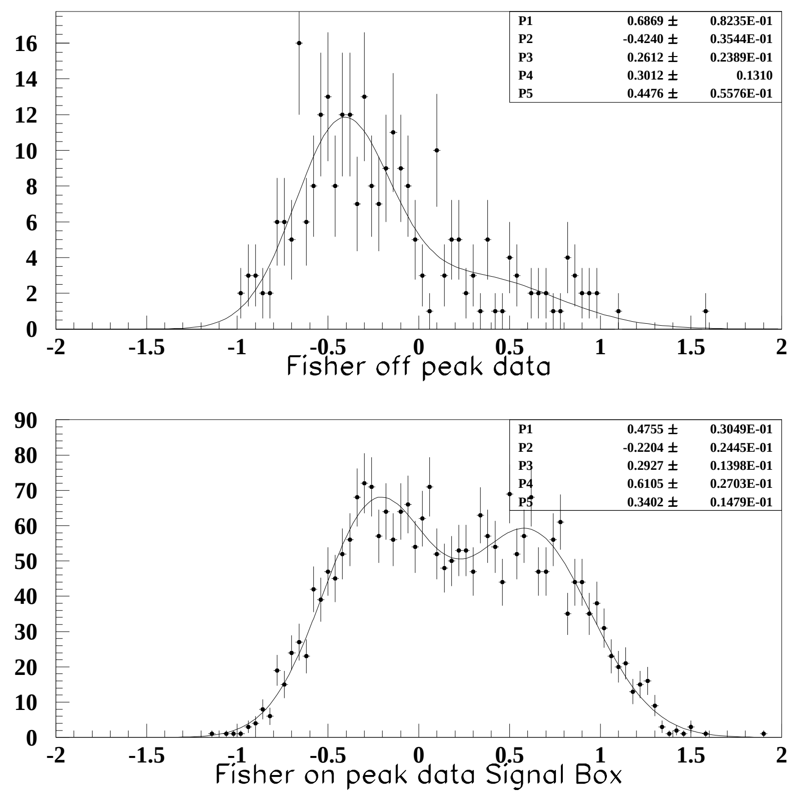

Figure 35: *Fisher discriminant variable obtained from the off-peak data for continuum events (top distribution) and from the $D\pi$ control sample for $B\overline{B}$ events (bottom distribution)*

the continuum the distribution of the Fisher variable $\mathcal{F}$ was fitted with a double Gaussian distribution :

$$f \times e^{-\frac{(\mathcal{F}-\mu_1)^2}{2\sigma_1^2}} + (1-f) \times e^{-\frac{(\mathcal{F}-\mu_2)^2}{2\sigma_2^2}}$$

The parameters are given in Table 5. The on peak data in the signal box contains 94% of $B\overline{B}$ events. The distribution have been fitted using a double Gaussian for the $B\overline{B}$ events and for the residual 6% of background events fixing the parameters of a double Gaussian distribution as obtained from the fit on the continuum events. The double peak structure is due to the very important weight of the $|cos\theta_{thr}|$ variable in the Fisher variable.

	f	μ_1	σ_1	μ_2	σ_2
continuum	0.687 ± 0.082	-0.424 ± 0.035	0.261 ± 0.024	0.301 ± 0.131	0.448 ± 0.056
$B\overline{B}$	0.476 ± 0.030	-0.220 ± 0.024	0.293 ± 0.014	0.610 ± 0.027	0.340 ± 0.015

Table 5: *Fitted parameters of the double Gaussian distributions for the $B\overline{B}$ and continuum components obtained using the $D\pi$ event sample.*

3.5 $B^- \to D^{*0}K^-$ decay mode

3.5.1 Selection criteria

The B^- candidate is formed combining a mass constrained D^{*0} candidate with a charged track identified as a Kaon with `Tight` criteria applied. The D^{*0} is reconstructed in the two channels $D^{*0} \to D^0\pi^0$ and $D^{*0} \to D^0\gamma$. The γ candidates for $D^{*0} \to D^0\gamma$ are requested to have a minimum raw energy of 100 MeV and a maximum lateral moment (LAT) of 0.8; the π^0 candidates from $D^{*0} \to D^0\pi^0$ are selected as pairs of photons with a minimum raw energy of 30 MeV, with an invariant mass within the range $[115, 150]$ MeV/c^2. The number of *merged* π^0s, made of a single cluster in the EMC, is negligible in the momentum range of interest. To improve the momentum resolution, the π^0 candidates are kinematically fit with their mass constrained to the nominal π^0 mass. Before combining a D^0 candidate with a soft π^0 or a photon to form a D^{*0}, a mass-constrained fit is applied to the D^0. The D^0 and the K^0_S selection criteria are the same as in the $B^- \to D^0K^-$ selection. The resolution of the $D^{*0} - D^0$ mass difference (Δm) is ~ 1.2 MeV/c^2 for $D^{*0} \to D^0\pi^0$ and $\sim 5.0\,\mathrm{MeV}/c^2$ for $D^{*0} \to D^0\gamma$. Figures 36 show the Δm distributions for D^{*0} from Monte Carlo signal events. The resolutions, measured on Monte Carlo signal events, are $2.6\,\mathrm{MeV}/c^2$

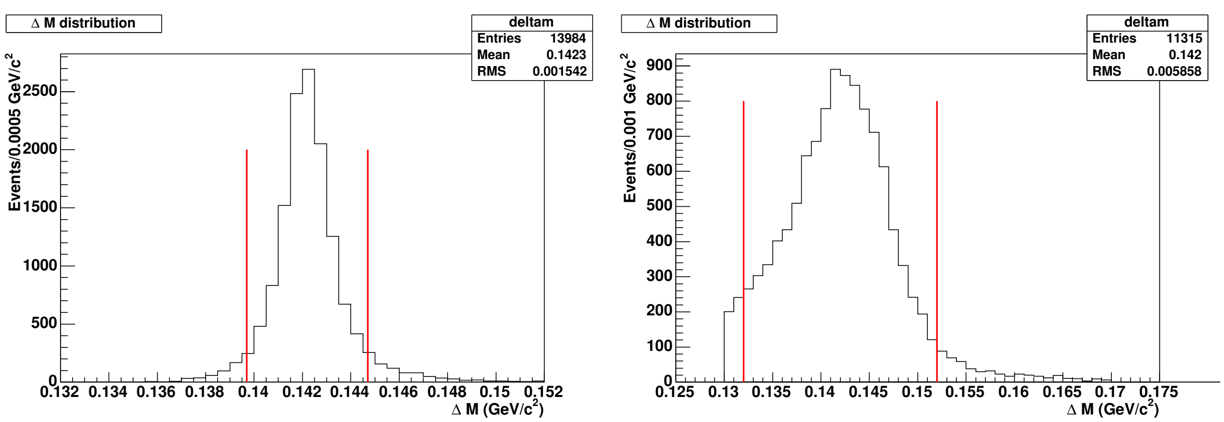

Figure 36: *The Δm mass difference distribution for signal Monte Carlo events. The two lines show the region we have considered as signal events in our event selection. (Left plot) Δm distribution for $D^0\pi^0$ signal events. The RMS is around $1.5\,\mathrm{MeV}/c^2$. (Right plot) Δm distribution for$D^0\gamma$ signal events. The RMS is around $5.8\,\mathrm{MeV}/c^2$.*

and 16.7 MeV for m_{ES} and ΔE, respectively. The cut $|\cos\theta_{thr}| < 0.8$ is required to suppress the background from continuum production of light quarks. If multiple B candidates are found in the same event after all the selection criteria are applied, we choose the one with the smallest $\chi^2 = \chi^2(\Delta m, m_{\pi^0})$ [13] for $D^0\pi^0$ and $\chi^2 = \chi^2(\Delta m)$ for $D^0\gamma$. This happens in 9% of the times for the $D^0\pi^0$ and in 3% of the times for the $D^0\gamma$. After the best choice selection the contamination of background events coming from true $D^0\gamma$ signal events into the $D^0\pi^0$ signal sample and viceversa is completely negligible. The best choice algorithm has an efficiency on Monte Carlo signal events of $75 \pm 3.0\%$ ($63 \pm 7\%$) for $D^0\pi^0$ ($D^0\gamma$). The correlation among the variables used in the χ^2 calculation and the fitted parameters, $m^2(K^0_S\pi^+)$ and $m^2(K^0_S\pi^-)$, has been evaluated on signal Monte Carlo and it is negligible. The final selection criteria, optimized as in the $B^- \to D^0K^-$ according to the best sensitivity on the γ value, are:

- $|\cos\theta_{thr}| < 0.8$
- `SMS kaon selector: Tight` on bachelor track
- $|M(D^0) - M(PDG)| <$ 12 MeV/c^2
- $|M(K^0_S) - M(PDG)| <$ 9 MeV/c^2
- $|\Delta m - \Delta m(PDG)| < 2.5$ MeV/c^2 in the $D^0\pi^0$ and $<$ 10 MeV/c^2 in the $D^0\gamma$
- $\cos\alpha_{K^0_S} >$ 0.99
- $|\Delta E| <$ 30 MeV

The overall efficiency is 4.3% for the $D^0\pi^0$ and 8.1% for the $D^0\gamma$ decay mode.

3.5.2 Signal yields

The background composition is studied with a Monte Carlo simulation. The background can be divided in two main categories: continuum background and $B\overline{B}$ background, beeing the continuum the dominant one. The $B\overline{B}$ background is in principle composed by a peaking (in m_{ES}) component and a not-peaking, which can be parametrized as the continuum background. The peaking background, potentially more difficult to reduce, consist of $D^{*0}\pi$ events, considerably suppressed applying the kaon-id requirement on the bachelor track and the tight $|\Delta E| <$ 30MeV cut. By simply counting the number of events in Monte Carlo simulation we can estimate the fraction of this background: $f_{\mathsf{Dh,mc}}([D^0\pi^0]K) == 0.12 \pm 0.03$ for $D^0\pi^0$ and $f_{\mathsf{Dh,mc}}([D^0\gamma]K) = 0.12 \pm 0.02$ for $D^0\gamma$. The results are fairly compatible with the $f_{\mathsf{Dh,mc}}(D^0K) = 0.06 \pm 0.02$ for the $B^- \to D^0K^-$ sample.

This fraction can be estimated also directly from the Data, evaluating the $D^{*0}\pi$ contribution fitting the ΔE distribution. The $D^{*0}\pi$ signal has been parametrized with a Gaussian with $\mu_{\mathsf{Dh,mc}}(D^{*0}\pi) = 50.8 \pm 0.2$ MeV mean, and $\sigma_{\mathsf{Dh,mc}}(D^{*0}\pi) = 21.0 \pm 0.2$ MeV width, both fixed to the Monte Carlo value. The fraction of $D^{*0}\pi$ events evaluated on data are $f_{\mathsf{Dh,data}}([D^0\pi^0]K) = 0.12 \pm 0.07$ and $f_{\mathsf{Dh,data}}([D^0\gamma]K) = 0.05 \pm 0.08$.

[13] $\chi^2(\Delta m, m_{\pi^0}) = \frac{(\Delta m - \Delta m_{PDG})^2}{\sigma^2_{\Delta m}} + \frac{(m_{\pi^0} - m_{\pi^0,PDG})^2}{\sigma^2_{m_{\pi^0}}}$

The Data/Monte Carlo comparison has been performed for the relevant variables used in the event selection. The agreement is satisfactory after we apply the cut $|cos(\theta_{thr}) < 0.8$. In Figure 37 it is shown the $m_{\rm ES}$ distribution for Monte Carlo simulated events, represented with filled colored histograms for each background component, and for data represented with points.

The yields for signal events are reported below from a $m_{\rm ES}$ fit, Figure 38 and from a ΔE

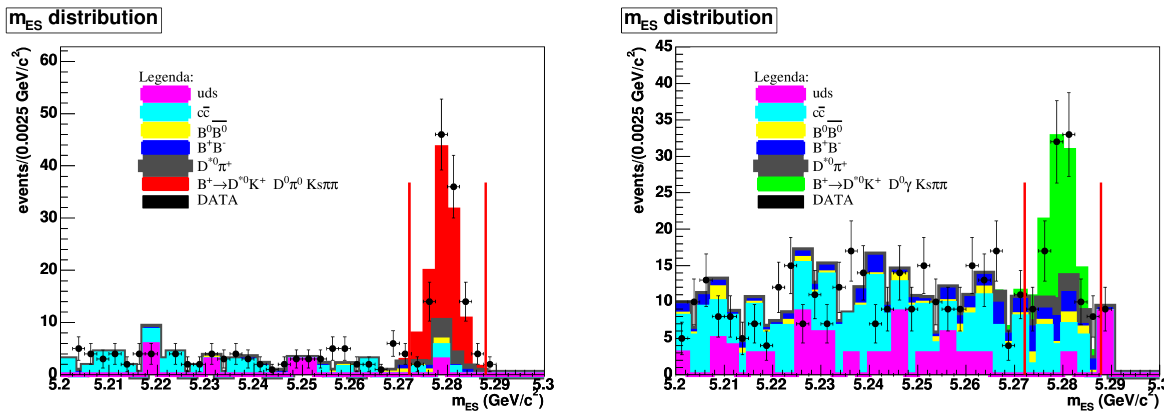

Figure 37: *The m_{ES} distribution obtained after applying the final selection criteria. The Monte Carlo samples are shown (filled histograms) together with the data (points). The number of events is normalized to 204 fb^{-1}. (Left plot) m_{ES} distribution for $D^0\pi^0$. (Right plot) m_{ES} distribution for $D^0\gamma$.*

fit Figure 39. From $m_{\rm ES}$ fit, $D^0\pi^0$:

$$N_{\sf Sig,data}([D^0\pi^0]K) = 102.9 \pm 13.3 \quad S/\sqrt{S+B} = 9.5 \quad f_{\sf Sig,data}([D^0\pi^0]K) = 0.89 \pm 0.04$$

while for the $D^0\gamma$ we have:

$$N_{\sf Sig,data}([D^0\gamma]K) = 54.5 \pm 12.4 \quad S/\sqrt{S+B} = 5.2 \quad f_{\sf Sig,data}([D^0\gamma]K) = 0.49 \pm 0.09$$

From ΔE fit:

$$f_{\sf Dh,data}([D^0\pi^0]K) = 0.06 \pm 0.03 \quad N_{\sf Sig,data}([D^0\pi^0]K) = 97.0 \pm 15.1 \quad \sigma_{\sf Sig,data}([D^0\pi^0]K) = 16.5 \pm 2.1$$
$$f_{\sf Dh,data}([D^0\gamma]K) = 0.00 \quad N_{\sf Sig,data}([D^0\gamma]K) = 45.7 \pm 16.0 \quad \sigma_{\sf Sig,data}([D^0\gamma]K) = 14.1 \pm 5.9$$

The yields with the best candidate choice per event, have been evalueted with the $m_{\rm ES}$ fit. For $D^0\pi^0$ we have:

$$N_{\sf Sig,data}([D^0\pi^0]K) = 95.8 \pm 12.4 \quad S/\sqrt{S+B} = 9.4 \quad f_{\sf Sig,data}([D^0\pi^0]K) = 0.92 \pm 0.03$$

while for the $D^0\gamma$ we have:

$$N_{\sf Sig,data}([D^0\gamma]K) = 46.5 \pm 11.5 \quad S/\sqrt{S+B} = 4.7 \quad f_{\sf Sig,data}([D^0\gamma]K) = 0.47 \pm 0.10$$

Another peaking background is the $D^0 \to 4\pi$ but it has a negligible contribution (<1%) after the cut on $\cos(\alpha_{K_S})$.

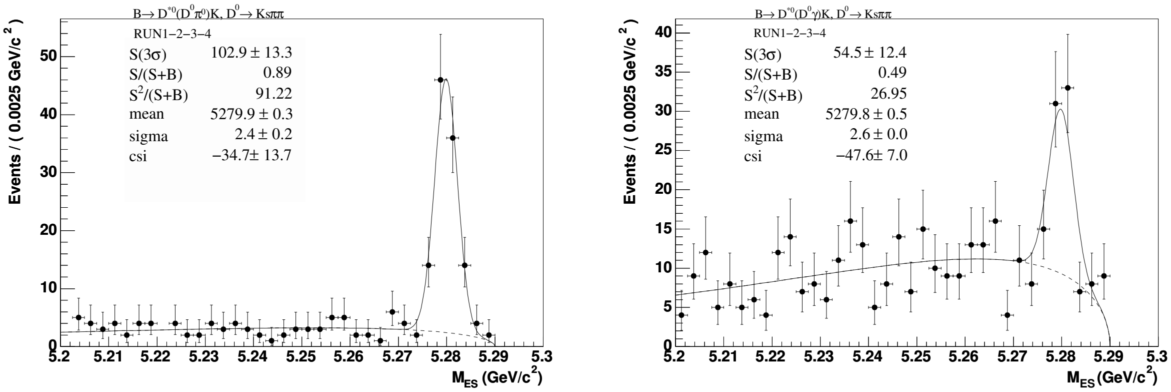

Figure 38: *The m_{ES} distribution obtained after applying the final selection criteria on $204fb^{-1}$ data sample. Data are represented by point with error bars, the fitted PDF is superimposed. (Left plot) m_{ES} distribution for $D^0\pi^0$. (Right plot) m_{ES} distribution for $D^0\gamma$.*

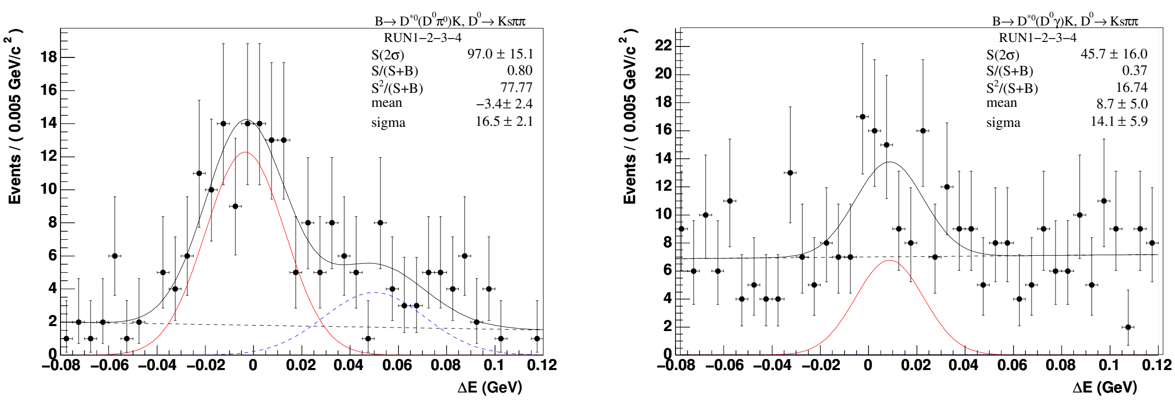

Figure 39: *The ΔE distribution obtained after applying the final selection criteria on $204fb^{-1}$ data sample. Data are represented by point with error bars, the fitted PDF is superimposed. The signal PDF is shown in red, while the PDF contribution for the $D^{*0}\pi$ sample is reported in blue. (Left plot) ΔE distribution for $D^0\pi^0$. (Right plot) ΔE distribution for $D^0\gamma$.*

3.5.3 Background characterization

The background composition is similar in the $D^{*0} \to D^0\pi^0$ and the $D^{*0} \to D^0\gamma$, but the amount of background is larger in the $D^{*0} \to D^0\gamma$ channel. In the following we consider background events excluding the peaking background. The fractions of background events amount to $1 - f_{\mathsf{Sig,data}}([D^0\pi^0]K) = 0.15 \pm 0.07$ and $1 - f_{\mathsf{Sig,data}}([D^0\gamma]K) = 0.33 \pm 0.07$.
We split the background events into 2 categories : continuum events and $B\overline{B}$ events as the two contribution in principle have different impact on the γ measurement. The $B\overline{B}$ events have variables of similar shape to the signal events and therefore they can have a higher weight in the likelihood fit with respect to the continuum events. The $B\overline{B}$ events have also different fraction of true D^0 and charge correlation with the bachelor charged track. The relative fraction of continuum events has been evaluated on Monte Carlo simulated events, and it amounts to $f_{\mathsf{Cont,mc}}([D^0\pi^0]K) = 0.88 \pm 0.03$ and $f_{\mathsf{Cont,mc}}([D^0\pi^0]K) = 0.86 \pm 0.02$. In the final fit this fraction are directly estimated from DATA, exploiting the Fisher information as discussed in the fit section.
This classification of the background, is useful for Data/MC comparison and selection criteria optimization, but in the final fit to the D^0 Dalitz plot it is further required to divide the background events in those with a true D^0 or a fake one. The fraction of true D^0 can be estimated from Monte Carlo simulation by simply counting the number of true D^0 and false D^0 of each background sample after the cuts. In continuum events the fraction of true D^0 is $R_{\mathsf{Cont,mc}}([D^0\pi^0]K) = 0.27 \pm 0.08$ and $R_{\mathsf{Cont,mc}}([D^0\gamma]K) = 0.13 \pm 0.02$.

In $B\overline{B}$ events the fraction are $R_{\mathsf{B\overline{B},mc}}([D^0\pi^0]K) = 0.11 \pm 0.06$ and $R_{\mathsf{B\overline{B},mc}}([D^0\gamma]K) = 0.16 \pm 0.03$. The fraction of true D^0 for the overall background, can be estimated also in real DATA using a D^0 mass fit, selecting events satisfying m_{ES} <5.272 MeV/c^2 and having removed the cut on the D^0 mass. In the fit to the D^0 invariant mass the mean and the width of the D^0 have been fixed to 1864 MeV/c^2 and 7 MeV/c^2 as found on the Monte Carlo simulation. Both data and MC show no evidence of such contribution, the statistics is small and the fraction of true D^0 is found to be zero within the errors :

$$\begin{aligned} R_{\mathsf{all,data}}([D^0\pi^0]K) &= 0.00 \pm 0.007 \\ R_{\mathsf{all,mc}}([D^0\pi^0]K) &= 0.0 \pm 1.0 \end{aligned} \tag{96}$$

$$\begin{aligned} R_{\mathsf{all,data}}([D^0\gamma]K) &= 0.20 \pm 0.07 \\ R_{\mathsf{all,mc}}([D^0\gamma]K) &= 0.17 \pm 0.13 \end{aligned} \tag{97}$$

The last parameter needed for the likelihood is the fraction of true D^0 associated with a charged particle of negative charge. From Monte Carlo simulation we evaluated the relative fraction $R_{\mathsf{Cont,mc}}$ for continuum events and $R_{\mathsf{B\overline{B},mc}}$ for $b\bar{b}$ events:

$$\begin{aligned} R^{RS}_{\mathsf{Cont,mc}}([D^0\pi^0]K) &= 0.23 \pm 0.11 \\ R^{RS}_{\mathsf{B\overline{B},mc}}([D^0\pi^0]K) &= 1 \end{aligned} \tag{98}$$

$$\begin{aligned} R^{RS}_{\mathsf{Cont,mc}}([D^0\gamma]K) &= 0.15 \pm 0.06 \\ R^{RS}_{\mathsf{B\overline{B},mc}}([D^0\gamma]K) &= 1 \end{aligned} \tag{99}$$

Even if the uncertainty on this fraction is large, the level of this background is low and the systematic error is expected to be small as confirmed by ToyMC studies. The summary of the values and errors obtained for the different parameters for the Dalitz Fit is given in Table 6 for $D^0\pi^0$ and in Table 7 for $D^0\gamma$ with $D^0 \to K_S^0\pi^+\pi^-$.

Parameter	Value from Data	Value from Monte-Carlo
$f_{\mathsf{Sig}}([D^0\pi^0]K)$ $(m_{\mathrm{ES}} > 5.272\,\mathrm{GeV}/c^2)$	0.85 ± 0.09	0.91 ± 0.05
$f_{\mathsf{Sig}}([D^0\pi^0]K)$ $(m_{\mathrm{ES}} > 5.2\,\mathrm{GeV}/c^2)$	0.53 ± 0.08	0.50 ± 0.07
$f_{\mathsf{Dh}}([D^0\pi^0]K)$	0.12 ± 0.07	0.04 ± 0.05
$f_{\mathsf{Cont}}([D^0\pi^0]K)$ $(m_{\mathrm{ES}} > 5.272\,\mathrm{GeV}/c^2)$	-	0.64 ± 0.13
$f_{\mathsf{Cont}}([D^0\pi^0]K)$ $(m_{\mathrm{ES}} > 5.2\,\mathrm{GeV}/c^2)$	-	0.88 ± 0.03
$R_{\mathsf{Cont}}([D^0\pi^0]K)$	-	0.27 ± 0.08
$R_{\mathsf{B\overline{B}}}([D^0\pi^0]K)$	-	0.11 ± 0.06
$R^{RS}_{\mathsf{Cont}}([D^0\pi^0]K)$	-	0.23 ± 0.11
$R^{RS}_{\mathsf{B\overline{B}}}([D^0\pi^0]K)$	-	1

Table 6: *Summary of the values for parameters for $D^0\pi^0$ used in the likelihood.*

Parameter	Value from Data	Value from Monte-Carlo
$f_{\mathsf{Sig}}([D^0\gamma]K)$ $(m_{\mathrm{ES}} > 5.272\,\mathrm{GeV}/c^2)$	0.67 ± 0.10	0.62 ± 0.08
$f_{\mathsf{Sig}}([D^0\gamma]K)$ $(m_{\mathrm{ES}} > 5.2\,\mathrm{GeV}/c^2)$	0.22 ± 0.04	0.16 ± 0.04
$f_{\mathsf{Dh}}([D^0\gamma]K)$	0.05 ± 0.08	0.01 ± 0.09
$f_{\mathsf{Cont}}([D^0\gamma]K)$ $(m_{\mathrm{ES}} > 5.272\,\mathrm{GeV}/c^2)$	-	0.66 ± 0.06
$f_{\mathsf{Cont}}([D^0\gamma]K)$ $(m_{\mathrm{ES}} > 5.2\,\mathrm{GeV}/c^2)$	-	0.86 ± 0.01
$R_{\mathsf{Cont}}([D^0\gamma]K)$	-	0.13 ± 0.02
$R_{\mathsf{B\overline{B}}}([D^0\gamma]K)$	-	0.16 ± 0.03
$R^{RS}_{\mathsf{Cont}}([D^0\gamma]K)$	-	0.16 ± 0.06
$R^{RS}_{\mathsf{B\overline{B}}}([D^0\gamma]K)$	-	1

Table 7: *Summary of the alues for parameters for $D^0\gamma$ used in the likelihood.*

3.5.4 The $B^- \to D^{*0}\pi^-$ control sample

The $B^- \to D^{*0}\pi^-$ control sample has been used for resolution studies and for the parametrization of the shapes of the relevant distributions as Fisher discriminant and ΔE and m_{ES}. The $\Delta E \in [20, 80]$ MeV cut is applied using the kaon hypothesis for the mass of the bachelor track. The background composition is quite different with respect to the $D^{*0}K$ and the peaking background in the m_{ES} variable is more consistent. The Helicity distribution of the D^0 respect to the D^{*0} flight direction has different shapes for $D^0\pi^0$ and $D^0\gamma$. In principle it can be used to characterize the signal distribution. The D^{*0} is a vector meson and it has to be fully polarized when it comes from the decay $B^- \to D^{*0}K^-$. If we define the helicity angle θ_{Hel} as the angle between the D^{*0} daughter (*e.g.* D^0) in the D^{*0} rest frame, respect to the D^{*0} flight

direction in the B rest frame, we can study the different helicity distribution for the $D^0\pi^0$ and $D^0\gamma$ decay. The helicity distribution can be calculated assuming a decay of a polarized vector meson into 2 pseudoscalar ($D^0\pi^0$) which is proportional to $\frac{dN}{d(\cos\theta_{Hel})} \propto \cos^2\theta_{Hel}$. If the final particles are 1 pseudoscalar plus 1 vector ($D^0\gamma$) the distribution is proportional to $\frac{dN}{d(\cos\theta_{Hel})} \propto \sin^2\theta_{Hel}$.
In Figure 40 is shown the comparison DATA/MC after the selection cuts for the $D^{*0}\pi$. The helicity cuts have been considered for the signal $B^- \to D^{*0}K^-$ but the significance and the purity of the sample does not improve significantly. For this reason we decided to avoid this variable from the selection.
The yields from data are in good agreement with Monte Carlo expectation. We find from the fit on data $N = 829 \pm 41$ for $B^- \to D^{*0}\pi^-$ with $D^{*0} \to D^0\pi^0$ signal events and $N = 407 \pm 76$ for $B^- \to D^{*0}\pi^-$ with $D^{*0} \to D^0\gamma$ signal events.

The shape of the Fisher discriminant distribution has been fitted with a double gaussian function. We have selected off-resonance data with an with energy in C.M. frame 20 MeV below the $\Upsilon(4S)$ nominal energy as pure continuum background and ah high purity sample of $B^- \to D^{*0}\pi^-$ as signal. The agreement is good for the Fisher distribution for $B^- \to D^0\pi^-$ and $B^- \to D^{*0}\pi^-$ events therefore we have decided to use a common parametrization for $B^- \to D^0K^-$ and $B^- \to D^{*0}K^-$ signal events in the final CP fit (see section 5).

	f	μ_1	σ_1	μ_2	σ_2
continuum	0.626 ± 0.021	-0.430 ± 0.006	0.249 ± 0.005	0.261 ± 0.029	0.439 ± 0.012
$B\overline{B}$	0.435 ± 0.014	0.642 ± 0.015	0.320 ± 0.008	-0.234 ± 0.011	0.309 ± 0.006

Table 8: *Fitted parameters of the double Gaussian distributions for the $B\overline{B}$ and off resonance components obtained using the $D^*\pi$ event sample. f is the fraction of the 1st gaussian, while $\mu_{1,2}$ and $\sigma_{1,2}$ are the mean and the resolution of the gaussian $1,2$.*

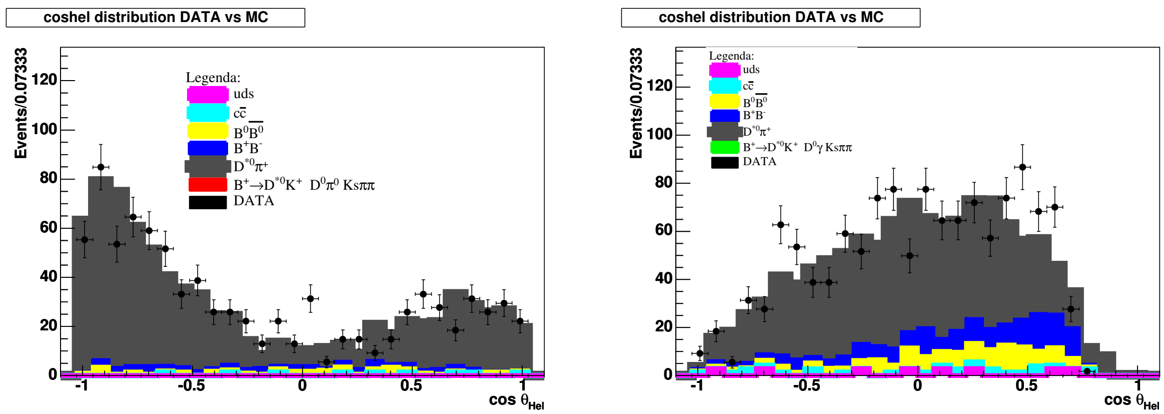

Figure 40: *The* $\cos\theta_{Hel}$ *distribution for* $D^{*0}\pi$ *obtained after applying the final selection criteria. Data are represented by point with error bars. (Left plot)* $\cos\theta_{Hel}$ *distribution for* $D^0\pi^0$*. (Right plot)* $\cos\theta_{Hel}$ *distribution for* $D^0\gamma$*.*

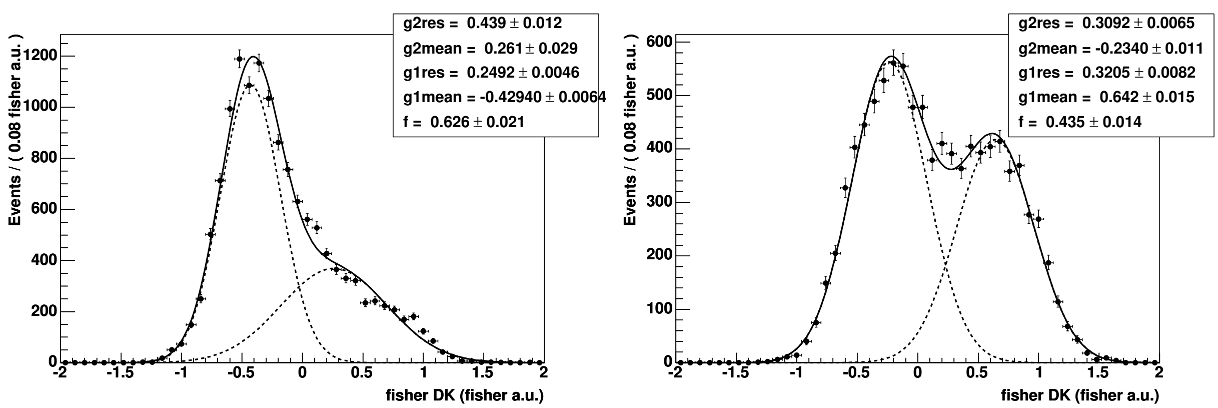

Figure 41: *The Fisher distributions for off-resonance data and* $D^*\pi$ *events. Data are represented by point with error bars, the fitted PDF is superimposed. (Left plot) Fisher distribution for off-resonance events. (Right plot) Fisher distribution for* $D^*\pi$ *events.*

4 Determination of the Dalitz model from $D^{*+} \to D^0\pi^+$ events

In this chapter we are going to discuss the parametrization of the $\mathcal{A}(D^0 \to K_S^0\pi^+\pi^-)$ decay amplitude introduced in section 1.5. The parametrization has been obtained using a Dalitz plot analysis technique [27] on the flavour tagged D^0 sample of events $D^{*+} \to D^0\pi_s^+$. [14]

4.1 Basics for a $D^0 \to K_S^0\pi^+\pi^-$ Dalitz analysis

The understanding of the final state interactions in exclusive weak decays is important to improve our ability to model decay rates and also to understand other important phenomena such as mixing and *CP* violation. In particular three-body decays represent a rich laboratory where to study interference among different resonances, which represents evidence of final-state interactions. The three-body decays of charm mesons often proceeds as quasi-two-body decays with resonant intermediate states. In most of the decays the resonances interfere among themselves, a Dalitz analysis considers these effects. We describe in the following two formalisms for the description of the Dalitz plane struture. The **Isobar Model** describes the decay amplitude as a sum of quasy-two-body amplitudes, that is sum of relativistic Breit-Wigner functions plus a non-resonant term which has constant phase and amplitude in the Dalitz plane. The **K-matrix** formalism [28] was developed in the frame of potential theory and basis on the general unitarity property of the scattering theory matrix .

4.1.1 Isobar Model Formalism

Since we are studying a decay of a spin-zero particle to three daughters, only two degrees of freedom are required to completely describe the kinematics of the decay. We have three particles, daughters of the D^0 which is three 4-momenta or 12 unknowns. The mass hypothesis of the daugters and the conservation of the energy and momentum in the D^0 decay reduces the unknowns to 12-3-4=5. Moreover the D^0 is a spinless particle and the decay amplitude is simmetric under spatial rotation, which means we have 2 remaining independent degrees of freedom.

There are three invariant masses that can be formed by considering all possible pairs of final state particles: $M^2_{K_S^0\pi^-} \equiv M^2_{12}$, $M^2_{K_S^0\pi^+} \equiv M^2_{13}$ and $M^2_{\pi^-\pi^+} \equiv M^2_{23}$. Only two of these are independent, however, since energy and momentum conservation results in the additional constraint

$$M^2_{D^0} + M^2_{K_S^0} + M^2_{\pi^-} + M^2_{\pi^+} = M^2_{K_S^0\pi^-} + M^2_{K_S^0\pi^+} + M^2_{\pi^-\pi^+}. \tag{100}$$

Choosing two of the above three invariant masses as dynamic variables has two compelling advantages: i) Their relativistic invariance means the Lorentz frame in which they are evaluated is irrelevant; ii) As the expression for the partial width in Equation 101 indicates, we expect that a scatter plot of events in the M^2_{12} vs M^2_{23} plane (known as a Dalitz Plot or Dalitz plane) will be uniformly distributed if phase-space alone determines the decay dynamics. This allows the decay fraction at each point to be readily correlated with the decay matrix element $\mathcal{M}$ without additional corrections:

[14] with π_s^+ we intend the charged low-momentum (soft) pion from the D^{*+} decay.

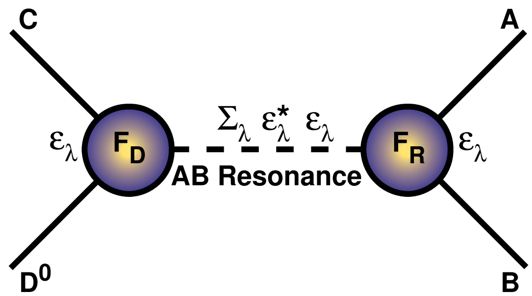

Figure 42: A Representation of the three body decay of $D^0 \to ABC$ through an AB resonance. The spin sum is performed to obtain the angular dependence of the decay.

$$d\Gamma = \frac{|\mathcal{M}|^2}{256\pi^3 M_D^3} dM_{12}^2 dM_{23}^2. \tag{101}$$

In this formalism the amplitude $\mathcal{M}$ can be written as a sum of a two body-decay matrix elements and a non-resonant term according to the following expression :

$$\mathcal{M} = a_{nr}e^{i\phi_{nr}} + \Sigma a_r e^{i\phi_r}\mathcal{A}_{spin}(ABC|r) \tag{102}$$

Each term of the sum is parametrized with an amplitude a_r and a phase ϕ_r. Let's assume the D meson is decaying into particle C plus a r resonance, followed by the decay of the r resonance into particles A and B. The function $\mathcal{A}_{spin}(ABC|r)$ gives the Lorentz invariant expression for the matrix element of D^0 meson as a function of position in the Dalitz plot. The functional dependence is different according to the spin of the resonance, every vertex in the decay diagram in Figure 42 contains a spin factor ε_λ which depends on the type of decay: scalar, vector, tensor, etc.

The matrix element for a vector decay is for example:

$$\mathcal{A}_1(ABC|r) = F_D(P_D^0 + P_C)_\mu \frac{\sum_\lambda \varepsilon_\lambda^{\mu *}\varepsilon_\lambda^\nu}{M_r^2 - M_{AB}^2 - iM_r\Gamma_{AB}}(P_A + P_B)_\nu F_r.^{15} \tag{103}$$

where P is the 4-momentum, M_r is the mass of the resonance. Form factors F_D and F_r attempt to model the underlying quark structure of the D^0 meson and the intermediate resonances. We use the Blatt-Weisskopf penetration factors shown in Table 9. These have one free parameter, R, which is the "radius" of the meson, and are dependent on the momentum P of the decay particles in the parent rest frame.

[15] The spin-sum in the numerator of Equation (103) is evaluated to give

$$\sum_\lambda \varepsilon_\lambda^{\mu *}\varepsilon_\lambda^\nu = -g^{\mu\nu} + \frac{P_{AB}^\mu P_{AB}^\nu}{M_{AB}^2}$$

Table 9: *Blatt-Weisskopf Penetration Form Factors. p_r is the momentum of either daughter in the meson rest frame. p_{AB} is the momentum of either daughter in the candidate rest frame (same as p_r except the parent mass used is the two-track invariant mass of the candidate rather than the mass of the meson). R is the meson radial parameter.*

Spin	Form Factor F_r
0	1
1	$\frac{\sqrt{1+R^2p_r^2}}{\sqrt{1+R^2p_{AB}^2}}$
2	$\frac{\sqrt{9+3R^2p_r^2+R^4p_r^4}}{\sqrt{9+3R^2p_{AB}^2+R^4p_{AB}^4}}$

Γ_{AB} is the "mass dependent width" which is a function of M_{AB}, the AB invariant mass, the momentum of either daughter in the AB rest frame p_{AB}, the momentum of either daughter in the resonance rest frame p_r, the spin of the resonance J, the width of the resonance Γ_r, and is expressed as [53]:

$$\Gamma_{AB} = \Gamma_r \left(\frac{p_{AB}}{p_r}\right)^{2J+1} \left(\frac{M_r}{M_{AB}}\right) F_r^2 \tag{104}$$

Equation 103 can be written as:

$$\mathcal{A}_1(ABC|r) = F_D F_r \frac{M_{AC}^2 - M_{BC}^2 + \frac{(M_D^2-M_C^2)(M_B^2-M_A^2)}{M_r^2}}{M_r^2 - M_{AB}^2 - iM_r\Gamma_{AB}}. \tag{105}$$

while for a spin zero resonance,

$$\mathcal{A}_0(ABC|r) = F_D F_r \frac{1}{M_r^2 - M_{AB}^2 - iM_r\Gamma_{AB}}. \tag{106}$$

Similar expressions holds for tensor particles:

$$\mathcal{A}_2(ABC|r) = \frac{F_D F_r}{M_r^2 - M_{AB}^2 - i\Gamma_{AB}M_r}\left[\left(M_{BC}^2 - M_{AC}^2 + \frac{(M_D^2-M_C^2)(M_A^2-M_B^2)}{M_r^2}\right)^2 \right.$$
$$\left. -\frac{1}{3}\left(M_{AB}^2 - 2M_D^2 - 2M_C^2 + \frac{(M_D^2-M_C^2)^2}{M_r^2}\right)\left(M_{AB}^2 - 2M_A^2 - 2M_B^2 + \frac{(M_A^2-M_B^2)^2}{M_r^2}\right)\right].^{16} \tag{107}$$

The isobar model is a quite simple phenomenological description of the decay amplitude, it describes accurately the Dalitz distributions for most of the decays, even if some high statistics studies show some discrepancies between the data and the theoretical distributions.

[16] In this case the spin sum has been previously calculated by Pilkuhn [53] to be

$$\sum_\lambda \varepsilon_\lambda^{*\mu\nu}\varepsilon_\lambda^{\alpha\beta} = \frac{1}{2}\left(T^{\mu\alpha}T^{\nu\beta} + T^{\mu\beta}T^{\nu\alpha}\right) - \frac{1}{3}T^{\mu\nu}T^{\alpha\beta}$$

4.2 $D^0 \to K_S^0 \pi^+ \pi^-$ sample selection

In order to determine the Dalitz model parametrization we have analyzed a sample of 81496 $D^0/\bar{D}^0$ signal events corresponding to an integrated luminosity of 91.5 fb^{-1} selecting the decay $D^{*+} \to D^0 \pi_s^+$, with $D^0 \to K_S^0 \pi^+ \pi^-$.
The K_S^0 candidates are selected from pairs of opposite charged tracks with an invariant mass within 9 MeV/c^2 from the nominal PDG mass [44]. The D^0 candidates are made combining the K_S^0 candidates with opposite charged tracks with an invariant mass within 14 MeV/c^2 from the nominal D^0 invariant mass [44]. In order to select events from the continuum we require a further cut on the D^0 candidate momentum in the $\Upsilon(4S)$ rest frame, $p^\star > 2.0\,\mathrm{GeV}/c$. It is worth noticing that the $D^{*+} \to D^0 \pi_s^+$ sample is ortogonal with respect to the sample we use for the CP fit, which are going to discuss in the next chapter.
The D^* candidates are formed combining the D^0 candidates with charged tracks. We finally require $\Delta m \equiv M(D^{*+}) - M(D^0)$ in the range [0.1448-0.1460] GeV/c^2 which allows to select a D^0 pure sample (see Fig.43). In the Dalitz plot analysis we use a sample of 41104(40392) $D^0(\bar{D}^0)$ candidates fitted simultaneously. The combinatorial background fraction is estimated to be $2.36 \pm 0.05\%$ by fitting the mass distribution to a double Gaussian for the signal and a flat background distribution. The result of the fit is shown in figure 43. The charge of the soft pion from the D^* decay tags the flavour of the D^0 meson without ambiguity.

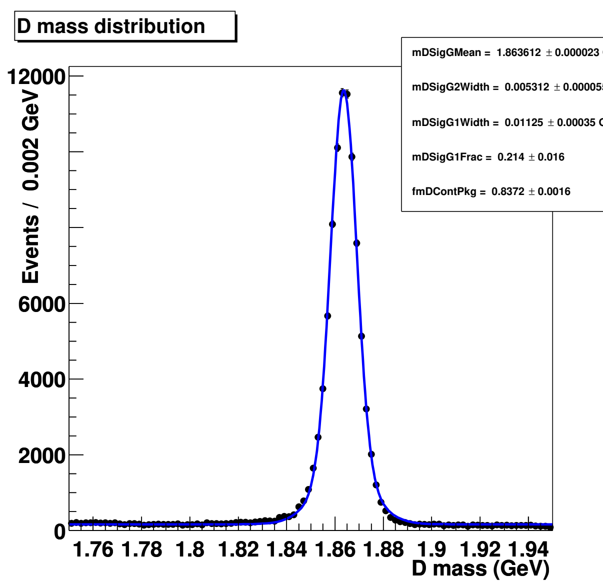

Figure 43: D^0 *mass distribution for the* $D^{*+} \to D^0 \pi_s^+$ *sample.*

---

where
$$T^{\mu\nu} = -g^{\mu\nu} + \frac{P^\mu P^\nu}{M^2}$$

4.3 Dalitz fit

We fit the distribution of the events in the Dalitz plane using the Isobar Model, which is described in Appendix 4.1. In this formalism the amplitude f can be written as a sum of quasi-two-body decay amplitudes plus a non-resonant term, according to the following expression :

$$f = a_{nr}e^{i\phi_{nr}} + \Sigma a_r e^{i\phi_r}\mathcal{A}_{spin}(ABC/r) \tag{108}$$

Each term of the sum is parametrized with an amplitude a_r and a phase ϕ_{nr}. Let us assume the D meson is decaying into particle C plus a r resonance, followed by the decay of the r resonance into particles A and B. The functional dependence is different according to the spin of the resonance, as explained in Appendix 4.1. The function $\mathcal{A}_{spin}(ABC/r)$ gives the Lorentz invariant expression for the matrix element of D^0 meson as a function of position in the Dalitz plot.
For $\pi\pi$ vector resonances ($\rho(770)$ and $\rho(1450)$) we are using Gounaris-Sakurai (GS) Breit-Wigner parametrization [67]. We attempt to parametrize our unknwoledge of the quark structure of the D^0 meson and of the intermediate r resonances with form factors F_D and F_r. A maximum likelihood fit has been made in order to describe the population on the Dalitz plot and to extract amplitudes a_{nr}, a_r and phases ϕ_{nr}, ϕ_r. The likelihood function has been written in the following way:

$$L = x \cdot \frac{\epsilon(m^2_{\pm}, m^2_{\mp})\left|f(m^2_{\pm}, m^2_{\mp})\right|^2}{\int |f(m^2_{\pm}, m^2_{\mp})|^2\, \epsilon(m^2_{\pm}, m^2_{\mp})d\mathcal{DP}} + (1-x)$$

where $1-x$ is the fraction of background events in the sample whose distribution is assumed to be flat and $\epsilon(m^2_{\pm}, m^2_{\mp})$ is the efficiency map determined in Monte Carlo simulation where the D^0 was allowed to decay isotropically (see Fig.44).
We checked that mass resolution effect are negligible all over the Dalitz plane if compared with intermediate resonance width. Nevertheless we kinematically constrain D^0 daughters momenta to the nominal D^0 mass avoiding candidates lying outside the kinematic allowed region. We compute the fit fractions defined as the integral of a single component divided by the coherent sum of all components:

$$\text{Fit Fraction} = \frac{\int \left|a_r e^{i\phi_r}\mathcal{A}(ABC|r)\right|^2 d\mathcal{DP}}{\int \left|\sum_j a_j e^{i\phi_j}\mathcal{A}(ABC|j)\right|^2 d\mathcal{DP}}. \tag{109}$$

where $d\mathcal{DP}$ indicates that the integral is performed over the Dalitz Plot. The sum of the fit fractions for all components of a fit will in general not be one because of interference, but a large deviation from one can be caused by unrealistic components in the model.

4.4 Efficiency correction

The Dalitz model PDF has to be corrected by efficiency non-uniformities in the Dalitz plot. The correction has been obtained by fitting to a third order polynomial

$$eff(x,y) = a_0\ [1 + a_1\ (x+y) + a_2\ (x^2+y^2+xy) + a_3\ (x^3+y^3+x^2y+xy^2)]$$

a sample of signal Monte Carlo event $D^{*+} \to D^0\pi_s^+$, $D^0 \to K_S^0\pi^+\pi^-$, where the D^0 was allowed to decay isotropically. The parameterization has been symmetrized for $x = m^2(K_S^0\pi^+)$ and $y = m^2(K_S^0\pi^-)$. Figure 44 shows the Dalitz plot distribution and the K_S^0 π^+ and K_S^0 π^- projections. In this figure the blue (dark) curves represent the result of the 3rd order polynomial unbinned likelihood fit, and the red (bright) curves represent the projection for a perfectly flat efficiency. It can be seen that except at the borders of the kinematically allowed region the efficiency correction is quite consistent with a flat distribution. In table 10 are reported the coefficients from the fit. We fixed $a_0 = 1$ being an arbitrary normalization factor.

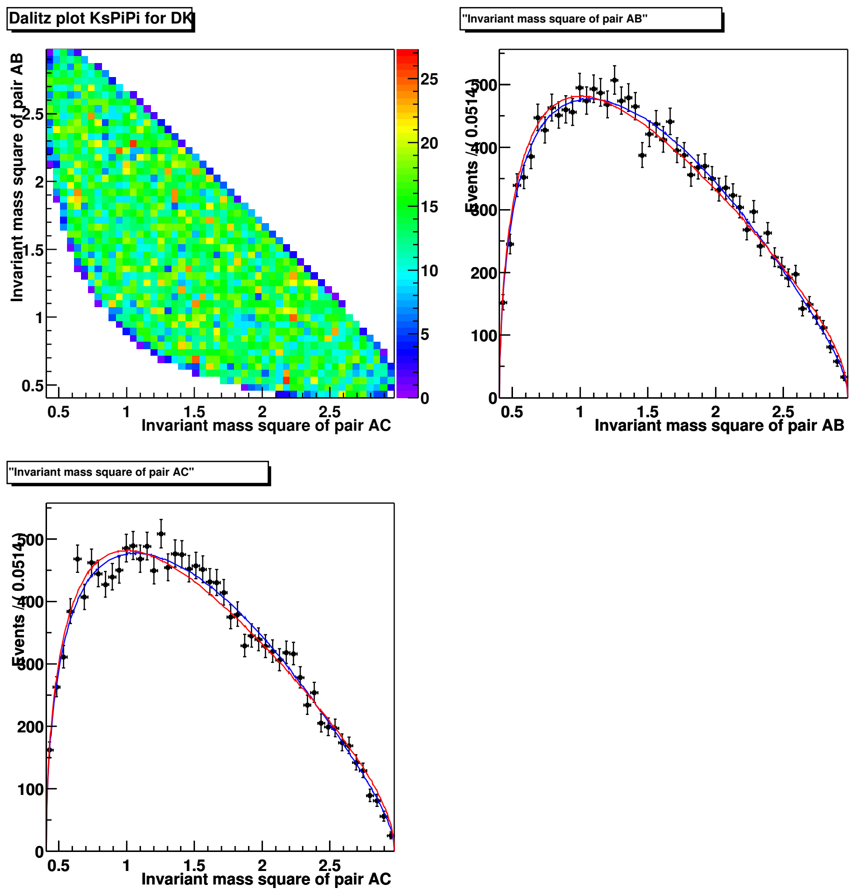

Figure 44: *Relative efficiency over the Dalitz* $(K_s\pi^+)$ *vs* $(K_s\pi^-)$ *for the signal Monte Carlo* $D^{*+} \to D^0\pi_s^+$, $D^0 \to K_S^0\pi^+\pi^-$ *sample. The blue (dark) curves represent the result of the symmetrized 3rd order polynomial fit (after momentum rescaling) while the red (bright) curves represent the projections for a perfectly flat efficiency.*

4.5 Nominal Dalitz Model

In order to parametrize the Dalitz distribution we have considered a model with 13 resonances with masses and widths equal to those published in PDG2004 [44] (see Tab.11) corresponding

Table 10: *Coefficients of the Dalitz efficiency correction parameterization used for the D^* control sample.*

Coefficient	Value
a_0	1
a_1	-0.58 ± 0.13
a_2	0.333 ± 0.038
a_3	-0.063 ± 0.006

to 18 quasi-two-body decay amplitudes and phases. There are 8 of type $(\pi\pi)$-resonance (σ_1, $\rho^0(770)$, $\omega(782)$, $f_0(980)$, σ_2, $f_2(1270)$, $f_0(1370)$ and $\rho(1450)$) and 5 of type $(K_s\pi^-)$-resonance ($K^*(892)$, $K_0^*(1430)$, $K_2^*(1430)$, $K^*(1410)$, $K^*(1680)$). We also include $K^*(892)$, $K_0^*(1430)$, $K_2^*(1430)$ Doubly Cabibbo suppressed transition decays. All the considered resonances are well established but the two scalar (π, π) resonances σ_1 and σ_2, which were proposed by Belle [59]. The masses and widths of these two scalars were obtained from an initial binned likelihood fit with the model described here with all phases and amplitudes floated together with the masses and widths of the two resonances. We used here a binned method since when floating the Breit-Wigner parameters in the fit the normalization integral has to be calculated at each step of the fit, which is very time consuming. The binning we used in this case consisted of an uniform grid of 200 bins, which corresponds to about 3 MeV/c^2 resolution on the $\pi^+\pi^-$ invariant mass, well below the expected width of the two scalars. Note that the binned likelihood method accounts naturally for empty bins so there is no need for making an adaptive binning. We used an unbinned likelihood fit to determine the phases and amplitudes of the Isobar Model. In Fig. 45,46,47,48,49 we show how each of the various two-body decay amplitudes contributes individually to the Dalitz plane distribution. The total phase and amplitude in Eq.108 are arbitrary. We have chosen amplitude unity and phase zero for the $K_S^0\rho$ mode which has the second biggest fit fraction below the $K^*(892)$ mode, according to the conventions adopted by CLEO [58] and Belle [59].

In Table 12 we show the results of the Dalitz analysis of the D^* sample. The total fit fraction is 1.25 which is the results of the inteference among resonances.

Small difference in the amplitudes and phases are possible when using different normalization techniques. We have checked on DK signal MC and CP blind fit [17] that the impact on this on γ is less than 0.5 degree, therefore it is negligible. Fig. 50 shows the projections of the fit results (corrected by efficiency) on top of data distributions.

4.6 χ^2 fit

A χ^2 fit has been also performed to explore quickly alternative model and to compute the goodness of the fit. We use an adaptative bins definition to guarantee a minimal number of

[17] A blind fit is a fit where the values of the fitted parameters are blinded while the values of the errors are shown. It is the strategy used in BABAR to evaluate the statistical and systematic errors in the optimization process avoiding possible experimental biases. Only when a satisfactory understanding of the analysis is reached, the collaboration allows the *unblinding*

Resonance	Mass (MeV/c^2)	Width (MeV/c^2)	Spin
$K^*(892)$	891.66	50.8	1
$K_0^*(1430)$	1412	294	0
$K_2^*(1430)$	1425.6	98.5	2
$K^*(1410)$	1414	232	1
$K^*(1680)$	1717	322	1
σ_1	484 ± 9 (from fit)	383 ± 14 (from fit)	0
$\rho^0(770)$	775.8	146.4	1
$\omega(782)$	782.6	8.5	1
$f_0(980)$	975	44	0
σ_2	1014 ± 7 (from fit)	88 ± 13 (from fit)	0
$f_2(1270)$	1275.4	185.1	2
$f_0(1370)$	1434	173	0
$\rho(1450)$	1406	455	1

Table 11: *Summary of the values for the masses and widths of the resonances used in the fit of the $D^0 \to K_s\pi^-\pi^+$ Dalitz plot using a flavour tagged D^0 sample $D^{*\pm} \to D^0\pi_s^\pm$ from the continuum. The masses and the widths for two scalars σ_1 and σ_2 have been obtained directly from the data, while for the remaining resonances we have used the nominal PDG2004 [44] values.*

Resonance	Amplitude	phase (degrees)	fit fraction (%)
$K^*(892)$	1.781 ± 0.018	131.0 ± 0.79	58.60
$\rho^0(770)$	1 (fixed)	0(fixed)	22.36
$K^*(892)$ DCS	0.1796 ± 0.0079	-44.1 ± 2.4	0.60
$\omega(782)$	0.0391 ± 0.0016	115.3 ± 2.5	0.56
$f_0(980)$	0.4817 ± 0.011	218.2 ± 2.2	6.09
$f_0(1370)$	2.25 ± 0.28	113.2 ± 4.4	3.20
$f_2(1270)$	0.922 ± 0.040	-21.3 ± 2.8	3.00
$K_0^*(1430)$	2.447 ± 0.073	-8.3 ± 2.0	8.32
$K_0^*(1430)$ DCS	0.368 ± 0.067	-342.2 ± 9.8	0.19
$K_2^*(1430)$	1.054 ± 0.045	-54.3 ± 2.5	2.74
$K_2^*(1430)$ DCS	0.075 ± 0.036	-104 ± 30	0.01
$K^*(1410)$	0.515 ± 0.071	154 ± 10	0.37
$K^*(1680)$	0.89 ± 0.29	-139 ± 19	0.28
$\rho(1450)$	0.515 ± 0.092	38 ± 13	0.24
σ_1	1.358 ± 0.040	-177.9 ± 2.4	9.27
σ_2	0.340 ± 0.024	-207.0 ± 3.8	1.34
Non resonant	3.53 ± 0.44	-232.4 ± 4.7	7.30

Table 12: *Summary of the amplitudes, phases and fit fraction of the different components obtained from the unbinned likelihood fit. The total fit fraction is* 1.25.

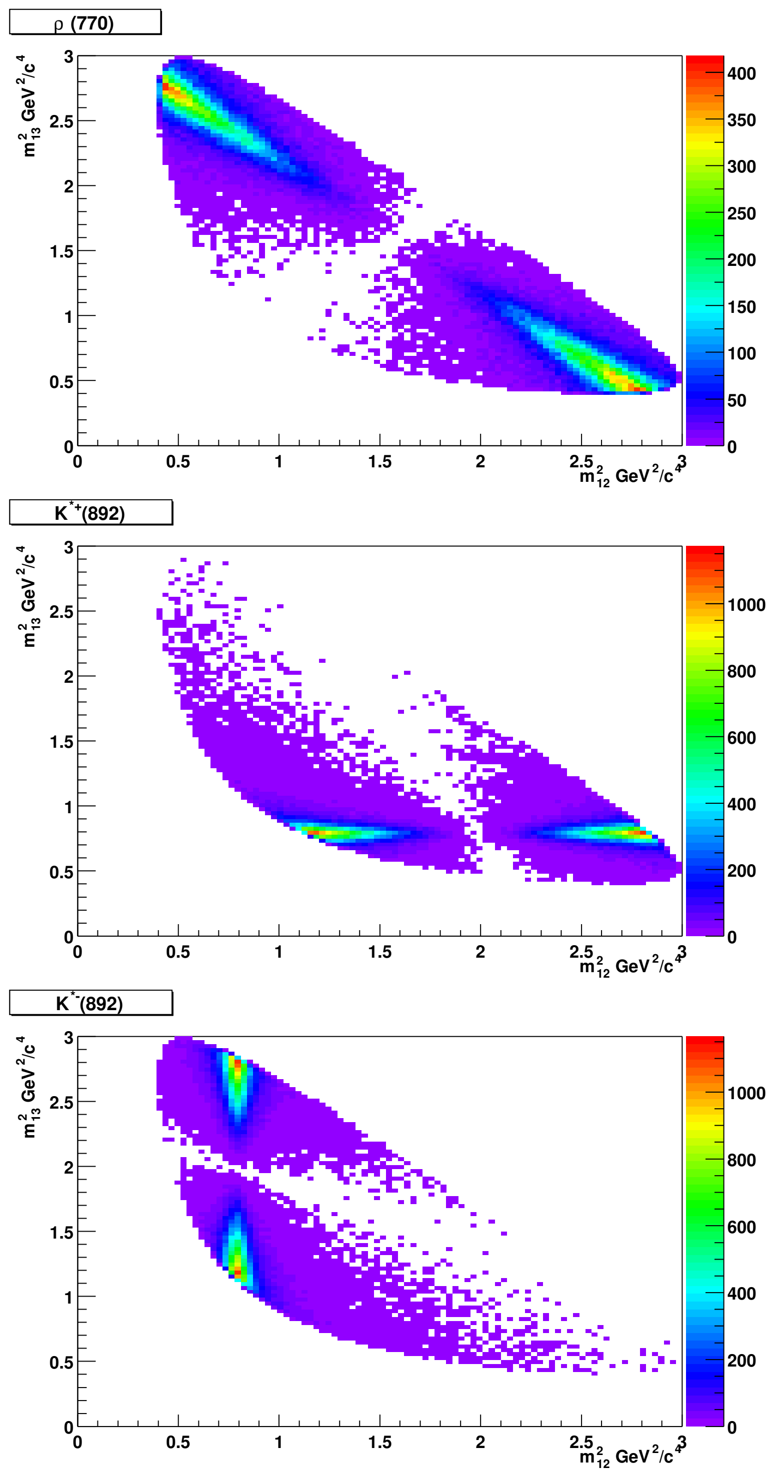

Figure 45: *Monte Carlo distribution of* ($m^2_{K_S\pi^+}$,$m^2_{K_S\pi^-}$) *for* D^0 *decaying into either* $\rho(770)K_S$ *(top) or* $K^{*-}(892)\pi^+$ *(middle) or* $K^{*+}(892)\pi^-$*[Doubly Cabibbo Suppressed decay] (bottom).*

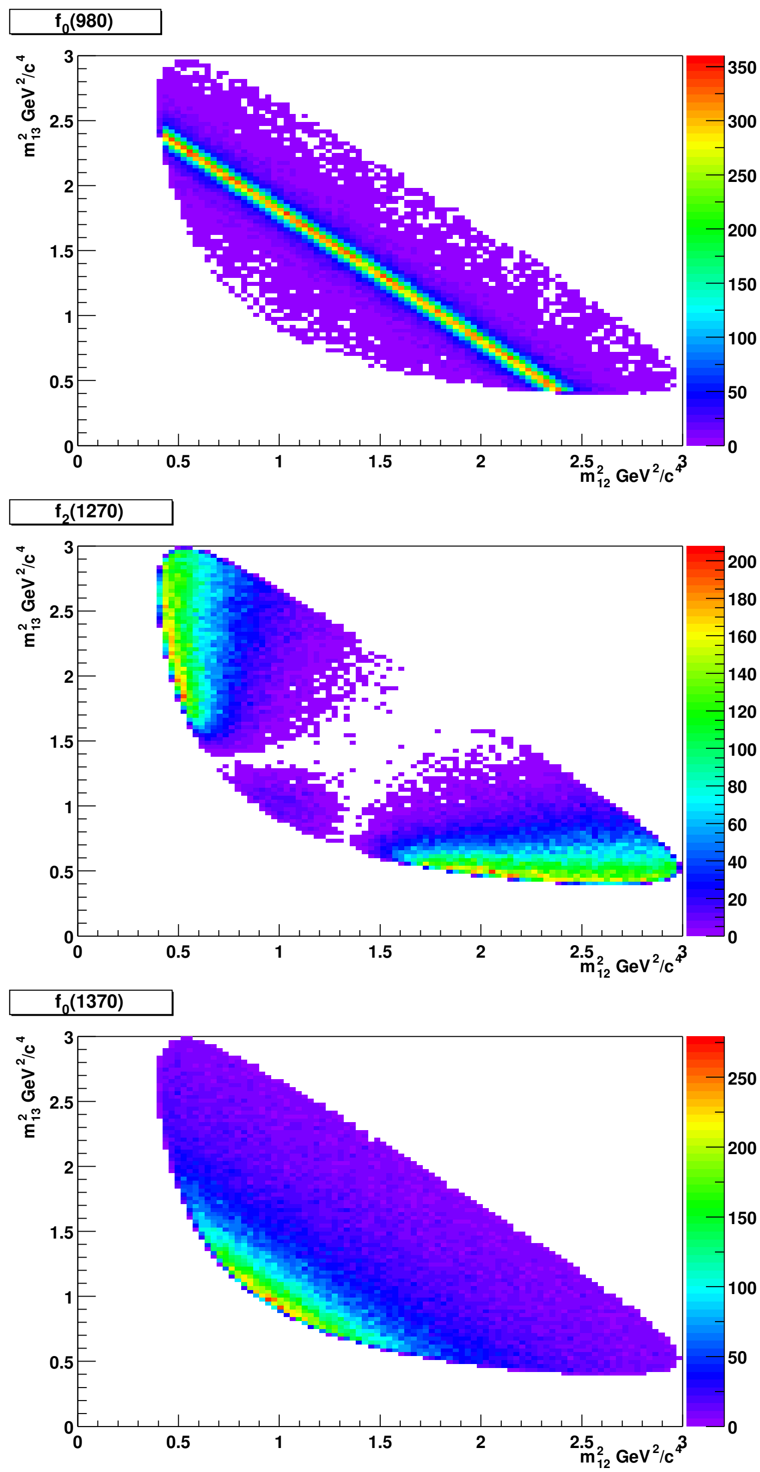

Figure 46: *Monte Carlo distribution of* $(m^2_{K_S\pi^+}, m^2_{K_S\pi^-})$ *for* D^0 *decaying into either* $f_0(980)K_S$ *(top) or* $f_2(1270)K_S$ *(middle) or* $f_0(1370)K_S$ *(bottom)*

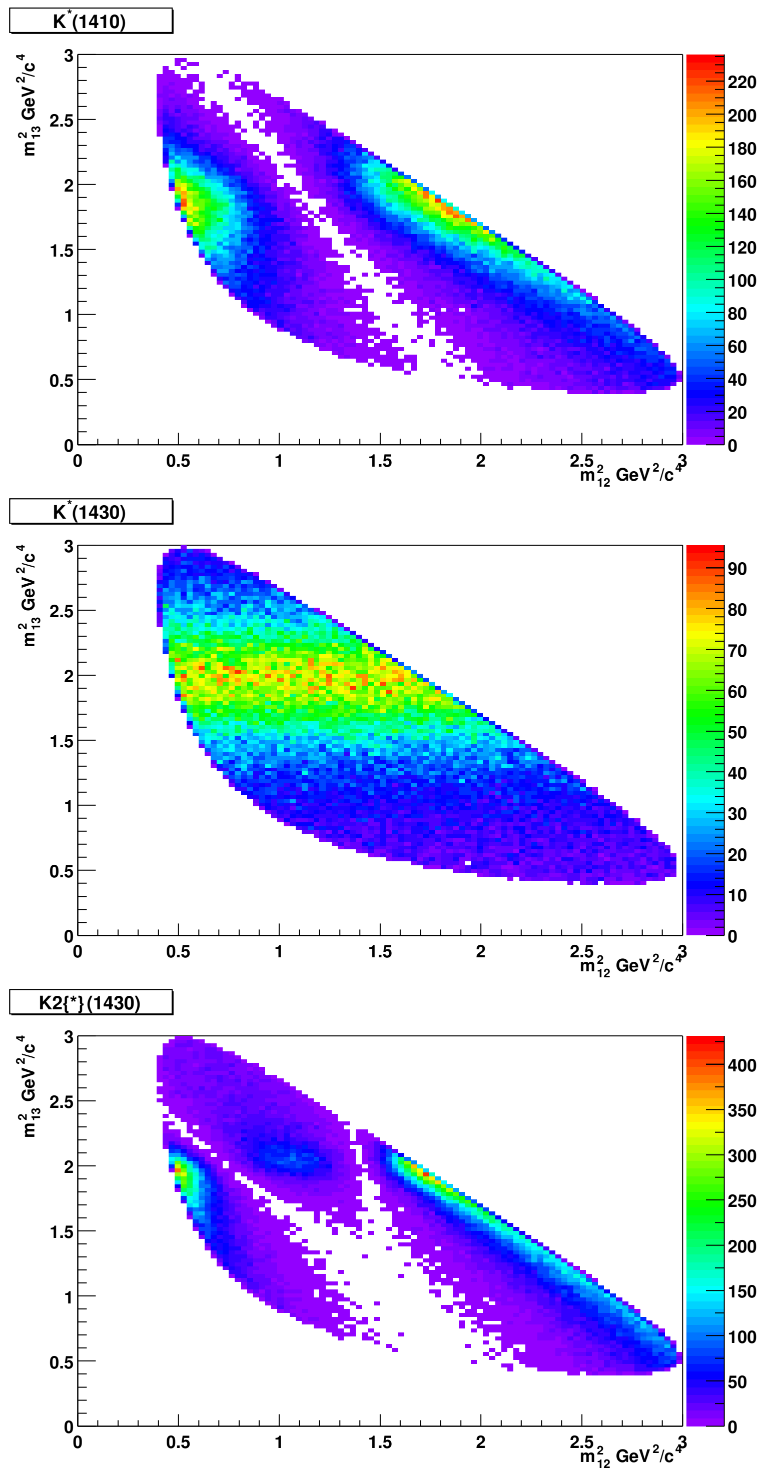

Figure 47: *Monte Carlo distribution of* ($m^2_{K_S\pi^+}$,$m^2_{K_S\pi^-}$) *for* D^0 *decaying into either* $K^{*-}(1410)\pi^+$ *(top) or* $K^{*-}(1430)\pi^+$ *(middle) or* $K_2^{*-}(1430)\pi^+$ *(bottom)*

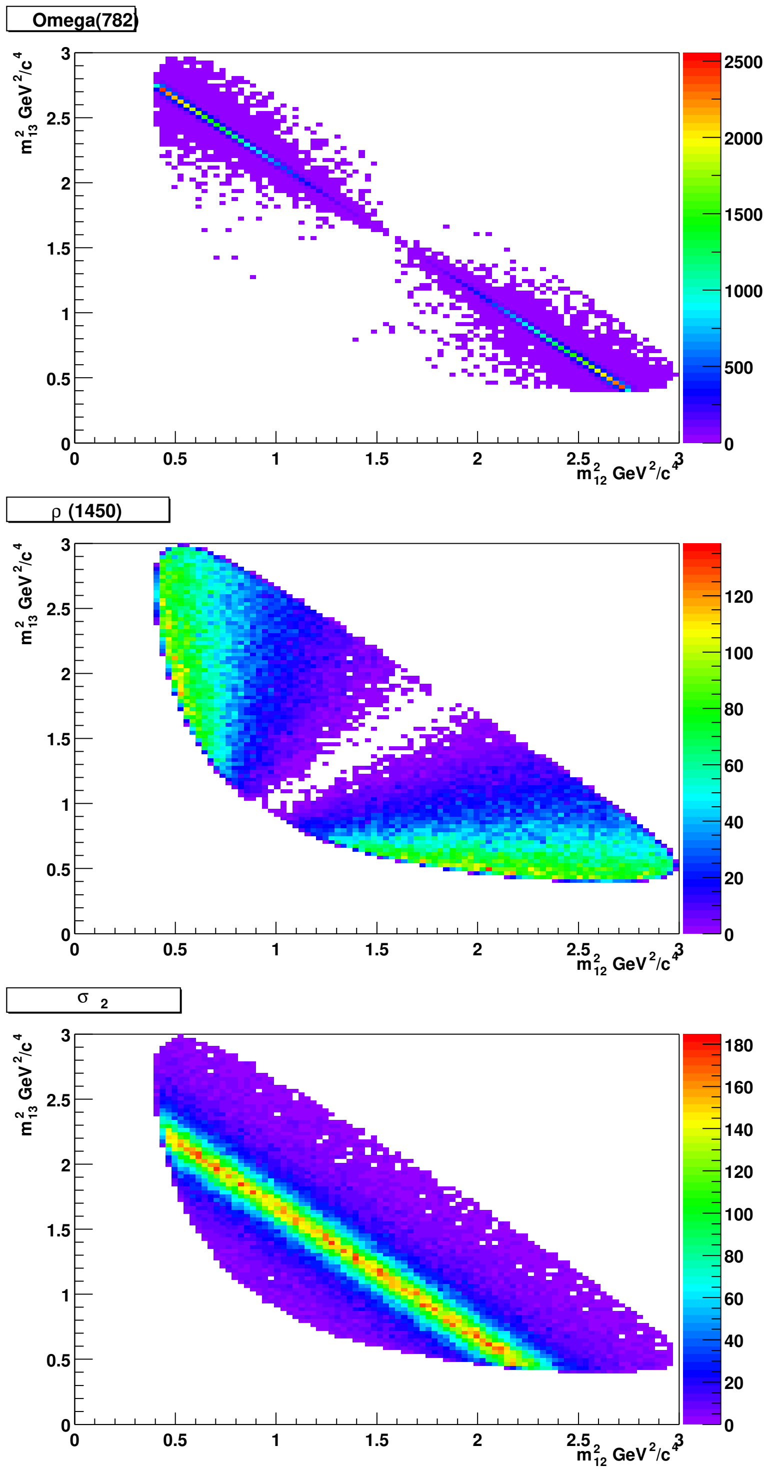

Figure 48: *Monte Carlo distribution of* $(m^2_{K_S\pi^+}, m^2_{K_S\pi^-})$ *for* D^0 *decaying into either* $\omega(782)K_S$ *(top) or* $\rho(1450)K_S$ *(middle) or* $\sigma_2 K_S$ *(bottom)*

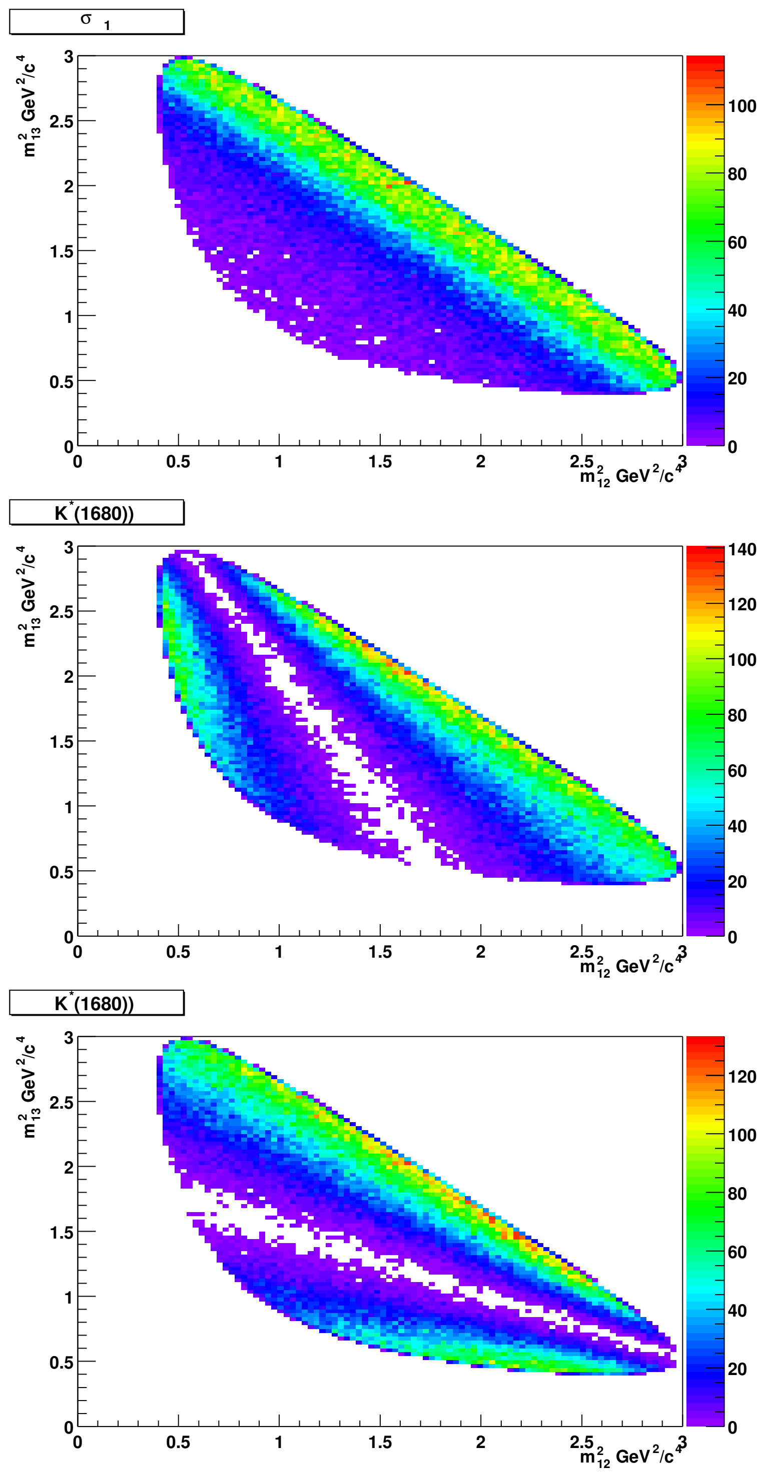

Figure 49: *Monte Carlo distribution of* ($m^2_{K_S\pi^+}$,$m^2_{K_S\pi^-}$) *for* D^0 *decaying into either* $\sigma_1 K_S$ *(top) or* $K^{*-}(1680)\pi^+$ *(middle) or* $K^{*+}(1680)\pi^-$*[Doubly Cabibbo Suppressed decay] (bottom)*

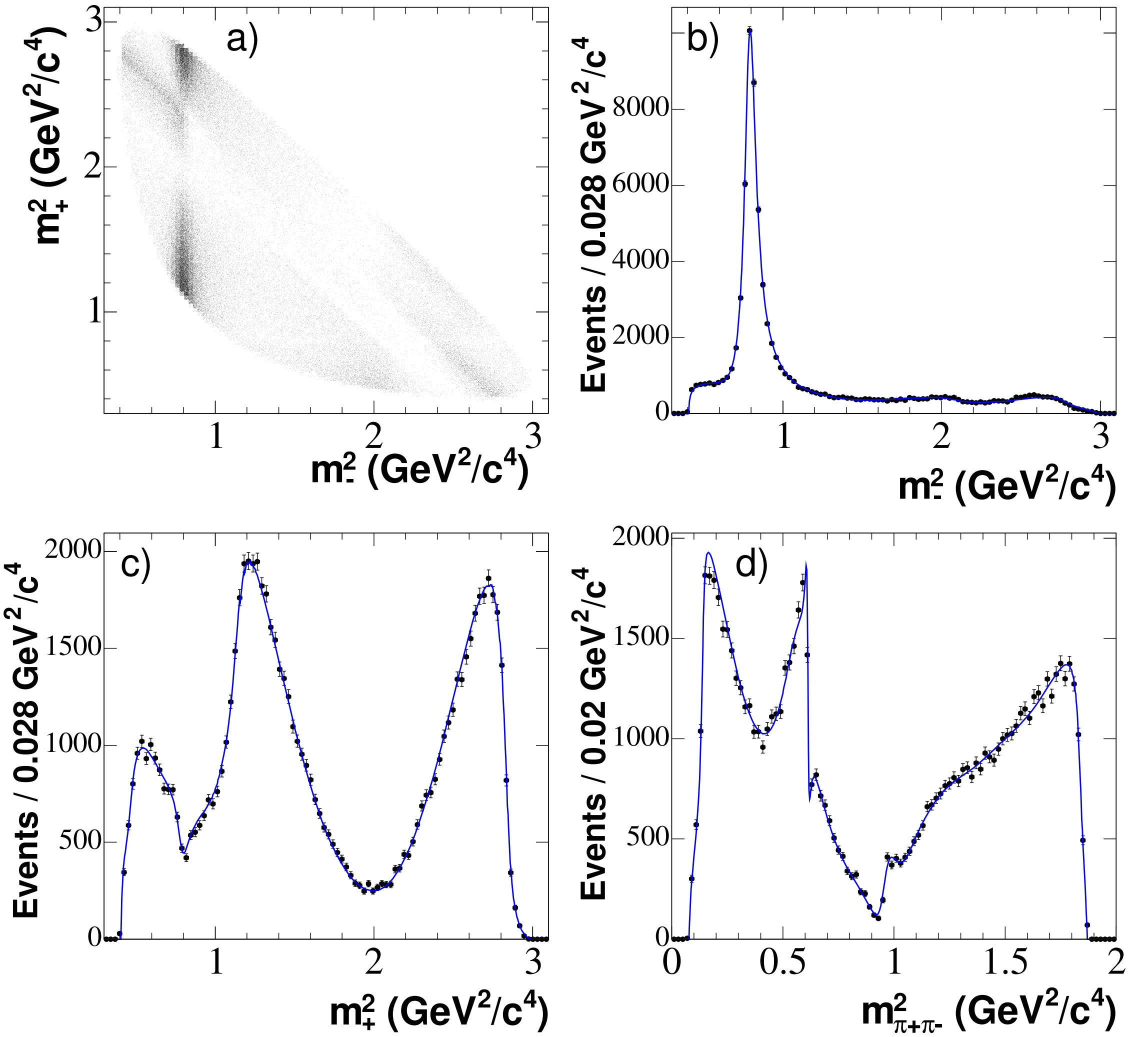

Figure 50: (a) The $D^0 \to K_S^0\pi^-\pi^+$ Dalitz distribution from $D^{*+} \to D^0\pi_s^+$ data events, and projections on (b) m_-^2, (c) m_+^2, and (d) $m_{\pi^+\pi^-}^2$. The curves are the fit projections.

entries for all the bins in the Dalitz plot.

After having found the preferred values for amplitudes and phases, we have also performed a χ^2-scan by varying in turn the masses and the widths of the not very well established scalars σ_1 and σ_2.

The results of the fit (amplitudes and phases) are shown in Table 14 and in Figures 51. We estimated the goodness of fit through a two-dimensional χ^2 test and obtain $\chi^2 = 3824$ for $3054 - 32$ degrees of freedom. The probability of such a χ^2 value is extremely small, which means the model does not describe accurately the Dalitz plane distribution. It has be taken into account this uncertainty in the Dalitz model in the systematic error on the CP fit parameters by extreme variations of the parameterization. It was found the resulting uncertainty on the CP parameters to be relatevely small compared to the statistical error.

With χ^2 scan we have also found preferred values for masses and widths some resonances (see Table 13).

Resonances	mass (GeV/c^2)	width (GeV/c^2)
$K^*(892)$	892.8 $\pm$ 0.24	49.4 $\pm$ 0.2
$\rho^0(770)$	775.1 $\pm$ 0.6	145.7 $\pm$ 1 .0
$f_0(1370)$	1433 $\pm$ 4	173 $\pm$ 5
$\rho(1450)$	1489 $\pm$ 7	219 $\pm$ 25

Table 13: *Summary of the calues of the masses and widths of the resonances used for the fit as obtained from from a χ^2-scan. The error bars are obtained by fixing all the parameters of the fit and floating the mass and the width of the corresponding resonance.*

Resonance	Amplitude	phase (degrees)
$K^*(892)$	1.794 $\pm$ 0.017	130.5 $\pm$ 0.7
$\rho^0(770)$	1 (fixed)	0(fixed)
$K^*(892)$ DCS	0.188 $\pm$ 0.009	311.7 $\pm$ 1.9
$\omega(782)$	0.033 $\pm$ 0.002	109.0 $\pm$ 4.7
$f_0(980)$	0.462 $\pm$ 0.011	203.8 $\pm$ 2.1
$f_0(1370)$	3.093 $\pm$ 0.218	124.7 $\pm$ 2.4
$f_2(1270)$	0.959 $\pm$ 0.036	345.2 $\pm$ 2.9
$K_0^*(1430)$	2.779 $\pm$ 0.064	350.9 $\pm$ 1.4
$K_0^*(1430)$ DCS	0.548 $\pm$ 0.058	32.4 $\pm$ 5.4
$K_2^*(1430)$	0.929 $\pm$ 0.046	309.6 $\pm$ 2.6
$K_2^*(1430)$ DCS	0.073 $\pm$ 0.029	223.6 $\pm$ 33.5
$K^*(1680)$	2.648 $\pm$ 0.20	202.3 $\pm$ 3.6
Non resonant	1.768 $\pm$ 0.262	100.3 $\pm$ 8.3
σ_1	1.067 $\pm$ 0.039	182.6 $\pm$ 2.0
σ_2	0.285 $\pm$ 0.024	151.1 $\pm$ 4.5
$K^*(1410)$	0.390 $\pm$ 0.043	269.7 $\pm$ 7.3
$\rho(1450)$	0.976 $\pm$ 0.082	28.4 $\pm$ 5.9

Table 14: *Summary of the amplitudes and phases of the different components obtained from the fit of Dalitz plot with χ^2 technique using masses and widths from χ^2 scan.*

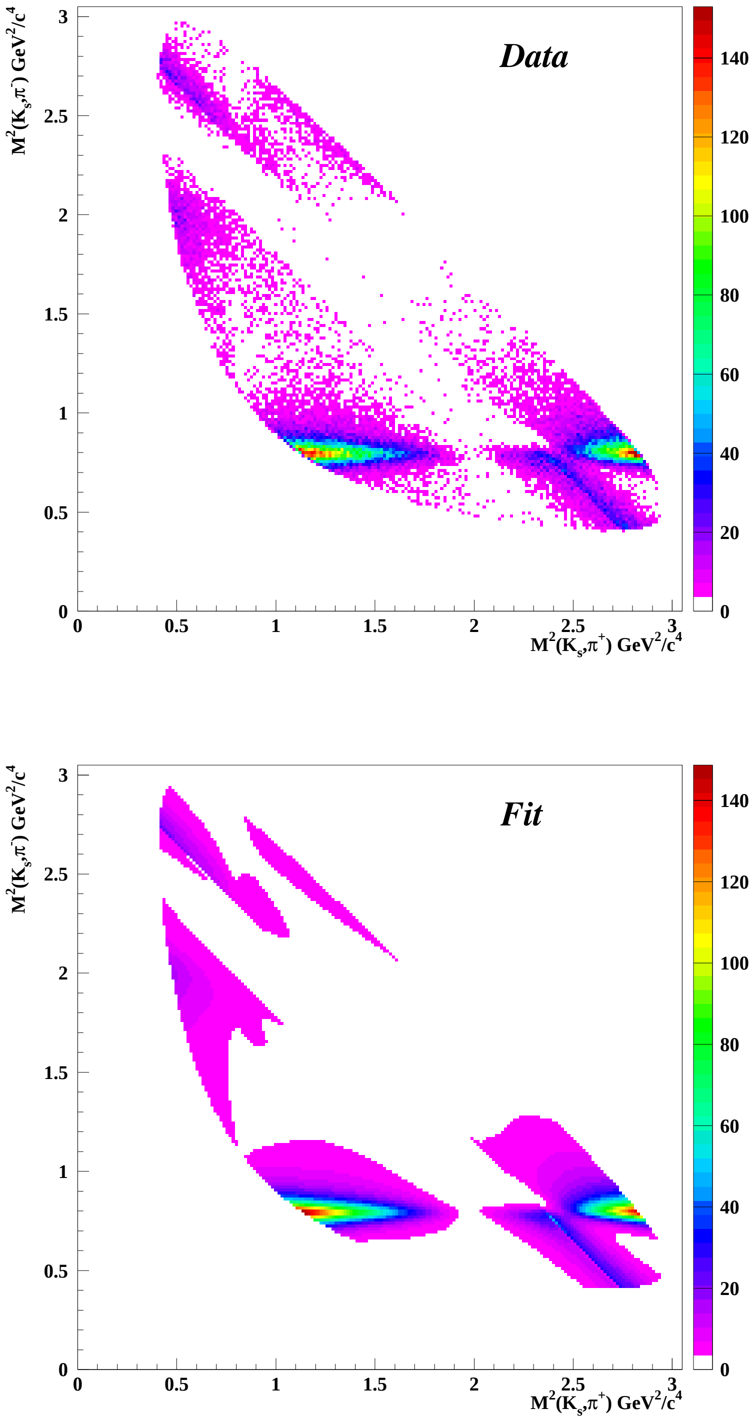

Figure 51: *Result of the χ^2 fit to the $\bar{D}^0 \to K^0\pi^+\pi^-$ Dalitz plot, using the flavour tagged D sample from the continuum. The Dalitz plot for the data (top plot) and the fitted PDF (bottom plot) are shown.*

5 Extraction of the CP parameters from the D^0 Dalitz distribution in $B^\pm \to D^{(*)}K^\pm$ decay

We describe in this section the likelihood definition and strategy used to extract the CP parameters from the D^0 Dalitz analysis. We first describe the generic PDF for a given B and D decay mode. This PDF is then replicated for different B decay modes we have considered in this analysis in order to make a combined fit. The overall fit strategy as well as the validation and sensitivity studies to decide the optimal analysis configuration are also described.

5.1 Likelihood definition

The generic probability density function PDF, distinguishes the following signal/background components:

- **Signal (Sig)**;
- **Continuum (Cont)** background. This is subdivided into two categories:
  - real D^0(**D0**). Here we distinguish between real D^0 mesons combined with a right sign random bachelor track (**RS**, i.e. the D^0 is seen as D^0) or a wrong one (**WS**, i.e. the D^0 is seen as $\overline{D}^0$). This splitting is needed in order to account for the misinterpretation of D^0 decays as $\overline{D}^0$, which is relevant for the Dalitz structure. As the background source are continuum events, this component does not contain CP violation (i.e. r_B=0);
  - fake D^0(**comb**). These are the fake D^0 generated by the combinatoric of the charged tracks. They are almost uniformly distributed in the Dalitz plane. A fit on the data and Monte Carlo simulated events has been used to parametrized their distribution, as described in the following paragraphs.
- $\boldsymbol{B\overline{B}}$ background. This is subdivided into the following categories:
  - $D\pi$ events (**Dh**). It is a source of background which is originated by the misidentification of the charged bachelor track. The high multiplicity of pion respect to the kaon make this background tough to reduce even after having applied stringent particle identification requirement for the kaon hypothesis. This component contains in principle CP violation, it has different r_B[18] and strong phase δ respect to the signal, but the same weak phase γ;
  - Signal wrong sign combination **SigWS**. real D^0's coming from a possibly CP violating channel (like signal) and a combinatorial wrong sign bachelor track from the other B (SigWS, i.e. the D^0 is seen as $\overline{D}^0$). This component has the same CP violation parameters as the signal, but the D^0 is seen as $\overline{D}^0$;

[18] $r_B(D\pi) = \frac{|\mathcal{A}(B^-\to\overline{D}^0\pi^-)|}{|\mathcal{A}(B^-\to D^0\pi^-)|} \simeq \frac{V_{ub}^*V_{cd}}{V_{cb}^*V_{ud}}\frac{1}{3} = 0.007$

- generic $B\overline{B}$ background ($\mathsf{B\overline{B}}$), other than $D\pi$. This includes $D^{(*)0}X$ candidates with either a missing particle or a particle from the other B decay, as well as events with a fake (combinatorial) D^0. This background type contains both peaking and non-peaking components (in $m_{\rm ES}$ and ΔE). The category is itself separated into two subtypes:
  * real D^0 ($\mathsf{D^0}$). As before, we distinguish between real D^0 mesons with a right sign (RS) or a wrong sign (WS) random bachelor track. By definition this category does not contain *CP* violating channels (i.e. r_B=0), which have their own component (SigWS);
  * fake D^0 (comb).

Note that the explicit separation of SigWS from $\mathsf{B\overline{B}}$ is needed since the *CP* violating effects are different. In the case of SigWS the interference effects are as in the signal (with the D^0 seen as $\overline{D}^0$, and viceversa), while in $\mathsf{B\overline{B}}$ the contribution from wrong sign is either non-interfering, or it is different to that of the signal (in case that there are *CP* violating residual channels).

The overall probability density function $\mathcal{P}^\alpha$ can then be written as:

$$\begin{aligned}
\mathcal{P}^\alpha \;\; = \;\; & f_{\mathsf{Sig}}\mathcal{P}^\alpha_{\mathsf{Sig}} + f_{\mathsf{Dh}}\mathcal{P}^\alpha_{\mathsf{Dh}} + f_{\mathsf{SigWS}}\mathcal{P}^{\overline{\alpha}}_{\mathsf{SigWS}} + \\
& f_{\mathsf{Cont}}\left\{(1-R_{\mathsf{Cont}})\mathcal{P}^{\mathsf{comb}}_{\mathsf{Cont}} + R_{\mathsf{Cont}}\left[R^{RS}_{\mathsf{Cont}}\mathcal{P}^\alpha_{\mathsf{Cont}} + (1-R^{RS}_{\mathsf{Cont}})\mathcal{P}^{\overline{\alpha}}_{\mathsf{Cont}}\right]\right\} + \\
& f_{\mathsf{B\overline{B}}}\left\{(1-R_{\mathsf{B\overline{B}}})\mathcal{P}^{\mathsf{comb}}_{\mathsf{B\overline{B}}} + R_{\mathsf{B\overline{B}}}\left[R^{RS}_{\mathsf{B\overline{B}}}\mathcal{P}^\alpha_{\mathsf{B\overline{B}}} + (1-R^{RS}_{\mathsf{B\overline{B}}})\mathcal{P}^{\overline{\alpha}}_{\mathsf{B\overline{B}}}\right]\right\}
\end{aligned} \tag{110}$$

where

- $\alpha = \mathsf{D^0}, \overline{\mathsf{D}}^0$. $\overline{\alpha}$ denotes the *CP* conjugate state of α;
- f_j is the fraction for component $j = \mathsf{Sig}, \mathsf{Cont}, \mathsf{Dh}, \mathsf{SigWS}, \mathsf{B\overline{B}}$;
- R_{Cont} ($R_{\mathsf{B\overline{B}}}$) is the fraction of real $D^0/\overline{D}^0$ in Cont ($\mathsf{B\overline{B}}$) background component;
- $R^{\mathsf{RS}}_{\mathsf{Cont}}$ ($R^{\mathsf{RS}}_{\mathsf{B\overline{B}}}$) is the fraction of right sign $D^0/\overline{D}^0$ in Cont ($\mathsf{B\overline{B}}$) background component;
- $\mathcal{P}^\alpha_j$ is the PDF for component j and real D^0 ($\alpha = \mathsf{D^0}$) or $\overline{D}^0$ ($\alpha = \overline{\mathsf{D}}^0$), while $\mathcal{P}^{\mathsf{comb}}_j$ is the PDF for component j and fake D^0.

In the general PDF definition of Eq. (110), we intentionally omitted explicit dependencies on variables, which are discussed in the following subsections.

5.1.1 Component fractions (yields) and selection PDF parameters

Before any attempt to extract the Dalitz *CP* content, a simpler fit can be performed in order to extract the yields (fractions) of the different signal and background components, as well as many as possible selection PDF shape parameters. We consider the following explicit dependence of the PDF:

$$\mathcal{P}^\alpha_j \;\; \equiv \;\; \mathcal{P}^\alpha_j(m_{\rm ES}, \Delta E, \mathcal{F}) \tag{111}$$

The extraction of the component fractions and selection PDF shapes can be then performed using a regular likelihood function

$$\mathcal{L} \;=\; \prod_{\alpha}\prod_{i=1}^{N_\alpha}\mathcal{P}^{\alpha}(i) \tag{112}$$

where $\mathcal{P}^{\alpha}(i)$ is the total PDF given by Eq. (110) for event i. If one is interested in the yields then an extended likelihood function should be used in order to obtain correctly the errors on the yields,

$$\mathcal{L}_{ext} \;=\; \frac{e^{-\eta}\eta^{N}}{N!}\prod_{\alpha}\prod_{i=1}^{N_\alpha}\mathcal{P}^{\alpha}(i) \tag{113}$$

where $N = N_{\mathsf{D^0}} + N_{\overline{\mathsf{D}}^0}$ is the total number of observed events, and η its expectation value according to Poisson statistics. The yields N_j can be calculated simply as $N_j = \eta f_j$, the fractions verifying $\sum_j f_j = 1$.

The multidimensionality of the PDF has been factorized assuming that all these variables are uncorrelated for all the components. The validity of this assumption has been verified on Monte Carlo simulated events,

$$\mathcal{P}^{\alpha}_{j}(m_{\rm ES},\Delta E,\mathcal{F}) \;=\; \mathcal{P}^{\alpha}_{j}(m_{\rm ES})\mathcal{P}^{\alpha}_{j}(\Delta E)\mathcal{P}^{\alpha}_{j}(\mathcal{F}) \tag{114}$$

and similarly for fake D^0's, $\mathcal{P}^{\mathsf{comb}}_{j}(m_{\rm ES},\Delta E,\mathcal{F})$. The parameterizations assumed for each of the unidimensional PDF's are listed in table 15. It has been verified that for the final set of variables and their cuts used in the final nominal fit (see sections 5.2, 5.3) the correlations are either negligible or have no effect on the measurements.

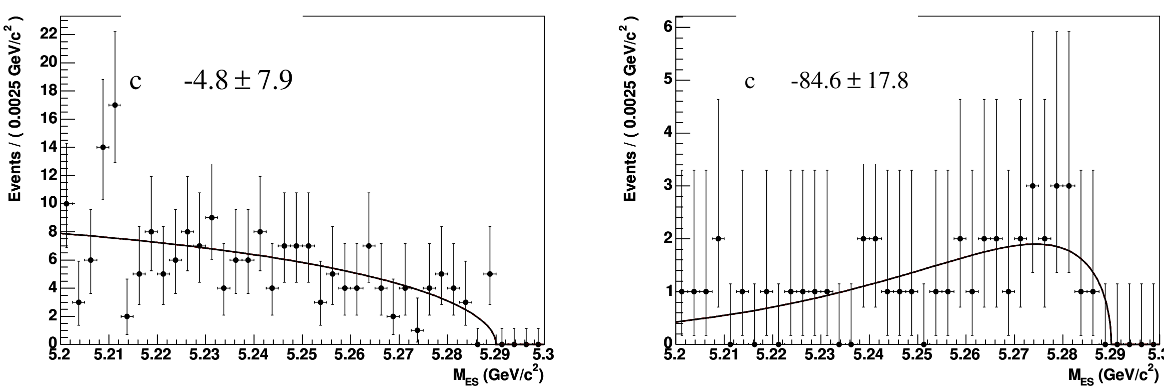

Figure 52: *The $m_{\rm ES}$ distribution for continuum and $B\overline{B}$ background events. The c parameter of the Argus function is quite different for the two background samples. Data are represented by point with error bars, the fit PDF is superimposed.* **Left plot:** *$m_{\rm ES}$ distribution for continuum events.* **Right plot:** *$m_{\rm ES}$ distribution for $B\overline{B}$ events.*

Even if the fisher $\mathcal{F}$ has a greater separation power also the $m_{\rm ES}$ distribution helps in the evaluation of the different background fractions. The $m_{\rm ES}$ distribution is different for

Component	Parameterization
$\mathcal{P}^{\alpha}_{\mathsf{Sig}}(m_{\rm ES})$	Gaussian (G_1)
$\mathcal{P}^{\alpha}_{\mathsf{Cont}}(m_{\rm ES}) = \mathcal{P}^{\mathsf{comb}}_{\mathsf{Cont}}(m_{\rm ES})$	Argus (A_1)
$\mathcal{P}^{\alpha}_{\mathsf{Dh}}(m_{\rm ES})$	Gaussian (G_1)
$\mathcal{P}^{\alpha}_{\mathsf{SigWS}}(m_{\rm ES})$	Gaussian+Argus ($B_1 + A_2$, B_1 has same mean as G_1, f_1)
$\mathcal{P}^{\alpha}_{\mathsf{B\overline{B}}}(m_{\rm ES}) = \mathcal{P}^{\mathsf{comb}}_{\mathsf{B\overline{B}}}(m_{\rm ES})$	Gaussian+Argus ($B_1 + A_2$, B_1 has same mean as G_1, f_2)
$\mathcal{P}^{\alpha}_{\mathsf{Sig}}(\Delta E)$	Gaussian (G_2)
$\mathcal{P}^{\alpha}_{\mathsf{Cont}}(\Delta E) = \mathcal{P}^{\mathsf{comb}}_{\mathsf{Cont}}(\Delta E)$	polynomial ($P1_1$)
$\mathcal{P}^{\alpha}_{\mathsf{Dh}}(\Delta E)$	Option 1: Gaussian (G_2, event-by-event shifted*)
	Option 2: Gaussian (G_3)
$\mathcal{P}^{\alpha}_{\mathsf{SigWS}}(\Delta E)$	Gaussian+polynomial ($G_4 + P2_1$, f_3)
$\mathcal{P}^{\alpha}_{\mathsf{B\overline{B}}}(\Delta E) = \mathcal{P}^{\mathsf{comb}}_{\mathsf{B\overline{B}}}(\Delta E)$	Gaussian+polynomial ($G_4 + P2_2$, f_4)
$\mathcal{P}^{\mathsf{D^0}}_{\mathsf{Sig}}(\mathcal{F})$	double Gaussian ($G_5 + G_6$, f_5)
$\mathcal{P}^{\alpha}_{\mathsf{Cont}}(\mathcal{F}) = \mathcal{P}^{\mathsf{comb}}_{\mathsf{Cont}}(\mathcal{F})$	double Gaussian ($G_7 + G_8$, f_6)
$\mathcal{P}^{\alpha}_{\mathsf{Dh}}(\mathcal{F})$	double Gaussian ($G_5 + G_6$, f_5)
$\mathcal{P}^{\mathsf{D^0}}_{\mathsf{SigWS}}(\mathcal{F})$	double Gaussian ($G_5 + G_6$, f_5)
$\mathcal{P}^{\alpha}_{\mathsf{B\overline{B}}}(\mathcal{F}) = \mathcal{P}^{\mathsf{comb}}_{\mathsf{B\overline{B}}}(\mathcal{F})$	double Gaussian ($G_5 + G_6$, f_5)

Table 15: *Parameterizations for the different unidimensional PDF components. A, G, B, $P1$, $P2$ denote, respectively, Argus, Gaussian, Bifurcated Gaussian, first order and second order polynomial functions. f denote the relative fraction of the first term of the parameters (if more than one are used). Indices denote a given set of different parameters. *See section 5.3. The parameterizations for $\alpha = \mathsf{D^0}$ and $\alpha = \overline{\mathsf{D}}^0$ use the same set of paramaters. The kinematic limit m_0 in the Argus parameterization (see Eq. 84) is fixed to 5.290* GeV/c^2.

Function	Parameters
Gaussian (G_i)	mean=μ_{G_i},width=σ_{G_i}
Argus (A_i)	slope=c_{A_i}, maxArg=m_0
Polynomial 1^{st} order $P1$	slope=$c1_{P1}$
Polynomial 2^{nd} order $P2$	slope=$c1_{P2}$, concavity=$c2_{P2}$

Table 16: *Description of the functions parameters we use to fit $m_{\rm ES}$,ΔE,$\mathcal{F}$. We fit directly from data most of the parameters, fixing the remaining ones from estimates evaluated on Monte Carlo simulated events as showed in Tab. 21.*

continuum and for $B\overline{B}$ events. The continuum events are rather flat in the $m_{\rm ES}$ distribution, while the $B\overline{B}$ are more numerous at high $m_{\rm ES}$ values. The c parameter of the Argus function is different for the two background samples. In Figures 52 are reported the shapes for $B\overline{B}$ simulated events, after all the selection criteria applied. The shapes for $D^0\pi^0$ and $D^0\gamma$ are consistent within the errors and they are assumed to be common in the likelihood fit, while for the D^0K we use independent shape parameters. Both the parameters are left floating in the fit on data for the shapes and the yields.

5.1.2 Dalitz distribution

When the information of the Dalitz plane distribution is added, the explicit dependence of the PDF becomes:

$$\mathcal{P}^{\alpha}_{j} \equiv \mathcal{P}^{\alpha}_{j}(m_{\rm ES}, \Delta E, \mathcal{F})\mathcal{P}^{\alpha}_{j}(s_{12}, s_{13}) \tag{115}$$

where $\mathcal{P}^{\alpha}_{j}(s_{12}, s_{13})$ [19] is the Dalitz plot dependent part of the PDF.
In the current analysis an isobar model has to been used to parameterize the Dalitz structure, as discussed in detail in chapter 4. The PDF for the D^0 Dalitz distribution for the signal events $\mathcal{P}^{\alpha}_{\mathsf{Sig}}(s_{12}, s_{13})$ takes into account the interference between the $b \to u\overline{c}s$ and $b \to c\overline{u}s$ amplitudes. Recalling equation (68) we have $\mathcal{P}^{\alpha,\overline{\alpha}}_{\mathsf{Sig}}(s_{12}, s_{13}) = |M_{-,+}|^2$, that is :

$$\mathcal{P}^{\alpha}_{\mathsf{Sig}}(s_{12}, s_{13}) = |f(s_{12}, s_{13}) + r_B e^{i(\delta-\gamma)} f(s_{13}, s_{12})|^2$$
$$\mathcal{P}^{\overline{\alpha}}_{\mathsf{Sig}}(s_{12}, s_{13}) = |f(s_{13}, s_{12}) + r_B e^{i(\delta+\gamma)} f(s_{12}, s_{13})|^2$$

where the $D^0 \to K^0_S\pi^+\pi^-$ decay amplitude $f(s_{12}, s_{13})$ is kept fixed in the fit as previously determined from the Dalitz analysis of the $D^0 \to K^0_S\pi^+\pi^-$ events from the $D^{*+} \to D^0\pi^+_s$ sample (see chapter 4).

The PDF for fake D^0's, comb, is indicated with $\mathcal{P}^{\mathsf{comb}}_{j}(s_{12}, s_{13})$ and it is expected to be similar to a uniform phase space distribution. The actual parametrization has been fitted on continuum events and on Monte Carlo simulated event for $B\overline{B}$ background, as explained in detail in section 5.1.4.
Note that by definition $\mathcal{P}^{\overline{\alpha}}_{\mathsf{SigWS}}(s_{12}, s_{13}) = \mathcal{P}^{\alpha}_{\mathsf{Sig}}(s_{13}, s_{12})$. $\mathcal{P}^{\alpha}_{j}(s_{12}, s_{13})$ for $j = (\mathsf{Sig}, \mathsf{Dh})$ contain the *CP* violating terms (i.e. $r_B, \gamma \neq 0$), while $\mathcal{P}^{\alpha}_{j}(s_{12}, s_{13})$ for $j = (\mathsf{Cont}, \mathsf{B\overline{B}})$ and $\mathcal{P}^{\mathsf{comb}}_{j}(s_{12}, s_{13})$ do not contain *CP* violating terms (i.e. r_B=0). An independent set of *CP*-violation parameters has been considered for $j = \mathsf{B\overline{B}}$ (by default fixed to zero) in order to study systematic errors induced by residual *CP* violating channels contributing to the $\mathsf{B\overline{B}}$ background. Either a regular likelihood as given in Eq. (112) or an extended extended likelihood as given in Eq. (113), can be used to extract the Dalitz plot information. The two possibilities are available in the fitter, but the extendend version of the likelihood has been used for the final results. The construction of the specific Dalitz model used in this analysis is discussed in detail in section 4.

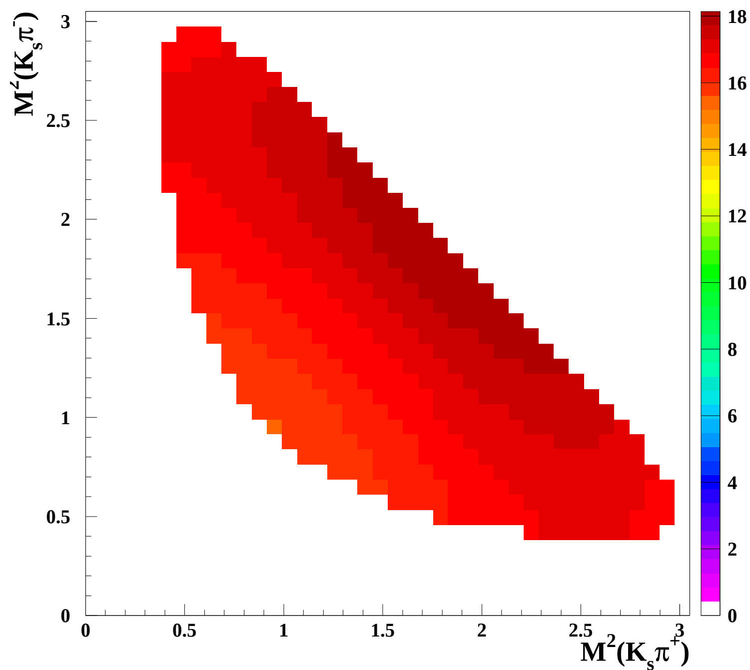

1

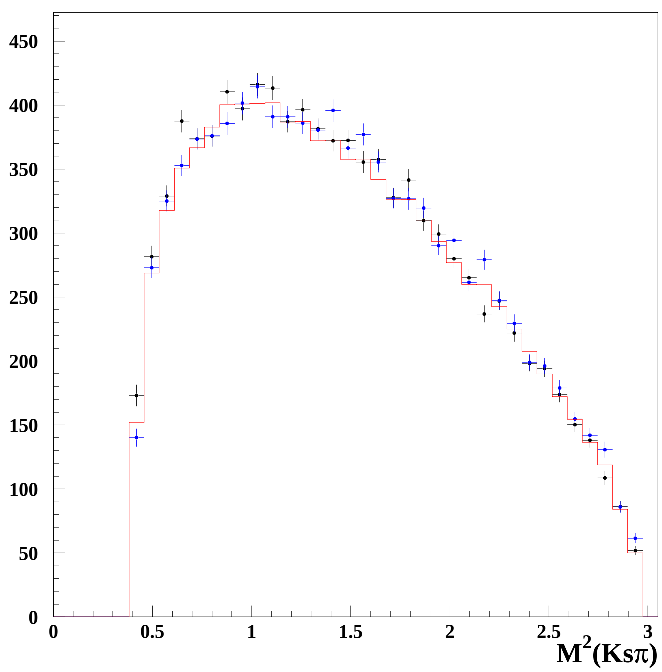

Figure 53: *Top: Fitted efficiency over the Dalitz* $(K_s\pi^+)$ *vs* $(K_s\pi^-)$. *The color code indicates the value (in percent) of the fitted efficiency. This is taken from high statistics* $B^- \to D^0\pi^-$ *signal Monte Carlo. Bottom: Efficiency fits for* $(K_s\pi^+)$ *(blue points) and* $(K_s\pi^-)$ *(black points). Numbers in the y-axis correspond to the efficiency summed over* $m^2(K_s\pi^-)$ *(blue points) and* $m^2(K_s\pi^+)$ *(black points). The line corresponds to the fit.*

5.1.3 Efficiency over the Dalitz plot

The efficiency on the signal events over the Dalitz plot ($m^2(K_s\pi^+) \equiv x$ *vs* $m^2(K_s\pi^-) \equiv y$) is given in the Figures 53. These reconstructed invariant masses have been calculated using the D^0 mass kinematical constraint. The Dalitz plot was divided in 40 bins and the efficiency has been fitted with a third-order polynomial function and considering the symmetry of the Dalitz plot:
$eff(x,y) = a_0\ [1 + a_1\ (x+y) + a_2\ (x^2+y^2+xy) + a_3\ (x^3+y^3+x^2y+xy^2)]$.
The values and the errors for these parameters are given in Table 17 and the fit is shown in Figure 53. It has been checked that the shape of the efficiency correction of Figure 53 does not depend upon the discriminating variables used in the Likelihood fit (Fisher and $m_{\rm ES}$).

	a_0	a_1	a_2	a_3
Parameters	0.204 ± 0.054	$-0.346^{+0.242}_{-0.142}$	$0.200^{+0.053}_{-0.088}$	$-0.035^{+0.013}_{-0.008}$

Table 17: *The values and the errors for the parameters of the third-order polynomial function obtained from the binned χ^2 fit to the efficiency on the signal $B^- \to D^0K^-$ Monte Carlo events over the Dalitz plot (($K_s\pi^+$) vs ($K_s\pi^-$)).*

Alternatively, we also used an unbinned likelihood method to fit to the 3rd order polynomial parameterization, removing dependencies on the binning of the Dalitz plot. The results of the fits to the $B^- \to D^{(*)0}K^-$ samples are given in table 18. The coefficients for the three subsamples, $B \to D^0K$, $B \to (D^0\pi^0)K$ and $B \to (D^0\gamma)K$, are consistent within statistical errors, therefore for the final CP fit we take the parameterization by combining all modes (also shown in the table). There is also good agreement between the fit results for the $B \to D^0K$ sample obtained with this method and those from the χ^2 fit (table 17).

Channel	a_0	a_1	a_2	a_3
$B \to D^0K$	1	-0.382 ± 0.103	0.197 ± 0.040	-0.032 ± 0.006
$B \to (D^0\pi^0)K$	1	0.261 ± 0.319	0.010 ± 0.108	-0.014 ± 0.015
$B \to (D^0\gamma)K$	1	0.041 ± 0.290	0.096 ± 0.095	-0.029 ± 0.012
All	1	-0.176 ± 0.104	0.143 ± 0.037	-0.028 ± 0.005

Table 18: *The values and the errors for the parameters of the third-order polynomial function obtained from the unbinned likelihood fit to the efficiency on the signal $B^- \to D^{(*)0}K^-$ Monte Carlo events over the Dalitz plot (($K_s\pi^+$) vs ($K_s\pi^-$)). The resulting coefficients for each decay mode show a good agreement, therefore the coefficients obtained by combining all the modes are used in the final fit.*

5.1.4 Background Dalitz shape

The parametrization of the PDF of the background in the Dalitz plane has been taken into account in the likelihood, see Eq. 110. The Dalitz distributions for the various backgrounds

[19] s_{12} and s_{13} are the squared invariant masses of the particle combinations 12 and 13.

can be extracted directly from data for continuum events or from Monte Carlo simulated events for the $B\overline{B}$ events. We have extracted from off-resonance data events the Dalitz shape for continuum $q\bar{q}$ selecting the D^0 mass sidebands in order to exclude the real D^0 (we request $M_{D^0} < 1.85$ GeV/c^2 or $M_{D^0} > 1.88$ GeV/c^2). For generic $B\bar{B}$ we use Monte Carlo events with no real D^0 (events with real D^0 were excluded using MC truth information). The selection criteria are identical to those used for the final sample, except the ΔE cut which we have relaxed to have larger statistics.
For all the decay modes (i.e. D^0K, $D^0\pi^0$, $D^0\gamma$), both the distributions ($q\bar{q}$ and $B\bar{B}$) have been fitted. For the $q\bar{q}$ distribution for the $D^0\pi^0$, $D^0\gamma$ we have considered to consider a common background distribution in order to have a consistent statics to perform the fit on off-resonance data. For the fit we have used a symmetric second order polynomial function:

$$a_0 + a_1(x + y) + a_2(x^2 + y^2 + xy) \tag{116}$$

with $m^2(K_s\pi^+) \equiv x$ and $m^2(K_s\pi^-) \equiv y$. The values of the parameters are given in Table 19.

Parameters	a_0	a_1	a_2
$B\bar{B}_{D^0K}$	$1.759 \pm .0.033$	-1.065 ± 0.012	0.2409 ± 0.0037
$B\bar{B}_{D^0\pi^0}$	1.4 ± 0.4	-0.8 ± 0.3	0.18 ± 0.06
$B\bar{B}_{D^0\gamma}$	6.80 ± 0.07	-3.93 ± 0.03	0.85 ± 0.01
$q\bar{q}_{D^0K}$	1.993 ± 0.054	-1.275 ± 0.020	0.344 ± 0.008
$q\bar{q}_{D^0\gamma+D^0\pi^0}$	0.52 ± 0.10	-0.27 ± 0.06	0.09 ± 0.01

Table 19: *The values and the errors for the parameters of the symmetric second-order polynomial function used for fitting the the distribution of the $q\bar{q}$ or $B\bar{B}$ over the Dalitz plots $((K_s\pi^+)$ vs $(K_s\pi^-))$.*

As an example, the fit result for $q\bar{q}_{D^0K}$ is shown on the bottom plot of Figure 54 and the projections are shown in Figure 55.

For the $B\overline{B}$ Monte Carlo the true D^0 candidates are also removed and the $m^2(K_S, \pi^{\pm})$ versus $m^2(K_S, \pi^{\mp})$ distribution is made. The distribution is shown on top of Figure 56 for $B\overline{B}_{D^0K}$ events. The fitted parameters of the second order polynomial are given in Table 19. The fit result is shown on the bottom plot of Figure 56 and the projections are shown in Figure 57.

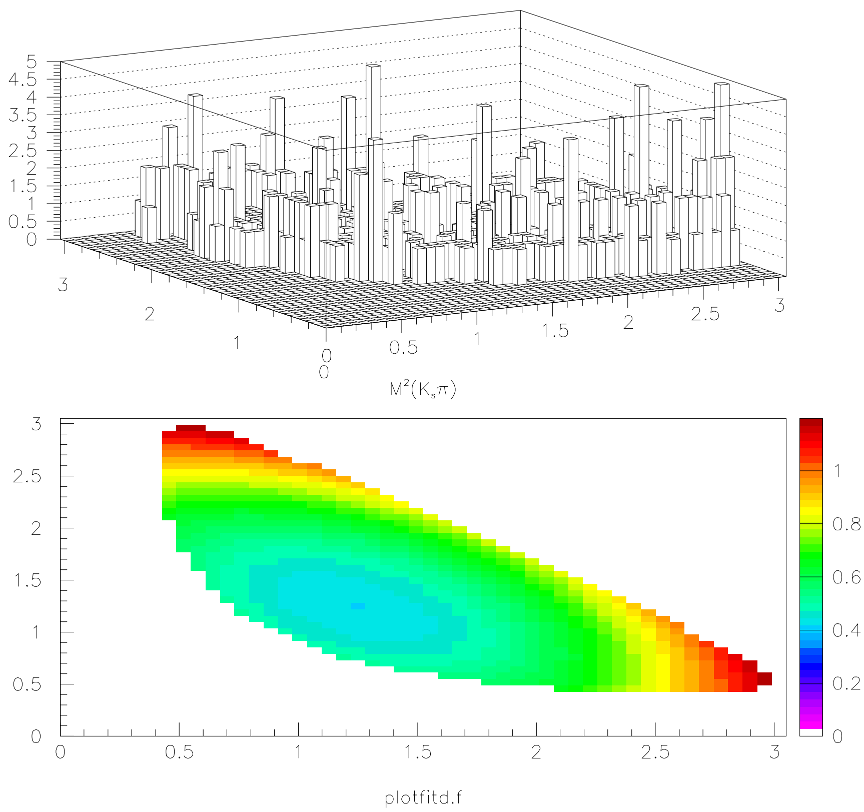

Figure 54: *Distributions of $m^2(K_S, \pi^+)$ versus $m^2(K_S, \pi^-)$ for the off-resonance D^0K data events on the top plot. The bottom plot shows the parametrizations for off-resonance D^0K events built from the parameters given in Table 19.*

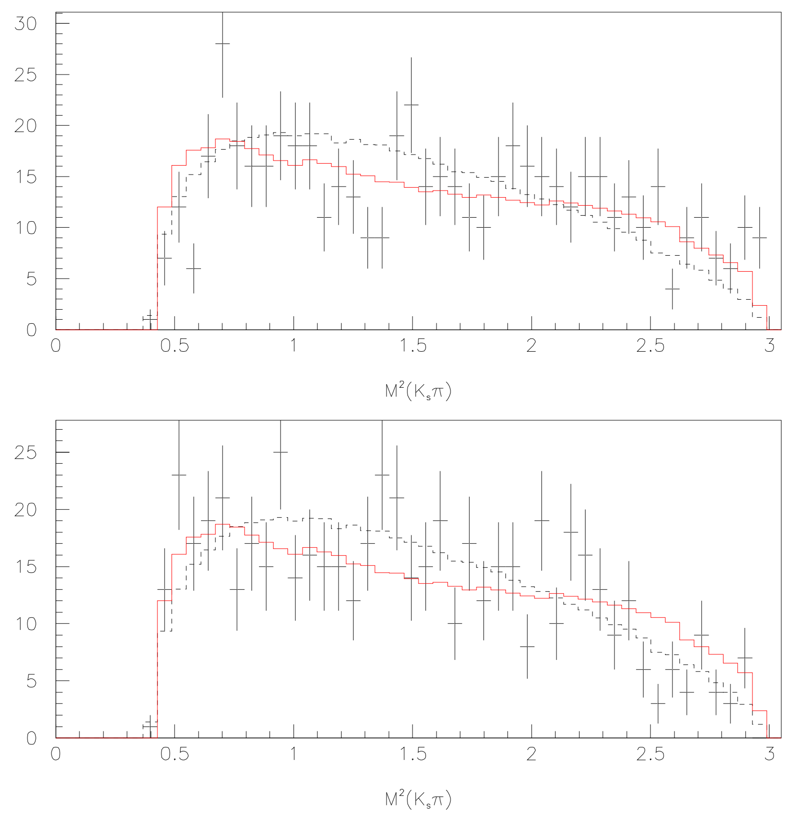

Figure 55: *Distributions of* $m^2(K_S, \pi^{\pm})$ *for* $B^{\pm}$ *candidates (top plot) and* $m^2(K_S, \pi^{\mp})$ *for* $B^{\pm}$ *candidates (bottom plot). The points represent the off-resonance* D^0K *data events, the histogram the result of the second order polynomial fit and the dashed histogram the projection of an uniform distribution.*

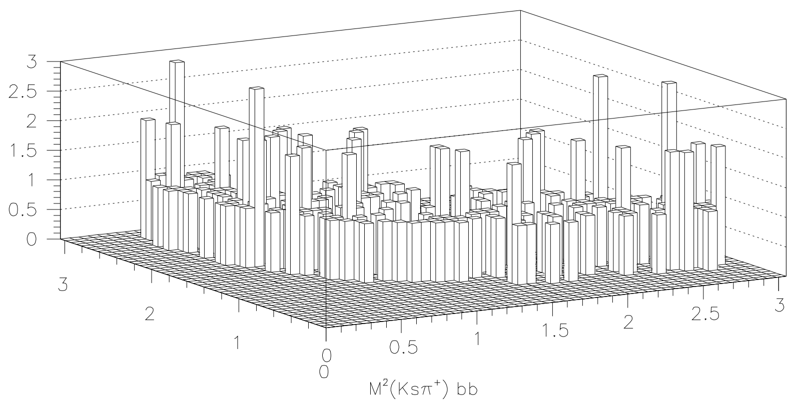

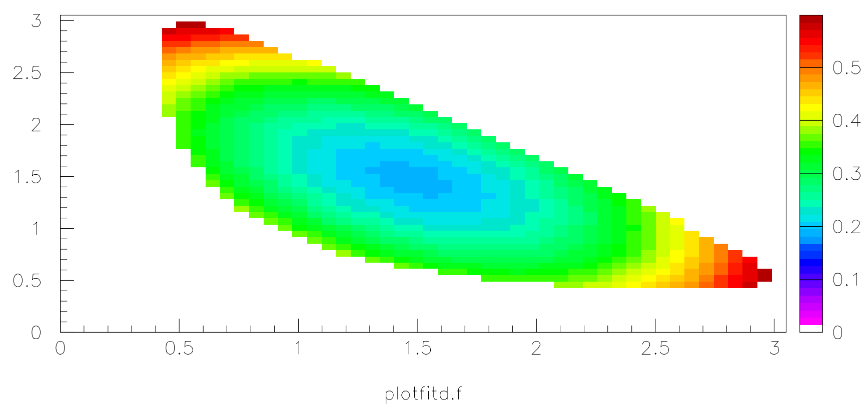

Figure 56: *Distributions of* $m^2(K_S, \pi^+)$ *versus* $m^2(K_S, \pi^-)$ *for the* $B\bar{B}$ *Monte Carlo for* D^0K *events on the top plot. The bottom plot shows the parametrizations for* $B\bar{B}$ D^0K *events built from the parameters given in Table 19.*

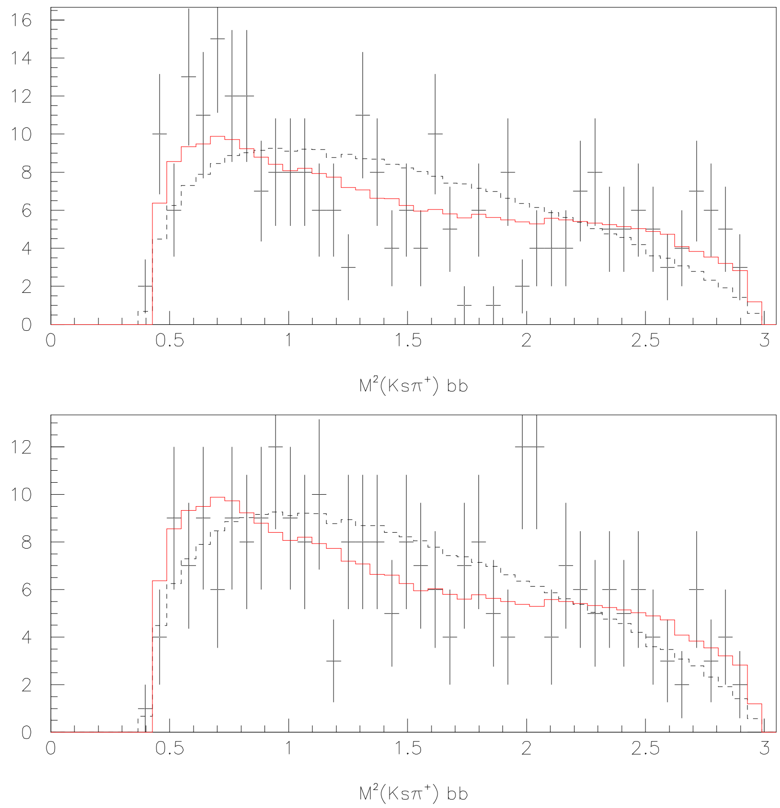

Figure 57: *Distributions of $m^2(K_S, \pi^\pm)$ for $B^\pm$ candidates (top plot) and $m^2(K_S, \pi^\mp)$ for $B^\pm$ candidates (bottom plot). The points represent the $B\bar{B}$ Monte Carlo D^0K events, the histogram the result of the second order polynomial fit and the dashed histogram the projection of an uniform distribution.*

5.1.5 PDF normalization issues

The normalization of the PDF when it contains the Dalitz part has to be performed numerically since no analytical evaluation is possible. Two different methods have been implemented, the first approach divides the full Dalitz plot into a grid of $N_{grid} \times N_{grid}$ cells, and the second method uses a Vegas Monte Carlo integration [45] with N_{Vegas} events. The nominal fit is performed using typically $N_{grid} = 200$, which corresponds to 3.5 MeV precision on the $K^0_S\pi^+$ and $K^0_S\pi^-$ masses. Cross-checks are performed by increasing the number of cells as well as using Vegas integration with $N_{Vegas} \approx 10^7$. A systematic error is evaluated to take into account the limited numerical precision (see section 6.2.6).

A second important issue related the PDF normalization is the sensitivity to a possible charge asymmetry between B^+ and B^-. As the sensitivity to the CP paramaters in this analysis comes exclusively from the interference between the $b \to u\bar{c}s$ and $b \to c\bar{u}s$ amplitudes and the combination of B^+ and B^- measurements. An independent normalization of the

PDF for B^+ and B^- does not reduce the physics sensitivity while it makes the measurement completely transparent to potential charge asymmetries. This has been checked by fitting a toy Monte Carlo sample of B^- only events (i.e. a sample with 100% charge asymmetry), where the fitted phases were $\theta_- = \delta - \gamma$ and $\theta_+ = \delta + \gamma$. When the PDF was normalized separately for B^+ and B^-, the statistical uncertainty returned by the fit for θ_+ was of about 360°, as expected since there are no B^+ events in the sample, while for θ_- it was identical to the case when there is no charge asymmetry (fit to the same sample of B^- events together with a sample with exactly the same number of B^+ events). [20] However, when the PDF was normalized for B^+ and B^- together, the error reported from the fit for θ_+ was similar to that of θ_-, and both angles were cleary biased. This simple exercise proves that the independent normalization of the Dalitz PDF for B^+ and B^- keeps all the *CP* sensitivity while avoid biases from charge asymmetries.

5.2 Nominal fit strategy

In order to minimize the systematic errors we want to extract from the data the maximum possible amount of informations: the Dalitz distributions for the various likelihood components, the sample composition and the discriminant variable shapes. In the following we describe the analysis strategy which we have adopted and we discuss some important validatation test.

Step 1: Selection PDF, shapes and yields. We perform a fit to the yields of the various likelihood components Sig, Cont, $\mathsf{B\overline{B}}$, Dh, with the "optimal" set of discriminant variables, $(m_{\rm ES}, \Delta E, \mathcal{F})$. The component SigWS has been fixed to zero since a study on a large sample of signal Monte Carlo simulated events has demonstrated that the contamination of that kind of events is completely negligible.

We extracted as many as possible parameters from the fit to the data themselves and fixing all the others to Monte Carlo estimates, see Tables 21 and 22. We have considered to include in the likelihood function also the invariant mass of the D^0 m_D, after having applied a tight kaon PID (as described in sections 3.4 and 3.5). We decided to exclude the variable m_D from the likelihood, after applying a tight cut at 2 sigma of the D mass, in order to avoid unsuitable correlations with the other discriminant variables. The nominal yields fit is performed simultaneously to the D^0K, $(D^0\pi^0)K$, $(D^0\gamma)K$, $D^0\pi$, $(D^0\pi^0)\pi$ and $(D^0\gamma)\pi$ samples in the ΔE region $[-80, 120]$ ($[20, 80]$) MeV for DK ($D\pi$) samples. In order to get reliable error estimates, the yields are not constrained to take positive values. For the $D\pi$ samples a loose kaon PID veto is applied to remove contamination from kaon sample and to insure that the samples are mutually exclusive, see sections 3.4 and 3.5.

The signal, continuum and $B\overline{B}$ shape parameters for the ($m_{\rm ES}$,ΔE,$\mathcal{F}$) variables (see Table 15) of each $D^{(*)}K$ sample are assumed to be the same as for its $D^{(*)}\pi$ relative control sample, but are different among the different $D^{(*)}K$ (i.e. D^0K, $(D^0\pi^0)K$, and $(D^0\gamma)K$) samples, with two exceptions:

[20] These fits were performed actually assuming a different r_B for B^- and B^+.

- First, in the Monte Carlo simulation it is found that the Argus $B\overline{B}$ parameter for $D^{(*)}K$ and $D^{(*)}\pi$ samples are significantly different, therefore they are assumed to be different. Due to the small amount of $B\overline{B}$ contamination these parameters are fixed to the values estimated from Monte Carlo in the ΔE signal region, $[-30, 30]$ and $[20, 80]$ MeV for $D^{(*)}K$ and $D^{(*)}\pi$ samples. For $D^{(*)}K$ samples we consider the ΔE signal range rather than the full range to take into account the dependence of the combinatorial $B\overline{B}$ background shape with the ΔE cut, since the final fit for the CP parameters is performed in the signal ΔE region (as described below). The effect of chosing these values rather than those of the full ΔE range has a negligible effect in the determination of the other shape parameters.
- The second exception is due to the presence, in the $D^{(*)}\pi$ samples only, of $B\overline{B}$ peaking background in the $m_{\rm ES}$ variable on top of the Argus combinatorial shape. According to the Monte Carlo simulation the fraction of this type of background with respect to the combinatorial $B\overline{B}$ is about 40%, with a width around 3.4 MeV. Therefore, in the nominal fit and only for $D^{(*)}\pi$ samples we add a Gaussian to the $B\overline{B}$ background component with a width fixed to 3.4 MeV, allowing to vary the fraction since ΔE provides a handle to separate it.

The fisher $\mathcal{F}$ is a useful tool for discriminating $B\overline{B}$ events from continuum events. The $\mathcal{F}$ distribution for different B decays is very similar; we assumed to be common to all B decay modes considered [21] after checking its consistency among the different samples in the Monte Carlo simulation.

The yields for all the different samples are taken as independent and are floated simultaneously. This also includes the continuum and $B\overline{B}$ yields since the Fisher discriminant provides some separation power. As an example, we have considered the events with $m_{\rm ES} < 5.272$ MeV and we have fit for the relative fraction of continuum events respect to $B\overline{B}$ once we have fixed the shape of the Fisher discriminant. The $m_{\rm ES}$ variable determines the fraction of signal while the Fisher discriminant determines the relative background fractions for continuum and $B\overline{B}$ background events. Figure 58 shows the fit for the $(D^0\gamma)K$ sample, where the fraction $f_{\sf Cont} = 0.80 \pm 0.12$ from data is compatible within the error with the MC expectation $f_{\sf Cont} = 0.86 \pm 0.01$. In this way all the yields and shape parameters are directly extracted $D^{(*)}K$ and $D^{(*)}\pi$ data. Extensive toy Monte Carlo studies have been performed to validate this fitting procedure.

Step 2: Determination of the Dalitz model which is described in section 4.

Step 3: Dalitz fit to extract the *CP* parameters Once the shape parameters and yields are extracted from data, as well as the Dalitz model, we can perform the fit to the D^0 Dalitz distribution to extract the CP parameters. Different basis of CP parameters can been adopted, we list below the two basis we have considered:

- **polar variables $\boldsymbol{r_B, \gamma, \delta}$** The polar variables have the advantage the fit returns directly the CP violating parameters with the corresponding errors. The disad-

[21] i.e. The $\mathcal{F}$ distribution is assumed to be identical for (Sig) $B^- \to D^{(*)}K^-$, (Dh) $B^- \to D^{(*)}\pi^-$, and generic $\mathsf{B\overline{B}}$ background.

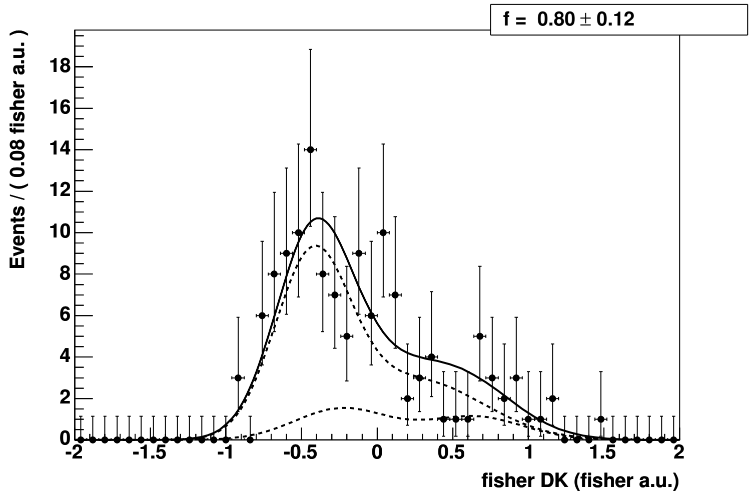

Figure 58: *The Fisher distribution for the background events, in the $(D^0\gamma)K$ decay mode, selected with all the final cuts but $m_{\rm ES} < 5.272$ MeV. The Fisher shapes are fixed and we fit for the relative contribution of background continuum respect to the $B\overline{B}$ events. The points represent data, the continous line is the PDF and the dashed lines are the PDF components for continuum (top) and $B\overline{B}$ events (bottom).*

vantage is the large non-gaussian behaviour of the errors, due basically to the physic boundary on the r_B parameters, $r_B > 0$.

- **cartesian variables $\boldsymbol{x_\pm, y_\pm}$** The cartesian variables, as we will discuss in detail in section 6.1.1, have no physic boundaries, therefore the errors are well behaving:

$$\begin{aligned} x_\pm &\equiv \mathrm{Re}(r_{B\pm}e^{i\theta_\pm}) = r_{B\pm}\cos\theta_\pm \\ y_\pm &\equiv \mathrm{Im}(r_{B\pm}e^{i\theta_\pm}) = r_{B\pm}\sin\theta_\pm \end{aligned} \tag{117}$$

with $\theta_\pm = \delta \pm \gamma$. The only apparent disadvantage is the introduction of a further variable in the *CP* fit, which actually it has been demonstrated it does not reduce to sensitivity to *CP* violation. After a detailed study of the non-gaussianity of the errors with a large number of pseudo-experiments lead us to decide to use the cartesian variables in the final *CP* fit.

The fit for the *CP* parameters is performed simultaneously to the DK and $D^{(*)}K$ sample. The parameters δ and r_B are in principle different for the $B^- \to D^0K^-$and $B^- \to D^{*0}K^-$, therefore we introduce the strong phase δ^*, and the amplitude ratio r^*_B for $B^- \to D^{*0}K^-$ decay. [22] The weak phase γ is the same for the two decays. The $D^0\pi^0$ and $D^0\gamma$ samples have the same r^*_B and also the relative phase between $b \to u\overline{c}s$ and $b \to c\overline{u}d$ decay amplitudes is the same:

$$\frac{\mathcal{A}(B^- \to \overline{D}^{*0}K^-)\mathcal{A}(\overline{D}^{*0} \to \overline{D}^0(\pi^0,\gamma))}{\mathcal{A}(B^- \to D^{*0}K^-)\mathcal{A}(D^{*0} \to D^0(\pi^0,\gamma))} = \frac{\mathcal{A}(B^- \to \overline{D}^{*0}K^-)}{\mathcal{A}(B^- \to D^{*0}K^-)} = r^*_b e^{i\delta^*} \tag{118}$$

[22] We have consequently introduced the cartesian variables $x^*_\pm, y^*_\pm$ for the $B^- \to D^{*0}K^-$decays

The only assumption used in equation (118) is the conservation of *CP* symmetry in the strong and electromagnetic interactions. Finally, it can be demonstrated that in the PDF for the signal Dalitz distribution we need to take into account an effective phase shift of 180° between the $(D^0\pi^0)K$ and the $(D^0\gamma)K$ [46]. The demostration basis on the conservation of the angular momentum and parity in the D^{*0} strong-electromagnetic decay. Therefore the signal Dalitz PDF for $B^{\pm}$ can be written as (assuming no *CP* asymmetry in D decays):

$$\begin{aligned} \mathcal{P}^{\alpha}_{\mathsf{Sig}}(s_{12},s_{13}) &= |f(s_{12},s_{13}) + \kappa r_B^{(*)} e^{i(\delta^{(*)}-\gamma)} f(s_{13},s_{12})|^2 \\ \mathcal{P}^{\overline{\alpha}}_{\mathsf{Sig}}(s_{12},s_{13}) &= |f(s_{13},s_{12}) + \kappa r_B^{(*)} e^{i(\delta^{(*)}+\gamma)} f(s_{12},s_{13})|^2 \end{aligned} \tag{119}$$

The factor κ, which takes the value +1 for the decay modes D^0K, $(D^0\pi^0)K$ and the value −1 for the $(D^0\gamma)K$ decay mode.

The *CP* fit is performed to the D^0K, $(D^0\pi^0)K$ and $(D^0\gamma)K$ samples in the ΔE signal region range $[-30, 30]$ MeV to reduce background contributions, especially from $D^0\pi$, $(D^0\pi^0)\pi$, and $(D^0\gamma)\pi$ events. The impact of fixing shapes on the *CP* violating parameters is small and it has been included in the systematic uncertainties. The fractions of real D^0's and right sign D^0's in both the Cont and $\mathsf{B\overline{B}}$ background components are fixed to the estimates found in sections 3.4 and 3.5. In the case of the fraction of real D^0's we take the estimate from data obtained assuming that there is no contribution from $B\overline{B}$ background. The additional input to the *CP* fit are the efficiency correction across the Dalitz plot and the Dalitz shape for continuum and $B\overline{B}$ background: the former is taken from off-resonance D^0 sideband data and the later from generic $B\overline{B}$ Monte Carlo.

5.3 ΔE parameterization

The ΔE distribution for $D\pi$ events can be parameterized in two different ways. First, using a Gaussian distribution centered at about 50 MeV with a width resulting from the convolution of the bachelor track momentum resolution and the ΔE resolution for DK events. This is the method described and used in sections where we describe the selection of the events: 3.4 and 3.5. The second parametization exploits the fact that the shift in ΔE between the kaon and pion hyphotesis is known on a event by event basis

$$\Delta E_{shift} = \Delta E_K - \Delta E_\pi = \gamma \left[\sqrt{m_K^2 + p^2} - \sqrt{m_\pi^2 + p^2}\right] \tag{120}$$

where p is the momentum of the bachelor track in laboratory frame and γ is the PEP-II boost factor. the DK PDF for ΔE distribution known once we know the distribution for $D\pi$ events, and viceversa. This can be exploited to improve the DK PDF knowledge using $D\pi$ events.

The correlation of ΔE with $m_{\rm ES}$ has been found to be negligible for all the difference background components (smaller than a few per cent), as shown in table 20. For signal it is at the level of 16%, as expected from the rule of thumb that the correlation among these two variables is given by the ratio of their widths, $\rho \sim \sigma_{m_{\rm ES}}/\sigma_{\Delta E} \sim 15\%$ [65]. In principle, this correlation needs to be taken into account in the PDF, however if the cut on ΔE is relatively tight the effect on the analysis is very small, and it has been included in the systematics. The effect of this correlation has been verified to be completely negligle on all the *CP* parameters being measured in this analysis.

Selection	B^+B^-	$B^0\overline{B}^0$	$c\overline{c}$	uds	Signal
No cut	0.018	0.035	-0.000	-0.007	-0.165
$\lvert\cos\theta_{thrust}\rvert < 0.8$ $\lvert M(D^0) - M(PDG)\rvert$ MeV $\lvert M(K^0_s) - M(PDG)\rvert < 10$ MeV $\lvert\Delta m - \Delta m(PDG)\rvert < 2.5$ MeV	0.088	0.027	-0.035	-0.073	-0.164

Table 20: ΔE-m_{ES} *correlation for signal and background events (obtained for the* $B \to D^{*0}K$ *sample). For the background samples the correlation is negligible, while for signal the correlation is consistent with the expectation of* $\sim -15\%$ *[65].*

5.4 Dalitz and *CP* fitters

Two independent and complementary Dalitz and *CP* fitters have been implemented using the Object Oriented C++ programming language and validated to each other. Although the two tools have been developed within the *RooFit* framework [47], their main goals are slightly different. The first package, called *RooDKDalitz*, is a more general tool designed to provide a flexible configuration to deal with combined fits of the different B (and eventually D) channels to be used in the analysis. It also provides the framework for the extraction of PDF shapes and yields as described in the previous sections. This code makes extensive use *EvtGenBase* classes [48], particularly those related with Dalitz plot kinematics. The second tool, called *RooBenDalitz*, is a simpler implementation mainly devoted for Dalitz and *CP* fits to the golden channel ($D^0 \to K^0_s\pi^+\pi^-$, $B \to D^0K^+/\pi^+$). The two fitting codes are therefore completely complementary, providing a robust validation of the fitting procedure. The nominal fit results will be those obtained with *RooDKDalitz*, but extensive cross-checks have been done with the second fitter, as well as many of the evaluations of the systematics uncertainties.

In addition to these two Dalitz and *CP* fitters, a much simpler binned Dalitz fitter was implemented with the goal of studying the Dalitz model since it provides a much faster execution time together with a direct evaluation of the $\chi^2/ndof$ of the Dalitz fit to the D^* control sample.

5.5 Fit results

5.5.1 Results from the combined shapes and yields fit

Yields and PDF shapes were first extracted by performing a simultaneous fit to all D^0K, $D^{*0}K$, $D^0\pi$, and $D^{*0}\pi$ data, following the strategy described in section 5.2. Fits to D^0K and $D^0\pi$ data alone were also performed and compared to the general fit results. Table 21

Shape parameter	$DK + D\pi$	$D^0K + D^0\pi$ only
ΔE		
$c1_{P2_2}(D^0K)$	-4.2 ± 1.7	-4.8 ± 1.9
$c1_{P2_2}((D^0\gamma)K)$	-3.8 ± 1.5	—
$c1_{P2_2}((D^0\pi^0)K)$	0.6 ± 3.7	—
$c1_{P1_1}(D^0K)$	-1.0 ± 0.4	-1.0 ± 0.4
$c1_{P1_1}((D^0\gamma)K)$	0.2 ± 0.9	—
$c1_{P1_1}((D^0\pi^0)K)$	-2.8 ± 1.6	—
$\mu_{G_2}(D^0K)$	-1.8 ± 0.4 MeV	-1.7 ± 0.4 MeV
$\mu_{G_2}((D^0\gamma)K)$	-2.1 ± 1.1 MeV	—
$\mu_{G_2}((D^0\pi^0)K)$	-1.5 ± 1.1 MeV	—
$\sigma_{G_2}(D^0K)$	15.2 ± 0.4 MeV	15.2 ± 0.4 MeV
$\sigma_{G_2}((D^0\gamma)K)$	13.1 ± 1.3 MeV	—
$\sigma_{G_2}((D^0\pi^0)K)$	18.2 ± 1.0 MeV	—
m_{ES}		
m_0	5.290 GeV	5.290 GeV
$c_{A_1}(D^0K)$	-21.7 ± 2.1	-22.6 ± 2.1
$c_{A_1}((D^0\gamma)K)$	-32.2 ± 5.2	—
$c_{A_1}((D^0\pi^0)K)$	-25.2 ± 9.2	—
$\mu_{G_1}(D^0K)$	5.27982 ± 0.00004 GeV	5.27982 ± 0.00004 GeV
$\mu_{G_1}((D^0\gamma)K)$	5.27985 ± 0.00011 GeV	—
$\mu_{G_1}((D^0\pi^0)K)$	5.27997 ± 0.00008 GeV	—
$\sigma_{G_1}(D^0K)$	2.35 ± 0.04 MeV	2.34 ± 0.04 MeV
$\sigma_{G_1}((D^0\gamma)K)$	2.02 ± 0.84 MeV	—
$\sigma_{G_1}((D^0\pi^0)K)$	2.61 ± 0.08 MeV	—
$c_{A_2}(D^0K)$	-50.5 ± 4.0 (MC fixed)	-50.5 ± 4.0 (MC fixed)
$c_{A_2}(D^0\pi)$	-79.4 ± 4.2 (MC fixed)	-79.4 ± 4.2 (MC fixed)
$c_{A_2}((D^0\pi^0)K)$	-85 ± 18 (MC fixed)	—
$c_{A_2}((D^0\pi^0)\pi)$	-48 ± 26 (MC fixed)	—
$c_{A_2}((D^0\gamma)K)$	-85 ± 18 (MC fixed)	—
$c_{A_2}((D^0\gamma)\pi)$	-68 ± 13 (MC fixed)	—
$\sigma_{B_1}(D\pi)$	3.4 MeV (MC fixed)	3.4 MeV (MC fixed)
$f_2(D^0\pi)$	0.28 ± 0.11	0.32 ± 0.12
$f_2(D^{*0}\pi)$	0.48 ± 0.07	—
Fisher		
f_6	0.57 ± 0.03	0.58 ± 0.03
μ_{G_7}	-0.458 ± 0.010	-0.453 ± 0.010
σ_{G_7}	0.230 ± 0.008	0.235 ± 0.009
μ_{G_8}	0.12 ± 0.04	0.14 ± 0.04
σ_{G_8}	0.465 ± 0.013	0.468 ± 0.013
f_5	0.570 ± 0.021	0.565 ± 0.028
μ_{G_5}	-0.162 ± 0.017	-0.162 ± 0.024
σ_{G_5}	0.328 ± 0.010	0.331 ± 0.013
μ_{G_6}	0.697 ± 0.019	0.691 ± 0.026
σ_{G_6}	0.304 ± 0.010	0.307 ± 0.013

Table 21: *D^0K, $(D^0\pi^0)K$ and $(D^0\gamma)K$ shape parameters extracted from the combined fits $DK+D\pi$ and $D^0K+D^0\pi$ only, in the ΔE region* $[-80, 120]$ MeV *for DK and* $[20, 80]$ MeV *for $D\pi$.*

Parameter	Value	Origin
Fractions of real D^0's in background		
$R_{\mathsf{Cont}}(D^0K)$	0.213 ± 0.054 (not updated to 0.221 ± 0.042)	Data (assume no $b\bar{b}$ contrib.)
$R_{\mathsf{Cont}}((D^0\gamma)K)$	0.27 ± 0.08	MC
$R_{\mathsf{Cont}}((D^0\pi^0)K)$	0.13 ± 0.02	MC
$R_{\mathsf{B\overline{B}}}(D^0K)$	0	MC
$R_{\mathsf{B\overline{B}}}((D^0\gamma)K)$	0.11 ± 0.06	MC
$R_{\mathsf{B\overline{B}}}((D^0\pi^0)K)$	0.16 ± 0.03	MC
Fractions of RS D^0's		
$R^{RS}_{\mathsf{Cont}}(D^0K)$	0.208 ± 0.033	MC
$R^{RS}_{\mathsf{Cont}}((D^0\gamma)K)$	0.23 ± 0.11	MC
$R^{RS}_{\mathsf{Cont}}((D^0\pi^0)K)$	0.15 ± 0.06	MC
$R^{RS}_{\mathsf{B\overline{B}}}(D^0K)$	1	MC
$R^{RS}_{\mathsf{B\overline{B}}}((D^0\gamma)K)$	1	MC
$R^{RS}_{\mathsf{B\overline{B}}}((D^0\pi^0)K)$	1	MC
Dalitz efficiency shape correction: 3rd order polynomial		
Table 18, All		MC
Dalitz shape for Cont: 3rd order polynomial		
Table 19, from D^0K Taken the same for $(D^0\gamma)K$ and $(D^0\pi^0)K$, checked consistency		Off-resonance data
Dalitz shape for $\mathsf{B\overline{B}}$: 3rd order polynomial		
Table 19, from D^0K Taken the same for $(D^0\gamma)K$ and $(D^0\pi^0)K$, checked consistency		$\mathsf{B\overline{B}}$ MC

Table 22: *Inputs fixed in the CP fit (other than the m_{ES}, ΔE and $\mathcal{F}$ shapes, which are given in table 21, and the Dalitz model, given in tables 11 and 12). We follow in this table the notation used in Eq. (110).*

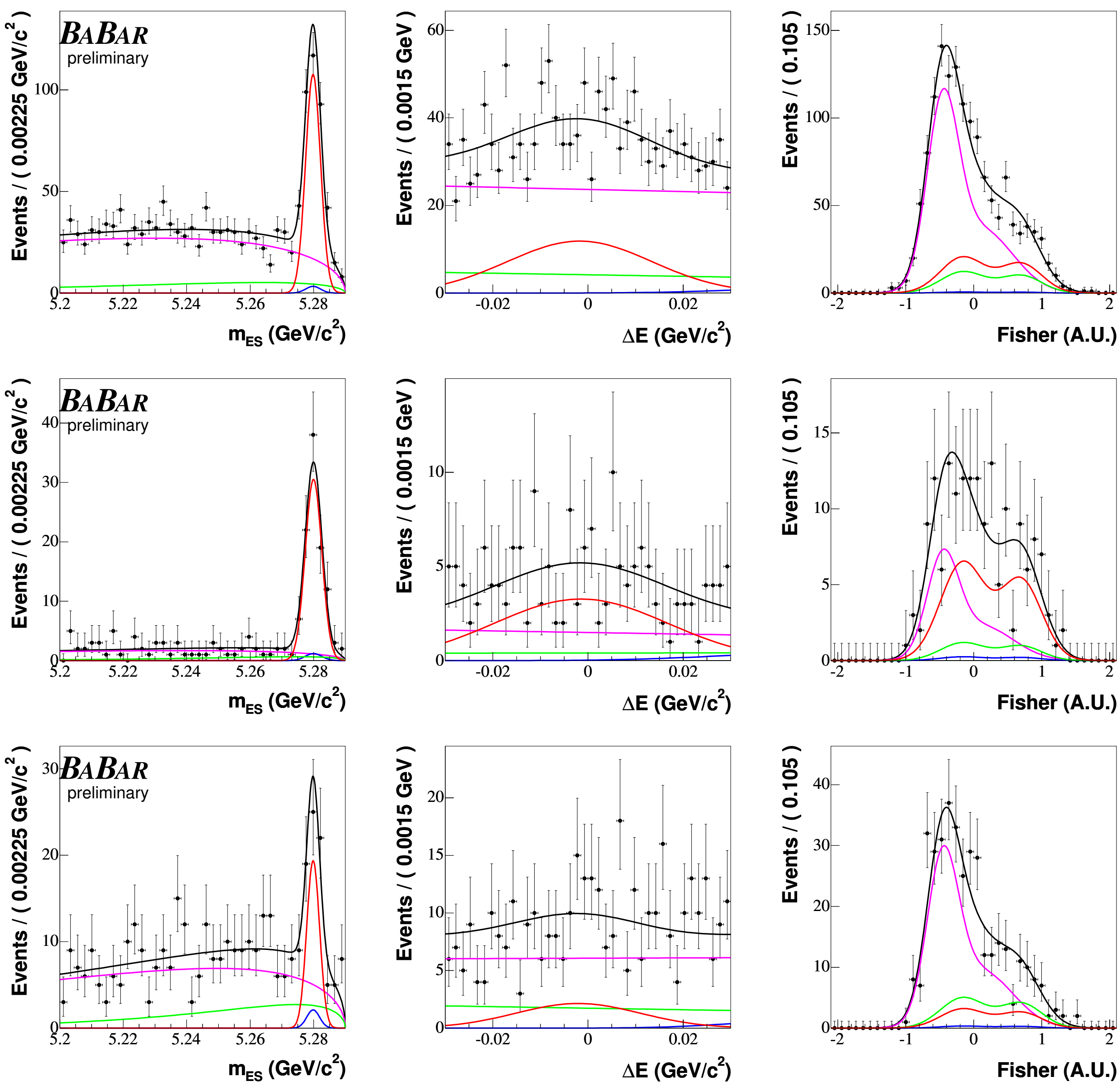

Figure 59: *D^0K (top row), $(D^0\pi^0)K$ (middle row) and $(D^0\gamma)K$ (bottom row) ΔE, $m_{\rm ES}$ and $\mathcal{F}$ shapes in the ΔE region* $[-30, 30]$ MeV, *compared to the data. Also shown are the different background components: signal (red), $D\pi$ (blue), $B\overline{B}$ (green) and* Cont *(magenta).*

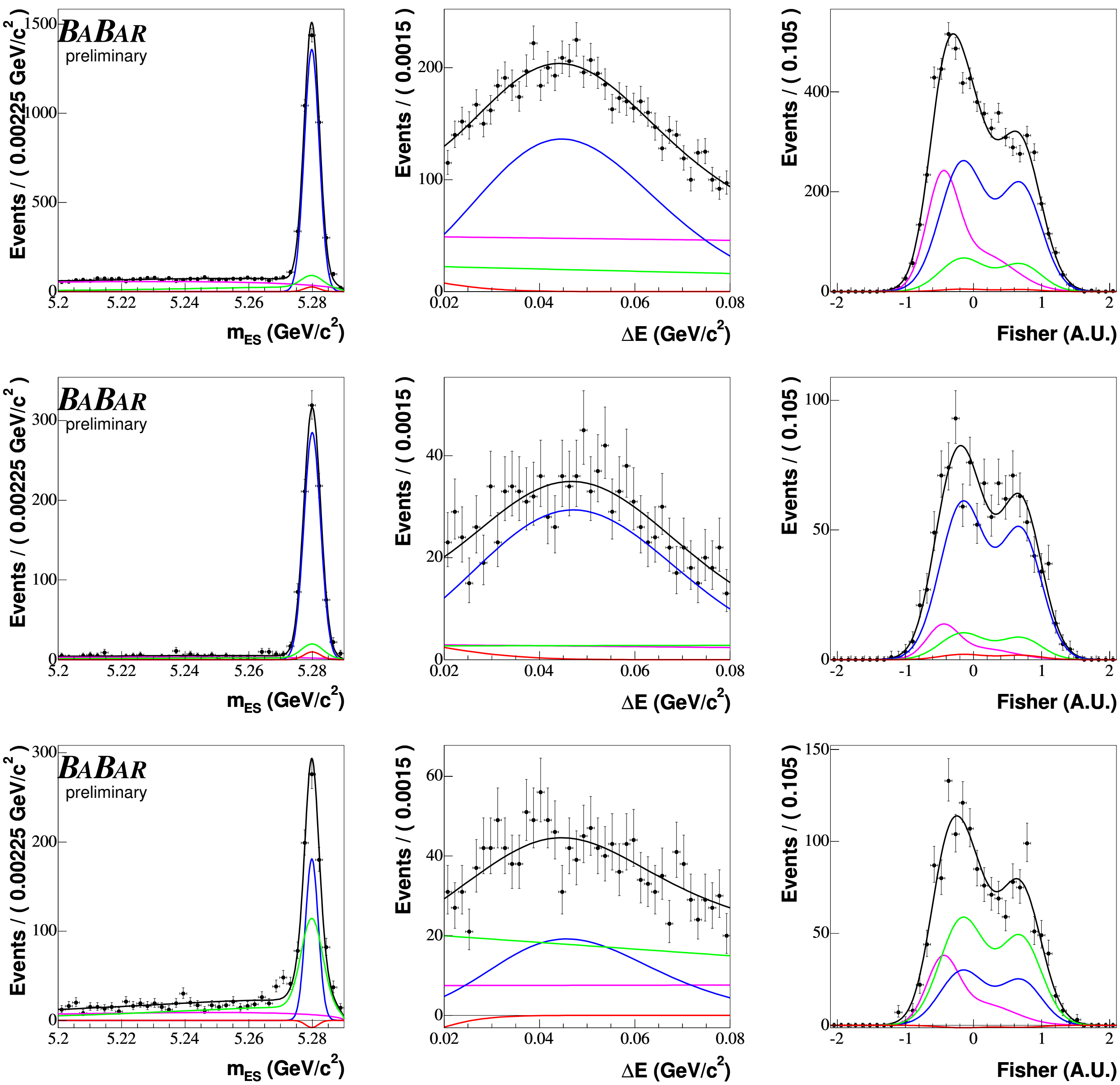

Figure 60: $D^0\pi$ *(top row)*, $(D^0\pi^0)\pi$ *(middle row) and* $(D^0\gamma)\pi$ *(bottom row)* ΔE, m_{ES} *and* $\mathcal{F}$ *shapes extracted from the combined fit are compared to the data, in the* ΔE *region* $[20, 80]$ MeV. *Also shown are the different background components: signal (red),* $D\pi$ *(blue),* $B\overline{B}$ *(green) and* Cont *(magenta).*

shows all shape parameters extracted from both fits, in the ΔE region $[-80, 120]$ MeV for kaon samples and $[20, 80]$ MeV for pion samples. The Argus parameter for $B\overline{B}$ background components was fixed to Monte Carlo estimates obtained separately for kaon and pion samples in the ΔE regions $[-30, 30]$ and $[20, 80]$ MeV, respectively. Due to the lack of statistics, the estimate for $(D^0\pi^0)K$ and $(D^0\gamma)K$ was made combining both samples. As described in sections 3.4 and 3.5, the $m_{\rm ES}$ $B\overline{B}$ peaking background contribution is negligible for all DK samples but it is not for $D\pi$ (both $D^0\pi$ and $D^{*0}\pi$). This has been estimated to be about 30%, relative to the $B\overline{B}$ combinatorial component, with Gaussian width of about 3.4 MeV. The value of the Gaussian width was fixed in the fit but the relative fraction of peaking with respect to combinatorial was left floated since ΔE provides a handle to obtain it directly from the data. The fit projections for kaon and pion data for $m_{\rm ES}$, ΔE and $\mathcal{F}$ are shown in figures 59 and 60 respecti vely. The corresponding yields are given in table 23.

Component	DK Yield	$D\pi$ Yield
	D^0K	$D^0\pi$
BB̄	480 ± 129	912 ± 139
Cont	3091 ± 137	1968 ± 99
Dh	131 ± 15	3554 ± 122
Sig	292 ± 21	68 ± 33
	$(D^0\gamma)K$	$(D^0\gamma)\pi$
BB̄	305 ± 47	797 ± 85
Cont	735 ± 51	308 ± 38
Dh	21 ± 8	407 ± 76
Sig	42 ± 9	-18 ± 11
	$(D^0\pi^0)K$	$(D^0\pi^0)\pi$
BB̄	98 ± 23	141 ± 39
Cont	199 ± 24	111 ± 20
Dh	27 ± 7	829 ± 41
Sig	94 ± 11	28 ± 20

Table 23: *D^0K, $D^0\pi$, $(D^0\pi^0)K$, $(D^0\pi^0)\pi$, $(D^0\gamma)K$ and $(D^0\gamma)\pi$ yields as extracted from the combined shapes fit in the ΔE region* $[-80, 120]$ MeV *for kaon samples and* $[20, 80]$ MeV *for pion data.*

5.5.2 Results from the *CP* fit

We performed the *CP* fit on the DK and $D^{*0}K$ data. The D^0K, $(D^0\pi^0)K$ and $(D^0\gamma)K$ yields were floated simultaneously with the *CP* parameters in order to reevaluate them given the tighter ΔE interval ($[-30, 30]$ MeV) used in the *CP* fit compared to the yields prefit. The obtained yields are given in table 24. Table 22 summarizes the fixed inputs used in the *CP* fit, which have to be added to the $m_{\rm ES}$, ΔE and $\mathcal{F}$ shapes, and the Dalitz model parameters. The *CP* results in cartesian coordinates are shown in table 25 and in table 26 and 27 are shown the correlation matrix among the *CP* parameters.

Component	DK Yield
	D^0K
BB̄	168 ± 36
Cont	947 ± 45
Dh	9 ± 8
Sig	282 ± 20
	$(D^0\gamma)K$
BB̄	69 ± 18
Cont	243 ± 22
Dh	5 ± 4
Sig	44 ± 8
	$(D^0\pi^0)K$
BB̄	16 ± 9
Cont	60 ± 11
Dh	3 ± 5
Sig	89 ± 11

Table 24: *D^0K, $D^0\pi$ and $(D^0\pi^0)K$ yields as extracted from the Dalitz CP fits (ΔE region $[-30, 30]$ MeV).*

Observable	D^0K	$D^{*0}K$
x_-	$0.0772^{+0.0688}_{-0.0708}$ [± 0.0692]	$-0.1306^{+0.0940}_{-0.0935}$ [± 0.0934]
y_-	$0.0635^{+0.0953}_{-0.0888}$ [± 0.0919]	$-0.1433^{+0.1064}_{-0.1059}$ [± 0.1049]
x_+	$-0.1287^{+0.0701}_{-0.0704}$ [± 0.0703]	$0.1397^{+0.0941}_{-0.0943}$ [± 0.0926]
y_+	$0.0186^{+0.0762}_{-0.0814}$ [± 0.0787]	$0.0131^{+0.1183}_{-0.1201}$ [± 0.1195]

Table 25: *Fit results for $(x_\pm, y_\pm)$ cartesian coordinates, for the D^0K and $D^{*0}K$ decay modes. The values inside square brackets are the quadratic errors calculated from the fit covariance matrix.*

Observable	x_-	y_-	x_+	y_+
x_-	1	2.5×10^{-2}	9.4×10^{-5}	-3.0×10^{-5}
y_-		1	-1.8×10^{-4}	-2.3×10^{-4}
x_+			1	6.0×10^{-2}

Table 26: *Correlation matrix for $(x_\pm, y_\pm)$ cartesian coordinates, for the D^0K decay mode.*

Observable	x_-	y_-	x_+	y_+
x_-	1	-1.7×10^{-1}	-6.3×10^{-3}	3.6×10^{-3}
y_-		1	-5.7×10^{-3}	2.6×10^{-3}
x_+			1	-2.7×10^{-1}

Table 27: *Correlation matrix for $(x^*_\pm, y^*_\pm)$ cartesian coordinates, for the $D^{*0}K$ decay mode.*

6 Extraction of γ: a Statistical Approach

As described in Chapter 5, the likelihood fit parameters γ, r_B, δ are affected by large non-Gaussian effects with the current statistics (205 fb^{-1}). We observe that for a relatively small dataset and for small absolute value of the amplitude ratio $r_B = |\mathcal{A}(b \to u\overline{c}s)/\mathcal{A}(b \to c\overline{u}s)|$, the likelihood fit returns a biased estimate of r_B, and the rms of γ and δ pulls are significantly larger than unity.
This can be understood since $\sigma^2(\gamma)$ is proportional to $\frac{1}{\frac{d^2 logL}{d^2\gamma}}$, and $\frac{d^2 logL}{d^2\gamma}$ is proportional to r_B, therefore it will be smaller for larger r_B. Since there r_B is positively biased the error returned by the maximum likelihood method will be smaller than what it should be to represent the statistical fluctuation (i.e. it does not define a confidence interval with the correct coverage properties). The nature of these non-Gaussian effects scaling with the size of the data sample are related to the small number of events in the region of the Dalitz plot sensitive to r_B (and γ) and to the polar coordinates representation of the space of fit parameters which impose the positive definiteness of r_B.

As a consequence, the usual assumption that the parameters at the maximum of the likelihood are unbiased estimators of true quantities it is not valid anymore, and more sophisticated techniques are needed to extract central values, errors and confidence intervals [49]. This also poses limitations to the way how systematic uncertainties have to be evaluated. For example, usual techniques based on the quadratic differences of fit errors between the nominal and alternative fit configurations are now not reliable since fit errors are not a good representation of the true statistical fluctuations. Similarly, one has to be very careful when looking at differences in central values since biases themselves are a function of the truth values.
For these reasons, we have employed and developed both **Frequentist** and **Bayesian** techniques to extract the confidence intervals, central values and errors. Since the Frequestist approach has several advantages for the extraction of both statistical and systematic uncertainties (in addition to avoiding the intrinsic arbitrary choice of the prior distributions of Bayesian methods) we have used it for presenting the final analysis results on r_B, γ and δ, using the Bayesian approach as an independent cross-check, see Appendix B. The systematic uncertainties assigned to the Bayesian results are those obtained with the Frequentist method, since the correct evaluation of these errors require the use of cartesian coordinates, which imply the use of the Frequentist approach.

6.1 Classical (Frequentist) technique

In the classical (Frequentist) approach, the confidence interval $[p_1, p_2]$ for parameter p, whose true value p^t is unknown, is such that has a probability

$$P(p \in [p_1, p_2]) = 1 - \alpha, \tag{121}$$

of containing the unknown true value. The limits of the interval, p_1 and p_2, are functions of the measured value of p. In particular the confidence interval will contain the unknown true point p^t in a fraction $1-\alpha$ of the experiments, or in other words, if the experiment is carried out many times, a fraction $1 - \alpha$ of those experiments will find the measured point within the given confidence region. If Eq. (121) is satisfied, one can say that the defined interval *covers* at the stated confidence-level, or that the interval has the correct *coverage*. In our case we have not 1-dimensional confidence-level interval but a 3-dimensional or 5-dimensional confidence-level regions, as the unknown vector parameters of parameters is

$$\mathbf{p}^{\mathrm{t}} = (r_B^t, \gamma^t, \delta^t) \qquad \text{or} \qquad \mathbf{p}^{\mathrm{t}} = (r_B^t, \gamma^t, \delta^t, r_B^{*t}, \delta^{*t}) \ . \tag{122}$$

The 3-dimensional (5-dimensional) confidence-level regions determined are $\alpha = 19.9\%, 72.1\%$ $(3.7\%, 42.8\%)$ corresponding to 1, 1.96 standard deviations respectively for each single parameter (regardless the others), in the case of a 3-dimensional (5-dimensional) Gaussian distribution[23]. We will quote finally for the error on the single parameters the statistical error corresponding to the 19.9% confidence region (1 standard deviation ellipsoid). The methodology used is similar to that used by Belle [50] although with some relevant differences, and requires knowledge of the probability density function, PDF, of the fitted parameters $\mathbf{z}_\pm = (x_\pm, y_\pm)$, as a function of the true parameters $\mathbf{p}^{\mathrm{t}}$. This PDF can be obtained using toy MC techniques, where large sets of experiments are generated and fitted using the full experimental likelihood function $\mathcal{L}_{exp}$, as will be discussed in section 6.1.2.

6.1.1 Cartesian coordinates

The 4-dimensional cartesian parameter space is defined by the variables $\mathbf{z}_\pm = (x_\pm, y_\pm)$, where

$$\begin{aligned} x_\pm &\equiv \mathrm{Re}(r_{B\pm} e^{i\theta_\pm}) = r_{B\pm} \cos\theta_\pm \\ y_\pm &\equiv \mathrm{Im}(r_{B\pm} e^{i\theta_\pm}) = r_{B\pm} \sin\theta_\pm \end{aligned} \tag{123}$$

with $\theta_\pm = \delta \pm \gamma$. The choice of this particular basis is important because no physics boundaries have to be imposed to the fit variables. The consequence, as proved later, is the Gaussian behavior of the errors and the absence of biases in the fit results. On the contrary, the choice of the polar coordinates base,

$$(r_B \ , \ \gamma \ , \ \delta) \ , \tag{124}$$

even if it has one parameter less, it contains one parameter with a physics boundary ($r_B > 0$). In this case it is found a biased distribution for the r_B fit values, where the bias is larger for smaller values of r_B and smaller data sample size. In addition, cartesian coordinates

[23]Or equivalently, χ^2 distribution with 3 (5) degrees of freedom.

are largely uncorrelated, while (r_B, γ, δ) are significantly correlated. The correlation matrix blocks for D^0K and $D^{*0}K$ modes obtained from the fit to the data sample are shown in tables 26 and 27, respectively. As shown later on the basis of Toy MC studies, the only sizeable correlations appear for pairs (x_+, y_+) and (x_-, y_-) within a given B decay mode. This contribution will be taken later into account in the Frequentist PDF. All the cross correlation terms between D^0K and $D^{*0}K$ samples are zero.

The cartesian coordinates are sensitive to the direct CP violation in the $B^\pm \to D^{(*)}K^\pm$ decay, through the distance d of the two points $(x_\pm, y_\pm)$ for $B^\pm$ decays respectively:

$$d = [(x_- - x_+)^2 + (y_- - y_+)^2]^{1/2} = 2r_B|\sin\gamma| \; . \tag{125}$$

A non null distance means evidence of direct CP violation.

Table 25 reports the $(x_\pm, y_\pm)$ nominal fit results on the data sample, for the D^0K and $D^{*0}K$ decay modes. In Figure 61 are shown the 68.3% and 95% confidence-level contours in the $(x_\pm, y_\pm)$ cartesian fit parameter space for the two channels. The distance d is the length of the segment between the B^+ (circle dot) and B^- (rectangular dot). The statistical significance of the CP violation will be discussed later in section 6.1.5. The contours have been obtained using the likelihood ratio method [44] ($\Delta\mathcal{L}_{exp} = 0.5, 1.921$, for 68.3% and 95% confidence-level regions) [49].

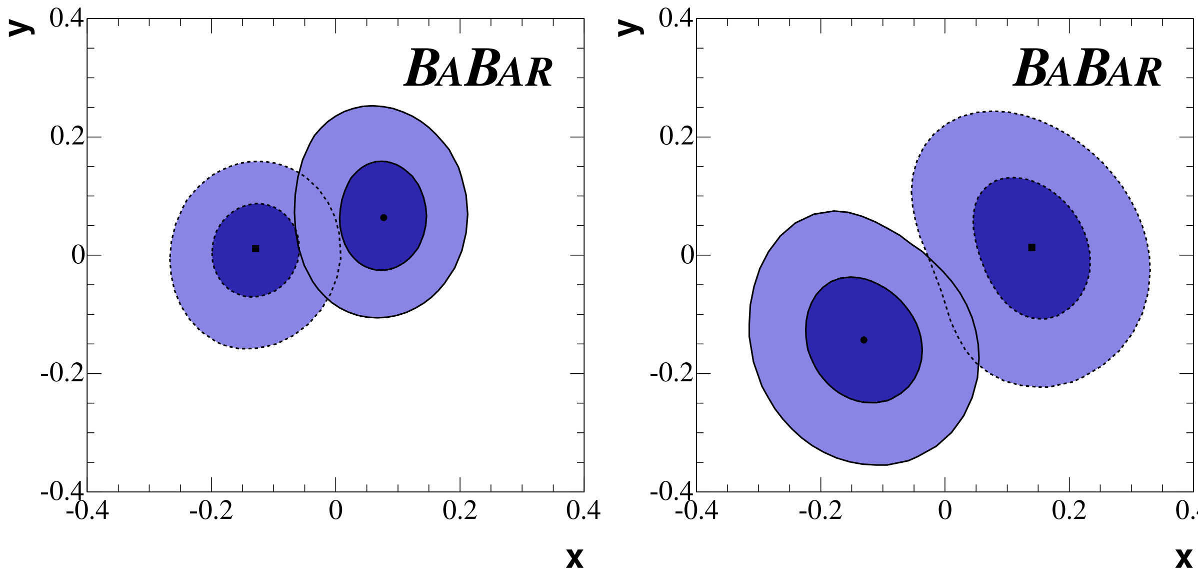

Figure 61: *68.3% (dark blue) and 95% (bright blue) confidence-level countours in the* $(x_\pm, y_\pm)$ *cartesian fit parameter space for* D^0K *(left) and* $D^{*0}K$ *(right). Solid (dotted) contours are for* B^- *(*B^+*) decays. Given the good Gaussian behavior of the cartesian parameters, these contours have been obtained using the standard likelihood ratio method (*$\Delta\mathcal{L}_{exp} = 0.5, 1.921$*) [49].*

From Toy Monte Carlo studies, described in detail in Appendix A, residual distributions of the cartesian fit parameters space doesn't show any significant bias. The errors from the fit are well calculated, pulls (residuals normalized to the fit errors) have $\sigma = 1$ within the errors for all the fit variables and means are consistent with zero. For this study we have used a set of about 2K Toy Monte Carlo experiments corresponding to the nominal data results (i.e. the generated $x_\pm$ and $y_\pm$ values are those found in the nominal fit, table 25). The linearity of the $(x_\pm, y_\pm)$ fit parameters together with the stability of their corresponding rms' (σ_{x+}, σ_{y+}, σ_{x-}, and σ_{y-}) versus the generated parameter values are demonstrated in figures 62 and 63, for the D^0K and $D^{*0}K$ samples respectively (error bars indicate the rms of the distribution at each generated point). These figures have been produced with 20K Toy Monte Carlo experiments with truth $(x_\pm, y_\pm)$ values obtained by generating randomly r_B and the weak and strong phases, in the ranges $[0, 0.3]$, $[-180°, 180°]$ and $[0, 360°]$, respectively. Using the same experiments we have also studied the stability of the rms of the residual and pull distributions in bins of the truth r_B value, as shown in Appendix A. From both studies we observe that the rms values are stable in the wide range of truth values within a precision of $< 10\%$. These results will be used in the parametrization of the Frequentist PDF, as described below.

6.1.2 Description of the method

Once we have demonstrated the Gaussian and linearity behavior of the cartesian fit parameter space, we can construct an analytical parameterization of the PDF. The 4-dimensional PDF is written as

$$\begin{aligned}\frac{d^4P}{d^2\mathbf{z}_+ d^2\mathbf{z}_-}(\mathbf{z}_+, \mathbf{z}_- | \mathbf{p}^{\mathrm{t}}) &= G_2\left(\mathbf{z}_+; r_B^t \cos(\delta^t + \gamma^t), r_B^t \sin(\delta^t + \gamma^t), \sigma_{x_+}, \sigma_{y_+}, \rho_+\right) \times \\ &\quad G_2\left(\mathbf{z}_-; r_B^t \cos(\delta^t - \gamma^t), r_B^t \sin(\delta^t - \gamma^t), \sigma_{x_-}, \sigma_{y_-}, \rho_-\right) \qquad (126)\end{aligned}$$

where

$$G_2\left(\mathbf{z}; \mu_x, \mu_y, \sigma_x, \sigma_y, \rho\right) = \frac{1}{2\pi\sigma_x\sigma_y\sqrt{1-\rho^2}} e^{-\frac{1}{2(1-\rho^2)}\left[\frac{(x-\mu_x)^2}{\sigma_x^2} + \frac{(y-\mu_y)^2}{\sigma_y^2} - \frac{2\rho(x-\mu_x)(y-\mu_y)}{\sigma_x\sigma_y}\right]} \qquad (127)$$

and $\mathbf{z}_\pm = (x_\pm, y_\pm)$ and $\mathbf{p} = (r_B, \gamma, \delta)$. The vectors $\mathbf{z}_\pm^{\mathrm{t}}$ and $\mathbf{p}^{\mathrm{t}}$, defined equivalently to $\mathbf{z}_\pm$ and $\mathbf{p}$ respectively, are the corresponding parameters in the truth parameter space. The Gaussian widths ($\sigma_{x\pm}$, $\sigma_{y\pm}$) and the correlations $\rho_\pm$ distributions can obtained either from the nominal full experimental likelihood $\mathcal{L}_{exp}$ Toy Monte Carlo experiments or from the fit to the data sample itself, since the agreement with the values found in data is very good, as shown in figures 74, **??** and 75 in Appendix A. Given this good agreement and in order to take into account the goodness of the fit to the data sample, we will use in the above PDF the values of the widths and correlations found in the data fit, summarized in tables 26, 27, and 25.

Once we have constructed and justified the PDF of the fit parameters as a function of the true parameters, the technical procedure to construct 3-dimensional confidence regions and their 1- and 2-dimensional is as follows. The confidence-level $1 - \alpha$ for each set of true parameters $\mathbf{p}^{\mathrm{t}}$ is calculated as

$$\alpha(\mathbf{p}^{\mathrm{t}}) = \int_D \frac{d^4P}{d^2\mathbf{z}_+ d^2\mathbf{z}_-}(\mathbf{z}_+, \mathbf{z}_- | \mathbf{p}^{\mathrm{t}}) d^2\mathbf{z}_+ d^2\mathbf{z}_- \ , \qquad (128)$$

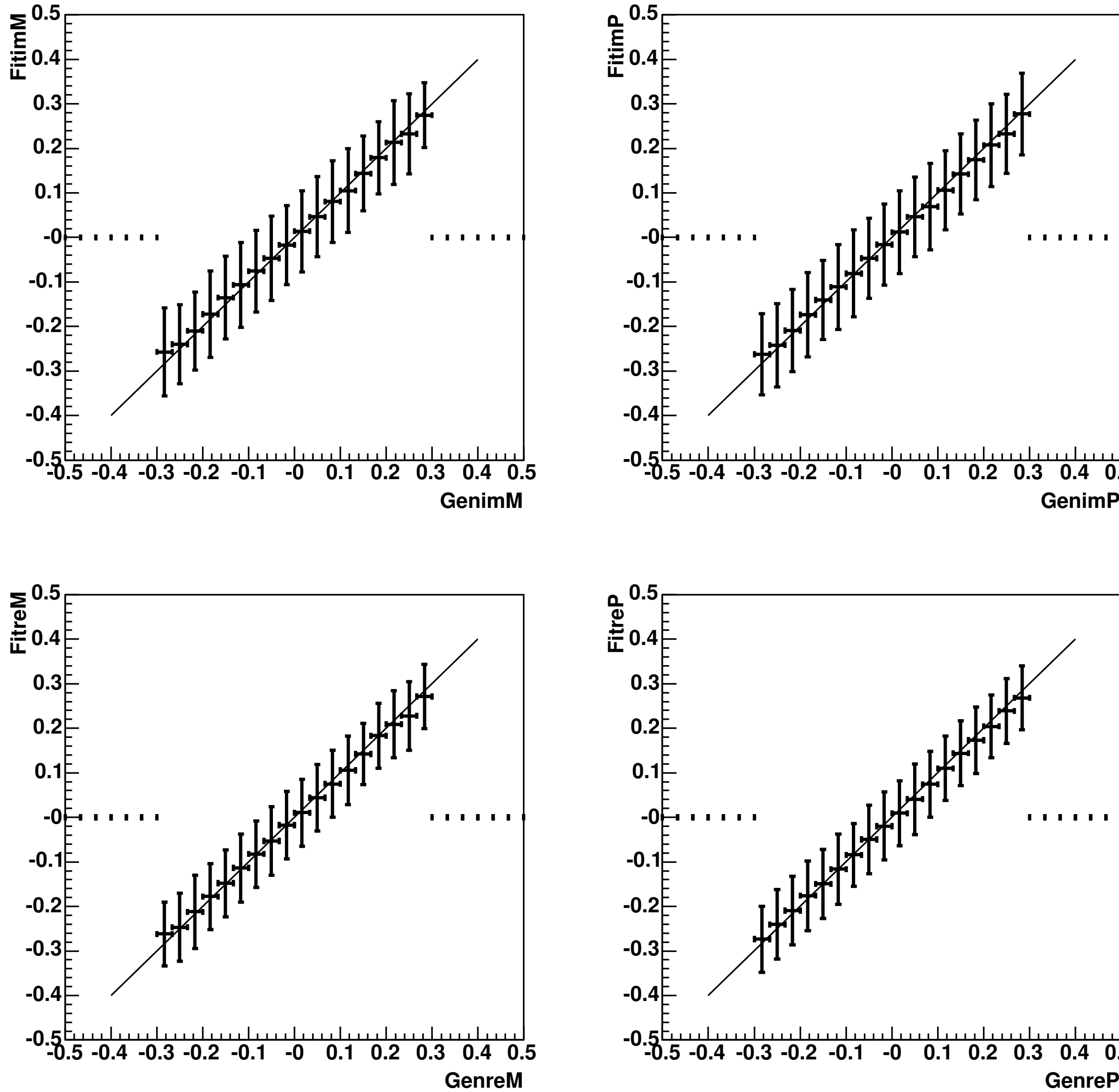

Figure 62: *Linearity of the $(x_{\pm}, y_{\pm})$ cartesian fit parameter space, for the D^0K mode. The truth (generated) values of $(x_{\pm}, y_{\pm})$ have been obtained by generating randomly r_B and the weak and strong phases. r_B was generated in the range $[0, 0.3]$. Error bars indicate the rms of the distribution at each generated point.*

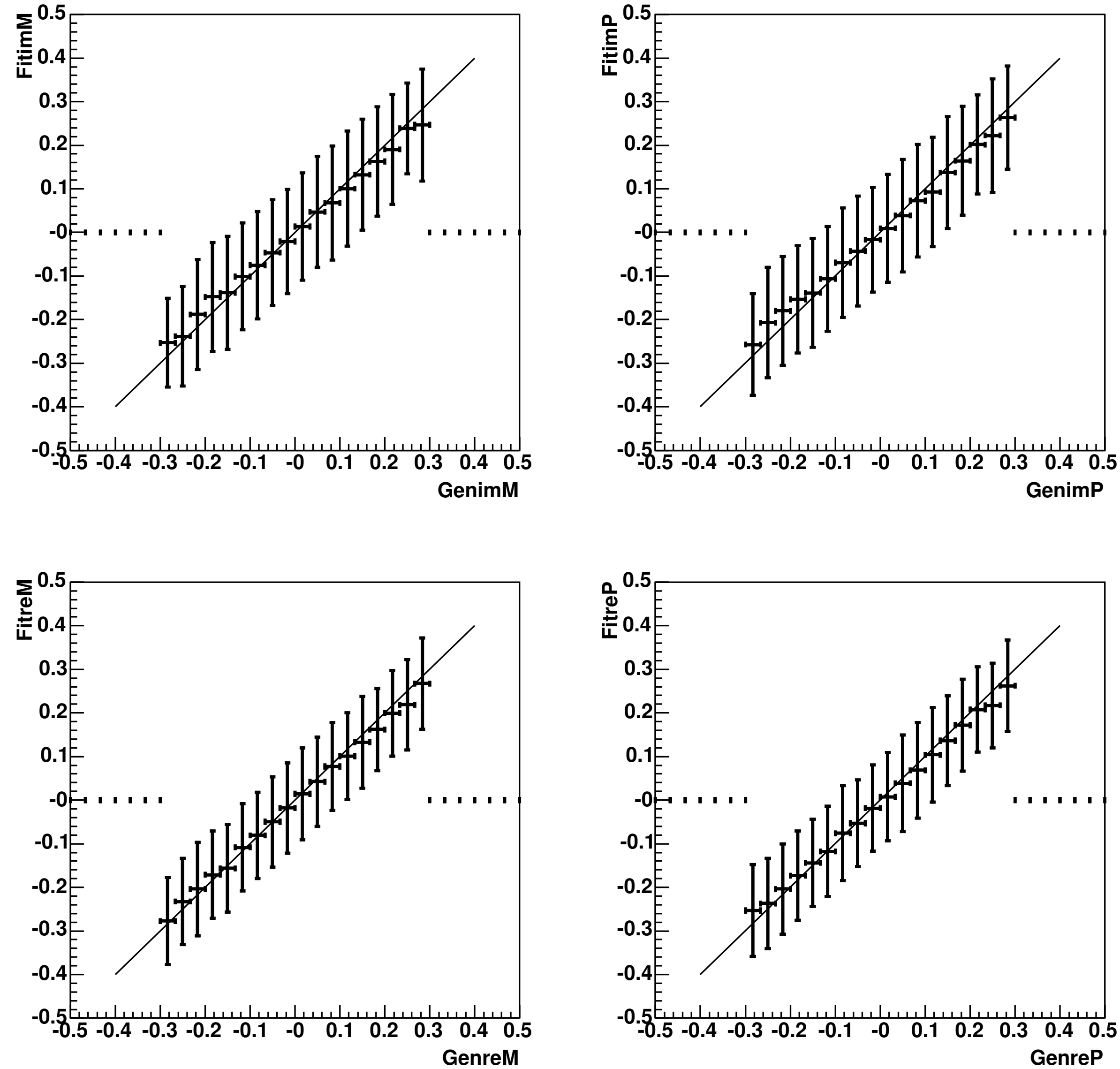

Figure 63: *Linearity of the* $(x_\pm, y_\pm)$ *cartesian fit parameter space, for the* $D^{*0}K$ *mode. The truth (generated) values of* $(x_\pm, y_\pm)$ *have been obtained by generating randomly* r_B *and the weak and strong phases.* r_B *was generated in the range* $[0, 0.3]$*. Error bars indicate the rms of the distribution at each generated point.*

where the integration domain D is given by the condition

$$\frac{d^4P}{d^2\mathbf{z}_+ d^2\mathbf{z}_-}(\mathbf{z}_+, \mathbf{z}_- | \mathbf{p}^{\mathrm{t}}) \geq \frac{d^4P}{d^2\mathbf{z}_+ d^2\mathbf{z}_-}(\mathbf{z}_+^{\mathrm{data}}, \mathbf{z}_-^{\mathrm{data}} | \mathbf{p}^{\mathrm{t}}) \ , \tag{129}$$

i.e. it includes all points in the fit parameter space closer to the truth point than the data point. The values of $\mathbf{z}_\pm^{\mathrm{data}}$ are those given in table 25.
To construct the 3-dimensional confidence region ($\mathbf{p}^{\mathrm{t}}$ space) we generate randomly a large set, $\mathcal{O}(10^9)$ of points $\mathbf{p}^{\mathrm{t}} \equiv (r_B^t, \gamma^t, \delta^t)$, in the ranges $[0, 0.4]$, $[-180°, 180°]$ and $[0, 360°]$. For each generated point $\mathbf{p}^{\mathrm{t}}$ the integral $\alpha(\mathbf{p}^{\mathrm{t}})$ is evaluated according to equations (128) and (129). If we are interested in building a 3-dimensional region of joint probability $1 - \alpha_0$, then we select only those points for which $\alpha(\mathbf{p}^{\mathrm{t}}) \leq \alpha_0$. The 2-dimensional and 1-dimensional contours are then built by projecting the 3-dimensional joint probability regions. The values $\alpha_0 = 0.19875, 0.72092$ correspond to the 1 and 1.96 standard deviation 3-dimensional ellipsoids, thus the 1-dimensional projections represent the 1 and 1.96 standard deviations of each individual parameter[24], regardless the other parameters[25]. This procedure results in a confidence domain with the minimum possible area and so has maximum power to exclude alternative hypotheses. The integral in Eq.(128) with the contour condition given by Eq. (129) can be evaluated analytically by performing a change of variable to 4-dimensional hyperspheric coordinates, with the subsequent gain in CPU and precision. The analytical calculation of the integral yields

$$\alpha(\mathbf{p}^{\mathrm{t}}) \quad = \quad 1 - e^{-\frac{1}{2}\bar{\rho}^2}\left(1 + \frac{\bar{\rho}^2}{2}\right) \ , \tag{130}$$

where

$$\bar{\rho}^2 \quad = \quad -2\ln\left[(2\pi)^2 \sigma_{x+}\sigma_{y+}\sigma_{x-}\sigma_{y-}\sqrt{(1-\rho_+^2)(1-\rho_-^2)}\lambda(\mathbf{p}^{\mathrm{t}})\right] \tag{131}$$

with

$$\lambda(\mathbf{p}^{\mathrm{t}}) \quad \equiv \quad \frac{d^4P}{d^2\mathbf{z}_+ d^2\mathbf{z}_-}(\mathbf{z}_+^{\mathrm{data}}, \mathbf{z}_-^{\mathrm{data}} | \mathbf{p}^{\mathrm{t}}) \ . \tag{132}$$

The correct coverage provided by our is demonstrated in section 6.1.6.

6.1.3 1- and 2-dimensional projections of confidence regions for D^0K and $D^{*0}K$

Applying this procedure separately to D^0K and $D^{*0}K$, and projecting in 1 and 2 dimensions we obtain the projections of the 3-dimensional regions of $1-\alpha_0$ joint probability. Figures 64 and 65 show the 2-dimensional projections of the the 19.9% (dark blue) and 72.1% (bright blue) confidence-level 3-dimensional regions for the D^0K and $D^{*0}K$ modes. Similarly, figures 66 and 67 show the 1-dimensional projections, which correspond to 1 and 1.96 sigma

[24] 1.96σ corresponds to a 95% probability content for the case of a 1-dimensional Gaussian distribution [49].
[25] These values of α_0 are the cumulative (upper) integral of a χ^2 probability distribution for $\chi^2 = 1^2, 1.96^2$ and $\nu = 3$ degrees of freedom [49].

standard deviation of each single parameter, regardless the values of the others. In the 1-dimensional projections we also show the projection of the PDF. Notice that both the 2- and 1-dimensional projections show the $\pm180°$ ambiguity in $\gamma^{(*)}$ and $\delta^{(*)}$. The probability density functions for r_B and r_B^* show clearly the non-Gaussian behavior we expect from Toy Monte Carlo, as well as the poor sensitivity to small values. Table 28 reports numerically the one dimensional 1σ and 1.96σ intervals[26]. The results include the intrinsic two fold ambiguity for $\gamma^{(*)}$ and $\delta^{(*)}$.

Parameter	1σ	1.96σ
r_B	[0.051,0.184]	[0,0.238]
γ	[33,108] [213,288]	–
δ	[67,142] [247,322]	–
r_B^*	[0.090],0.248]	[0.027,0.318]
γ^*	[36,106] [216,286]	[11,140] [191,320]
δ^*	[262,332] [82,152]	[234,363] [54,183]

Table 28: *The 1σ (1.96σ) intervals for r_B, δ, γ (D^0K) and r_B^*, γ^* and δ^* ($D^{*0}K$). For γ and δ the ±180 degree solution is also indicated.*

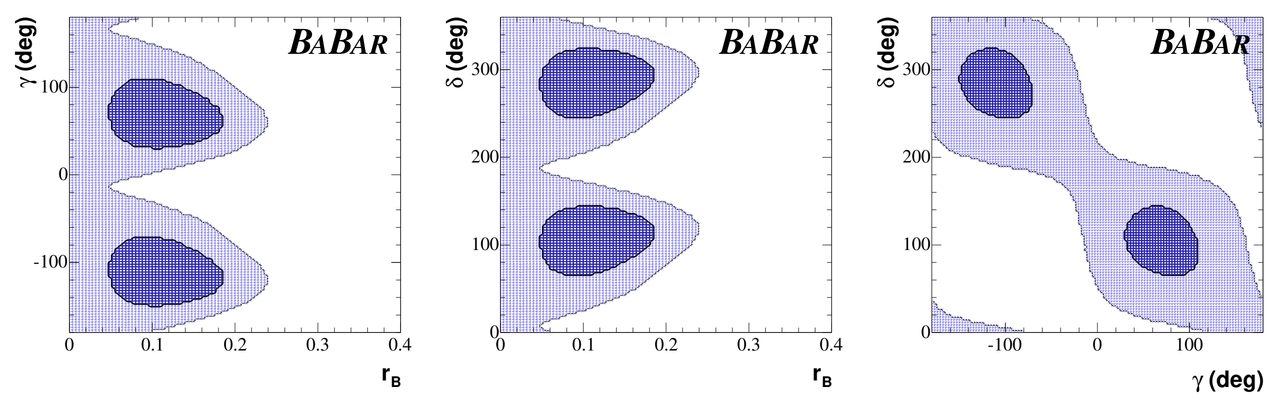

Figure 64: *2-dimensional projections of the 19.9% (dark blue) and 72.1% (bright blue) confidence-level 3-dimensional regions for the D^0K mode.*

6.1.4 Combination of D^0K and $D^{*0}K$ decay modes

We have combined the two event samples, D^0K and $D^{*0}K$, in order to obtain a more accurate measurement of γ. The method we have used for the combination of the results is identical to that used for each B decay mode separately, but now we have five true parameters $\mathbf{p}^{t}=$

[26] The numerical confidence intervals have been obtained using 10^9 points and an step variation (precision) of 0.0002 on r_B and $0.1°$ on the angles, while for the 2- and 1-dimensional figures a poorer precision of 10^7 points and an step variation of 0.004 and $3°$ is enough (a better, publication quality could be obtained with 5×10^7 points and an step variation of 0.001 and $1°$).

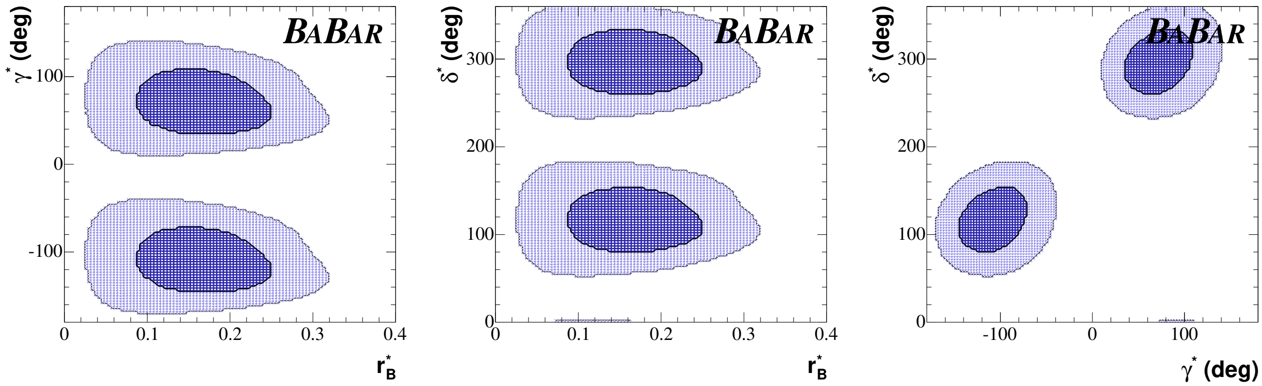

Figure 65: *2-dimensional projections of the 19.9% (dark blue) and 72.1% (bright blue) confidence-level 3-dimensional regions for the $D^{*0}K$ mode.*

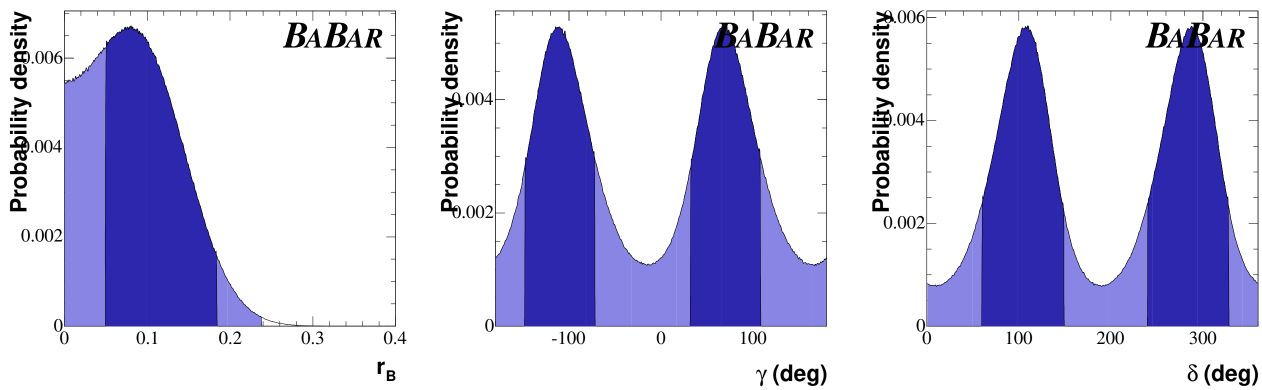

Figure 66: *Probability density functions for r_B, γ and δ together with the 1-dimensional projections of the 19.9% (dark blue) and 72.1% (bright blue) confidence-level 3-dimensional regions for the D^0K mode.*

$(\gamma^t, r_B^t, \delta^t, r_B^{*t}, \delta^{*t})$ and an 8-dimensional cartesian space for the measured parameters $(\mathbf{z}_\pm, \mathbf{z}^*_\pm)$ $= (x_\pm, y_\pm, x^*_\pm, y^*_\pm)$. The PDF in this case reads

$$\begin{aligned}\frac{d^8P}{d^2\mathbf{z}_+ d^2\mathbf{z}_- d^2\mathbf{z}^*_+ d^2\mathbf{z}^*_-}(\mathbf{z}_+, \mathbf{z}_-, \mathbf{z}^*_+, \mathbf{z}^*_-|\mathbf{p}^{\rm t}) &= \frac{d^4P}{d^2\mathbf{z}_+ d^2\mathbf{z}_-}(\mathbf{z}_+, \mathbf{z}_-|r_B^t, \gamma^t, \delta^t) \times \\ &\quad \frac{d^4P}{d^2\mathbf{z}^*_+ d^2\mathbf{z}^*_-}(\mathbf{z}^*_+, \mathbf{z}^*_-|r_B^{*t}, \gamma^t, \delta^{*t}) \ . \end{aligned} \tag{133}$$

The confidence-level $1 - \alpha$ for each set of true parameters $\mathbf{p}^{\rm t}$ is now calculated as

$$\alpha(\mathbf{p}^{\rm t}) = \int_D \frac{d^8P}{d^2\mathbf{z}_+ d^2\mathbf{z}_- d^2\mathbf{z}^*_+ d^2\mathbf{z}^*_-}(\mathbf{z}_+, \mathbf{z}_-, \mathbf{z}^*_+, \mathbf{z}^*_-|\mathbf{p}^{\rm t}) d^2\mathbf{z}_+ d^2\mathbf{z}_- d^2\mathbf{z}^*_+ d^2\mathbf{z}^*_- \ , \tag{134}$$

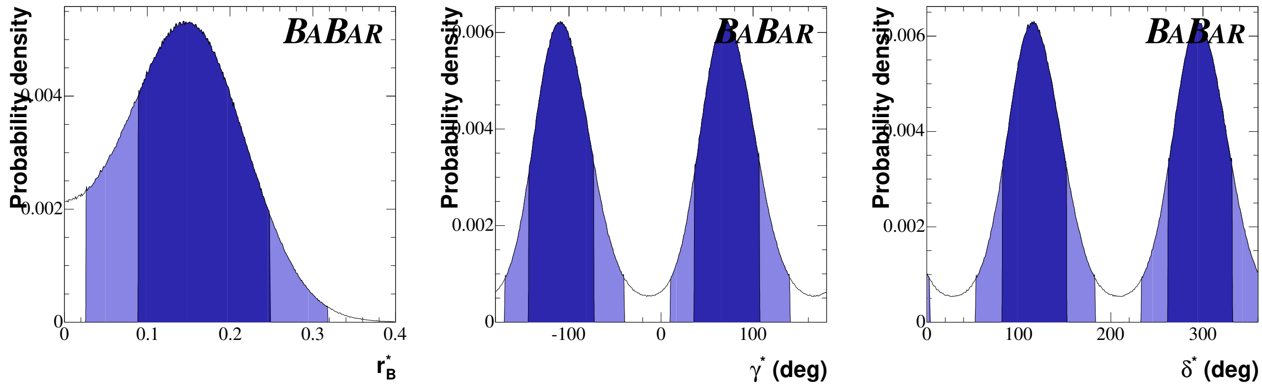

Figure 67: *Probability density functions for* $r_B{}^*$, γ *and* δ^* *together with the 1-dimensional projections of the 19.9% (dark blue) and 72.1% (bright blue) confidence-level 3-dimensional regions for the* $D^{*0}K$ *mode.*

where the integration domain D (the confidence region) is given by the condition

$$\frac{d^8P}{d^2\mathbf{z}_+d^2\mathbf{z}_-d^2\mathbf{z}^*_+d^2\mathbf{z}^*_-}(\mathbf{z}_+,\mathbf{z}_-,\mathbf{z}^*_+,\mathbf{z}^*_-|\mathbf{p}^{\mathrm{t}}) \geq \frac{d^8P}{d^2\mathbf{z}_+d^2\mathbf{z}_-d^2\mathbf{z}^*_+d^2\mathbf{z}^*_-}(\mathbf{z}_+^{\mathrm{data}},\mathbf{z}_-^{\mathrm{data}},\mathbf{z}^{*\ \mathrm{data}}_+,\mathbf{z}^{*\ \mathrm{data}}_-|\mathbf{p}^{\mathrm{t}}) \quad (135)$$

As before, the above integral can be calculated analytically:

$$\alpha(\mathbf{p}^{\mathrm{t}}) = 1-e^{-\frac{1}{2}\bar{\rho}^2}\left(1+\frac{\bar{\rho}^2}{2}+\frac{\bar{\rho}^4}{8}+\frac{\bar{\rho}^6}{48}\right) , \quad (136)$$

where

$$\bar{\rho}^2 = -2\ln\left[(2\pi)^4\sigma_{x_+}\sigma_{y_+}\sigma_{x_-}\sigma_{y_-}\sigma^*_{x_+}\sigma^*_{y_+}\sigma^*_{x_-}\sigma^*_{y_-}\sqrt{(1-\rho_+^2)(1-\rho_-^2)(1-\rho_+^{*2})(1-\rho_-^{*2})}\lambda(\mathbf{p}^{\mathrm{t}})\right] \quad (137)$$

with

$$\lambda(\mathbf{p}^{\mathrm{t}}) \equiv \frac{d^8P}{d^2\mathbf{z}_+d^2\mathbf{z}_-d^2\mathbf{z}^*_+d^2\mathbf{z}^*_-}(\mathbf{z}_+^{\mathrm{data}},\mathbf{z}_-^{\mathrm{data}},\mathbf{z}^{*\ \mathrm{data}}_+,\mathbf{z}^{*\ \mathrm{data}}_-|\mathbf{p}^{\mathrm{t}}) . \quad (138)$$

The 5-dimensional confidence region in $\mathbf{p}^{\mathrm{t}}$ space is constructed by generating a large number, $\mathcal{O}(10^{10})$ of points $\mathbf{p}^{\mathrm{t}} \equiv (r_B^t, \gamma^t, \delta^t, r_B^t{}^*, \delta^*)$, in the ranges $[0, 0.4]$, $[-180°, 180°]$, $[0, 360°]$, $[0, 0.4]$, and $[0, 360°]$, respectively, and selecting the points for which $\alpha(\mathbf{p}^{\mathrm{t}}) \leq \alpha_0 = 0.03743, 0.42756$. These values α_0 correspond to the 1 and 1.96 standard deviation 5-dimensional ellipsoids, thus the 1-dimensional projections represent the 1 and 1.96 standard deviations of each individual parameter, regardless the other parameters [27]. As before, the 2- and 1-dimensional contours are then built by projecting the 5-dimensional joint probability regions. Figures 68 and 69 show the 2-dimensional projections of the 3.7% (dark

[27] These values of α_0 are the cumulative (upper) integral of a χ^2 probability distribution for $\chi^2 = 1^2, 1.96^2$ and $\nu = 5$ degrees of freedom [49].

blue) and 42.8% (bright blue) confidence-level 5-dimensional regions for D^0K and $D^{*0}K$ modes (γ is common). The corresponding 1-dimensional projections, together with the PDF projections, are shown in figure 70. Notice that both the 2- and 1-dimensional projections show the $\pm 180°$ ambiguity in γ and $\delta^{(*)}$.

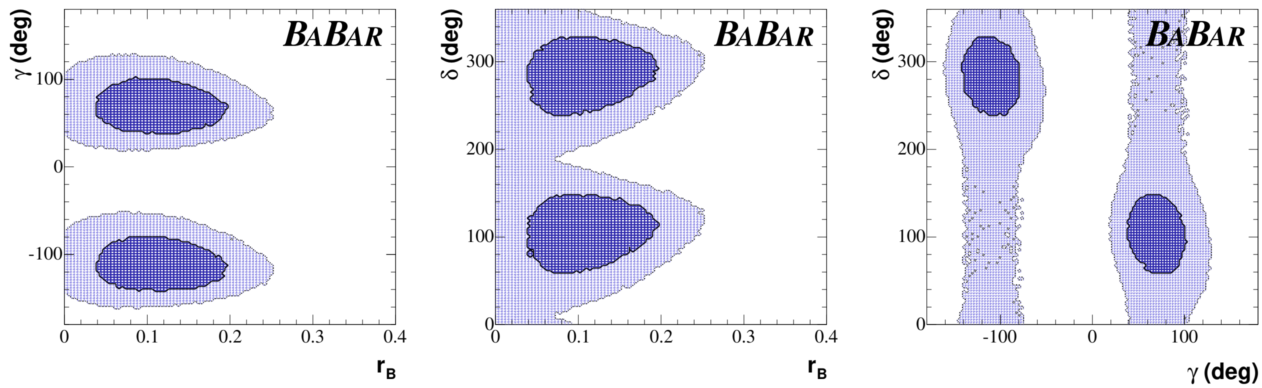

Figure 68: *2-dimensional projections of the 3.7% (dark blue) and 42.8% (bright blue) confidence-level 5-dimensional regions for the D^0K - $D^{*0}K$ combined mode. The r_B and δ variables are for the D^0K decay sample.*

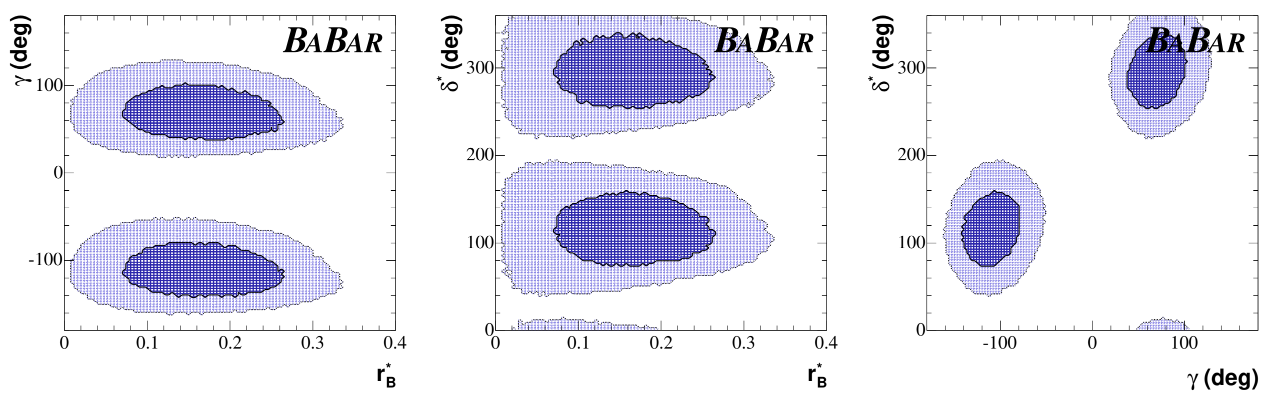

Figure 69: *2-dimensional projections of the 3.7% (dark blue) and 42.8% (bright blue) confidence-level 5-dimensional regions for the D^0K - $D^{*0}K$ combined mode. The ${r_B}^*$ and δ^* variables are for the $D^{*0}K$ decay sample.*

Table 29 reports numerically the 1-dimensional 1σ and 1.96σ intervals[28]. The results include the intrinsic two fold ambiguity for γ and $\delta^{(*)}$. In the last column of the table we also report central values of the true parameters with 1σ errors. The central values for the

[28]The numerical confidence intervals have been obtained using 10^10 points and an step variation (precision) of 0.0002 on r_B and 0.1° on the angles, while for the 2- and 1-dimensional figures a poorer precision of 10^7 points and an step variation of 0.004 and 3° is enough (a better, publication quality could be obtained with 5×10^7 points and an step variation of 0.001 and 1°).

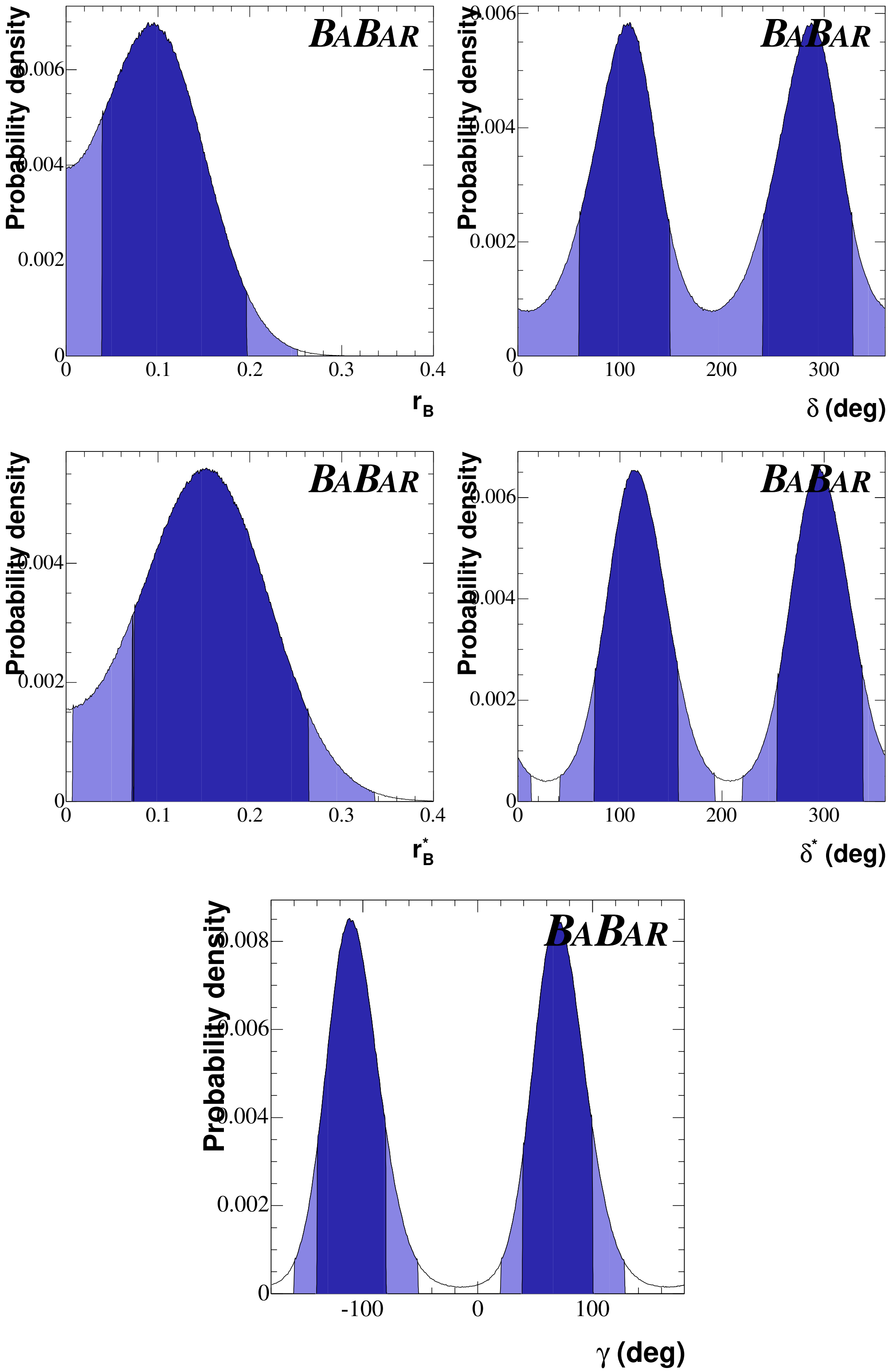

Figure 70: *Probability density functions for r_B, δ, $r_B{}^*$, δ^* and γ together with the 1-dimensional projections of the 3.7% (dark blue) and 42.8% (bright blue) confidence-level 5-dimensional regions for the D^0K - $D^{*0}K$ combination.*

true parameters are estimated as the mean value of the interval (statistical only). The central value and one standard deviation (which corresponds to the 3.7% confidence-level region for the case of a 5-dimensional Gaussian distribution) for γ is therefore $\gamma = (70 \pm 31)^\circ$, while the 1.96 standard deviation interval (which corresponds to the 42.8% confidence-level region for a 5-dimensional Gaussian distribution) is $20^\circ < \gamma < 128^\circ$ ($200^\circ < \gamma < 308^\circ$).

Parameter	1σ	1.96σ	Central value with error (1σ)
γ	[39,101] [219,281]	[20,128] [200,308]	70 ± 31
r_B	[0.040,0.196]	[0,0.253]	0.118 ± 0.079
r_B^*	[0.073],0.265]	[0.007,0.336]	0.169 ± 0.096
δ	[59,149] [239,329]	–	104 ± 45
δ^*	[255,338] [75,158]	[220,374] [40,194]	296 ± 41

Table 29: *The 1σ (1.96σ) D^0K-$D^{*0}K$ combined intervals for r_B, $r_B{}^*$, δ, δ^*, and γ (angles are in degree). In the last column the central values with 1σ errors are also reported. For the γ, δ and δ^* intervals the ± 180 degree solution is also indicated.*

6.1.5 Significance of *CP* violation

The significance of *CP* violation can be determined by finding the confidence-level $1 - \alpha_{\not{CP}}$ for the most probable *CP* conserving point $\mathbf{p}^{\rm t}_{CP}$, i.e. the $\mathbf{p}^{\rm t}$ point with $r^t_B = 0$ or $\gamma^t = 0$,

$$\mathbf{p}^{\rm t}_{CP} = \{\mathbf{p}^{\rm t} | \mathbf{p}^{\rm t} = (r^t_B = 0, \gamma^t, \delta^t) \text{ or } \mathbf{p}^{\rm t} = (r^t_B, \gamma^t = 0, \delta^t)\} \ . \tag{139}$$

for which $\alpha(\mathbf{p}^{\rm t})$ is minimal. In this way, $1 - \alpha_{\not{CP}}$ represents the *CP* conservation confidence-level, and therefore $\alpha_{\not{CP}}$ represents the *CP* violation confidence-level (or significance of *CP* violation).

In the case of the combined measurement of γ we can evaluate the *CP* significance as follows

$$\mathbf{p}^{\rm t}_{CP} = \{\mathbf{p}^{\rm t} | \mathbf{p}^{\rm t} = (r^t_B = 0, r^{*t}_B = 0, \gamma^t, \delta^t, \delta^{*t}) \text{ or } \mathbf{p}^{\rm t} = (r^t_B, r^{*t}_B, \gamma^t = 0, \delta^t, \delta^{*t})\} \ . \tag{140}$$

For the D^0K we have $\alpha_{\not{CP}} = 0.655$ in $\mathbf{p}^{\rm t}$=(r^t_B,γ^t,δ^t)=(0.043,0°,124°), for the $D^{*0}K$ we have $\alpha_{\not{CP}} = 0.828$ in $\mathbf{p}^{\rm t}$=(r^{*t}_B,γ^t,δ^{*t})=(0.070,0°, 280°), while for the combined measurement we have $\alpha_{\not{CP}} = 0.791$ in $\mathbf{p}^{\rm t}$=(r^t_B,γ^t,δ^t,r^{*t}_B,δ^{*t})=(0.044,0°,123°,0.073,279°). We quote *CP* violation in the D^0K at 65.5% CL, in the $D^{*0}K$ at 82.8% CL and in the combined measurement at the 79.1% CL. These confidence-levels correspond to the 1.82, 2.24, and 2.68 standard deviation ellipsoids.

6.1.6 Coverage test with the experimental likelihood

A simple and powerful check that the whole procedure has been applied and implemented correctly, including the simplifications made when constructing the analytical forms of the Frequentist PDFs, Eqs. (126) and (133), is to check the coverage given by the estimated

confidence regions using the experimental likelihood $\mathcal{L}_{exp}$. The test makes use of the Frequentist definition of coverage, as given in section 6.1: a region with confidence-level $1-\alpha_0$ will contain the unknown true point in a fraction $1-\alpha_0$ of the experiments, or in other words, if the experiment is carried out many times, a fraction $1-\alpha_0$ of those experiments will find the measured point within the given confidence region.
The procedure was the following: about 20K Toy Monte Carlo experiments tuned to the data were generated with truth values of r_B, γ, δ, $r_B{}^*$ and δ^*, reported in Table 29. These values represent the vector of true parameters, $\mathbf{p}^{\rm t} = (r_B^t, \gamma^t, \delta^t, r_B^{*t}, \delta^{*t})$. Each experiment was then fit in cartesian coordinates, obtaining a set of $\mathbf{z}^i = (x_\pm^i, y_\pm^i, x_\pm^{*i}, y_\pm^{*i})$ values from which the confidence-level $1-\alpha(\mathbf{p}^{\rm t})$ was calculated using Eqs. (134) and (135). Now the *data* point $\mathbf{z}^{data}$ is substituted by the *Toy Monte Carlo experiment* $\mathbf{z}^i$ point. If the procedure provides the correct coverage then the fraction of Toy Monte Carlo experiments verifying $\alpha(\mathbf{p}^{\rm t}) \leq \alpha_0$ should consistent with α_0 .

The coverage as a function of the value of α_0 in bins of size 0.1 is shown in figure 71. Within errors, the coverage is correct for all the possible confidence-level values.

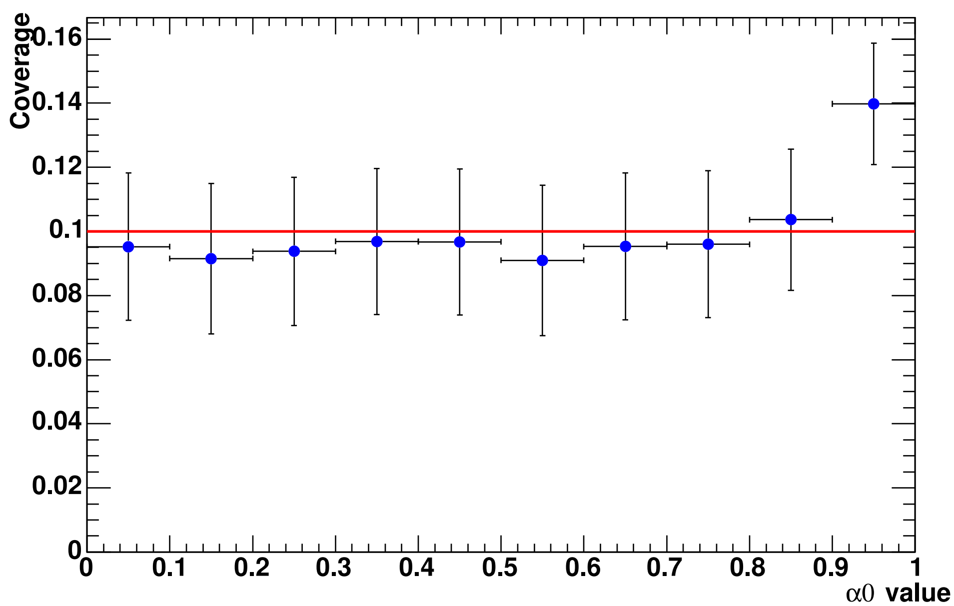

Figure 71: *Distribution of the α_0 value in the ToyMonte Carlo experimental likelihood (coverage) for the central values of truth r_B and r_B^* values (table 29). The red line represents the perfect coverage case, blue points are the coverage value from the ToyMC experiments for each α_0 bin of size 0.1. The error bars are due to the limited statistics of experiments (20K). Within errors, the coverage is correct for all the possible confidence-level values.*

The coverage check has been repeated by changing the truth value of r_B and r_B^* by $\pm 1\sigma$ (according to the last column of table 29), keeping the same values for the phases. Moving r_B and r_B^* is enough for the purpose of this check since what we want to study is any potential change in the coverage by the scaling of the cartesian coordinates. A total of 10K experiments were generated for each of these points. The $\alpha_0 = 3.74\%$ (42.76%) 5-dimensional confidence-level coverage for the lower 1σ bound is $4.1 \pm 0.2\%$ and for the upper bound is $3.6 \pm 0.2\%$. Again, taking into account the statistical errors, the coverage is correct for all the possible confidence-level values.

Finally, as a sanity check, we used the same Toy Monte Carlo experiments to check directly the 1-dimensional coverage provided by the cartesian coordinates $(x_{\pm}, y_{\pm}, x^*_{\pm}, y^*_{\pm})$, which turn to be perfectly consistent with 68.3% (95%) with an error from the limited number of Toy Monte Carlo experiments of 0.006 (0.007).

6.2 Systematic uncertainties

The systematic uncertainties on the *CP* parameters (r_B, γ, δ) can be included very easily, within the Frequentist method, by replacing the statistical errors $\sigma_{x\pm}$ and $\sigma_{y\pm}$ in Eqq. 126, 133 with the total error $\sqrt{\sigma^2_{x\pm} + \sigma^2_{x\pm,syst}}$ and $\sqrt{\sigma^2_{y\pm} + \sigma^2_{x\pm,syst}}$, respectively. As the statistical uncertainties dominate yet this measurement and the largest systematic uncertainties are uncorrelated among the two samples, it is appropriate to assume that the global correlations $\rho_\pm$ remain unchanged with respect to their statistical values. In any case, it has been checked that the impact of the correlation on the confidence regions/intervals negligible. Table 30 summarizes the main systematic uncertainties of the measurement in cartesian coordinates, for the D^0K and $D^{*0}K$ decay modes. For comparison, we indicate the Dalitz model systematics by using the CLEO model –like the nominal one but excluding the following resonances: σ_1, σ_2, $K_0^*(1430)$ DCS, $K_2^*(1430)$ DCS, $K^*(1410)$, and $\rho(1450)$– and a model like the nominal one but excluding only the σ_1 and σ_2 resonances. We use the CLEO model to quote final Dalitz model systematics, but the alternative model excluding only the σ's has essentially the same effect, on both cartesian and polar variables; in other words, the Dalitz model effect is almost exclusively due to the non well established σ_1 and σ_2 resonances.

Table 31 reports the 1σ and 1.96σ intervals for $r_B{}^{(*)}$, γ, and $\delta^{(*)}$, as obtained by repeating the Frequentist procedure with each systematic uncertainty contribution included. In the last column of the table we also report the central values with 1σ error breakdown (statistical, experimental systematic and Dalitz model systematic).

The significance of *CP* violation becomes now 51.2% CL in $\mathbf{p}^t = (r^t_B, \gamma^t, \delta^t)$=(0.038,0°,116°) for D^0K, 75.9% CL in $\mathbf{p}^t = (r^{*t}_B, \gamma^t, \delta^{*t})$ =(0.078,0°, 279°) for $D^{*0}K$, and 65.1% CL in $\mathbf{p}^t = (r^t_B, \gamma^t, \delta^t, r^{*t}_B, \delta^{*t})$=(0.033,0°,117°,0.082,279°) for the combined measurement. These confidence levels correspond to the 1.56, 2.05, and 2.36 standard deviation ellipsoids (88.1%, 96.0%, and 98.2% probability content for the case of 1-dimensional Gaussian distributions).

In the following subsections we describe how each systematic uncertainty contribution in the cartesian coordinate space has been evaluated.

6.2.1 $m_{\rm ES}$, ΔE and Fisher shapes

The effect of fixing the PDF shapes in the *CP* fit has been evaluated by performing a simultaneous PDF shape and *CP* fit. Since the extraction of the shapes relies mainly on the $D\pi$ sample, the *CP* and shapes fit is performed simultaneously to the DK and $D\pi$ samples, whith shapes fixed and floated. The systematics was then taken as the quadratic difference of the errors reported by the two fits. In all cases the difference between the central values of the two fits is well below the statistical difference.

The $m_{\rm ES}$ endpoint in the Argus parameterization is fixed in the nominal fit to 5.290 GeV (the same value is also used as integration limit of the $m_{\rm ES}$ PDF). To estimate the effect of it in the determination of the signal yields and its impact on the *CP* parameters we have varied it by ± 0.5 MeV. It was found to be completely negligible.

6.2.2 Background composition

The uncertainty due to the fraction of real D^0's in background is estimated by varying this parameter within its statistical error and then repeating the fit to the data sample. In order

Source	x_+	y_+	x_-	y_-	x^*_+	y^*_+	x^*_-	y^*_-
$m_{\rm ES}, \Delta E, \mathcal{F}$ shapes	0.0105	0.0086	0.0088	0.0141	0.0196	0.0218	0.0218	0.0146
Real D^0 fraction	0.0050	0.0047	0.0061	0.0036	0.0035	0.0049	0.0028	0.0032
Right sign D^0's	0.0157	0.0090	0.0070	0.0211	0.0065	0.0163	0.0108	0.0103
Eff. in the Dalitz plot	0.0078	0.0085	0.0089	0.0119	0.0067	0.0119	0.0040	0.0079
Tracking efficiency	0.0082	0.0080	0.0095	0.0123	0.0058	0.0109	0.0051	0.0046
Cont bkg. Dalitz shape	0.0195	0.0096	0.0160	0.0149	0.0133	0.0084	0.0083	0.0046
BB bkg. Dalitz shape	0.0026	0.0072	0.0069	0.0130	0.0061	0.0098	0.0029	0.0003
Invariant mass resolution	0.0031	0.0023	0.0022	0.0016	0.0031	0.0023	0.0022	0.0016
Dalitz amplitude and phases	0.0012	0.0069	0.0050	0.0033	0.0043	0.0138	0.0079	0.0079
SubTotal	0.0301	0.0226	0.0258	0.0368	0.0275	0.0373	0.0280	0.0223
Dalitz model (CLEO)	0.0324	0.0214	0.0185	0.0424	0.0253	0.0560	0.0206	0.0249
Total (CLEO)	0.0442	0.0311	0.0318	0.0561	0.0374	0.0673	0.0348	0.0334
Dalitz model (no σ_1, σ_2)	0.0336	0.0258	0.0207	0.0374	0.0255	0.0464	0.0209	0.0396
Total (no σ_1, σ_2)	0.0451	0.0343	0.0331	0.0525	0.0375	0.0595	0.0349	0.0454

Table 30: *Summary of the contributions to the systematic error in cartesian coordinates,* $(x_\pm, y_\pm)$ *and* $(x^*_\pm, y^*_\pm)$*.*

Parameter	1σ	1.96σ	Central value with error (1σ)
γ	[36,106] [216,286]	[13,136] [193,316]	$70 \pm 31\ ^{+12}_{-10}\ ^{+14}_{-11}$
r_B	[0.025,0.211]	[0,0.277]	$0.118 \pm 0.079 \pm 0.034\ ^{+0.036}_{-0.034}$
r^*_B	[0.066],0.274]	[0,0.352]	$0.169 \pm 0.096\ ^{+0.030}_{-0.028}\ ^{+0.029}_{-0.026}$
δ	[48,155] [228,335]	–	$104 \pm 45\ ^{+17}_{-21}\ ^{+16}_{-24}$
δ^*	[251,342] [71,162]	–	$296 \pm 41\ ^{+14}_{-12} \pm 15$

Table 31: *The* 1σ *(*1.96σ*)* D^0K*-*$D^{*0}K$ *combined intervals including systematic uncertainties for* r_B*,* ${r_B}^*$*,* δ*,* δ^* *and* γ *(angles are in degree). In the last column the central values with* 1σ *error break-down are reported: the first errors are statistical, the second are experimental systematics, and the third are Dalitz model systematics. For the* γ*,* δ *and* δ^* *intervals the* ± 180 *degree solution is also reported.*

to be conservative, we have moved up and down by one sigma these fractions for all the samples –D^0K, $(D^0\pi^0)K$ and $(D^0\gamma)K$– and components (Cont and B$\overline{\text{B}}$) simultaneously. In the case of the B$\overline{\text{B}}$ fraction for D^0K events, an upper limit of 10% was used to evaluate this systematics. The larger between the half difference between the two fits and the quadratic difference of the fit errors is assigned as systematic uncertainty.

A potential difference in the number of real D^0's in the continuum background between B^+ and B^- events could fake CP violating effects in the signal. No significant difference between B^+ and B^- has been found in Monte Carlo. Nevertheless, we account for any potential effect by introducing an independent set of CP parameters for the continuum background with a real D^0. By repeating the nominal fit with this new set of parameters we found a negligible impact on the CP parameters.

The fraction of right sign (RS) D^0's is taken from Monte Carlo simulation. We have estimated this contribution from the variation of the CP parameters in the fit to the data sample when a value of 0.5 is assumed instead of the nominal values. As before, we take the larger between the difference of central values and the quadratic difference of fit errors. The change observed on the CP parameters is consistent with the larger between the bias and the rms from a set of Toy Monte Carlo experiments generated with the nominal value and fit with 0.5.

6.2.3 Dalitz efficiency

To estimate the effect from the Dalitz efficiency the nominal CP fit was repeated by assuming a flat distribution instead of the nominal 3rd order polynomial parameterization. In addition, we have evaluated a systematics due to tracking and K^0_S reconstruction efficiency over the Dalitz plot. It has been evaluated by repeating the fit using alternative values of the 3rd order polynomial parameterization coefficients with: i) the tracking efficiency correction applied on the 2 pions from the D^0 decay and the bachelor kaon; and ii) tracking efficiency correction applied to the pions from the K^0_S decay. In all cases, we take the larger between the difference of central values and the quadratic difference of fit errors. The uncertainties from the two corrections have been added quadratically.

6.2.4 Dalitz shape for combinatorial background

The Dalitz shape for combinatorial continuum events is estimated by using off-resonance data. The correction for $B\overline{B}$ combinatorial background is obtained from Monte Carlo simulation. The systematics from this correction is estimated from the difference on the CP parameters when flat distributions are assumed instead. We take the larger between the difference of central values and the quadratic difference of fit errors.

6.2.5 Limited mass resolution

The nominal Dalitz model assumes perfect mass resolution. Given that all the resonances present in the $D^0 \to K^0_S\pi^+\pi^-$ decay are quite wide compared to the estimated mass resolution (about 4 MeV^2 for a $K^0_S\pi^+$ mass squared of about 1 GeV^2, we expect the effect to be completely negligible. Only the $\omega(782)$ has an intrinsic width comparable to the mass resolution (about 6 MeV^2 for a squared $\pi^+\pi^-$ mass of 0.8 GeV^2, but the sensitivity of the CP

parameters is in this case suppressed. To evaluate the effect of the limited mass resolution on the Dalitz plot, two different fits were performed to the reweighted signal Monte Carlo. The first fit used the reconstructed $K_S^0\pi^+$ and $K_S^0\pi^-$ masses, while the second was performed with the Monte Carlo truth masses (perfect resolution). The difference of fit values was taken as our systematic uncertainty. The errors from the fit for the different parameters were basically unchanged between the two fits.

6.2.6 Dalitz PDF normalization

We have investigated a possible systematic uncertainty due to the limited numerical precision in the evaluation of the Dalitz PDF normalization integral. It has been done by increasing by a factor 25 the number of cells in the integration grid, on both Toy Monte Carlo experiments and the data fit. This corresponds to 5 times more bins on each dimension, i.e. $N_{grid} = 200 \rightarrow 1000$, or equivalently a precision of 1.1 MeV precision on the $K_S^0\pi^+$ and $K_S^0\pi^-$ masses. In both cases the change in the CP parameters was found to be negligible. As cross-check, the nominal fit was also redone by using Vegas Monte Carlo integration with $N_{Vegas} = 1.6 \times 10^7$ events. Again, the effect on the CP parameters was found equally to be negligible.

6.2.7 Statistical errors on Dalitz amplitudes and phases

The phases and amplitudes of the Dalitz model are fixed to the values found from the fit to the high statistics $D^{*+} \rightarrow D^0\pi_s^+$ sample. We expect its effect to be negligible. Nevertheless, we estimated its effect by performing a simultaneous DK and $D^{*+} \rightarrow D^0\pi_s^+$ fit with all these parameters floated. The uncertainty is taken as the larger between the difference of central values and the quadratic difference of the errors reported by the two fits. The difference of central values is in all cases consistent with the quadratic difference of the statistical errors.

6.2.8 Dalitz model systematics

The Dalitz model systematics is the single most important contribution to the total systematic uncertainty. To evaluate it, we generated about 500 Toy Monte Carlo experiments [29] tuned to the data sample using the nominal Dalitz model. The experiments were then fit using the nominal model, the CLEO model and a third model identical to the nominal one but excluding only the σ_1 and σ_2 resonances. To get ride of statistical fluctuations and avoid overestimation of the systematic error, each sample was generated with *infinite* statistics (in practice, 10K events per B decay channel). To be conservative, only D^0K and $(D^0\pi^0)K$ events have been used (10K events each) since it was found that the effect for $(D^0\pi^0)K$ and $(D^0\gamma)K$ is anticorrelated due to the effective π radians shift between the strong phases, which change the sign for all cartesian components (sine and cosine terms). The systematic uncertainty is finally assigned as the quadratic sum of the mean and rms of the experiment-by-experiment differences.
The problem with this technique is which values for r_B^t, r_B^{*t}, γ^t, δ^t, and δ^{*t} are used in the generation of the experiments. Given the current large statistical errors (table 29), taking

[29] The pseudo-experiments were generated onlyh with signal events, because we want to evaluate only the systematic error coming from the Dalitz model assumption.

the central values would be just a choice among others, especially if the effect turns out to be multiplicative with the truth (generated) value. Unfortunately, it has been verified that the systematic uncertainty for all cartesian components evaluated in this way strongly depends with the values of r_B^t and r_B^{*t} (increases almost linearly with it, since cartesian *CP* parameters depend linearly with r_B and r_B^*), and smoothly with the values of γ^t, δ^t, and δ^{*t}. This dependency has also been verified when the *CP* fit is performed to $r_B{}^{(*)}$, γ and $\delta^{(*)}$ directly. For example, for $r_B^t = 0.12$ the effect on γ is about 10°, but for $r_B^t = 0.03$ it is about 14°. On the contrary, the change on $r_B(r_B^*)$ itself increases almost linearly with $r_B^t(r_B^{*t})$. These dependencies have also been noticed by Belle [50], and the solution they have adopted and claimed to be conservative is to scan the phases for fixed $r_B^t = 0.13$, taking the largest variation from the scan. However, we prefer an alternative solutioin since fixing $r_B^t = 0.13$ does not seem to be most conservative estimate.

The solution we have finally adopted to quote the Dalitz model systematics is the following. As we know that cartesian coordinates behave almost perfectly as independent Gaussians, for each single experiment we generate randomly all the 8 cartesian components, following independent Gaussian distributions with mean and width values as measured in the data (table 25). The rest of the procedure is identical to what was described above. Taking the systematic uncertainty from the mean and rms of the experiment-by-experiment differences for each component, we integrate over the others, which is exactly what we want (meaning of 1σ interval, independent of all the other variables). Note that this procedure cannot be used in polar coordinates due to the non-Gaussian behavior in this case, in addition to the large correlation among these parameters. The quadratic sum of the offsets and rms' are quoted in table 30.

All the three Dalitz models used are based on Breit-Wigner parameterization of resonances, except for the $\rho(770)$ and $\rho(1450)$ for which we use Gounaris-Sakurai parametrization to model better the tails. Since Breit-Wigner amplitudes can only describe well narrow resonances, we introduced the Blatt-Weisskopf penetration factors for the intermediate resonances and a resonance width q^2 dependence to deal with broad states. These quantities and models have, however, large theoretical uncertainties and might be a substantial source of systematic uncertainties. To evaluate these potential effects we have also used two alternative Dalitz models, one using Breit-Wigners also for the $\rho(770)$ and $\rho(1450)$ resonances, and the other without Blatt-Weisskopf form factors. The mean and rms values of the experiment-by-experiment differences for these two models are found to be completely negligible.

As a final check related to the Dalitz model we have studied the impact on the *CP* parameters by imposing the constraint that the phase difference between doubly-Cabibbo suppressed (DCS) and Cabibbo favored (CF) K^* resonances below 1.440 GeV/c^2 ($K\eta'$ threshold) is $(-1)^J$, where J is the spin of the resonance. This is a consequence of the Watson theorem [52]. The constraint applies to $K^*(892)$, $K_0^*(1430)$ and $K_2^*(1430)$, which should have a DCS-CF relative phase of 180°, 0° and 0°, respectively. The fit results to the D^* sample are consistent with this prediction, within statistical errors. To perform this check we have repeatedthe D^* Dalitz fit imposing the constraint on the DCS-CF relative phases, and then the *CP* parameters were obtained by repeating the *CP* fit with this constraint applied. Table 32 shows the *CP* fit results obtained with this constraint. These results should be compared to those of table 25. The results of both fits are consistent within the statistical differences, while there is no evidence of improvement in statistical power. Therefore, no systematic error is assigned. The same conclusion is obtained when the fit is performed in polar coordinates.

Observable	D^0K	$D^{*0}K$
x_-	0.0776 ± 0.0689	-0.1325 ± 0.0934
y_-	0.0613 ± 0.0926	-0.1401 ± 0.1061
x_+	-0.1258 ± 0.0703	0.1333 ± 0.0925
y_+	0.0081 ± 0.0792	0.0213 ± 0.1226

Table 32: *Fit results for $(x_\pm, y_\pm)$ cartesian coordinates with the constraint $(-1)^J$ on the phase difference between doubly-Cabibbo suppressed (DCS) and Cabibbo favored (CF) $K^*(892)$, $K_0^*(1430)$ and $K_2^*(1430)$ resonances applied, for the D^0K and $D^{*0}K$ decay modes.*

7 Conclusions

The final results we are going to present in the next paragraph have been reported in a journal paper and submitted to the Physical Review Letter [70].

7.1 Final Results

Using an integrated luminosity of 205 fb^{-1} corresponding to the summer 2004 available data sample, we have performed a Dalitz analysis of $B^- \to D^{(*)}K^-$, with $D^* \to D^0\pi^0, D^0\gamma$, $D^0 \to K_S\pi^+\pi^-$ decays, obtaining the following CP-violating parameter results:

$$\begin{aligned}
x_- \equiv \mathrm{Re}(r_{B_-}e^{i\theta_-}) &= \quad 0.077 \pm 0.069(\mathrm{stat.}) \pm 0.026(\mathrm{exp.\ syst.}) \pm 0.019(\mathrm{model\ syst.})\ , \\
y_- \equiv \mathrm{Im}(r_{B_-}e^{i\theta_-}) &= \quad 0.064 \pm 0.092(\mathrm{stat.}) \pm 0.037(\mathrm{exp.\ syst.}) \pm 0.042(\mathrm{model\ syst.})\ , \\
x_+ \equiv \mathrm{Re}(r_{B_+}e^{i\theta_+}) &= -0.129 \pm 0.070(\mathrm{stat.}) \pm 0.030(\mathrm{exp.\ syst.}) \pm 0.032(\mathrm{model\ syst.})\ , \\
y_+ \equiv \mathrm{Im}(r_{B_+}e^{i\theta_+}) &= \quad 0.019 \pm 0.079(\mathrm{stat.}) \pm 0.023(\mathrm{exp.\ syst.}) \pm 0.021(\mathrm{model\ syst.})\ , \\
x_-^* \equiv \mathrm{Re}(r_{B_-^*}e^{i\theta_-^*}) &= -0.131 \pm 0.093(\mathrm{stat.}) \pm 0.028(\mathrm{exp.\ syst.}) \pm 0.021(\mathrm{model\ syst.})\ , \\
y_-^* \equiv \mathrm{Im}(r_{B_-^*}e^{i\theta_-^*}) &= -0.143 \pm 0.105(\mathrm{stat.}) \pm 0.022(\mathrm{exp.\ syst.}) \pm 0.025(\mathrm{model\ syst.})\ , \\
x_+^* \equiv \mathrm{Re}(r_{B_+^*}e^{i\theta_+^*}) &= \quad 0.140 \pm 0.093(\mathrm{stat.}) \pm 0.028(\mathrm{exp.\ syst.}) \pm 0.025(\mathrm{model\ syst.})\ , \\
y_+^* \equiv \mathrm{Im}(r_{B_+^*}e^{i\theta_+^*}) &= \quad 0.013 \pm 0.120(\mathrm{stat.}) \pm 0.037(\mathrm{exp.\ syst.}) \pm 0.056(\mathrm{model\ syst.})\ ,
\end{aligned}$$

where $\theta_\pm^{(*)} = \delta^{(*)} \pm \gamma$, with γ the CKM weak phase, $\delta^{(*)}$ the strong phase of the $B^- \to D^{(*)}K^-$ decay, and ${r_B}^{(*)}$ the absolute value of the ratio of the corresponding $\mathcal{A}(b \to u\bar{c}s)$ and $\mathcal{A}(b \to c\bar{u}s)$ amplitudes, $r_B = |A(b \to u\bar{c}s)/A(b \to c\bar{u}s)|$. The first errors are statistical, the second are experimental systematics and the third are the uncertainities related on the assumptions on the representation of the D^0 decay amplitude in the different regions of the Dalitz plane.

A classical (Frequentist) analysis of the previous results yields the following results for the CP-violating parameters γ, $\delta^{(*)}$ and ${r_B}^{(*)}$:

$$\begin{aligned}
\gamma &= 70(250)^\circ \pm 31^\circ(\mathrm{stat.})^{+12^\circ}_{-10^\circ}(\mathrm{exp.\ syst.})^{+14^\circ}_{-11^\circ}(\mathrm{model\ syst.}) \quad [13^\circ, 136^\circ]\ , \\
\delta &= 104(284)^\circ \pm 45^\circ(\mathrm{stat.})^{+17^\circ}_{-21^\circ}(\mathrm{exp.\ syst.})^{+16^\circ}_{-24^\circ}(\mathrm{model\ syst.}) \quad [0^\circ, 360^\circ]\ , \\
\delta^* &= 296(116)^\circ \pm 41^\circ(\mathrm{stat.})^{+14^\circ}_{-12^\circ}(\mathrm{exp.\ syst.}) \pm 15^\circ(\mathrm{model\ syst.}) \quad [0^\circ, 360^\circ]\ , \\
r_B &= 0.118 \pm 0.079(\mathrm{stat.}) \pm 0.034(\mathrm{exp.\ syst.})^{+0.036}_{-0.034}(\mathrm{model\ syst.}) \quad [0, 0.277]\ , \\
r_B^* &= 0.169 \pm 0.096(\mathrm{stat.})^{+0.030}_{-0.028}(\mathrm{exp.\ syst.})^{+0.029}_{-0.026}(\mathrm{model\ syst.}) \quad [0, 0.352]\ .
\end{aligned}$$

The errors are classified as above. The $(\gamma, \delta, \delta^*) \to (\gamma + 180^\circ, \delta + 180^\circ, \delta^* + 180^\circ)$ ambiguity solutions is also given. The values inside square brackets indicate the 1.96 standard deviation intervals (95% confidence-level for a 1-dimensional Gaussian distribution). The significance of CP violation is 2.4 standard deviations. Similar results can be obtained using a Bayesian statistic technique based on a somehow debatable uniform a priori distribution forγ, $\delta^{(*)}$ and ${r_B}^{(*)}$. In figure 72 (Left), it is shown the constraints on the $(\bar{\rho}, \bar{\eta})$ plane with measurement from tree level processes only: V_{ub}/V_{cb} from B semileptonic decays and γ from charged B decays [56]. The exclusion of the $\bar{\eta} = 0$ solution at 95% probability, estabilishes CP violation within the Standard Model.

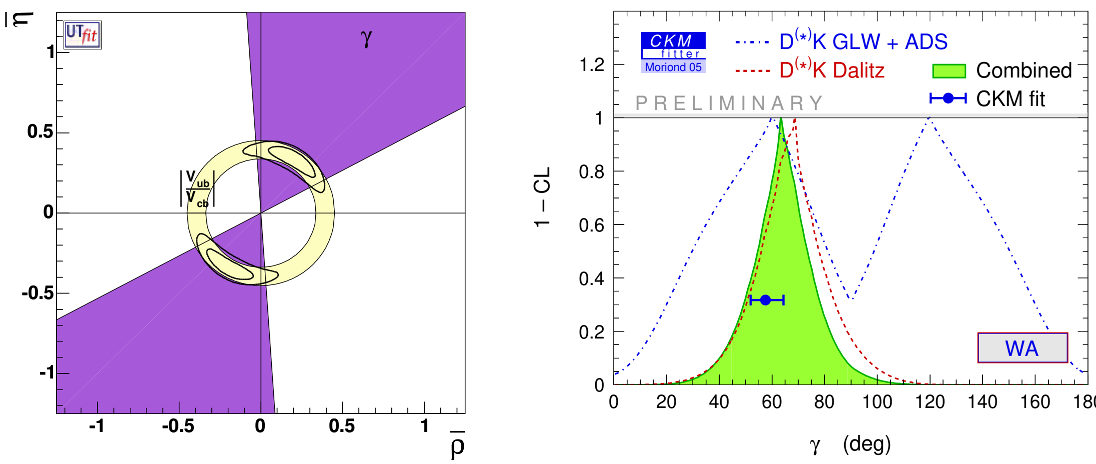

Figure 72: (Left) Constraints in the $(\bar{\rho}, \bar{\eta})$ with tree level processes.In particular, $\bar{\eta} = 0$ is excluded a 95% probility, definitely establishing CP violation as a feature of the Standard Model. (Right) Constraints on γ from $B \to D^{(*)}K$ decays (GLW+ADS and Dalitz analyses) compared to the prediction from the global CKM fit (not including these measurements).

The predictions of the Standard Model Theory for the angle γ from the CKM fit [57] are consistent with the constraints resulting from the experimental measurements, both *BABAR* and Belle combined, as shown in figure 72 (Right).

7.2 Perspectives

The present analysis, with the analogous one from Belle [50], is the best single measurement of the angle γ. The difference between the two statistical sensitivities on the γ value, i.e. $\simeq 30°$ for *BABAR* with respect to $\simeq 18°$ for Belle, can be explained in terms of the larger value of r_B fitted from the Belle data [30]. In figure 73 it is shown the strong dependence of the statistical sensitivity to the angle γ as a function of r_B. At present no precise measurement is available for the r_B value, for this reason it is not easy to make predictions for the future sensitivity to γ.

The analysis is still dominated by the statistical error but as soon as larger statistics will be available the systematic uncertainty will play a different role. In the near future we are planning to include a new decay mode: the $B^- \to DK^{*-}$. The statistical error on γ will improve as we will have a larger signal sample, but a more accurate treatment will be needed. $B^- \to DK^{(*)-}$ mode is a quasi-two-body decay, the main difference with respect to a 2-body decay is that the strong phase δ and the r_B value are in principle depending on

[30] $r_B = 0.26^{+0.10}_{-0.14} \pm 0.03 \pm 0.04, r_B^* = 0.20^{+0.19}_{-0.17} \pm 0.02 \pm 0.04$ first error is statistical, second experimental systematic and the third is the Dalitz model one.

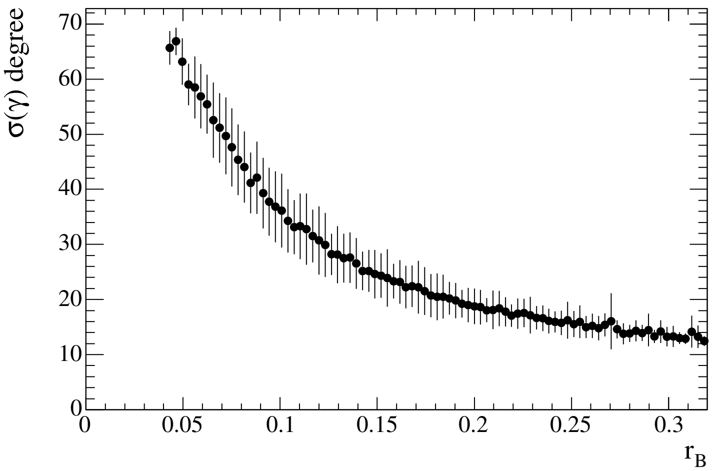

Figure 73: Error on γ as a function of the r_B parameter with the present statistics, corresponding to an integrated luminosity of $\sim 200fb^{-1}$.

the point in the B phase space. Furthermore a non-resonant component, $B^- \to D(K\pi)^-$, interferes with the quasi-two-body $B^- \to DK^{*-}$ resonant decay. These complications can be taken into account using an effective parameterization for the decay amplitude [71] and they do not represent a limit to the analysis.

The error on modelling the events in the Dalitz plane, can be improved and better evaluated using a different parametrization respect to the Isobar model we are using at present. The K-matrix formalism allows a more correct treatment for the S-wave component in the D decay amplitude [72], [28]. Recent studies, still very preliminary, don't show an evident disagreement among the phase motion and amplitudes over the phase space with respect to the Isobar model.

On the other hand even in presence of a very large sample, this error will dominate the measurement. In that perspective we are starting a detailed ToyMC study in order to evaluate the sensitivity using the model independent approach for the γ extraction in presence of a very large sample as we have discussed in section 1.5.1. The analysis with the model independent method can profit from the possible future measurements of the c_i and s_i coefficients coming from the $CLEO_C$ experiment.

References

[1] J. H. Christenson, J. W. Cronin, V. L. Fitch and R. Turlay,Phys. Rev. Lett. **13**, 138 (1964).

[2] B. Aubert *et al.* [BABAR Collaboration],Phys. Rev. Lett. **87**, 091801 (2001)

[3] K. Abe *et al.* [Belle Collaboration],Phys. Rev. Lett. **87**, 091802 (2001)

[4] B. Aubert *et al.* [BABAR Collaboration],Phys. Rev. Lett. **93**, 231801 (2004)

[5] B. Aubert *et al.* [BABAR Collaboration],arXiv:hep-ex/0412067.

[6] B. Aubert *et al.* [BaBar Collaboration],Phys. Rev. Lett. **93**, 131801 (2004)

[7] Y. Chao *et al.* [Belle Collaboration],Phys. Rev. Lett. **93**, 191802 (2004)

[8] N. Cabibbo, *Phys. ReV. Lett.* **10**, 531 (1963);
M. Kobayashi and T. Maskawa, *Prog. Theor. Phys.* **49**, 652 (1973).

[9] A. Angelopoulos *et al.* [CPLEAR Collaboration],Phys. Lett. B **444**, 43 (1998).

[10] L. Wolfenstein,Phys. Rev. Lett. **51**, 1945 (1983).

[11] H. Burkhardt *et al.* [NA31 Collaboration],Phys. Lett. B **206**, 169 (1988).

[12] V. Fanti *et al.* [NA48 Collaboration],Phys. Lett. B **465**, 335 (1999)

[13] A. Alavi-Harati *et al.* [KTeV Collaboration],Phys. Rev. Lett. **83**, 22 (1999)

[14] A. B. Carter and A. I. Sanda, Phys. Rev. Lett. **45** (1980) 952;Phys. Rev. D **23** (1981) 1567.

[15] I. I. Bigi and A. I. Sanda, Nucl. Phys. **B193** (1981) 85;Nucl. Phys. **B281** (1987) 41.

[16] I. Dunietz and J. Rosner, Phys. Rev. D **34** (1986) 1404.

[17] The *BABAR* Physics Book, (1998)

[18] The Heavy Flavor Averaging Group, http://www.slac.stanford.edu/xorg/hfag/ (Summer 2003 and Winter 2004 averages)

[19] M. Gronau and D.London, *Phys. Lett.* **B253**, 483 (1991).

[20] M. Gronau and D. Wyler, *Phys. Lett.* **B265**, 172 (1991).

[21] For a recent discussion, see M. Neubert and B. Stech, CERN-TH/97-99 (1997), hep-ph/9705292,to appear in *Heavy Flavours II*, Eds.A. J. Buras and M. Lindner, World Scientific, Singapore (1998).

[22] B. Aubert *et al.* [BABAR Collaboration], Phys. Rev. Lett. **92**, 202002 (2004); B. Aubert *et al.* [BABAR Collaboration], Phys. Rev. D **71**, 031102 (2005)

[23] D. Atwood, I. Dunietz and A. Soni, *Phys. Rev. Lett.* **78**, 3257 (1997);

[24] B. Aubert *et al.* [the BABAR Collaboration],arXiv:hep-ex/0408028.

[25] R. Fleischer, Int. Jour. Mod. Phys. **A12** (1997) 2459.

[26] A. Giri, Yu. Grossman, A. Soffer and J. Zupan, *Phys. Rev.* **D68**, 054018 (2003).

[27] R. H. Dalitz, *Phil. Mag.* **44**, 1068 (1953).

[28] V. V. Anisovich and A. V. Sarantsev,Phys. Lett. B **382**, 429 (1996)

[29] E. M. Aitala *et al.* [E791 Collaboration],Phys. Rev. Lett. **86**, 770 (2001).

[30] PEP-II - An Asymmetric B Factory, Conceptual Design Report,SLAC-418, LBL-5379 (1993).

[31] The *BABAR* Physics Book, Physics at an Asymmetric B Factory, P.F. Harrison, H.R. Quinn, Editors, SLAC-R-504 (1998).

[32] GEANT Detector Description and Simulation tool, CERN Program Library,Long Writeup W5013 (1994).

[33] T. Sjostrand and M. Bengtsson, Comput. Phys. Commun. **43**, 367 (1987).

[34] E. Barberio and Z. Was, Comput. Phys. Commun. **79**, 291 (1994).

[35] *BABAR* Technical Design Report, SLAC-R-457 (1995).

[36] B. Aubert *et al.* [BABAR Collaboration],Nucl. Instrum. Meth. A **479**, 1 (2002)

[37] P. Billoir, Nucl. Instr. Methods **A225** (1984) 225.

[38] B.N. Ratcliff, SLAC-PUB-5946 (1992); B. N. Ratcliff,SLAC-PUB-6067 (1993); P. Coyle *et al.,* Nucl. Instr. Methods **A343** (1994) 292.

[39] *BABAR* Analysis Document, **BAD116**.

[40] S. Brandt, Ch. Peyrou, R. Sosnowski, and A. Wroblewski, Phys. Lett. **12**, 57 (1964); E. Fahri, Phys. Rev. Lett. **39**, 1587 (1977).

[41] J. D. Bjorken, S. J. Brodsky, Phys. Rev. D **1**, 1416 (1970).

[42] G. C. Fox and S. Wolfram, Nucl. Phys. **B149**, 413 (1979).

[43] A. Drescher *et al.*, Nucl. Instr. Methods **A237**, 464 (1985).

[44] S. Eidelman *et al.* [Particle Data Group],Phys. Lett. B **592** (2004) 1.

[45] P. Lepage, A New Algorithm for Adaptive Multidimensional Integration, Journal of Computational Physics 27, 192-203, (1978)

[46] A. Bondar and T. Gershon, Phys. Rev. D **70**, 091503 (2004).3

[47] http://roofit.sourceforge.net/

[48] D. Lange, A. Ryd, *BABAR* Analysys Document, **BAD522**.

[49] S. Eidelman *et al.* [Particle Data Group Collaboration], Phys. Lett. B **592**, 1 (2004) (section on Statistics). See also for example: G. Zech, (hep-ex/0106023).

[50] A. Poluektov et al (Belle Coll.), Phys. Rev. D **70** 072003 (2004).

[51] G.J. Feldman and R.D. Cousins, Phys. Rev. D **57** 3873 (1998).

[52] K. M. Watson, Phys. Rev. **88** 1163 (1952).

[53] H. Pilkuhn, *The Interactions of Hadrons.* Amsterdam: North-Holland (1967).

[54] M. Gronau and D. London, *Phys. Lett.* **B253**, 483 (1991);
M. Gronau and D. Wyler, *Phys. Lett.* **B265**, 172 (1991);
I. Dunietz, *Phys. Lett.* **B270**, 75 (1991);
I. Dunietz, *Z. Phys.* **C56**, 129 (1992);
D. Atwood, G. Eilam, M. Gronau and A. Soni, *Phys. Lett.* **B341**, 372 (1995);
D. Atwood, I. Dunietz and A. Soni, *Phys. Rev. Lett.* **78**, 3257 (1997);

[55] C. Campagnari, O. Long and W. Verkerke, *BABAR* Analysis Document, **BAD 728**

[56] M. Ciuchini et al., *JHEP 0107* **013** (2001) (hep-ph/0012308).
for the updates see the web page : http:\\www.utfit.org

[57] Eur. Phys. J. C **21**, 225 (2001),[arXiv:hep-ph/0104062].

[58] S. Kopp et al. (CLEO Coll.) *Phys. Rev.* **D63** 092001 (2001);
H. Muramatsu et al. (CLEO Coll.) *Phys. Rev. Lett.* **89** 251802 (2002), Erratum-ibid: **90** 059901 (2003);

[59] K. Abe et al (Belle Coll.) (hep-ph/0308043).

[60] Aubert et al.(BaBar Collaboration, (hep-ex/0311032)

[61] A. Palano, Dalitz plot analysis of $D^0 \to K_s^0 K^+ K^-$. *BABAR* Analysis Document **BAD 911**.

[62] A. Palano, Dalitz plot analysis of $D^0 \to K_S^0 \pi^+\pi^-$, $D^0 \to K_S^0 K^+\pi^-$, and $D^0 \to K_S^0 K^+ K^-$. *BABAR* Analysis Document **BAD 120**.

[63] ARGUS Collaboration, H. Albrecht *et al.*, Z. Phys. C **48**, 543 (1990).

[64] http://www.slac.stanford.edu/BF/www/Physics/TrackEfficTaskForce/TrackingTaskForce-2003.html
http://www.slac.stanford.edu/BF/www/Physics/TrackEfficTaskForce/Recipe/KsTracks-R10.html

[65] J. Smith, A. Soffer, R. Waldi, Recomendation for Exclusive B reconstruction Analysis Variables. *BABAR* Analysis Document **BAD 407**.

[66] Phys. Rev. Lett. **78** 22 (1997)

[67] Phys. Rev. Lett. **21** 244 (1968)

[68] http://www.slac.stanford.edu/BFROOT/www/Physics/WednesdayMeetings/W073004/Neri.pdf http://www.slac.stanford.edu/BFROOT/www/Physics/WednesdayMeetings/W080404/Neri.pdf

[69] B. Aubert *et al.* [BABAR Collaboration],arXiv:hep-ex/0408088.

[70] B. Aubert *et al.* [BABAR Collaboration],arXiv:hep-ex/0504039.

[71] M. Gronau,Phys. Lett. B **557**, 198 (2003)

[72] M. R. Pennington,arXiv:hep-ph/9905241.

A Cartesian coordinates: Toy MC studies

Extensive Toy MC studies have been performed in order to verify the Gaussian behavior of the errors of the cartesian fit variables. In the following we show the results on the D^0K sample. Very similar results have been obtained also in the $D^{*0}K$ decay mode.

Figures 74 show the residual, error and pull distributions of the cartesian fit parameters obtained from a set of about 2K Toy MC experiments corresponding to the nominal fit to the data sample. The arrows show the results found in the data. The goodness-of-fit, estimated by counting the number of experiments with a likelihood value larger than that found in the data, is around 50%, perfectly in agreement with the value found when the fit is performed in polar coordinates. Similarly, figure 75 shows all the correlation coefficients for the two samples. From these figures we conclude that the cartesian fit parameters space behaves to an excellent approximation as single and independent Gaussians. The little (on average) correlation for the pair of variables (x_+, y_+) and (x_-, y_-) within a sample (D^0K or $D^{*0}K$) is taken into account in the PDF of the fitted parameters as a function of the generated parameters. The agreement between the simulation and the data is remarkable. From a closer look at the residual and pull distributions it is observed that in some case the mean values of the distributions are slightly biases. These biases are in all cases one order of magnitude below the statistical precision, and are due to the limited precision in the numerical Dalitz PDF normalization. Increasing the precision from the nominal 200×200 grid to 1000×1000 the biases essentially disappear.

Figures 76 show the residual distributions together with their mean values and rms of $(x_\pm, y_\pm)$ for D^0K, in 6 bins (0.05 units width each) of r_B truth. Despite the large (unrealistic) range of r_B truth, the width of the distributions are in all cases consistent within 10%, with no significant biases. Similarly, figures 77 and show the corresponding pull distributions, which have widths always consistent with unity.

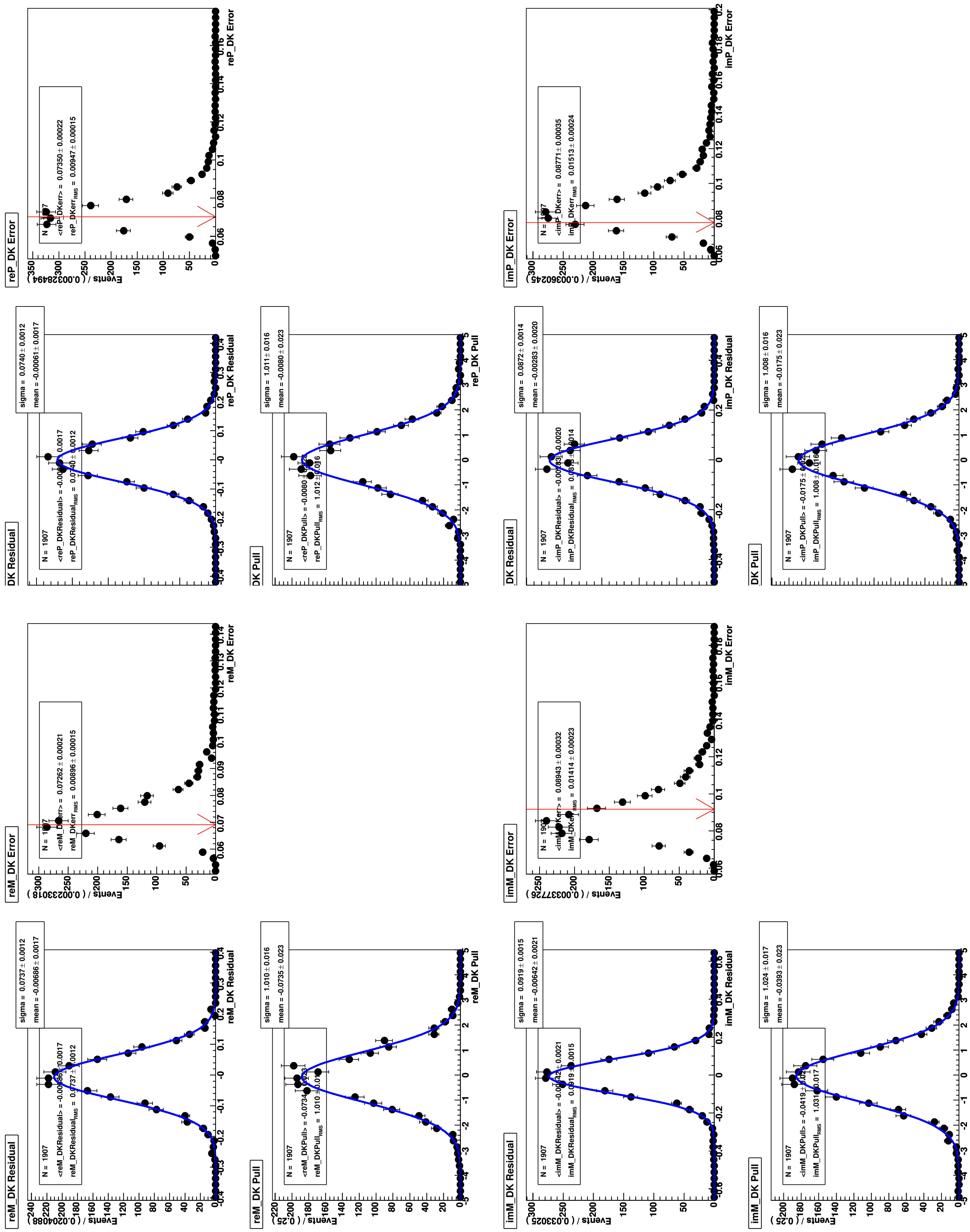

Figure 74: *Residual, error and pull distributions for x_+ (top left in landscape), y_+ (top right in landscape), x_- (bottom left in landscape) and y_- (bottom right in landscape) for the D^0K sample for the nominal Toy MC. The arrows show the results found in the data.*

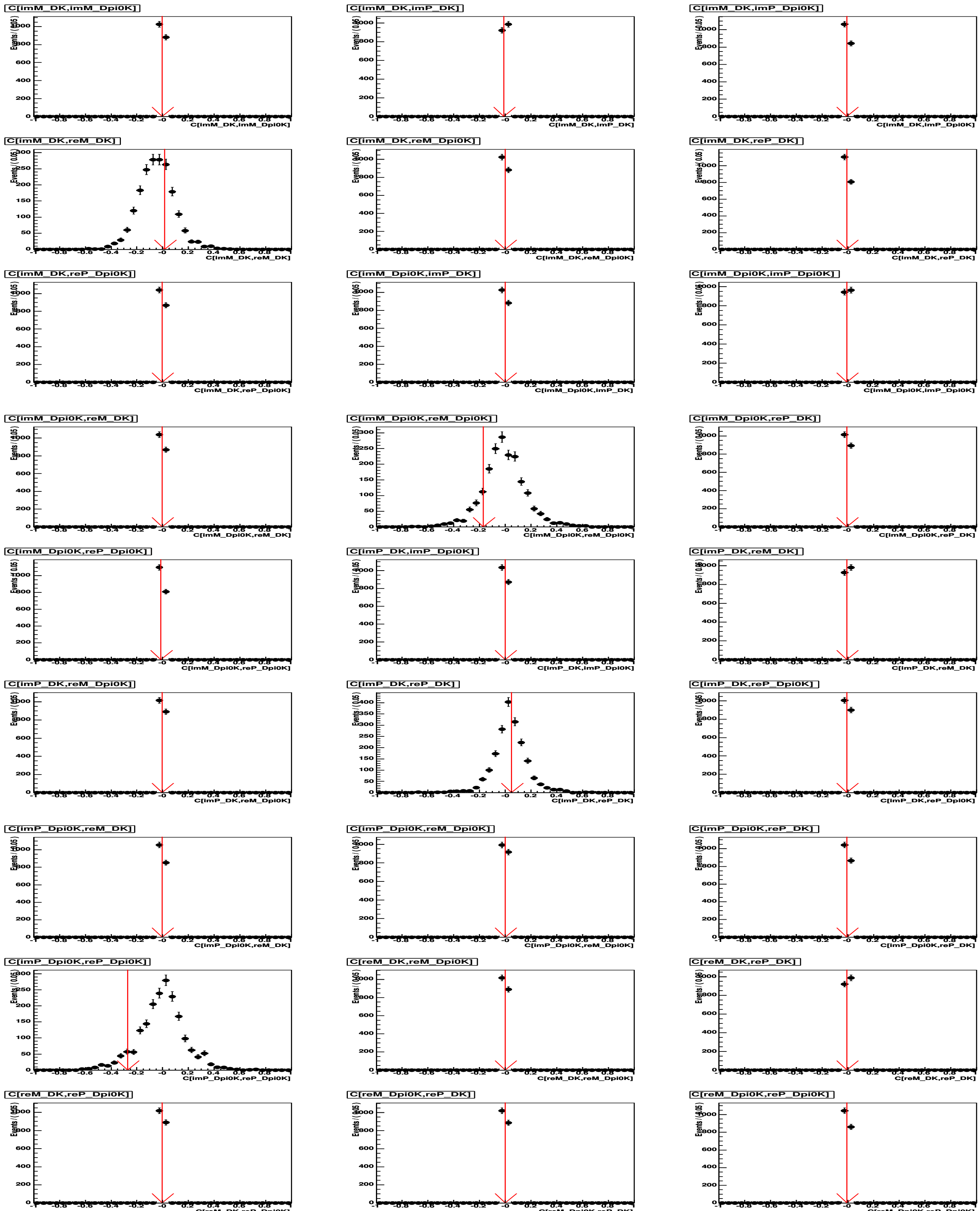

Figure 75: *Correlation coefficients among $(x_\pm, y_\pm)$ fit parameters for the D^0K and $D^{*0}K$ samples for the nominal Toy MC. The arrows show the results found in the data. It is clearly seen that the only non zero correlations appear for the pairs (x_+, y_+) and (x_-, y_-) within a given sample.*

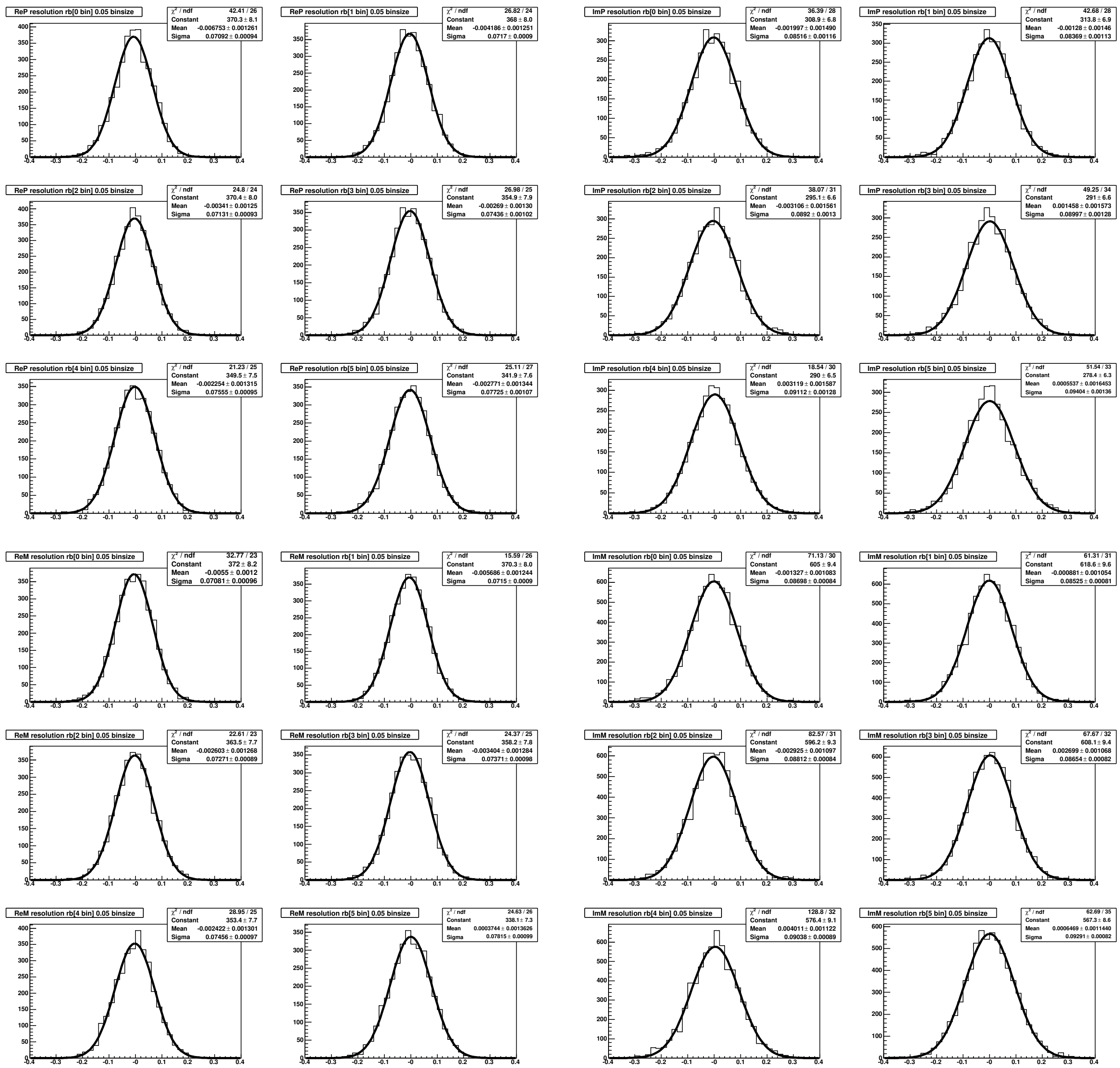

Figure 76: *Dependence of the rms of $(x_\pm, y_\pm)$ residual distributions, $(\sigma_{x\pm}, \sigma_{y\pm})$, in 6 bins of the truth r_B value, for the D^0K mode. The truth (generated) value of r_B has been obtained randomly in the range $[0, 0.3]$. As the the truth phases (both γ and δ) have also been generated randomly the obtained rms is averaged over all possible values of the phases.*

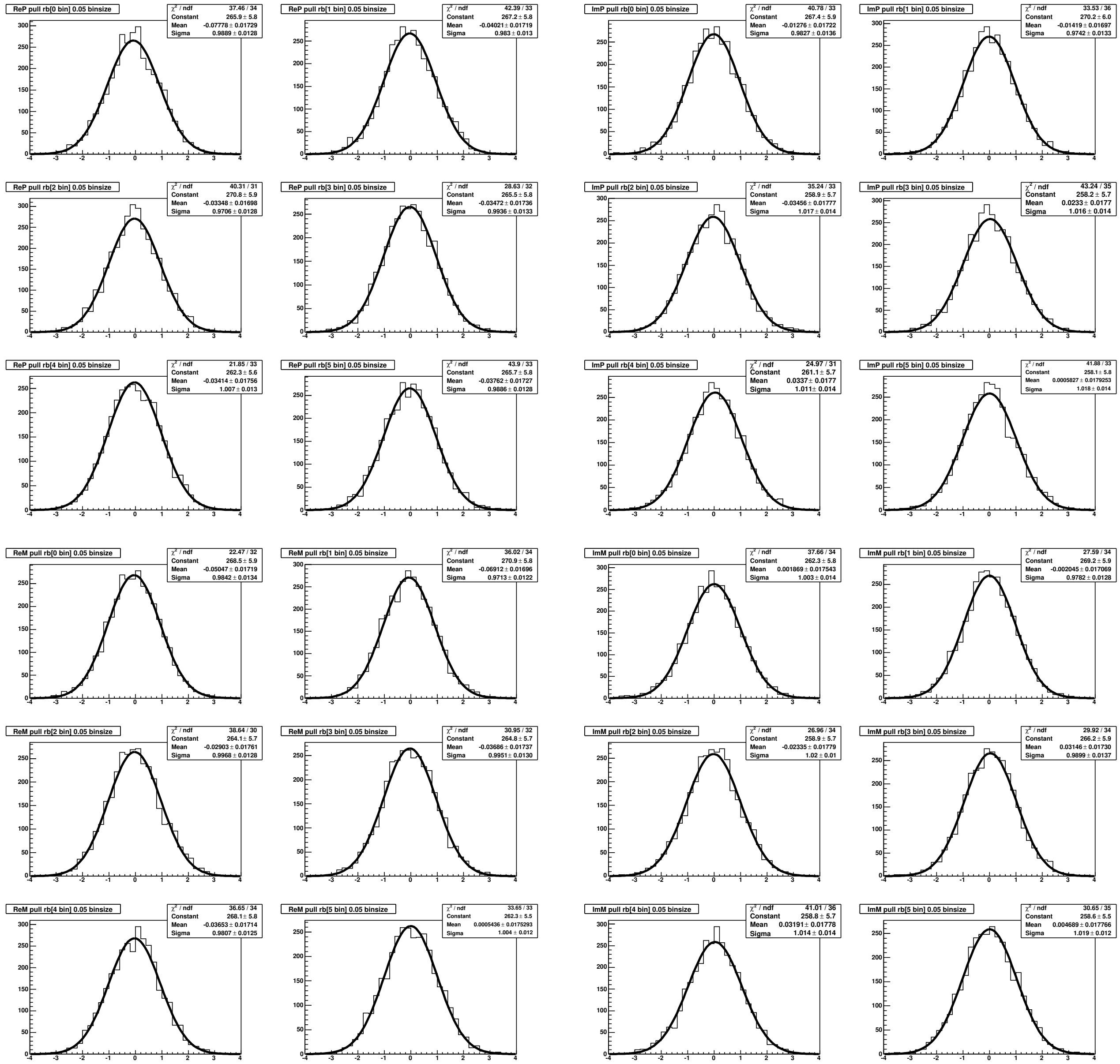

Figure 77: *Dependence of the rms of $(x_\pm, y_\pm)$ pull (residual normalized to the error) distributions in 6 bins of the truth r_B value, for the D^0K mode. The truth (generated) value of r_B has been obtained randomly in the range $[0, 0.3]$. As the the truth phases (both γ and δ) have also been generated randomly the obtained rms is averaged over all possible values of the phases.*

B Bayesian technique

B.1 Description of the method

The estimation of the confidence regions/intervals with the Bayesian approach requires the evaluation of the likelihood function $\mathcal{L}_{exp} \equiv \mathcal{L}_{exp}(r_B, \gamma, \delta)$ in the whole range of definition of r_B, γ and δ, $[0, 1]$, [-π,π] and [0,2π], respectively, with the yields floated at each given *CP* point. The estimate of the confidence region for the *CP* parameters implies a choice of *a priori* distribution. For this check we arbitrarily assume a uniform a priori distribution for each of the *CP* parameters r_B, γ and δ.

We define confidence region $D(\mathcal{C})$ at a given $\mathcal{C}$ confidence level the region in γ-r_B space such

$$\frac{\int_{D(\mathcal{C})} dr_B d\gamma \int_0^{2\pi} d\delta \mathcal{L}_{exp}(r_B, \gamma, \delta)}{\int_0^1 \int_{-\pi}^{\pi} \int_0^{2\pi} \mathcal{L}_{exp}(r_B, \gamma, \delta)\, dr_B d\gamma d\delta} = \mathcal{C} \ . \tag{141}$$

The $D(\mathcal{C})$ definition is arbitrary (this is always the case for confidence region) and we choose to define it by starting the integration procedure by the maximum of the likelihood function and by requiring that the likelihood value at any point in the boundary of D be the same (integration over all likelihood values larger than the value at the boundary). Notice that this can easily give disjoint region.

Similarly we can define the 1-dimensional confidence interval at $\mathcal{C}$ confidence level for, say, r_B, as

$$\frac{\int_{I(C)} dr_B \int_{-\pi}^{+\pi} d\gamma \int_0^{2\pi} d\delta \mathcal{L}_{exp}(r_B, \gamma, \delta)}{\int_0^1 dr_B \int_{-\pi}^{\pi} d\gamma \int_0^{2\pi} d\mathcal{L}_{exp}(r_B, \gamma, \delta)\, dr_B d\gamma d\delta} = \mathcal{C} \ , \tag{142}$$

where again $I(\mathcal{C})$ can be a set of disjoint interval.

In this way we expect that such intervals have the correct coverage. Notice that the effect of the bias on r_B is completely irrelevant for γ and δ measurements (we make no use of the concept of fitted r_B value).

B.2 1- and 2-dimensional confidence regions for D^0K and $D^{*0}K$

In figure 78 we show the confidence region for $\gamma^{(*)}$ versus ${r_B}^{(*)}$, for D^0K and $D^{*0}K$. The red region is the 68% CL region while the yellow one is the 95% CL. Similarly, figures 79 and 80 show the confidence regions for $\gamma^{(*)}$ versus $\delta^{(*)}$ and $\delta^{(*)}$ versus ${r_B}^{(*)}$, for D^0K and $D^{*0}K$. In figures 81 and 82 we show the probability density functions for ${r_B}^{(*)}$, $\gamma^{(*)}$ and $\delta^{(*)}$ for D^0K and $D^{*0}K$, respectively, obtained by integrating the experimental likelihood for all the values of the other variables: $\gamma^{(*)}$, $\delta^{(*)}$; ${r_B}^{(*)}$, $\delta^{(*)}$; and ${r_B}^{(*)}$, $\gamma^{(*)}$. On the same figures we show the confidence intervals at 68% (red) and 95% (yellow) CL. Notice that the likelihood distribution is nicely showing the $\pm\pi$ ambiguity in $\gamma^{(*)}$ and $\delta^{(*)}$. The probability density function for ${r_B}^{(*)}$ shows clearly the non-Gaussian behavior we expect from Toy Monte Carlo, showing the poor sensitivity to small values of ${r_B}^{(*)}$. In figure 83 we show the probability density function for γ from the combination of the D^0K and $D^{*0}K$ likelihoods, integrated over r_B, ${r_B}^*$, δ and δ^*.

Table 33 reports the confidence intervals for the various parameters (statistical only). For the central values we quote the expectation value using the experimental likelihood, and the 1σ error is given by the 68% confidence limit region around the expectation value. For the phases we have symmetrized the errors taking the largest between the positive and negative errors. The results include the intrinsic two fold ambiguity for the weak and strong phases.

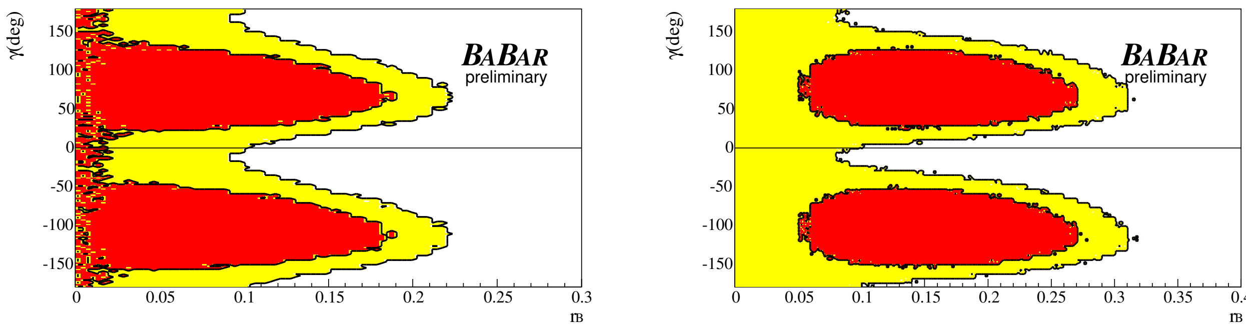

Figure 78: *68% (red) and 95% (yellow) Bayesian confidence region in* $\gamma^{(*)}$*-*${r_B}^{(*)}$ *plane for* D^0K *(left) and* $D^{*0}K$ *(right).*

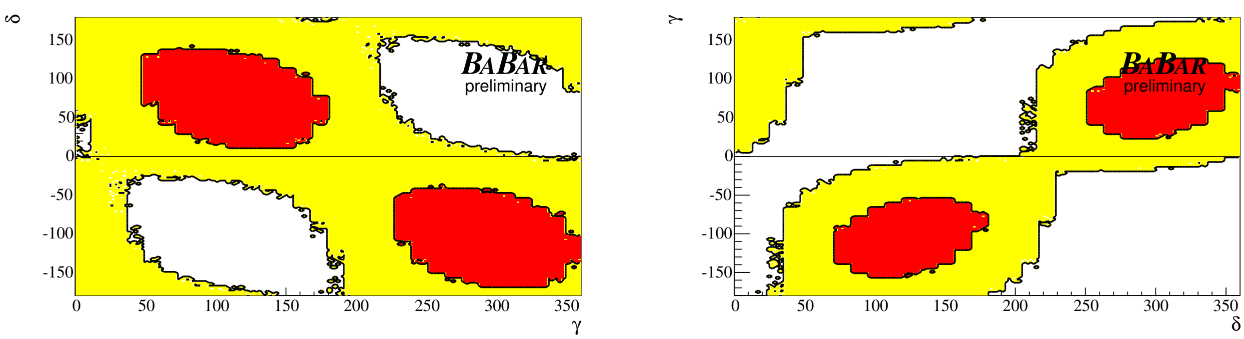

Figure 79: *68% (red) and 95% (yellow) Bayesian confidence region in* $\gamma^{(*)}$*-*$\delta^{(*)}$ *plane for* D^0K *(left) and* $D^{*0}K$ *(right).*

Since the Frequentist method is the one adopted to quote final results no dedicated evaluation of systematic uncertainties has been performed. However, with a very good approximation we can assign the symmetrized experimental and Dalitz model systematic errors obtained in the Frequentist approach, as given in table 34.

Comparing the Bayesian results with those of the Frequentist method, we observe that we obtain similar results. This is not intended to be a proof of the validity of one method versus the other because we know that the two statistical approaches are completely different and it is not possible to make comparisons. Besides that, it is nice to know that the results are similar.

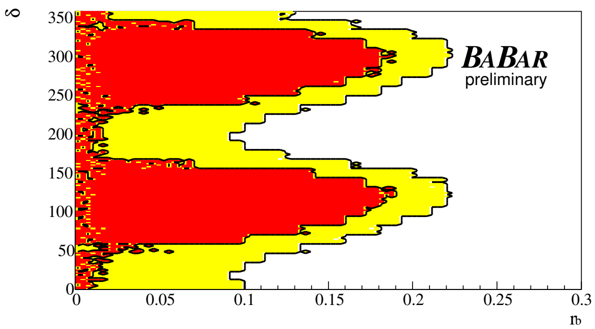

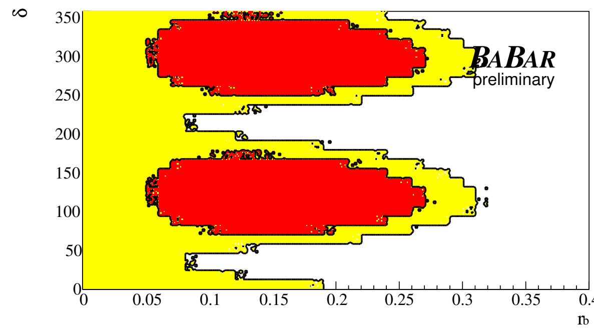

Figure 80: *68% (red) and 95% (yellow) Bayesian confidence region in $\delta^{(*)}$-$r_B{}^{(*)}$ plane for D^0K (left) and $D^{*0}K$ (right).*

Parameter	68% CL (stat. only)	95% CL (stat. only)	Central value with error (1σ)
γ	[-147,-65] [33,114]	[-180,-23] [-2,157] [179,180]	70 ± 44
γ^*	[-140,-72] [41,108]	[-172,-31] [9,148]	73 ± 35
δ	[74,155] [253,335]	[0,13] [189,192] [212,360]	114 ± 41
δ^*	[89,157] [269,337]	[0,16] [55,195] [234,360]	303 ± 34
r_B	[0.01,0.13]	[0,0.19]	$0.087^{+0.041}_{-0.074}$ [0.071 ± 0.058]
r_B^*	[0.08,0.22]	[0,0.27]	$0.155^{+0.070}_{-0.077}$ [0.152 ± 0.074]
γ (combined)	[-132,-83] [48,97]	[-156,-50] [23,130]	70 ± 26

Table 33: *Bayesian confidence intervals for $\gamma^{(*)}$, $\delta^{(*)}$ and $r_B{}^{(*)}$ (statistical only). Angles are given in degree. The Bayesian confidence intervals for the combination of the D^0K and $D^{*0}K$ channels is also given. In the last column the central values with 1σ errors are also reported. For the $\gamma^{(*)}$ and $\delta^{(*)}$ intervals the $\pm180°$ solution is also indicated. For the central values we quote the expectation value using the experimental likelihood, and the 1σ error is given by the 68% confidence limit region around the expectation value. For the phases we have symmetrized the errors taking the largest between the positive and negative errors.*

Parameter	Central value with error (1σ)
γ (combined)	$70 \pm 26 \pm 11 \pm 13$
δ	$114 \pm 41 \pm 19 \pm 20$
δ^*	$303 \pm 34 \pm 13 \pm 15$
r_B	$0.087^{+0.041}_{-0.074} \pm 0.034 \pm 35$ [$0.071 \pm 0.058 \pm 0.034 \pm 35$]
r_B^*	$0.155^{+0.070}_{-0.077} \pm 0.029 \pm 0.028$ [$0.152 \pm 0.074 \pm 0.029 \pm 0.028$]

Table 34: *Bayesian central values with 1σ statistical and systematic errors for γ, $\delta^{(*)}$ and $r_B{}^{(*)}$ (angles are in degree). The first errors are statistical, the second are experimental systematics and the third are Dalitz model systematics. The statistical errors are the same as those reported in table 34. The systematic uncertainties are the symmetrized systematic errors obtained with the Frequentist approach, as reported in table 31.*

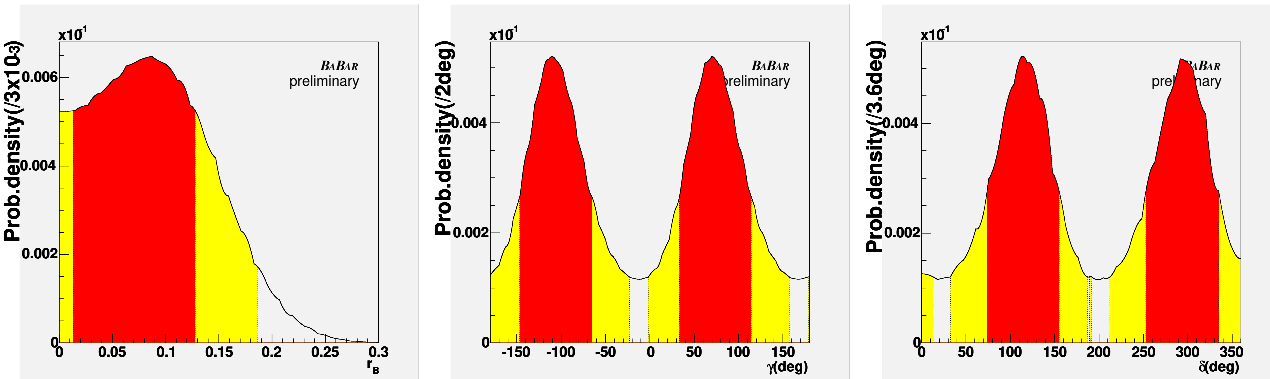

Figure 81: *Probability density functions for* r_B, γ *and* δ *for* $D^0 K$. *68% (red) and 95% (yellow) Bayesian confidence intervals are shown.*

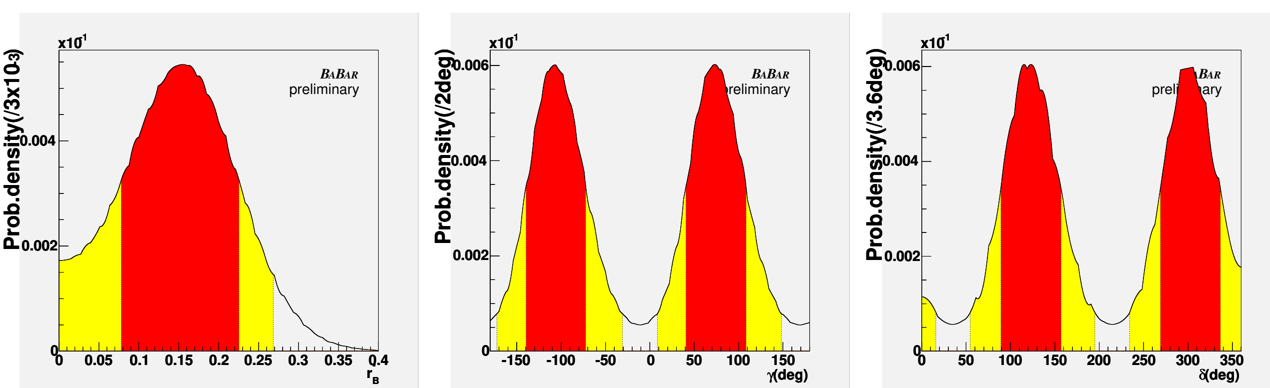

Figure 82: *Probability density functions for* $r_B{}^*$, γ^* *and* δ^* *for* $D^{*0}K$. *68% (red) and 95% (yellow) Bayesian confidence intervals are shown.*

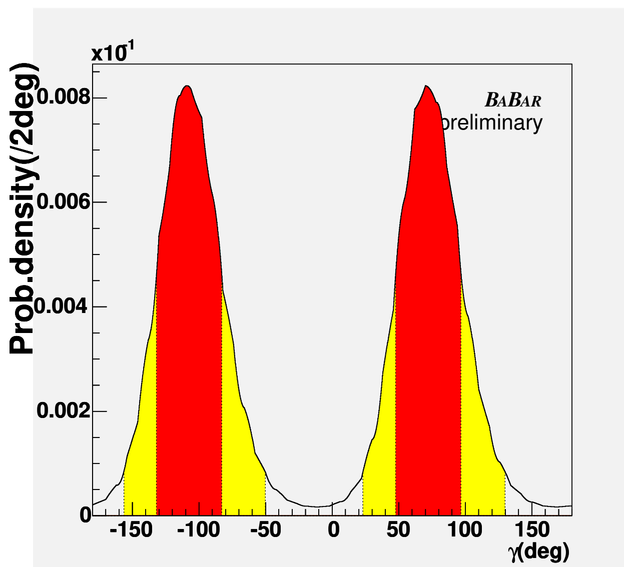

Figure 83: *Probability density function for γ for the D^0K-$D^{*0}K$ combination. 68% (red) and 95% (yellow) Bayesian confidence intervals are shown.*